STUDYING ELECTRONS ON HELIUM VIA SURFACE ACOUSTIC WAVE TECHNIQUES

By

Heejun Byeon

A DISSERTATION

Submitted to
Michigan State University
in partial fulfillment of the requirements
for the degree of

Physics and Astronomy - Doctorate of Philosophy

2020

ABSTRACT

STUDYING ELECTRONS ON HELIUM VIA SURFACE ACOUSTIC WAVE TECHNIQUES

By

Heejun Byeon

This thesis describes novel methods and experiments for investigating electrons floating on the surface of liquid helium by utilizing surface acoustic wave (SAW) techniques. Electrons on helium are an ideal system for studying a non-degenerate two-dimensional electron system (2DES), Wigner cyrstallization, and the coupling of a 2DES to a bosonic field. The electrons in this system are also interesting with regard to quantum information science due to their predicted long coherence time. An evanescent coupling of electrons to high-frequency SAWs submerged beneath the liquid helium provides a probe of the high-frequency conductivity of the 2DES and can be used to create SAW-driven charge transport of the electron system and opens the door for resonant interaction between SAWs and collective modes of the electron system.

Before employing SAW techniques, we first examined the low-frequency transport properties of electrons on helium at several tens of kHz using a lock-in method, which confirms the realization of a stable and reproducible 2D electron system on liquid helium. Furthermore, taking advantage of the capactive coupling of the electron layer and submerged electrodes, we are able to precisely control AC current flows in the 2DES and achieve the analog of a field-effect transistor with electrons on helium and demonstrate the applicability of long wavelength transport at high temperature and low electron density.

By coupling SAWs to the system, the SAW-liquid helium interaction is investigated by measuring the loss of SAW energy into the liquid. We find that the attenuation of the SAW

in bulk liquid helium is dominated by the radiation of compressional wave into the liquid, in a good agreement with theory and previous experiments. However, for sufficiently thin helium coverage (several tens of nm), the attenuation anomalously increases beyond that measured in a thick helium layer. This novel phenomenon is likely associated with the electrostrictive actuation of the helium surface. Furthermore, this study is a prerequisite for quantitatively analyzing the SAW measurement results obtained for the 2DES on the liquid helium surface.

In last two chapters, we present a detailed study of the SAW coupling to surface electrons floating above liquid helium in both the weak and the strong coupling regimes. These experiments demonstrate find acoustoelectric charge transport and the SAW attenuation in this system of electrons on helium for the first time. These experiments open the door to a new class of studies with this system. These include quantized charge pumping, the possibility of electrical metrology, and ultimately single electron state transfer with electrons floating on the helium. Also, this coupled system can be utilized to study a commensurate-incommensurate transition of the 2DES under a time-dependent periodic electric potential (i.e. a standing piezoelectric SAW). Furthermore, the high-sensitivity of the SAW to the spatial structure of the 2DES can provide a new method of studying the 2D phase transition in the electrons on helium system.

Copyright by
HEEJUN BYEON
2020

ACKNOWLEDGMENTS

First of all, I would like to thank my thesis advisor, Johannes Pollanen, who offered a research opportunity to me five years ago at Michigan State University. He has taught me all about the low temperature experimental physics through numerous discussions and by working closely with me in the lab. I deeply appreciate Johannes for sharing his expertise and deep insight of physics whenever encountering problems. But most importantly, his positive mindset and enthusiasm for physics always motivates me not to be afraid of failure and take a step forward from it.

I also would like to thank my thesis committee, especially Mark Dykman for helpful discussions about electrons on helium early in my Ph.D. Also, his course on quantum fluid and quantum transport has been one of the most influential classes of my academic career and greatly helped widen my knowledge about quantum physics.

Many people at Michigan State have helped me complete my Ph.D. work. Among the faculty, I would like to thank Vladimir Zelevinsky and Scott Bogner for their outstanding graduate lectures. I am also grateful to Norman Birge for advice about nano-fabrication processes. Among my fellow group members, there were Liangji, Justin, Anna, Joshua, Kostya, Stephen, Niyaz, Trayn, Evan, Brennan, Joe, and Camille. I would especially like to thank Liangji and Justin for their assistance with SAW device fabrication and measurements. Also, thanks to Kostya and Niyaz, who have provided constructive and meaningful discussion about electrons on helium. I am indebted to Reza Loloee for his technical assistance and keeping the CMP labs running smoothly. Thanks to Baokang Bi for the training and great advice about fabrication processes.

Lastly, I am particularly indebted to my wife and family for their unfailing support and encouragement during my Ph.D. study at Michigan State.

The projects described in this thesis were partially supported by the National Science Foundation under grant numbers DMR-1708331 and DMR-2003815.

TABLE OF CONTENTS

LIST OF TABLES

LIST OF FIGURES

Chapter 1

Brief Introduction to Electrons on Helium

Electrons on helium are a unique two-dimensional electron system (2DES), where electrons are able to float several nanometers above the liquid helium surface due to Pauli repulsion at short ranges and attraction at long range caused by induced positive image charges inside the helium. Because of the strong Coulomb interaction between electrons, the system of electrons floating on helium is an ideal model for experimental realization of an electronic crystal phase of strongly correlated electrons predicted originally by Wigner in 1934 [5, 6, 17]. In the liquid phase, electrons on helium exhibit the features of the strongly correlated non-degenerate liquid with unusual transport properties at low frequency [18, 19, 20, 21]. The absence of defect in this system leads to the highest mobility in all of condensed matter ($\mu > 10^8$ cm^2/Vs) [22], which is several orders of magnitude larger than two-dimensional electron systems (2DESs) in semiconductor materials (μ_{Si}, $\mu_{\mathrm{GaAs}} < 10^6$ cm^2/Vs). In addition, the ultra clean physical environment in which electrons reside in vacuum above the defect-less liquid helium substrate, can exclude many potential source of interaction with the electrons leading to slow electron decoherence. Thus, as a candidate for quantum information processing, this system has been actively investigated in recent years [23, 24, 25, 26, 27, 28].

A surface acoustic wave (SAW) on a peizoelectric substrates is accompanied by dynamic electric fields and an electric potential wave, which can interact with a 2D electron system located within approximately one wavelength above or below the piezo-substrate surface. Such an interaction enables SAWs to be versatile tools for exploring wavelength and frequency dependent electronic properties of 2DESs. In semiconductor 2DESs, surface acoustic wave techniques have been successful for studying the integer [29, 30, 31] and fractional [32] quantum Hall regimes, demonstrating the gate-controlled acoustoelectric transport [33, 34], as well as for investigating the 2D metal-to-insulator transition [35]. In particular, short wavelengths of high-frequency SAWs ranging from tens of nanometer to several micrometer allow for the study of commensurability effects when the SAW wavelength becomes comparable to some length scale within the 2DES [36, 37]. However, SAW methods has not been previously employed to investigate electrons on helium. The extension of SAW techniques to electrons on helium would allow for the study not only of the wave-vector and frequency dependent conductivity in a high-frequency regime but also collective dynamics and resonant response of the strongly correlated quantum system to high-frequency SAW excitation. In addition, the high-sensitivity of SAW to the spatial structure of 2DESs can be utilized to develop powerful tools for studying 2D phase transition driven by unbinding of topological defects. Furthermore, acoustoelectric charge transport driven by a travelling SAW potential has recently attracted particular attention as a means of controlling and transporting single electrons. Employing micro-/nano-structures (quasi 1D channels and 0D quantum dots) and the lack of disorder can make the system of electrons on helium an excellent platform for realizing SAW-driven single-electron devices, or potentially utilized as a novel method to trap single electrons for quantum information science or quantum metrology application [38].

Chapter 2

Electrons on Helium

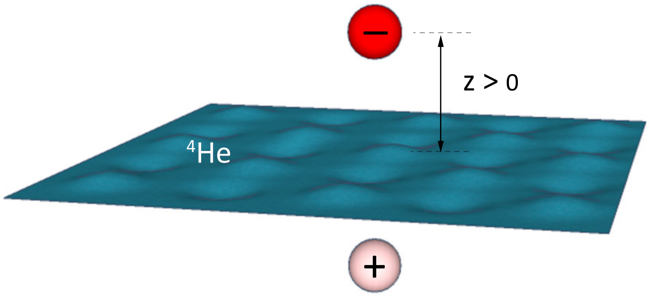

Figure 2.1: Single electron above the surface of the liquid helium along with an image charge below the surface. The helium surface supports thermally excited quantized capillary waves called ripplons, which weakly interact with the electron.

A two-dimensional electron system (2DES) floating above the surface of superfluid helium was first theoretically proposed by Cole and Cohen [39] and by Shikin [40] and first achieved experimentally Williams *et al.* [41]. Since then, it has attracted great interest in condensed matter physics due to a rich variety of physics including Wigner crystallization [5], 2D plasmons [7], and unique polaronic effects [42], and the formation of a strongly correlated nondegenerate 2D electron fluid [18, 43]. The system is also interesting in Quantum Information Science (QIS) with the possibility of long-lived qubits with electrons on helium, arising from ultra-clean environment. In this chapter, the basic properties of surface electrons formed on a liquid helium substrate are introduced and discussed.

2.1 Surface Electron States on Liquid Helium

An electron in the vicinity of the surface of liquid ^{4}He is attracted to the surface by the electrostatic image force arising from the polarization of the dielectric liquid as shown in Fig. 2.1. As surface electrons (SEs) are far distant from the helium surface, the image potential energy for $z > 0$ can be written as [44]

$$V_{\text{im}}(z) = -\frac{\Lambda e^2}{z + z_0} \approx -\frac{\Lambda e^2}{z} \tag{2.1}$$

with

$$\Lambda = \frac{\epsilon - 1}{4(\epsilon + 1)}, \tag{2.2}$$

where ϵ is the dielectric constant of liquid ^{4}He, e is the elementary charge, and z_0 is an offset parameter to avoid the singularity at the interface with a typical value of $z_0 \simeq 1$Å. In inert gases such as helium, the last electronic shell of the atoms is completely filled with no available states for additional electrons. This means liquids made from the noble gases usually have a strong repulsive barrier to electron injection. For ^{4}He, the height of this barrier is approximately $V_b \sim 1$ eV [45, 46]. Since z_0 is much smaller than average distance $\langle z \rangle$ of the electrons from the liquid surface and the barrier energy largely exceeds the attractive binding energy (< 1 meV), the total potential energy V_{e} can be simplified as follows

$$V_{\text{e}}(z) = -\frac{\Lambda e^2}{z} \quad (z > 0) \quad \text{or} \quad +\infty \quad (z \leq 0). \tag{2.3}$$

Therefore, at low temperature, the electrons are confined in a potential well produced by V_{e} with quantized motion normal to the surface (Fig. 2.2). Parallel to the surface, electrons can be considered as nearly free particles.

2.1.1 Rydberg Surface State

The wave function of the electrons above the surface of liquid helium can be separated into a plane wave representing in-plane motion and a one-dimensional (1D) quantized wave function χ_{n} for vertical motion:

$$\Psi_{\mathrm{n}}(\vec{r}, z) = \frac{1}{\sqrt{S_{\mathrm{A}}}} e^{i\vec{k}\cdot\vec{r}} \chi_{\mathrm{n}}(z), \tag{2.4}$$

where $\vec{k}$ is 2D in-plane wave vector, $\vec{r}$ is the position vector in the plane, n is the quantum number describing vertical motion of the electron, and S_{A} is the surface area containing electrons. Assuming perfectly flat helium surface, the motion of SEs perpendicular to the liquid resembles a one-dimensional hydrogen atom with a reduced nuclear charge Λe. Thus, the energy E_{n} of the vertical motional eigenstate is given by [40]

$$E_{\mathrm{n}} = -\frac{\Lambda^2 m_{\mathrm{e}} e^4}{2\hbar^2 n^2} = -\frac{R_y^*}{n^2}, \quad n = 1, 2, 3, ... \tag{2.5}$$

where R_y^* is the effective Rydberg energy and m_{e} is electron mass. For liquid ^{4}He, R_y^* is estimated to be ~ 0.658 meV from $\epsilon = 1.05723$ and $\Lambda \simeq 6.95 \times 10^{-3}$. The energy eigenstates of this motion in the position basis $\chi_{\mathrm{n}}(z) = \langle z|n\rangle$ are determined by solving one-dimensional Schrödinger equation:

$$\left[-\frac{\hbar^2}{2m_{\mathrm{e}}}\frac{\partial^2}{\partial z^2} - \frac{\Lambda e^2}{z}\right]\chi_{\mathrm{n}} = E_{\mathrm{n}}\chi_{\mathrm{n}}. \tag{2.6}$$

The wave functions of two lowest states $\chi_1(z)$ and $\chi_2(z)$ are

$$\chi_1(z) = \frac{2}{a^{3/2}} z e^{-z/a}, \tag{2.7}$$

$$\chi_2(z) = \frac{1}{\sqrt{2}a^{3/2}} z(1 - z/2a) e^{-z/2a}, \tag{2.8}$$

where a is an effective Bohr radius of the electron state defined by

$$a = \frac{1}{\Lambda} \frac{\hbar^2}{m_e e^2} = \frac{a_0}{\Lambda} \tag{2.9}$$

with $a_0 = \hbar^2/m_e e^2 \simeq 0.53$ Å. The effective Bohr radius is about 76 Å for liquid ^{4}He. Fig. 2.2 shows the lowest energy levels E_n and the probability, of vertical motional wave function $|\chi_n|^2$ alongside the potential energy V_e. The average distance of the electron from the surface of liquid helium $\langle z \rangle \sim a_0 \simeq 76$Å is much larger than the spacing of the helium atoms $r_0 \sim 2a_0 \simeq 1$ Å, which leads to negligible scattering from the corrugation of the

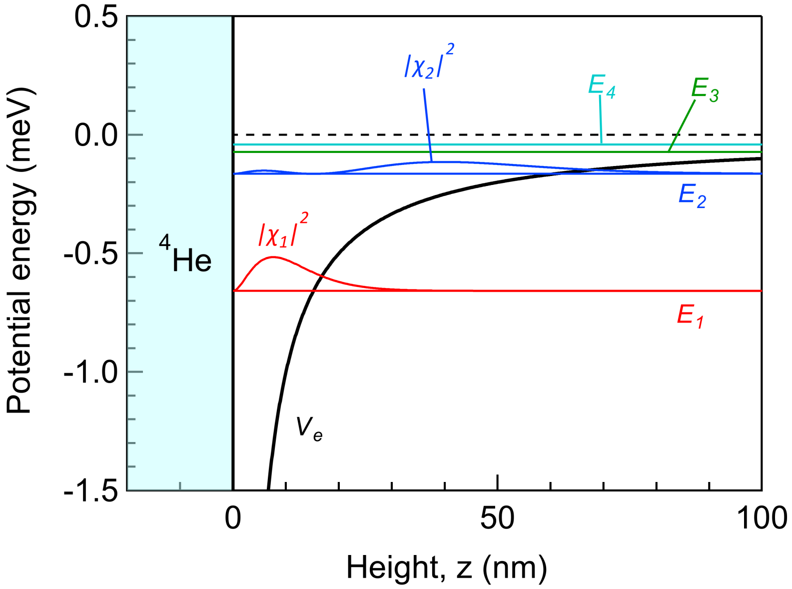

Figure 2.2: Energy spectrum and the probability for wave functions of an electron bound to the helium surface.

surface due to individual atoms. Thus, electrons staying relatively far away from the surface are able to move like free particles. The average distance from the surface for three lowest electron energy levels is given by

$$\langle 1|z|1\rangle \simeq 141\ \text{Å}, \quad \langle 2|z|2\rangle \simeq 456\ \text{Å}, \quad \langle 3|z|3\rangle \simeq 1027\ \text{Å}. \tag{2.10}$$

The ground state energy is $E_1 = -0.66$ meV (-7.63 K) and the first and the second excited state energies are $E_2 = -0.16$ meV (-1.91 K) and $E_3 = -0.07$ meV (-0.85 K). The energy required for a transition of the electron from the ground state to the first excited state is $E_2 - E_1 = 5.72$ K, which is significantly larger than the working temperature of our experiments T $\sim$ 1 K, meaning that most of electrons are in the lowest Rydberg energy level E_1. The transition frequency between these states $\nu_{\mathrm{n}\to\mathrm{m}}$ can be estimated from the hydrogen atom-like spectral series:

$$\nu_{\mathrm{n}\to\mathrm{m}} = \frac{E_{\mathrm{m}} - E_{\mathrm{n}}}{h} = \frac{R_y^*}{h}\left(1/n^2 - 1/m^2\right). \tag{2.11}$$

This yields $\nu_{1\to 2} \simeq 119.3$ GHz and $\nu_{1\to 3} \simeq 141.3$ GHz, which is in good agreement with spectroscopic measurement data $\nu_{1\to 2} \simeq 125.9 \pm 0.2$ GHz and $\nu_{1\to 3} \simeq 148.6 \pm 0.3$ GHz [1]. Note that these estimations were made based on the infinite potential barrier approximation at $z = 0$ (equation 2.3). In reality, the potential barrier at the surface has a finite energy $V_{\mathrm{b}} \sim 1$ eV and a not completely flat helium surface leads to a small disturbance in the barrier position at $z = 0$. Thus, they are responsible for a small deviation of ~5 % between theory and experiment for the energy levels [47].

2.1.2 External Field Effects

In most experiments, an external electric field $E_\perp$ normal to the electron layer is typically applied, which modifies the asymptotic form of the potential V_e:

$$V_\mathrm{e} = V_\mathrm{im} + V_\mathrm{b} + eE_\perp z. \tag{2.12}$$

The barrier V_b can still be approximated by an infinite barrier $V_\mathrm{b} = \infty$ for $z \leq 0$ and $V_\mathrm{b} = 0$ for $z > 0$ while $V_\mathrm{im}(z) = -\Lambda e^2/z$ for $z > 0$ and $V_\mathrm{im}(z) = 0$ for $z \leq 0$ as described in the previous section. A positive field $E_\perp$ produces a linearly increasing potential V_e for large z leading to a more stable bound state of electrons by pressing them into the surface more strongly. For the case of a negative pressing field ($E_\perp < 0$), the trapping potential has a triangular shape with increasing z allowing electrons to escape the surface via the tunneling as shown in Fig. 2.3 (a).

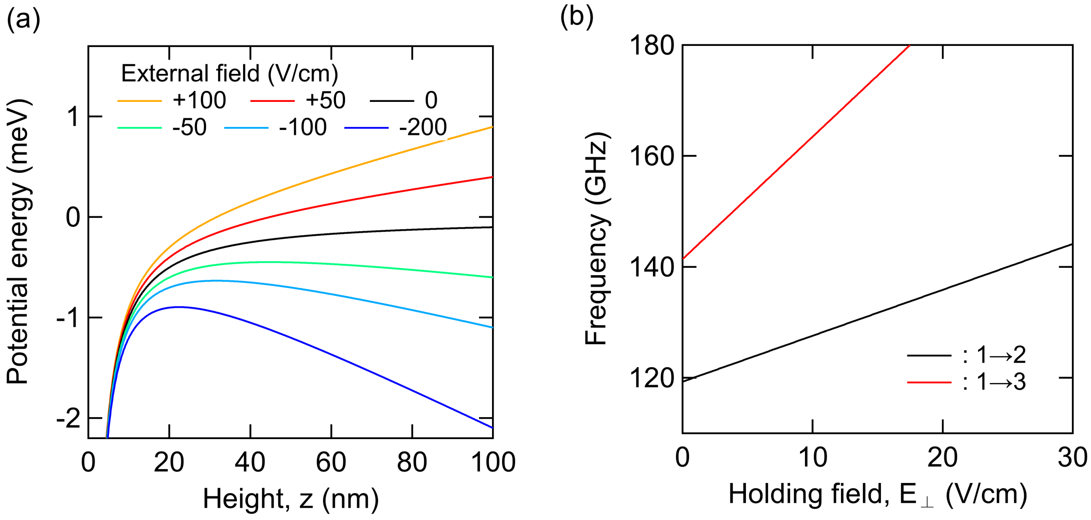

Figure 2.3: (a) Potential energy V_e change at different external fields. (b) Linearly Stark-shifted transition frequency for $1 \rightarrow 2$ and $1 \rightarrow 3$ Rydberg transitions.

The wave function of the ground state can be found with a variational method using a trial wave:

$$\chi_1(z) = \frac{2}{b^{3/2}} z e^{-z/b}. \tag{2.13}$$

This has the same shape as the ground state wave function at $E_\perp = 0$ in equation 2.7 except that the zero-field effective Bohr radius a is replaced with the pressing field dependent one $b = b(E_\perp)$. The relationship between $b(E_\perp)$ and a is given by [10].

$$\frac{b}{a} = \frac{4}{3\lambda}\sinh\left(\frac{1}{3}\text{arcsinh}\left(\frac{9\lambda}{4}\right)\right) \tag{2.14}$$

with $\lambda = \sqrt{E_\perp/E_\mathrm{c}}$ where a characteristic field $E_\mathrm{c} = \hbar^2/2m_\mathrm{e}ea^3$. Here λ is a parameter that represents the strength of the holding field compared to $E_\mathrm{c} \simeq 0.9$ kV/cm. At weak holding fields ($\lambda \ll 1$), the first order correction to the energy levels can be found via perturbation theory, which produces a result that is equivalent to the linear Stark shift:

$$\Delta E_\mathrm{n}^1 = eE_\perp \langle n|z|n\rangle. \tag{2.15}$$

This linear shift has been observed in spectroscopic measurement of transitions between bound electron states above the liquid helium surface [48]. Fig. 2.3 (b) shows the calculation of the Stark shifted transition frequencies in the limit of small electric fields obtained from equation 2.15, revealing the slope 0.83 and 2.21 GHz/Vcm^{-1} for 1→2 and 1→3 transitions, respectively. At stronger pressing fields ($\lambda \gg 1$) not satisfying the condition $\Delta E_\mathrm{n}^1 \ll E_\mathrm{n+1} - E_\mathrm{n}$, the perturbation approach is not applicable and the correction term ΔE_n becomes nonlinear to $E_\perp$. In this regime, the variational calculation of the Stark shift matches the experiment [1] as shown in Fig. 2.4. One can neglect the image potential term V_im in equation 2.12 in the limit of strong field. In this case, wave function $\chi_\mathrm{n}(z)$ is reduced to the Airy equation [49].

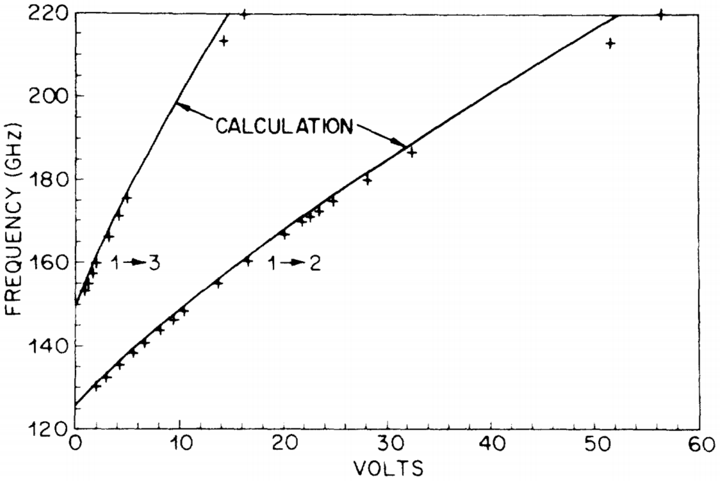

Figure 2.4: Transition frequencies versus voltage across the experimental cell. The voltage between the top and bottom plates inside the cell is swept by a triangular wave form applied in a way that maintains the helium surface at the same positive potential. This process allows for varying the pressing field acting on the electrons without change in the number of electrons. The crosses are measured data points while the solid curves are the result of the variational calculation (from Ref. [1]).

2.1.3 Thin Film Effects

A thin superfluid helium film can cover a dielectric substrate due to the van der Waals interaction between helium atom and the substrate. For surface electrons on such a helium film, the potential energy of an electron is affected by image charges located in the dielectric as well as in the film (see Fig. 2.5). If we neglect image charges in the metal for a thick dielectric layer, the potential energy V_e in the presence of an external electric field may be approximately written as [50]

$$V_\mathrm{e}(z) \simeq -\frac{\Lambda e^2}{z} - \frac{\Lambda_\mathrm{s} e^2}{z+d} + eE_\perp z, \tag{2.16}$$

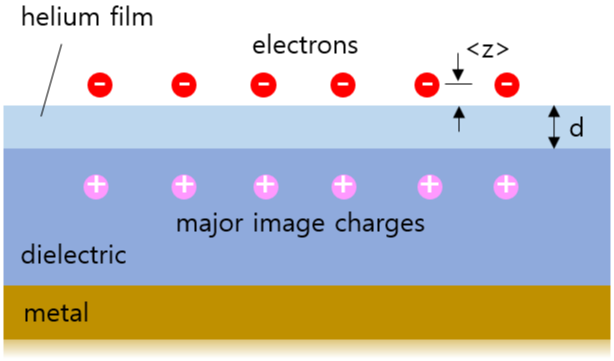

Figure 2.5: Schematic of electrons on helium film on a dielectric substrate. Major image charges are represented by + symbols in the dielectric substrate. The role of the metal depends on the thickness of the dielectric as described in the text.

where $\Lambda = \dfrac{\epsilon - 1}{4(\epsilon + 1)}$ is the image charge factor for the helium film, $\Lambda_\mathrm{s} = \dfrac{\epsilon_\mathrm{s} - \epsilon}{4(\epsilon_\mathrm{s} + \epsilon)}$ is that for the substrate, d and ϵ_s are the thickness of the film and dielectric constant of the substrate. For a relatively thick helium film ($\langle z \rangle / d \ll 1$), the potential is further approximated by

$$V_\mathrm{e} \simeq -\frac{\Lambda_\mathrm{s} e^2}{d} - \frac{\Lambda e^2}{z} + (F_\mathrm{d} + eE_\perp)\, z, \tag{2.17}$$

where $F_\mathrm{d} = \Lambda_\mathrm{s} e^2/d^2$. The main correction to the binding energy of the surface electron is revealed in the first term in equation 2.17. If the substrate is a metal covered by a 300Å thick helium film, $\Lambda_\mathrm{s} e^2/d \approx 140$ K meaning highly populated ground state even at no external field. The second term represents an attractive potential due to the polarization of the liquid helium and the last term is associated with the image force induced by the solid substrate leading to an enhanced pressing field (i.e. $E_\perp \to E_\perp + F_\mathrm{d}/e$). For instance, a metal substrate covered by a 100 nm thick charged helium film yields an effective pressing field $E_\mathrm{d} = F_\mathrm{d}/e \simeq 36$ kV/cm due to the substrate, which is significantly bigger than E_c in equation 2.14. Also, the average distance of the electron from the film surface $\langle z \rangle = 3b/2$ for this case can be estimated from equation 2.14 and leads to $\langle z \rangle \approx 40$ Å, which is substantially decreased compared to the bulk helium case at weak field ($\langle z \rangle \approx 140$ Å).

The electron-electron interaction in the 2DES above helium film is screened by image charges induced inside the substrate. For a metallic substrate ($\epsilon_{\mathrm{s}} \to \infty$), the Coulomb interaction $V(r)$ is given by

$$V(r) = e^2 \left(\frac{1}{r} - \frac{1}{\sqrt{r^2 + (2d)^2}} \right), \tag{2.18}$$

where r is the mean inter-electron distance. For $d \ll r$ the Coulomb interaction is modified into a dipole interaction $V(r) \to 2e^2 d^2 / r^3$ [51]. This suppressed interaction affects the dispersion relation for collective modes of the electron system [52] and leads to the modification of the phase diagram. In particular, Peeters and Platzman evaluated the melting curve in the presence of the screening effect from the substrate [53], which predicts that the fluid phase persists down to T = 0 at low density for a metallic substrate in contrast to the Wigner crystal state for bulk helium.

2.2 Wigner Solid

In 1934, Eugene Wigner predicted an ordered phase of a 2D or 3D electron gas in a positive background when the potential energy dominates the average kinetic energy at low density [17]. To minimize their relative potential energy, the electrons form a bcc (body-centered-cubic) lattice in 3D and a triangular lattice in 2D. This electron crystal is called Wigner solid (WS). Clear examples of physical systems realizing the WS were not found until Crandall and Williams proposed electrons on liquid helium system in 1971 [54]. This is because the system fulfills the requirement for Wigner lattice including an uniform positive potential provided by underlying metal plate for bulk helium and lower electron density ($n_{\mathrm{s}} \approx 10^6 - 10^9$ cm^{-2}). In 1979, the 2D Wigner solid transition was indeed observed in the system of electrons on helium by Grimes and Adams [5]. They discovered a sudden appearance of the resonance below T = 0.457 K associated with coupled plasom-ripplon modes. This is the first experimental demonstration of the WS.

For the case of a degenerate semiconductor 2DES, no direct observation of the WS has been achieved so far due to difficulty in achieving low density. However, positive evidence of a magnetically induced Wigner solid in GaAs/AlGaAs heterojuctions was reported by Andrei *et al.* [55]. Recently, bilayer semiconductor heterostructures have attracted interest for direct detection of the WS since the mutual interaction of parallel layers of two 2DESs could allow for the WS transition at much higher electron density in the quantum regime even without external fields [56]. More recently, twisted bilayer graphene (TBLG), well-known for a superconducting state at magic angle [57], also has been gaining the interest due to the possible existence of the WS in this system [58]. However, experimental confirmation is required.

The transition from an electron liquid to a Wigner solid can be characterized by the dimensionless plasma parameter Γ_{p}

$$\Gamma_{\mathrm{p}} = \frac{\langle V \rangle}{\langle K \rangle}, \tag{2.19}$$

where $\langle V \rangle$ and $\langle K \rangle$ represent mean electron-electron Coulomb potential and mean kinetic energy respectively, which are given by

$$\langle V \rangle = \frac{e^2}{r_0} = e^2 \sqrt{\pi n_{\mathrm{s}}}, \tag{2.20}$$

$$\langle K \rangle = \frac{1}{n_{\mathrm{s}}} \int_0^\infty d\varepsilon \nu(\varepsilon) f(\varepsilon) \varepsilon. \tag{2.21}$$

Here, $r_0 = 1/\sqrt{\pi n_\mathrm{s}}$ is inter-electron spacing, $\nu(\varepsilon) = \dfrac{m_\mathrm{e}}{\pi\hbar^2}$ is the two-dimensional density of states, and $f(\varepsilon) = \dfrac{1}{1 + e^{(\varepsilon-\mu)}/\tau}$ is Fermi-Dirac distribution function.

For a degenerate 2DES when T → 0, the mean kinetic energy is given by

$$\langle K \rangle = \frac{\int_0^{\varepsilon_\mathrm{F}} d\varepsilon \nu(\varepsilon)\varepsilon}{\int_0^{\varepsilon_\mathrm{F}} d\varepsilon \nu(\varepsilon)} = \frac{\varepsilon_\mathrm{F}}{2}, \tag{2.22}$$

where $\varepsilon_\mathrm{F} = \dfrac{\hbar^2 \pi n_\mathrm{s}}{m_\mathrm{e}}$ is the Fermi energy. Introducing the Bruckner parameter $r_\mathrm{s} = r_0/a_\mathrm{B}$ [44], where the mean interparticle distance r_0 is measured in units of the Bohr radius $a_\mathrm{B} = \hbar^2/m_\mathrm{e}e^2$, simplifies $\langle V \rangle$ and $\langle K \rangle$:

$$\langle V \rangle = \frac{e^2}{r_0} = \frac{a_\mathrm{B}}{r_0}\frac{e^2}{a_\mathrm{B}} = \frac{2}{r_\mathrm{s}} R_y, \tag{2.23}$$

$$\langle K \rangle = \frac{\hbar^2 \pi n_\mathrm{s}}{2m_\mathrm{e}} = \frac{\hbar^2}{2m_\mathrm{e} r_0^2} = a_\mathrm{B}\frac{e^2}{2r_0^2} = \frac{1}{r_\mathrm{s}} R_y, \tag{2.24}$$

where $R_y = \dfrac{e^2}{2a_\mathrm{B}} = \dfrac{me^4}{2\hbar^2} = 13.6$ eV is the Rydberg constant. Thus, the plasma parameter for degenerate case ($\varepsilon_\mathrm{F} \gg k_\mathrm{B}\mathrm{T}$) has the compact form:

$$\Gamma_\mathrm{pq} = 2r_\mathrm{s}. \tag{2.25}$$

When $r_\mathrm{s} \gg 1$ at lower density, the potential energy between electrons far exceeds their kinetic energy leading to electron crystallization. For GaAs/AlGaAs heterostructures, quantum Monte Carlo simulations predict that the electron system can crystallize when $r_\mathrm{s} \geq r_\mathrm{s}^{(\mathrm{c})} = 31$ or $\Gamma_\mathrm{pq} \geq \Gamma_\mathrm{pq}^{(\mathrm{c})} = 62$ [59]. This system has a typical density ranging from 10^{11} to 10^{12} cm^{-2} and the relation $r_\mathrm{s} = r_0/a_\mathrm{B} = m_\mathrm{e}e^2/\hbar^2\sqrt{\pi n_\mathrm{s}}$ yields $r_\mathrm{s} \sim 0.5 - 2$, which is much smaller than the critical value $r_\mathrm{s}^{(\mathrm{c})} = 31$. Here, m_e and e were replaced with the effective mass

$m_e^* \simeq 0.066\, m_e$ and screened electron charge $e/\sqrt{\epsilon} \simeq e/\sqrt{12.5}$ for GaAs. Therefore, it is extremely challenging to directly observe a Wigner solid in a semiconductor 2DES.

For a non-degenerate 2DES in the low density limit where $k_B T \gg \varepsilon_F$, the mean kinetic energy is $\langle K \rangle = k_B T$ and thus we obtain the plasma parameter in the classical regime:

$$\Gamma_{pc} = \frac{e^2 \sqrt{\pi n_s}}{k_B T} = \frac{e^2}{r_0} \frac{1}{k_B T}. \tag{2.26}$$

For $1 < \Gamma_{pc} < 100$ (low density and high temperature), electrons behave like a correlated fluid system while for $\Gamma_{pc} > 100$ the Coulomb potential dominates thermal fluctuations of the kinetic energy and leads to phase transition to an ordered state (i.e. the WS) [50]. Regarding the critical value $\Gamma_{pc}^{(c)}$ for the Wigner transition when $\Gamma_{pc} \geq \Gamma_{pc}^{(c)}$, there has been extensive research based on a variety of techniques to experimentally determine this value, which are shown in the following table. Note that specification of the system is omitted for the case of electron on helium in the Table 2.1. Most of these experimental values are in reasonable agreement with theoretical estimation in the range of $\Gamma_{pc}^{(c)}$ 120 - 130 [66]. At the maximum attainable density $n_s \approx 2 \times 10^9$ cm^{-2} for electrons above a bulk helium surface, the melting temperature $T_m \simeq 1$ K, obtained from equation 2.26 with $\Gamma_{pc} = 130$, is much higher than $\varepsilon_F = \hbar^2 \pi n_s / m_e \simeq 56$ mK, indicating classical solid-to-liquid transition. For $n_s > 2 \times 10^9$ cm^{-2} on bulk liquid helium, the restoring forces in the liquid that counteract a surface deformation resulting from electron pressure are no longer sufficient to confine the charge at the surface (electrohydrodynamic instability) [67]. Peeters and Platzman pointed out that a quantum liquid transition can be achievable on a helium film supported by the metal substrate [53] due to the higher attainable density ($n_s \sim 10^{11}$ cm^{-2}) [68] and the screened Coulomb interaction by the substrate (dipolar interaction $\sim 1/r_0^3$). Particularly,

Reference	$\Gamma_{\mathrm{pc}}^{(\mathrm{c})}$	T(K)	Experiments/Method
Grimes and Adams (1979) [5]	137 ± 15	0.4 - 0.7	Longitudinal coupled electron-ripplon mode
Marty *et al.* (1980) [60]	118 ± 10	0.3 - 0.6	Longitudinal coupled electron-ripplon mode
Gallet *et al.* (1982) [61]	140 ± 10	0.3 - 0.7	Transverse sound mode
Mehrota *et al.* (1982) [62]	124 ± 4	0.2 - 0.7	Mobility
Kajita (1985) [63]	138 ± 25	1.4 - 2.5	Conductivity (electrons on neon)
Mellor and Vinen (1990) [64]	130 ± 3	0.1 - 0.2	Shikin modes (positive ions on helium)
Shirahama and Kono (1995) [65]	127	0.1 - 1	Conductivity

Table 2.1: Experimental results for the critical value of the plasma parameter $\Gamma_{\mathrm{pc}}^{(\mathrm{c})}$ at which the liquid-to-solid transition occurs.

their calculation reveals a quantum fluid which persists down to T $= 0$ K as $n_{\mathrm{s}} \rightarrow 0$. This is because the potential energy ($\sim 1/r_0^3 \sim n_{\mathrm{s}}^{3/2}$) decreases with density n_{s} faster than the kinetic energy ($\sim 1/r_0^2 \sim n_{\mathrm{s}}$).

2.2.1 Phase Diagram

Platzman and Fukuyama calculated the phase diagram for electrons on bulk helium with the assumption of a constant plasma parameter (i.e. $\Gamma_{\mathrm{pq}}^{(\mathrm{c})} = \Gamma_{\mathrm{pc}}^{(\mathrm{c})} = \Gamma_{\mathrm{p}}^{(\mathrm{c})} = 3$) along the melting curve (see Fig. 2.6) [2]. In the classical regime at high temperate and low density, the melting curve in Fig. 2.6 is given by equation 2.26:

$$n_{\mathrm{s}} = \left(\frac{\Gamma_{\mathrm{p}}^{(\mathrm{c})}}{\sqrt{\pi} e^2} \right)^2 k_{\mathrm{B}}^2 T^2. \tag{2.27}$$

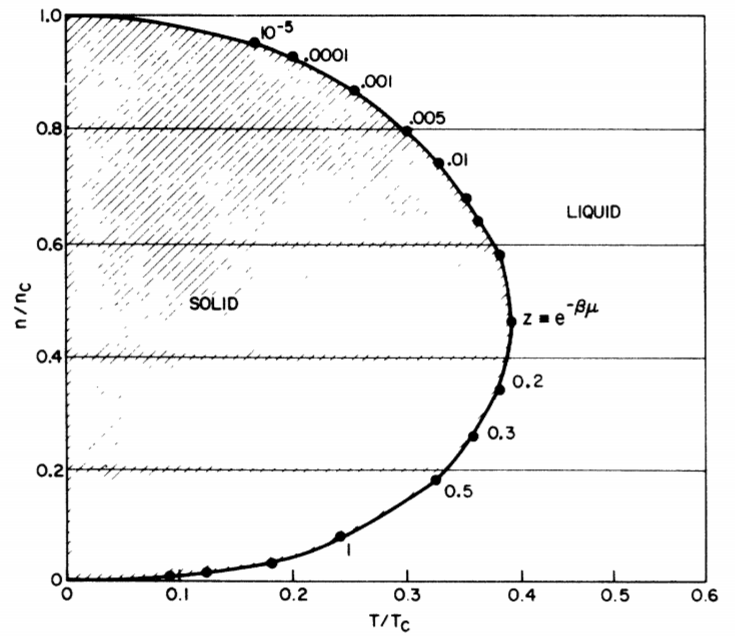

Figure 2.6: Phase diagram of a 2D Coulomb liquid (from Ref. [2]). Temperature T and electron density n are expressed in a unit of n_c and Tc, respectively. Here $n_\mathrm{c} = 4\pi^{-1}(a_\mathrm{B}\Gamma_\mathrm{p}^{(\mathrm{c})})^{-2}$ and $k_\mathrm{B}T_\mathrm{c} = 2m_\mathrm{e}e^4/\hbar^2(\Gamma_\mathrm{p}^{(\mathrm{c})})^2$.

In the zero temperature limit, the critical density n_c for melting is given by equation 2.25 with $r_\mathrm{s} = r_0/a_\mathrm{B} = 1/a_\mathrm{B}\sqrt{n_\mathrm{s}\pi}$:

$$n_\mathrm{c} = \frac{4}{\pi}\left(a_\mathrm{B}\Gamma_\mathrm{p}^{(\mathrm{c})}\right)^{-2}. \tag{2.28}$$

If $\Gamma_\mathrm{p}^{(\mathrm{c})} = 137$ is taken [5], the critical density is $n_\mathrm{c} \simeq 2.4 \times 10^{12}$ cm^{-2}. In the general case at any density and temperature, the kinetic energy $\langle K\rangle$ and electron density n_s may have the analytic form:

$$n_\mathrm{s} = \frac{1}{\pi}\int_0^\infty kdk\frac{1}{e^{\beta(\varepsilon_\mathrm{k}-\mu)}+1} = \frac{1}{\pi}\frac{m_\mathrm{e}k_\mathrm{B}T}{\hbar^2}\ln\left(1+1/z\right) \tag{2.29}$$

$$\langle K\rangle = \frac{1}{n_\mathrm{s}}\frac{1}{\pi}\int_0^\infty kdk\frac{\varepsilon_\mathrm{k}}{e^{\beta(\varepsilon_\mathrm{k}-\mu)}+1} = k_\mathrm{B}T\frac{-\mathrm{Li}_2(-1/z)}{\ln(1+1/z)}, \tag{2.30}$$

where $z = e^{-\beta\mu}$, μ is the chemical potential, $\beta = 1/k_{\mathrm{B}}T$, and $\mathrm{Li}_2(z)$ is called the dilogarithm function:

$$\mathrm{Li}_2(z) = -\int_0^z t^{-1}\ln(1-t)dt \text{ for } z \leq 1. \tag{2.31}$$

Inserting equations 2.29 and 2.30 into equation 2.19, we can obtain the parametric equations for the phase boundary:

$$n_{\mathrm{s}}/n_{\mathrm{c}} = \frac{1}{4}\frac{\ln^4(1+1/z)}{-{\mathrm{Li}_2}^2(-1/z)}, \tag{2.32}$$

$$T/T_{\mathrm{c}} = \frac{1}{2}\frac{\ln^3(1+1/z)}{-{\mathrm{Li}_2}^2(-1/z)}, \tag{2.33}$$

where T_{c} is the characteristic temperature defined by

$$k_{\mathrm{B}}T_{\mathrm{c}} = \frac{2m_{\mathrm{e}}e^4}{\hbar^2\left(\Gamma_{\mathrm{p}}^{(\mathrm{c})}\right)^2}. \tag{2.34}$$

From Landen's identity $\mathrm{Li}_2(z) = -\mathrm{Li}_2(\frac{z}{z-1}) - \frac{1}{2}\ln^2(1-z)$ for $z < 1$, the dilogarithm function $\mathrm{Li}_2(-1/z)$ can be expanded to

$$\mathrm{Li}_2(-1/z) = -\frac{1}{2}\ln^2(1+\frac{1}{z}) - \mathrm{Li}_2(\frac{1}{1+z}). \tag{2.35}$$

Substituting equation 2.35 into equations 2.32 and 2.33, the parametric equations for $n_{\mathrm{s}}/n_{\mathrm{c}}$ and T/T_{c} are now equivalent to the original equations written in [2], which are used for the numerical plot in Fig. 2.6. Note that this phase diagram gives only a qualitative picture since the plasma parameter along the phase boundary might not be the same in classical and quantum regime. In reality, the experimental value of $\Gamma_{\mathrm{pc}}^{(\mathrm{c})}$ for the classical case is approximately 130, which is roughly two times larger than $\Gamma_{\mathrm{pq}}^{(\mathrm{c})} = 62$ for the quantum case obtained from quantum Monte Carlo simulation as discussed in the section 2.2.

2.2.2 2D Melting Mechanism

The existence of 2D crystals has long been a fascinating topic in condensed matter physics and was first theoretically explored by Peierls [69] and Landau [70] in 1930. They pointed out that long-range order in 2D should be destroyed by thermal fluctuation at any finite temperature. Mermin and Wagner further demonstrated that magnetic and crystalline long-range order could not exist in 1D or 2D [71, 72]. However, although there is no true long-range order in 2D, spatial correlations decay algebraically according to a power law and can be extended over a finite system size (i.e. quasi-long-range translational order) according to KTHNY (Kosterlitz-Thouless-Halperin-Nelson-Young) theory [73, 74, 75, 76]. Furthermore, this predicted that 2D crystal also has long-range bond orientational order as well as quasi-long-range positional order. Based on KTHNY theory, the 2D melting mechanism is briefly summarized below.

In a crystalline phase, the structure factor $S(\vec{q})$ can be defined by [75]

$$S(\vec{q}) = \sum_{\vec{R}} e^{i\vec{q}\cdot\vec{R}} \langle e^{i\vec{q}\cdot[\vec{u}(\vec{R})-\vec{u}(\vec{0})]} \rangle, \tag{2.36}$$

where $\vec{q}$ is the scattering vector, $\vec{R}$ the lattice point, $\vec{u}(\vec{R})$ displacement vector at lattice site $\vec{R}$, and the summation is over all lattice sites $\{\vec{R}\}$. In a 3D solid, $S(\vec{q})$ can be approximated by considering the case $|\vec{u}| \ll |\vec{R}|$:

$$S(\vec{q}) \simeq \sum_{\vec{R}} e^{i\vec{q}\cdot\vec{R}} = (2\pi)^3 \sum_{\vec{G}} \delta^3(\vec{q} - \vec{G}), \tag{2.37}$$

where $\vec{G}$ is a reciprocal lattice vector. Thus, Bragg peaks are delta function at $\vec{q} = \vec{G}$ in three dimension. Also, a 3D crystal has a non-zero correlation function $C_{\vec{G}}$ at large R, which represents long-range positional order. This function is defined by [75]

$$C_{\vec{G}} \equiv \langle \rho_{\vec{G}}(\vec{R}) \rho^*_{\vec{G}}(\vec{0}) \rangle, \tag{2.38}$$

$$\rho_{\vec{G}} \equiv e^{i\vec{G}\cdot[\vec{R}+\vec{u}(\vec{R})]}. \tag{2.39}$$

However, in 2D crystals, Jancovici pointed out that fluctuation in long-wavelength phonon modes leads to the displacement $\vec{u}(\vec{R})$ diverging logartithmatically and the spatial correlation function decays algebraically: $C_{\vec{G}} \sim R^{-\eta_{\vec{G}}(\mathrm{T})}$ [77]. Thus, when the sample size is infinite ($R \to \infty$), no long-range translational order exists in 2D. Nevertheless, for a finite sample size, the correlation function can survive due to the algebraic decay. This quasi-long-range positional order can be destroyed by an unbinding of dislocation pairs (formation of isolated dislocations) at the melting temperature $\mathrm{T_m}$. A dislocation stands for an irregularity within the crystal structure showing an sudden change of atomic arrangement as shown in Fig. 2.7 (c). Thus, at $\mathrm{T} \geq \mathrm{T_m}$, dislocation-mediated melting of the 2D crystal occurs. In this case, the correlation function of 2D fluid has exponential decay:

$$C_{\vec{G}}(\vec{R}) \sim e^{-|\vec{R}|/\xi_+(\mathrm{T})} \quad \text{for } \mathrm{T} > \mathrm{T_m} \tag{2.40}$$

with the correlation length

$$\xi_+ \sim \exp(C/|t|^{0.36963\ldots}), \tag{2.41}$$

where C is a positive constant and $t = (\mathrm{T} - \mathrm{T_m})/\mathrm{T_m}$. This exponential decay implies only short-range positional order and thus the absence of Bragg peaks in the fluid phase.

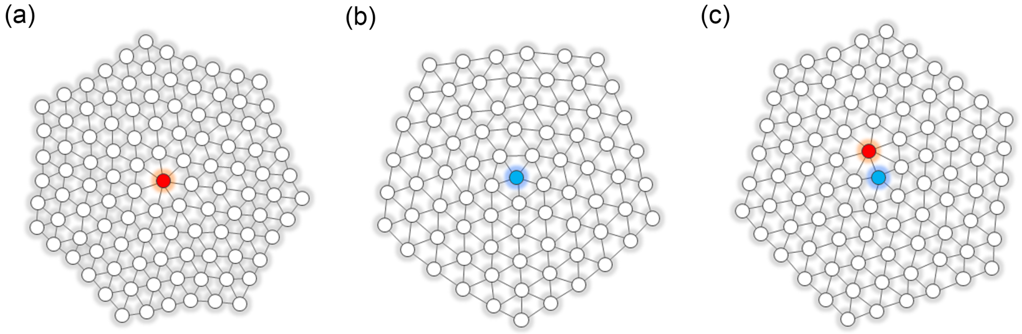

Figure 2.7: Topological defects in a triangular lattice. Isolated disclinations with (a) seven folder and (b) five folder symmetry rather than six folder. An isolated dislocation (c) is composed of a bound pair of such disclinations, showing undisrupted orientational order at long distance.

Another feature distinguishing 2D crystals from 3D crystals is the structure factor, which can be measured in diffraction-type measurements. In contrast to delta function Bragg peaks for 3D as mentioned above, the structure factor in 2D has power law singularity:

$$S(\vec{q}) \sim |\vec{q} - \vec{G}|^{-2+\eta_{\vec{G}}(\mathrm{T})}. \tag{2.42}$$

The exponent $\eta_{\vec{G}}$ is related to the Lamé elastic constants μ and λ by

$$\eta_{\vec{G}} = k_{\mathrm{B}}\mathrm{T}|\vec{G}|^2 \frac{3\mu + \lambda}{4\pi\mu(2\mu + \lambda)}. \tag{2.43}$$

Here λ and μ are the incompressibility and the shear modulus. Lastly, the solid to liquid transition temperature $\mathrm{T_m}$ in the 2D system is given by

$$\mathrm{T_m} = \frac{a_0^2}{4\pi k_{\mathrm{B}}} \frac{\mu(\mu + \lambda)}{2\mu + \lambda}. \tag{2.44}$$

From equation 2.26, corresponding critical value $\Gamma_{\mathrm{p}}^{(\mathrm{c})}$ is given by

$$\Gamma_{\mathrm{p}}^{(\mathrm{c})} = \frac{4\pi e^2\sqrt{\pi n_{\mathrm{s}}}}{a_0^2}\frac{2\mu+\lambda}{\mu(\mu+\lambda)}. \tag{2.45}$$

Considering the incompressibility of the electron crystal ($\lambda = \infty$) [78], one can simplify $\mathrm{T_m}$ and $\Gamma_{\mathrm{p}}^{(\mathrm{c})}$ as

$$\mathrm{T_m} = \frac{a_0^2}{4\pi k_{\mathrm{B}}}\mu, \tag{2.46}$$

$$\Gamma_{\mathrm{p}}^{(\mathrm{c})} = \frac{4\pi e^2\sqrt{\pi n_{\mathrm{s}}}}{a_0^2}\frac{1}{\mu}, \tag{2.47}$$

where $a_0 = (2/\sqrt{3}n_{\mathrm{s}})^{1/2}$ is a lattice constant of the 2D triangular electron lattice, which is energetically favored. Thus, if the shear modulus μ is given, one can estimate $\Gamma_{\mathrm{p}}^{(\mathrm{c})}$ from equation 2.47. One way to do this is to use μ obtained from the transverse sound velocity c_t in a 2D electron crystal: $c_t = \sqrt{\mu/\rho}$ where $\rho = m_{\mathrm{e}}n_{\mathrm{s}}$ is a mass density of the crystal. In the long wavelength limit (low temperature), a transverse phonon has a linear dispersion relation [4]: $\omega_{\mathrm{t}} = c_t q$ with $c_t = \sqrt{0.138\frac{e^2}{m_{\mathrm{e}}r_0}}$, where $\omega_{\mathrm{t}}(q)$ is a frequency of the transverse phonon mode at a wavevector q and $r_0 = 1/\sqrt{\pi n_{\mathrm{s}}}$ is the inter-electron spacing. This yields $\mu = 0.138\sqrt{\pi}e^2 n_{\mathrm{s}}^{3/2}$. Using this calculated value of μ, Thouless theoretically obtained $\Gamma_{\mathrm{p}}^{(\mathrm{c})} = 78.71$ [78], which does not agree well with experimental result of Grimes and Adams $\Gamma_{\mathrm{p}}^{(\mathrm{c})} = 137 \pm 15$ [5]. Morf calculated the temperature dependence of the shear modulus μ using molecular dynamics simulations, revealing a linear decrease of μ with increasing T (see equation 2.63) and for further increasing T a sharp drop of μ along with the onset of electron diffusion [79]. This estimation of μ yields $\Gamma_{\mathrm{p}}^{(\mathrm{c})} = 128.2$, which fits well the experiments.

Beside the positional order described above, another type of the ordering characterizes the

2D crystal: long-range order in the nearest neighbor bond-orientation. Nelson and Halperin found that unbinding of dislocation pairs leads to melting into a new type of liquid crystal at $\mathrm{T} \rightarrow \mathrm{T_m}$, characterized by power-law decay of orientational order. This "hexatic phase" [75] corresponds to an orientational correlation function given by

$$g_6(r) \sim r^{-\eta_6(\mathrm{T})}, \tag{2.48}$$

with

$$\eta_6 = \frac{18 k_\mathrm{B} \mathrm{T}}{\pi K_\mathrm{A}}. \tag{2.49}$$

Here the exponent η_6 is proportional to T and K_A is the Frank constant [80]. Due to this quasi-long-range orientational order, a diffraction pattern for an infinite size sample would show an isotropic ring just like isotropic liquid phase. In real experiments (finite size sample), this pattern is modified into the sixfold modulation (see Fig. 2.8). By further increasing temperature ($\mathrm{T} \rightarrow \mathrm{T_i}$), the orientational order is disrupted by another type of the defect, the disclination. Dissociation of disclination pairs leads to isotropic fluid phase. This topological defect can be viewed as a particle having the wrong number of nearest neighbors as shown in Fig. 2.7. Also, the dislocation mentioned above can be regarded as a bound pair of disclinations. Now, the corresponding correlation function shows an exponential decay (i.e. short range orientation order):

$$g_6(r) \sim e^{-r/\xi_6(\mathrm{T})}, \tag{2.50}$$

where $\xi_6(\mathrm{T}) \sim e^{b/|\mathrm{T}-\mathrm{T_i}|^{1/2}}$ and b is a constant.

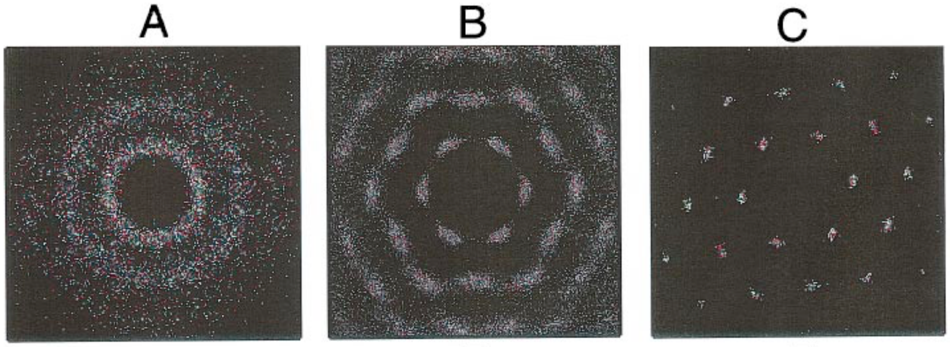

Figure 2.8: Computed diffraction pattern of three different phases in 2D: Isotropic fluid phase (A), hexatic phase (B), and crystalline phase (C). Images are taken from Ref. [3]

2.3 Collective Modes of a Two Dimensional Electron System (2DES)

2.3.1 Plasmons

Plasmons are collective excitations formed in the electron gas or liquid, which propagate as longitudinal charge density oscillation through the bulk or the surface. For the 3D case, the dispersion relation for plasmons is given by the Bohm-Gross equation [81] in the presence of random thermal motion:

$$\omega_{\mathrm{3D}}^2(q) = \omega_{\mathrm{p}}^2 + \frac{3k_{\mathrm{B}}\mathrm{T}}{m_{\mathrm{e}}} q^2, \tag{2.51}$$

where $\omega_{\mathrm{3D}}(q)$ is the plasma frequency at wave-number q and $\omega_{\mathrm{p}} = \sqrt{\frac{4\pi n_{\mathrm{e}} e^2}{m_{\mathrm{e}}}}$ is a finite angular frequency independent of q. In the long-wavelength limit ($q \to 0$), plasma frequency $\omega_{\mathrm{3D}}(q) = \omega_{\mathrm{p}}$ has non-zero value. In contrast to bulk plasmons, the plasma frequency of a 2D electron system (2DES) goes to zero in this limit with the dispersion relation:

$$\omega_{\mathrm{2D}}(q) = \sqrt{\frac{2\pi n_{\mathrm{e}} e^2}{m_{\mathrm{e}}}} q^{1/2}. \tag{2.52}$$

This square-root dependence on q is a universal features of the 2DES with unscreened Coulomb interactions. In actual experiments, metal electrodes can screen the electric fields and thus results in the modification of the dispersion relation of the 2DES [52]:

$$\omega_{\mathrm{2D}}^2(q) = \frac{4\pi n_{\mathrm{e}} e^2}{m_{\mathrm{e}}} \frac{q}{\coth(qd) + \epsilon_{\mathrm{s}} \coth(qd_{\mathrm{s}})}, \tag{2.53}$$

where d and d_{s} denote the distance of the 2DES from the electrodes above and beneath the 2D electron layer, $\epsilon_{\mathrm{s}} \simeq 1$ is the dielectric constant of the liquid helium. From equation 2.53, one can easily show that a long-wavelength plasmon mode ($qd < 1$ and $qd_{\mathrm{s}} < 1$) has a linear dispersion relation:

$$\omega_{\mathrm{2D}}(q) \simeq q \sqrt{\frac{4\pi n_{\mathrm{e}} e^2}{m_{\mathrm{e}} \alpha_{\mathrm{d}}}}, \tag{2.54}$$

with $\alpha_{\mathrm{d}} = 1/d + \epsilon_{\mathrm{s}}/d$. In the short-wavelength limit, one can find the square-root dependence of ω_{2D} on q which is a typical feature of 2D plasmons:

$$\omega_{\mathrm{2D}}(q) \simeq q^{1/2} \sqrt{\frac{4\pi n_{\mathrm{e}} e^2}{m_{\mathrm{e}}(1 + \epsilon_{\mathrm{s}})}}. \tag{2.55}$$

This 2D plasmon dispersion relation was experimentally verified by Grimes and Adams using standing-wave resonance in plasma of electrons floating above helium surface [7].

2.3.2 Phonons

A 2D solid can exhibit another type of the collective excitation, normal modes of the lattice, so-called phonons. Bonsall and Maradudin calculated the phonon dispersion relation for the hexagonal lattice of a 2D electron crystal by solving the eigenvalues of the dynamical matrix [4]. The corresponding dispersion curve is shown in Fig. 2.9.

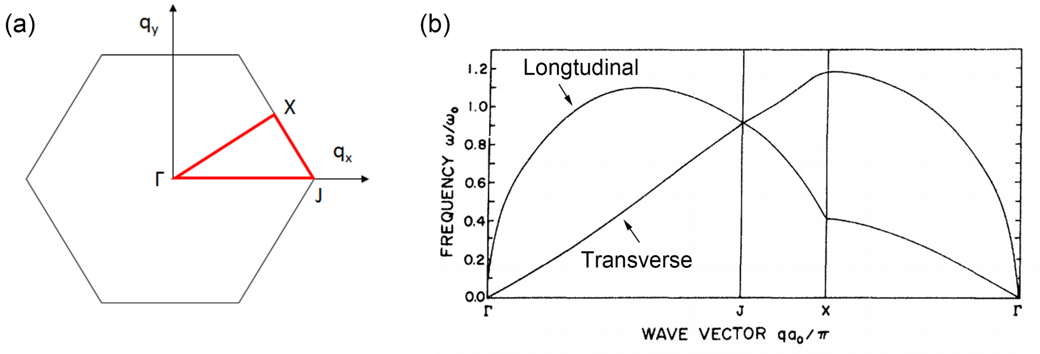

Figure 2.9: (a) First Brillouin zone for the two-dimensional, hexagonal lattice. (b) Phonon dispersion curve along the boundary of the first Brillouin zone (red line in (a)). The frequency ω_0 is defined by $\omega_0 = 8e^2 m^* a_0^3$, a_0 is the lattice constant. Figure taken from Ref. [4]

In the long-wavelength limit, the frequency of phonon modes for 2D triangular electron lattice has the asymptotic form [82]:

$$\omega_l = \sqrt{\frac{2\pi e^2 n_\mathrm{e}}{m_\mathrm{e}}} q^{1/2}, \tag{2.56}$$

$$\omega_t = c_t q, \quad c_t^2 = \frac{0.138 e^2 \sqrt{\pi n_\mathrm{e}}}{m_\mathrm{e}}, \tag{2.57}$$

where ω_l and ω_t represent longitudinal and transverse modes and c_t is the transverse sound velocity. The longitudinal phonon in this limit in the 2D electron crystal has the same dispersion relation as plasmons in the 2D electron gas (i.e. see equation 2.52), indicating that this phonon mode by itself is irrelevant for observing a phase transition to the electron solid. However, transverse phonons arise from a resistance to shear stress which does not exist in a fluid or gas phase, so they are good indicator of a Wigner solid transition. This shear mode (transverse phonons) was experimentally demonstrated in an electron lattice on helium by Deville *et al.* [83]. Shear stress was created by a transverse Lorentz force in this experiment. One can relate the longitudinal and transverse sound velocity to Lamé elastic constant λ and μ:

$$c_l = \sqrt{\frac{\lambda + 2\mu}{m_\mathrm{e} n_\mathrm{e}}}, \tag{2.58}$$

$$c_t = \sqrt{\frac{\mu}{m_\mathrm{e} n_\mathrm{e}}}, \tag{2.59}$$

where $m_\mathrm{e} n_\mathrm{e}$ is the mass density of Coulomb (electron) crystal. From the above equations, the incompressibility λ and the shear modulus μ are given by

$$\lambda = m_\mathrm{e} n_\mathrm{e} \left(c_l^2 - 2c_t^2 \right), \tag{2.60}$$

$$\mu = m_\mathrm{e} n_\mathrm{e} c_t^2. \tag{2.61}$$

In the limit of small wave numbers ($q \to 0$ at $\mathrm{T} \to 0$), the longitudinal velocity $c_l = \dfrac{\partial \omega_l}{\partial q} \sim q^{-1/2}$ diverges and thus the Coulomb crystal can be thought to be incompressible with $\lambda \to \infty$ from equation 2.60. Also, from equations 2.57 and 2.61 the shear modulus in this limit is given by

$$\mu = 0.138\sqrt{\pi} e^2 n_\mathrm{e}^{3/2} \quad \text{for T} \to 0. \tag{2.62}$$

For finite temperature below the melting point $\mathrm{T_m}$, Morf [79] showed that shear modulus linearly decreases with increasing T up to $\mathrm{T} \simeq 0.9\mathrm{T_m}$, which has the following form

$$\mu(\mathrm{T}) = \mu(0) \left(1 - 30.8 \frac{k_\mathrm{B}\mathrm{T}}{\sqrt{\pi n_\mathrm{e}} e^2} \right). \tag{2.63}$$

Here $\mu(0)$ is equivalent to equation 2.62.

Up to now, we have described two branches of phonon modes in zero magnetic field and assumed that the 2D electron lattice is formed on a smooth substrate. In reality, they are strongly affected by both magnetic fields and surface deformation of the substrate. The magnetic field normal to the crystal mixes longitudinal and transverse phonons, leading to new modes $\omega_{\pm}(q)$. Moreover, a new mode appears at low frequency ω_{-} decreases with increasing magnetic field B as $\omega_{-} \sim 1/\omega_{\mathrm{c}}$ (i.e. this branch softens with applied B-field) [82]. Here $\omega_{\mathrm{c}} = eB/m_{\mathrm{e}}c$ is the cyclotron frequency. Also, for 2D electrons on a soft substrate, surface deformation is inevitable and it can alter the effective mass of the system. A representative example of this latter case is electrons on liquid helium. In this system, each electron indents the helium surface and creates a small dimple beneath them with a depth of ~ 1Å. Especially, in the Wigner solid regime, electrons in the lattice sites forms a periodic array of dimples on the helium surface. Fisher and Halperin showed that this dimple array can follow electrons at low frequency, resulting in increase of effective mass ($m_{\mathrm{e}} \rightarrow m^{*} = m_{\mathrm{e}} + m_{\mathrm{d}}$) and thus reduced phonon frequency $\sqrt{m_{\mathrm{e}}/m^{*}}\omega_{l,t}$ [6], where m_{d} is effective mass of the dimple and $\omega_{l,t}$ is the frequency of two phonon branches at no surface depression described above. In the presence of oscillatory motion of electron crystal, the disturbances of superfluid helium surface generates a quantized capillary wave called a ripplon, which can couple to vibrational modes of a 2D solid. This coupled mode will be discussed in section 2.3.3.

2.3.3 Phonon-Ripplon Coupling

Shikin suggested that driving the 2D electron crystal against the helium surface with a perpendicular RF electric field should produce a series of resonances due to the excitation of standing capillary waves (ripplons) whose wavelength is commensurate with the electron lattice constant [84]. However, Grimes and Adams experimentally demonstrated ripplons can be resonantly excited using an alternating electric field parallel to the charged helium surface [5]. It turns out that the resonant excitation of ripplons by horizontal motion of the

WS is more effective than by the WS moving normal to the plane (Shikin modes) due to the strong electron binding to the helium surface [44]. To achieve horizontal motion of each electron, they applied a RF signal to a lower circular plate submerged beneath the liquid helium. When ripplons are resonantly excited at certain RF frequencies in the presence of an electron crystal, they affect the impedance of the electron layer. Instead of measuring this impedance directly, they detected the derivative of the impedance with respect to the electron density dR/dN_{s} to minimize noise, where R and N_{s} are the real part of the impedance and the areal electron density. To do this, they applied an audio-frequency signal to the electron confinement ring to modulate N_{s} and synchronously detected dR/dN_{s} at the modulation frequency. Fig. 2.10 shows their experimental result in which resonant features in dR/dN_{s} derivative suddenly appear below $\mathrm{T} = 0.457$ K, arising from the crystallization of the electron system.

The two lowest resonance frequencies labeled W and X in Fig. 2.10 at $\mathrm{T} \cong 0.42$ K do not match the expected values from the dispersion relation of resonantly excited ripplons (equation 2.64). An explanation for this discrepancy was given by Fisher, Halperin, and Platzman [6]. In this work, they showed that the phonon spectrum of a 2D electron crystal is strongly affected by the interaction with ripplons, and as a result a coupled longitudinal phonon-ripplon mode appears providing good agreement with all resonance frequencies in the experiments of Grimes and Adams. If there is no interaction between the 2D electron lattice vibration and ripplons, the frequency spectrum of phonons at long wavelength is given by equations 2.56 and 2.57. Also, the ripplons resonantly excited by electron displacements in the crystal have the following dispersion relation:

$$\Omega_{\mathrm{n}}^2 = \frac{\sigma}{\rho} G_{\mathrm{n}}^3, \tag{2.64}$$

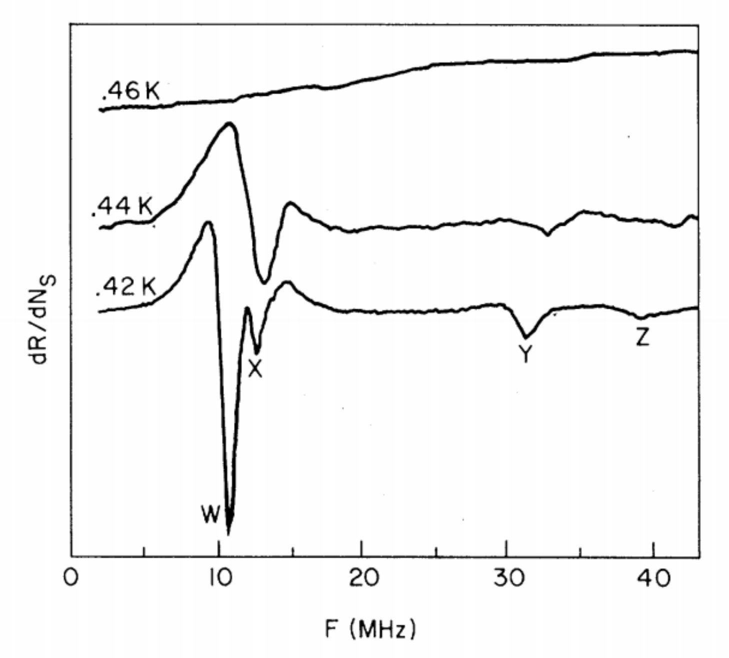

Figure 2.10: Coupled plasmon-ripplon resonances. The resonance only appear below 0.457 K where the sheet of electrons has crystallized into a triangular lattice (from Ref. [5]). dR/dN_s and F denote the derivative of the impedance of the electron layer with respect to the electron density and the frequency of the RF signal applied to the underlying electrode used to generate horizontal electron motion. A detailed description of a measurement setup is presented in the text.

where σ and ρ are the surface tension and density of the liquid helium while G_n is a reciprocal lattice vector of the electron lattice. For a triangular lattice, G_n is given by [85]

$$G_\mathrm{n} = \frac{2^{3/2}\pi}{3^{1/4}}\sqrt{n_\mathrm{e}}\sqrt{n}, \quad n = l^2 + m^2 + lm, \tag{2.65}$$

where $l, m = 0, \pm1, \pm2, \pm3, ...$ and thus integer number $n = 1, 3, 4, 7, ...$ In the presence of the phonon-ripplon interaction, the frequency spectrum of the coupled modes is determined by the secular equation [6]. For coupled longitudinal phonon-ripplon modes such as those observed in the Grimes and Adams experiment, the corresponding frequency spectrum can be obtained from [6]:

$$\omega^2 - \omega_l^2(q) - \frac{1}{2}\sum_{\vec{G_\mathrm{n}}} V^2_{\vec{G_\mathrm{n}}}\,\frac{\omega^2}{\omega^2 - \Omega^2_\mathrm{n}(G)} = 0, \tag{2.66}$$

where the coupling constant $V_{\vec{G}}$ has the form

$$V_{G_\mathrm{n}} = V^0_{G_\mathrm{n}}\exp(-nW_1) \equiv V_\mathrm{n} \quad \text{with } 0.5 < W_1 < 0.7 \text{ near } \mathrm{T_m}. \tag{2.67}$$

Here ω represents the frequency of coupled modes, ω_l and Ω denote the frequency of the longitudinal phonon in equation 2.56 and the ripplon frquency in equation 2.64 respectively.

For the lowest mode ($n = 1$) and long wavelength, the frequency ω is far below the ripplon frequency Ω_1 so that the dimple underneath each electron can follow the motion of the electron. Disregarding V_{G_n} for $n \geq 3$ due to their exponential decay (shown in equation 2.67), we can obtain an analytical solution from the equation 2.66

$$\omega(q) \simeq \frac{\omega_l}{\sqrt{1+3V_1^2\Omega_1^2}}. \tag{2.68}$$

Note that $\sum_{\vec{G_{\rm n}}} V_{\vec{G_{\rm n}}}^2$ in equation 2.66 is equivalent to $\sum_{G_{\rm n}} 6V_{\vec{G_{\rm n}}}^2$ for $n < 7$ due to a six-fold degeneracy [44]. Equation 2.68 indicates that the frequency of coupled longitudinal phonon-ripplon mode is equivalent to reduced bare longitudinal phonon frequency with a renormalized mass. In other words, $m_{\rm e}$ in equation 2.56 is replaced with $m_{\rm e}(1+3V_1^2\Omega_1^2)$ and $m_{\rm e}3V_1^2\Omega_1^2$ can be considered as mass contribution from the ripplon. This feature can be seen by comparing the dashed curve and the lowest solid curve in Fig. 2.11. With an increase in wave number q ($\omega_l \gg \omega \sim \Omega_1$), we can additionally ignore the first term ω^2 on the left-hand side of the secular equation 2.66, leading to

$$\omega^2(q) \simeq \frac{\Omega_1^2}{1+3V_1^2/\omega_l^2}. \tag{2.69}$$

This illustrates that the frequency ω approaches an upper-limit Ω_1 with increasing q as shown by the lowest solid line and the lowest dashed horizontal line in Fig. 2.11. Near other ripplon frequencies $\omega \sim \Omega_{3,4}$, we have the solution:

$$\omega^2(q) \simeq \Omega_{\rm n}^2\left(1-\frac{3V_{\rm n}^2}{\omega_l^2+3V_1^2}\right) \quad \text{for } n = 3, 4. \tag{2.70}$$

Since $V_{3,4}^2 \ll V_1^2$, the frequency ω is less affected by the phonon frequency ω_l and quite close to the frequency of the bare ripplon mode as shown by the two solid curves in the middle of Fig. 2.11. At higher frequency $\omega \gg \Omega_1$, the dimple underneath each electron can be regarded as motionless and the corresponding solution of the secular equation gives the dispersion relation:

$$\omega(q) = \sqrt{\omega_{\mathrm{d}}^2 + \omega_l^2}, \tag{2.71}$$

where $\omega_{\mathrm{d}}^2 = 1/2 \sum_{\vec{G_{\mathrm{n}}}} V_{\vec{G}}^2$ is the frequency of the single electron oscillation in the static dimple. The non-zero value of the frequency spectrum at $q = 0$ resembles an optical-like mode as shown by the top solid curve in Fig. 2.11 . So far, we have discussed how the dispersion relation is altered due to longitudinal phonon-ripplon coupling. As Fisher, Halperin, and Platzman pointed out, the dispersion relation of coupled modes of transverse phonons can be qualitatively similar to the longitudinal phonons case because it can be obtained from the same secular equation 2.66 with ω_l replacing ω_t.

2.4 Transport Properties of Electrons on Helium

The charge transport properties are usually characterized by the mobility of charge carriers. At low electron density, in which electron-electron interaction can be neglected, the mobility of electrons on helium surface is determined by two different scattering mechanisms depending on temperature [86, 87]. ^{4}He vapor atoms are the dominant electron scatters at T $\geq$ 1 K, whereas electron-ripplon scattering dominates at T $\leq$ 0.8 K. Since Sommer and Tanner experimentally determined the mobility of surface electrons on helium for the first time [88], many groups have reported experimental values of the mobility in various temperature ranges using different techniques [7, 8, 9, 89, 90, 91]. Also, it has been studied theoretically by Saitoh [10], Shikin and Monarkha [49]. Fig. 2.12 shows experimental data of the mobility from some of groups together with a theoretical calculation from Saitoh [10]. In this figure, the electron mobility increases exponentially with decreasing temperature T down to $\sim$ 1 K due to the exponential decay of the ^{4}He vapor pressure. The moderate

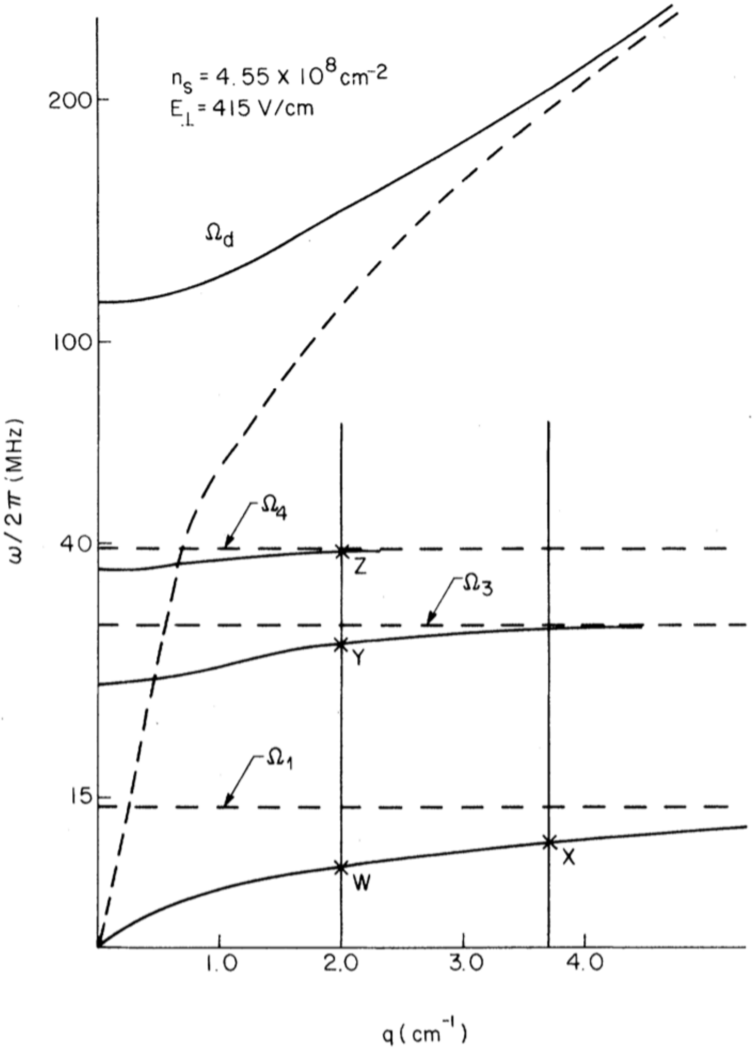

Figure 2.11: Dispersion relation of the longitudinal phonon-ripplon coupled modes (solid curves). The dashed curve is the bare longitudinal phonon spectrum of the electron crystal and the horizontal dashed lines represent the bare ripplon resonance frequencies when ignoring the phonon-ripplon coupling. The vertical lines are the wave vectors excited in the experiment. The resonances are labeled as in Ref. [5]. Figure taken from Ref. [6].

change of the mobility below T $\simeq$ 0.8 K results from the slow temperature dependence of the electron-ripplon scattering rate. At arbitrary temperature, the scattering rate $1/\tau$ is given by

$$\frac{1}{\tau(\varepsilon_{\mathrm{k}})} = \frac{1}{\tau_{\mathrm{V}}(\varepsilon_{\mathrm{k}})} + \frac{1}{\tau_{\mathrm{R}}(\varepsilon_{\mathrm{k}})}, \tag{2.72}$$

where τ_{V} and τ_{R} denote the energy, ε_{k}, dependent relaxation time for electron-^{4}He scattering and electron-ripplon scattering, respectively. From the total relaxation time $\tau(\varepsilon_{\mathrm{k}})$, the electron mobility is defined as

$$\mu = \frac{e\langle\tau(\varepsilon_{\mathrm{k}})\rangle}{m^*} \tag{2.73}$$

where m^* is the electron effective mass. In the next two subsections 2.4.1 and 2.4.2, a more detailed discussion of these two scattering mechanisms will be presented.

2.4.1 ^{4}He Vapor Scattering

When an electron strikes an atom, the scattering is determined by a competition between the short-range repulsion arising from the Pauli principle and the long-range polarization attraction. For the helium atom, the repulsion dominates the scattering due to the very low atomic polarizability of helium, leading to a positive scattering length $a_{\mathrm{s}} = 1.19a_0 \simeq 0.63$ Å and a scattering cross section $\sigma_{\mathrm{s}} = 4\pi a_{\mathrm{s}}^2 \simeq 4.98$ Å^2 for low-energy electrons [92]. Using the Boltzmann transport equation for electron-He gas scattering, Saitoh calculated the relevant scattering rate $1/\tau_{\mathrm{V}}$, which is given by

$$\frac{1}{\tau_{\mathrm{V}}} = \frac{3\pi\hbar\sigma_{\mathrm{s}}n_{\mathrm{V}}}{8m_{\mathrm{e}}b}, \tag{2.74}$$

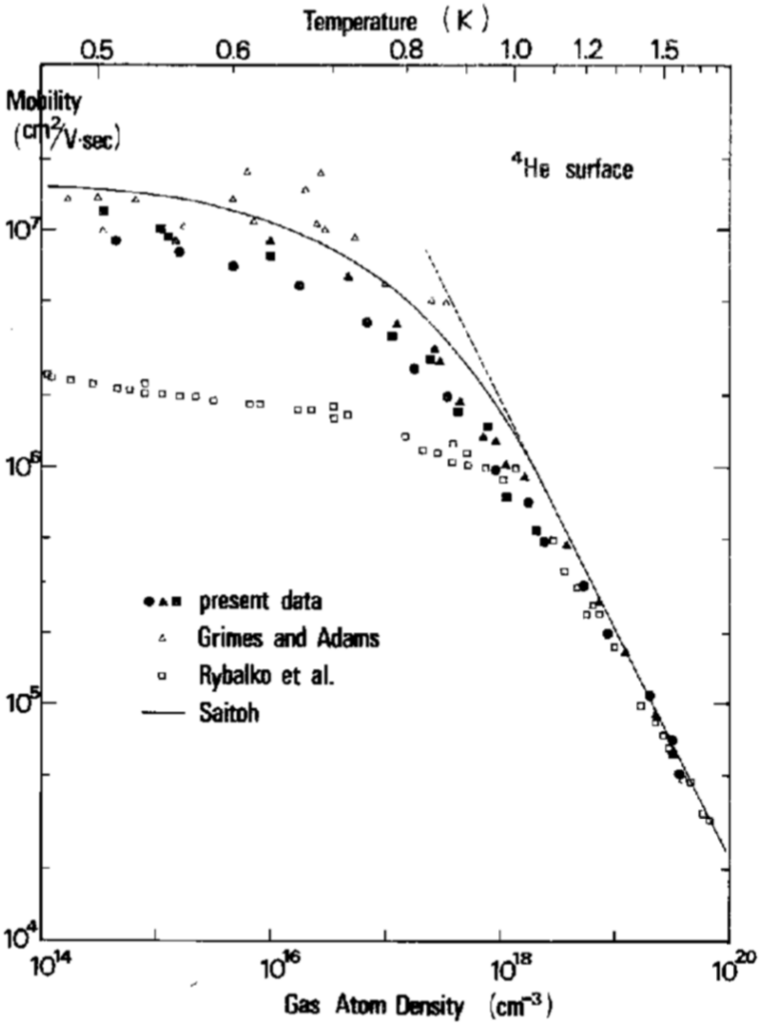

Figure 2.12: Mobility of electrons on helium versus the temperature and ^{4}He vapor density. Experimental data from Grimes and Adams [7], Rybalko *et al.* [8], and Iye [9] are shown together with a theoretical analysis from Saitoh [10]. The dashed line is the mobility considering vapor atom scattering alone. Figure taken from Ref. [9].

where b is the effective Bohr radius in the presence of a vertical holding field from equation 2.14 and n_{v} is the saturated vapor density of the ^{4}He gas, which is given by [10]

$$n_{\mathrm{v}}(\mathrm{T}) = \left(\frac{M k_{\mathrm{B}} \mathrm{T}}{2\pi\hbar^2}\right)^{3/2} \exp\left(\frac{-Q_{\mathrm{v}}}{k_{\mathrm{B}}\mathrm{T}}\right). \tag{2.75}$$

Here $M = 6.646 \times 10^{-27}$ kg is the mass of a ^{4}He atom and Q_{v} denotes the vaporization energy of ^{4}He ($Q_{\mathrm{v}}/k_{\mathrm{B}} \simeq 7.17$ K from [10]). Since the scattering time τ_{v} does not depend on the electron energy, the mobility due to helium vapor scattering can be obtained from equation 2.73

$$\mu_{\mathrm{v}} = \frac{e\tau_{\mathrm{v}}}{m^*} = \frac{8eb}{3\pi\hbar\sigma_{\mathrm{s}} n_{\mathrm{v}}} \quad \text{with } m^* \simeq m_{\mathrm{e}} \text{ for } {}^4\text{He}. \tag{2.76}$$

In this expression, it is obvious that the mobility μ_{v} depends on both the vertical holding field dependent effective Bohr radius $b(E_\perp)$ and the vapor density $n_{\mathrm{v}}(\mathrm{T})$. Particularly, we can expect an exponential decay of the mobility as T increases originating from the temperature dependence of the vapor density in equation 2.75, which agrees with experimental data for $\mathrm{T} \geq 1$ K as seen in Fig. 2.12.

2.4.2 Ripplon Scattering

As the temperature decreases below 0.8 K, the ^{4}He vapor density becomes very low and the electron mobility is limited by the electron interaction with thermal capillary waves on the helium surface (ripplons). These ripplons are characterized by the following dispersion relation [93]:

$$\Omega_{\mathrm{q}}^2 = \left(gq + \frac{\sigma q^3}{\rho}\right) \tanh(qd), \tag{2.77}$$

where $g = 9.81$ m/s^2 is the gravitational acceleration, σ the surface tension of helium, ρ the mass density of the fluid, and d the thickness of the fluid layer. The first term describes a gravity wave and the second term is associated with the capillary wave. When $q \gg q_{\mathrm{c}} = \sqrt{g\rho/\sigma}$, the capillary wave term predominantly determines the frequency spectrum of the ripplon and the gravity waves are neglected. For liquid ^{4}He, the surface tension σ and the mass density ρ are 0.37 dyn/cm and 0.145 g/cm^3 respectively [50] and therefore the corresponding q_{c} is $\sim$ 20 cm^{-1}, which means that the capillary waves dominate the dispersion relation for the wave number $q \gg 20$ cm^{-1}. The ripplon wave number q involved in electron scattering is of the order of thermal electron wave number $q \sim 2k_{\mathrm{T}}$, where $k_{\mathrm{T}} = \sqrt{2m_{\mathrm{e}}k_{\mathrm{B}}\mathrm{T}}/\hbar$ is thermal deBrogile wave number [44]. In the temperature region 0.1 K $\leq$ T $<$ 1 K, the range of relevant q is approximately between $\sim 10^5$ and $\sim 10^6$ cm^{-1}, which far exceeds $q_{\mathrm{c}} = 20$ cm^{-1}. Therefore, for thick helium film ($d > 100$ nm $\rightarrow \tanh(qd) \sim 1$), the dispersion relation in equation 2.77 reduces to

$$\Omega_{\mathrm{q}}^2 = \sigma q^3/\rho. \tag{2.78}$$

In this reduced form, the energy of ripplons taking part in electron scattering is given by

$$\hbar\Omega_{\mathrm{q}} = \sqrt{\frac{\sigma}{\rho\hbar}}\left(8m_{\mathrm{e}}k_{\mathrm{B}}\mathrm{T}\right)^{3/4}, \tag{2.79}$$

which is much smaller than thermal energy $k_{\mathrm{B}}\mathrm{T}$. For instance, $\hbar\Omega_{\mathrm{q}}$ is $\sim 1\times10^{-2}$ K at T = 1 K and $\sim 4\times10^{-4}$ K at T = 0.01 K. This implies that only long wavelength ripplons with an energy far smaller than the thermal energy can scatter with electrons. The occupation number N_{q} for ripplons is given by [49]

$$N_{\mathrm{q}} = \{\exp\left(\frac{\hbar\Omega_{\mathrm{q}}}{k_{\mathrm{B}}\mathrm{T}}\right) - 1\}^{-1}, \tag{2.80}$$

which is formally equivalent to the occupation number of surface-bound bosonic quasiparticles i.e. harmonic oscillator excitations. By solving the Boltzmann transport equation, Saitoh obtained the relaxation time $\tau_{\mathrm{R}}(\varepsilon_{\mathrm{k}})$ for electron-ripplon scattering [10]:

$$\begin{aligned}\frac{1}{\tau_{\mathrm{R}}(\varepsilon_{\mathrm{k}})} = \frac{k_{\mathrm{B}}\mathrm{T}}{4\hbar\sigma a^2}\Bigg[&\frac{(eE_{\perp}a)^2}{\varepsilon_{\mathrm{k}}} + 2(eE_{\perp}a)\left(\ln\frac{16E_{\mathrm{b}}}{\varepsilon_{\mathrm{k}}} - 3\right)\\ &+ \frac{3\varepsilon_{\mathrm{k}}}{2}\left\{\left(\ln\frac{16E_{\mathrm{b}}}{\varepsilon_{\mathrm{k}}} - \frac{19}{6}\right)^2 + \left(\frac{\pi^2}{3} - \frac{115}{36}\right)\right\}\Bigg],\end{aligned} \tag{2.81}$$

where $a = a_0/\Lambda$ is the effective Bohr radius with zero electric field normal to the plane and E_{b} is defined as

$$E_{\mathrm{b}} = \frac{\hbar^2}{2m_{\mathrm{e}}b^2}. \tag{2.82}$$

The relaxation time approximation gives a non-equilibrium electron distribution function in the presence of a drift field $\vec{E}_{\parallel}$ parallel to the electron plane, which is given by

$$f(\varepsilon_{\mathrm{k}}) \simeq f_0(\varepsilon_{\mathrm{k}}) - e\,\tau_{\mathrm{R}}(\varepsilon_{\mathrm{k}})\,\vec{v}_{\mathrm{k}}\cdot\vec{E}_{\parallel}\,\frac{\partial f_0}{\partial\varepsilon_{\mathrm{k}}}, \tag{2.83}$$

where $\vec{v}_{\mathrm{k}}$ is the electron velocity and equilibrium electron distribution function $f_0(\varepsilon_{\mathrm{k}})$ for the non-degenerate system is

$$f_0(\varepsilon_{\mathrm{k}}) = \frac{\pi\hbar^2 n_{\mathrm{e}}}{m_{\mathrm{e}}k_{\mathrm{B}}\mathrm{T}}\exp\left(-\frac{\varepsilon_{\mathrm{k}}}{k_{\mathrm{B}}\mathrm{T}}\right). \tag{2.84}$$

From the drift current density $\vec{j} = e\int_0^\infty d\varepsilon_\mathrm{k}\,\vec{v}_\mathrm{k}\,D(\varepsilon_\mathrm{k})\,f(\varepsilon_\mathrm{k})$, the conductivity is obtained from Ohm's law:

$$\sigma_0 = \frac{e^2}{m_\mathrm{e}}\int_0^\infty d\varepsilon\,D(\varepsilon)\left[-\tau_\mathrm{R}(\varepsilon)\,\varepsilon\,\frac{\partial f_0}{\partial\varepsilon}\right], \tag{2.85}$$

where $D(\varepsilon) = m_\mathrm{e}/\pi\hbar^2$ is the electron density of states in 2D. The DC electron mobility $\mu = \sigma_0/n_\mathrm{e}e$ is given by

$$\mu = \frac{e}{m_\mathrm{e}}\langle\tau_\mathrm{R}(\varepsilon)\rangle, \tag{2.86}$$

where the average of $\tau_\mathrm{R}(\varepsilon)$ is

$$\langle\tau_\mathrm{R}(\varepsilon)\rangle = \frac{1}{n_\mathrm{e}}\int_0^\infty d\varepsilon\,D(\varepsilon)\left[-\tau_\mathrm{R}(\varepsilon)\,\varepsilon\,\frac{\partial f_0}{\partial\varepsilon}\right] = \int_0^\infty d\varepsilon\,\frac{\varepsilon\,\tau_\mathrm{R}(\varepsilon)}{k_\mathrm{B}^2\mathrm{T}^2}e^{-\varepsilon/k_\mathrm{B}\mathrm{T}}. \tag{2.87}$$

Using the approximation $\langle\tau_\mathrm{R}(\varepsilon)\rangle = \tau_\mathrm{R}(\varepsilon = k_\mathrm{B}\mathrm{T})$ in equation 2.81, the average collision time due to electron-ripplon scattering at $\vec{E}_\perp = 0$ can be approximately given by

$$\tau_\mathrm{R}(\mathrm{T}) \equiv \langle\tau_\mathrm{R}(\varepsilon)\rangle \simeq \frac{8\hbar\sigma a^2}{3k_\mathrm{B}^2\mathrm{T}^2}\left(\ln 0.67\frac{E_0}{\mathrm{T}}\right)^{-2} \tag{2.88}$$

with $E_0 = \hbar^2/2m_\mathrm{e}a^2$, which has a much weaker temperature dependence compared to the collision time for helium vapor scattering in equation 2.74. At non-zero pressing field ($\vec{E}_\perp \neq 0$), the ripplon-limited collision time for $\mathrm{T} < 0.8$ K is suppressed with increasing $\vec{E}_\perp$ under the same approximation, as shown in Fig. 2.13. This is because a larger value of $\vec{E}_\perp$ presses the electrons more strongly against the helium surface leading to an enhancement of the electron-ripplon interaction [7]. However, for high temperature where the vapor density dominates the electron scattering, the effect of the holding field on scattering becomes weaker.

In the limit of the strong field, equation 2.81 is simply given by

$$\frac{1}{\tau_{\mathrm{R}}(\varepsilon)} \simeq \frac{k_{\mathrm{B}}\mathrm{T}}{4\hbar\sigma a^2}\frac{(eE_{\perp}a)^2}{\varepsilon}, \tag{2.89}$$

and therefore the integral equation 2.87 yields $\langle\tau_{\mathrm{R}}(\varepsilon)\rangle = 8\hbar\alpha/(eE_{\perp})^2$ which depends only on the holding field.

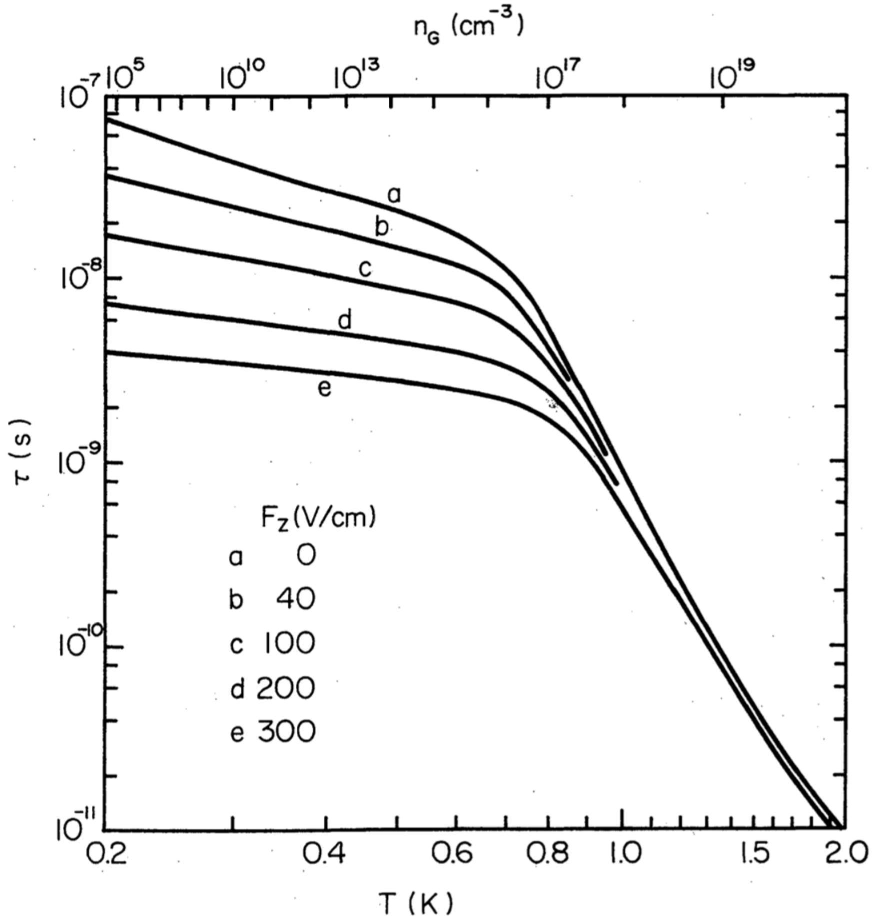

Figure 2.13: Collision time τ as a function of temperature for various holding electric fields F_{z} (from Ref. [10]).

2.5 Superfluid Liquid Helium

To understand the unique properties of 2D electrons on helium, it is crucial to understand the physics of the underlying liquid ^{4}He substrate supporting the surface electrons. In the experiments described in this thesis, the surface electrons are formed on liquid ^{4}He at $T \simeq 1.55$ K. At this temperature, the liquid helium is composed of mostly superfluid. Thus, we first start with a brief review of superfluid ^{4}He in subsection 2.5.1. In subsection 2.5.2, we will discuss helium film formation in the different geometries used in this Ph.D. project. This is important since a liquid helium thickness smaller than a SAW wavelength is required to observe the SAW-electrons coupling described in chapter 7 . The last subsection 2.5.3 will describe the decrease in the helium film thickness by surface electrons and the critical electron density at which the hydrodynamic instability of the film appears.

2.5.1 Superfluidity of Liquid ^{4}He

Helium exhibits remarkable properties as a quantum substance. Unlike all other liquids, it remains a quantum liquid even at $T = 0$ K at ambient pressure. To solidify the helium, one needs to apply a large pressure as shown in Fig. 2.14. This unique feature originates from the very weak binding force between helium atoms and the large quantum mechanical zero-point energy [11]. In particular, the neutral ^{4}He atom, composed of 2 protons and 2 neutrons in the nucleus and 2 electrons orbiting, has zero net spin and forms a bosonic liquid below the boiling point $T_b = 4.21$ K, which is governed by Bose-Einstein statics. When cooled down to the "lambda point" $T_\lambda = 2.17$ K, a remarkable transition takes place (Fig. 2.14) related to Bose-Einstein condensation and some portion of the liquid becomes a superfluid with vanishing viscosity as $T \to 0$. In addition to zero viscosity, superfluids have several unusual

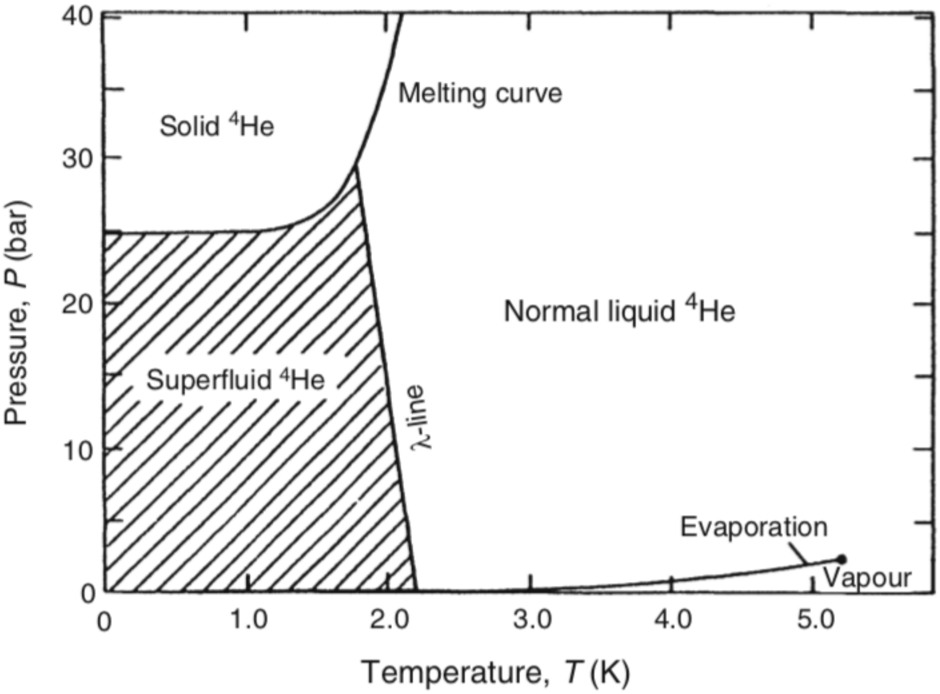

Figure 2.14: Phase diagram of ^{4}He (from Ref. [11]).

properties, which are summarized below.

Specific Heat

Fig. 2.15 shows an anomalous increase of the specific heat of liquid ^{4}He at the transition to the superfluid near 2.18 K, which resembles the Greek letter "λ" and is thus called the λ-transition. This astonishing behavior was first measured by L.J. Dana and H. Kamerlingh Onnes in 1920 although they didn't publish the result. Later, this observation was explained with two-fluid theory [94] and subsequently by Landau introduced the concept of quasi-particles rotons [95]. Above the λ-transition, ^{4}He behaves like a classical fluid due to very low density. Below the λ-point, it becomes a bosonic quantum liquid exhibiting a rapidly decreasing entropy and specific heat with decreasing temperature. In particular, the fast decrease of the specific heat in the temperature range $1 - 2.18$ K is associated with higher energy rotons excitation. Below T = 0.6 K, the heat capacity decreases as T^3 due to phonon excitation.

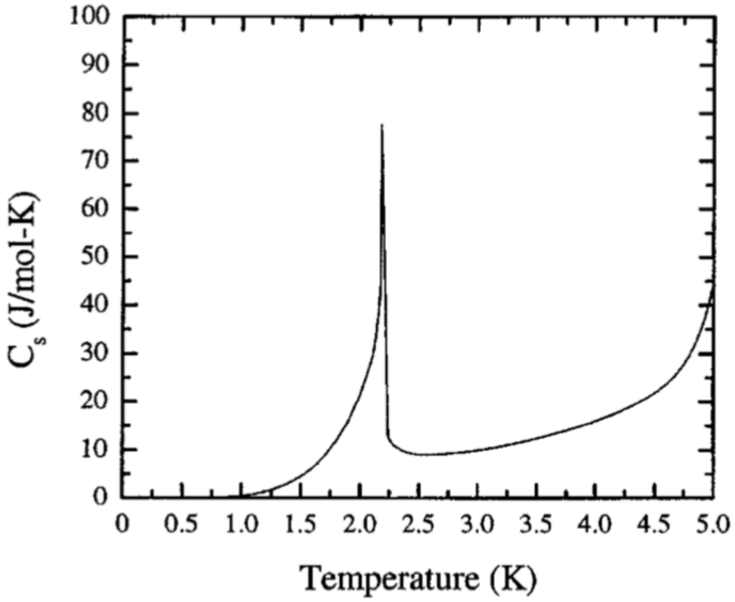

Figure 2.15: Specific heat of liquid ^{4}He as a function of temperature at saturated vapor pressure. The specific heat has a sharp peak as T → T_λ. Figure taken from Ref. [12].

Thermal Conductivity

Below the λ-transition, the superfluid has an extremely high thermal conductivity hundreds times larger than that of copper under the same conditions [96]. It is known that heat transport in this regime occurs through unique thermal counterflow mode existing only in superfluid helium, where the normal fluid moves away from the heat source and superfluid moves toward it to maintain zero net mass flow. This leads to very effective thermal transport although superfluid turbulence limits the heat flow [97]. This high thermal conductivity makes superfluid helium a very efficient medium for creating a homogeneous temperature as well as transporting heat at low temperatures.

Viscosity

In the superfluid state, the wave functions of each atom overlap and the fluid act as if they were one macroscopic quantum system. Consequently, the atoms do not collide with each other, which leads to zero friction or a vanishing viscosity. This allows for persistent flow of superfluid helium similar to a persistent current in a superconducting state. Particularly, frictionless superfluid can flow through any pore or hole in a container unless the fluid velocity exceeds a critical value. Thus, the container is impermeable to normal fluid helium for T $\geq$ 2.18 K but may show a superfluid helium leak below $\sim$2.18 K. Also, if two containers having different superfluid level are connected, frictionless flow of superfluid film between them is driven by the difference in gravitational potential and equalizes their levels. For an open container, a film of superfluid will creep out and escape.

Sound Waves

Neglecting viscosity term at low temperature, the two-fluid model gives two wave equations [94]:

$$\frac{\partial^2 \rho}{\partial t^2} = \nabla^2 P \tag{2.90}$$

$$\frac{\partial^2 S}{\partial t^2} = \frac{\rho_\mathrm{s}}{\rho_\mathrm{n}} S^2 \nabla^2 \mathrm{T}, \tag{2.91}$$

where the total density ρ of the liquid helium is the sum of the densities of the normal fluid ρ_n and superfluid component ρ_s, P the pressure, and S the entropy. These equations yield two solutions with two different sound velocities:

$$u_1 \simeq \left(\frac{\partial P}{\partial \rho}\right)_\mathrm{S}^{1/2}, \quad u_2 \simeq \left(\frac{\rho_\mathrm{s}}{\rho_\mathrm{n}} \frac{\mathrm{T}S^2}{C_\mathrm{p}}\right)^{1/2} \tag{2.92}$$

Here P and C_{p} are the pressure and the specific heat of the fluid at constant pressure, respectively. u_1 is the velocity of ordinary density waves in a fluid driven by changes in pressure, which is referred to first sound. In this wave, the two components of the fluid move in phase with each other (i.e. the velocities of the two components are the same $\vec{v}_{\mathrm{s}} = \vec{v}_{\mathrm{n}}$). Below the lambda point ($\mathrm{T} < \mathrm{T}_\lambda$), there are entropy waves driven by temperature differences with velocity u_2, which are called second sound. This is a quantum mechanical phenomena in which the two components are out of phase with constant total density $\partial\rho/\partial t = 0$. The second sound velocity u_2 is zero at the lambda point and reaches ∼20 m/s at $\mathrm{T} \simeq 1.8$ K, which is approximately ten times slower than first sound velocity $u_1 \simeq 2.3 \times 10^2$ m/s [12]. In 1959 Kenneth Atkins predicted two more sound waves in liquid helium below the lambda point, which he called third sound and fourth sound [98]. Few years later, both third and fourth sound were experimentally observed by Everitt *et al.* [99] and Rudnick and Shapiro [100]. Third sound is a long-wavelength surface wave on a thin film of the liquid helium, in which the superfluid component oscillates but the normal component remains locked to the substrate. Fourth sound is a pressure and density wave similar to the first sound. However, this compressional wave only propagates in the superfluid component while the normal component remains stationary. Such a condition can be achieved in porous media such packed powders [100]. The velocities of the third and the fourth sound are given by [12, 100]

$$u_3^2 \simeq 3\alpha/d^3 \;\text{ for a thin film } (d < 30\text{Å}), \tag{2.93}$$

$$u_4^2 = \frac{\rho_{\mathrm{s}}}{\rho}u_1^2 + \frac{\rho_{\mathrm{n}}}{\rho}u_2^2 \simeq \frac{\rho_{\mathrm{s}}}{\rho}u_1^2\,(u_1 \gg u_2), \tag{2.94}$$

where α is the van der Waals constant.

2.5.2 Helium Film Formation

Inside a container partially filled with liquid helium, adsorption of helium atoms from the vapor phase leads to formation of vertical liquid helium film on the wall. Finite viscosity usually prevents movement of such a film. However, in the superfluid state, the vanishing viscosity allows the film to crawl up the wall as mentioned before. The film thickness is closely related to the van der Waals potential (between the helium and the walls of the container or substrate surface) which depends on the height above a bulk liquid helium reservoir. At a height h above bulk helium (Fig. 2.16 (a)), the chemical potential of the film can be written as [11]

$$\mu_{\mathrm{f}} = \mu_0 + \rho g h - \alpha / d^n, \tag{2.95}$$

where μ_0 is the chemical potential of the bulk helium and $\rho g h$ is gravitational potential. The last term in equation 2.95 represents the van der Waals potential of the substrate, which attracts the liquid helium film. The thickness of the film d can be determined using the thermal equilibrium condition ($\mu_{\mathrm{f}} = \mu_0$):

$$d = \left(\frac{\alpha}{\rho g h} \right)^{1/n}. \tag{2.96}$$

The exponent n depends on ^{4}He film thickness. For large film thickness, n is 4, whereas n is 3 for the thin film case. For a metal substrate, the characteristic thickness of the transition region between $n = 3$ and $n = 4$ is theoretically predicted to be ~50 nm [101].

In a micro-channel geometry, $1 - 2$ μm thick liquid helium film can be formed in the channel by capillary action as shown in Fig. 2.16 (b). This type of device has several merits for studying surface electrons on helium, including a very uniform helium thickness, high

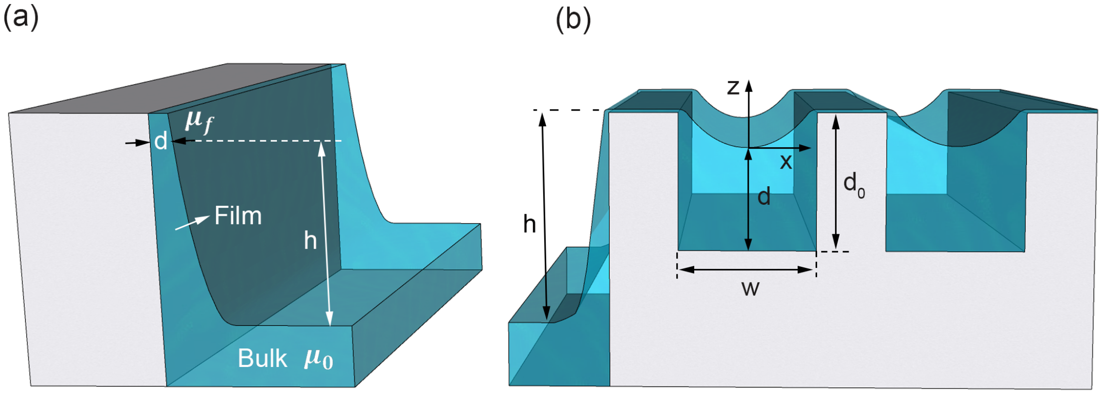

Figure 2.16: Helium film formation: (a) Van der Waals film on a vertical wall of the substrate. μ_0 and μ_f are the chemical potential of the bulk helium and the thin film of helium located at height h above the bulk level. (b) Helium film formation inside the channel of the microchannel array by capillary force. Here w, d_0, d, and h represent channel with, channel depth, helium film thickness in the channel, and the distance between the channel top and the bulk helium level in the reservoir.

mobility similar to that on bulk helium [102], increasing hydrodynamic stability [103], and well-confined surface electrons regions. Assuming that the profile of the liquid in the channel has a semicircular form with the curvature radius R, the thickness of the liquid film $d(x)$ at an arbitrary position x in the channel (see Fig. 2.16 (b)) is given by

$$d(x) = d_0 - z(w/2) + z(x) \tag{2.97}$$

with $z(x) = R\left(1 - \sqrt{1-(x/R)^2}\right)$ and $R = \sigma/\rho g h$. When $h = 1$ mm, the radius $R \approx 270$ μm using $\sigma = 0.378 \times 10^{-3}$ N/m and $\rho = 0.145$ g/cm^3. Generally, R is much larger than a channel width w of a few tens of micrometers, forming a self-stablized helium film in the gap. The parameter $z(x)$ has the approximate form $z(x) \simeq x^2/2R$ for this case. This simplifies equation 2.97 to

$$d(x) = d_0 - \frac{w^2}{8R} + \frac{x^2}{2R} \tag{2.98}$$

When $h \to 0$ and $R \to \infty$, the channel is fully filled with the film having thickness $d(x) = d_0$. At the center of the channel ($x = 0$), the film thickness is $d(x = 0) = d_0 - w^2/8R$.

2.5.3 Charged Helium Film and Stability

When electrons are deposited onto the surface of the helium film, the charged helium surface becomes more unstable and the film thickness is reduced by the electrostatic pressure of the electrons. In particular, an electrohydrodynamic (EHD) instability can be caused by surface electrons and places a limit on the maximum surface electron density that can be achieved. This will be briefly reviewed first, followed by a discussion of the charged helium film thickness.

EHD Instability and Critical Electron Density

In the presence of electrons above a bulk helium surface, the dispersion relation of the ripplons (capillary waves) in equation 2.77 is modified into [68]

$$\Omega_{\mathrm{q}}^2 = \left(gq + \frac{\sigma q^3}{\rho} - \frac{4\pi e^2 n_{\mathrm{e}}^2}{\rho} q^2 \right) \tanh(qd), \tag{2.99}$$

This indicates a softening of the capillary waves spectrum due to the presence of electrons. By solving equation 2.99, one can find the wave number q_{c} at which the instability first occurs ($\Omega_{\mathrm{q}}^2 < 0$), which is given by

$$q_{\mathrm{c}} = \sqrt{\frac{g\rho}{\sigma}} \tag{2.100}$$

The corresponding critical electron density is given by

$$n_{\mathrm{c}} = \frac{(g\rho\sigma)^{1/4}}{(2\pi e^2)^{1/2}}, \tag{2.101}$$

which theoretically predicts the maximum attainable density on the surface of bulk helium. For liquid ^{4}He, a surface tension $\sigma \simeq 0.37$ dyn/cm and mass density $\rho \simeq 0.145$ g/cm^3 yield $q_\mathrm{c} \simeq 20$ cm^{-1} and $n_\mathrm{c} \simeq 2.2 \times 10^9$ /cm^2.

For a superfluid thin film formed by the Van der Waals interaction, the attraction between the helium and substrate stabilizes the charged surface and thus the capillary waves spectrum may be written as [68]

$$\Omega_\mathrm{q}^2 = \left[\left(\frac{3\alpha}{\rho d^4} + g\right) q + \frac{\sigma}{\rho} q^3 - \frac{4\pi e^2 n_\mathrm{e}^2}{\rho} \varepsilon_\mathrm{s} q^2\right] \tanh(qd) \tag{2.102}$$

when $qd \ll 1$. Here α and ε_s denote the Van der Waals constant and the dielectric constant of the solid substrate, respectively. The electrohydrodynamic instability occurring at the wave number $q_\mathrm{c} = \sqrt{3\alpha/\sigma}/d^2$ leads to the maximum attainable electron density, which is given by

$$n_\mathrm{c} = \sqrt[1/4]{\frac{3\alpha\sigma}{(2\pi e^2 \varepsilon_\mathrm{s} d^2)^2}} \tag{2.103}$$

For a glass substrate covered with 10 nm thick helium film, $\varepsilon_\mathrm{s} \simeq 5$ and $3\alpha/\rho g d^4 \simeq 2 \times 10^8$ [68] yield $n_\mathrm{c} \simeq 1.2 \times 10^{11}/$ cm^2 and $q_\mathrm{c} \simeq 2.7 \times 10^5$ cm^{-1} respectively. Furthermore, Hu and Dahm theoretically showed that a charged helium film can be stable at any electron density and that the maximum density is only restricted by tunneling to the substrate [104]. This is expected to become important when $d < 35$ Å. The corresponding maximum density is $\sim 1.5 \times 10^{11}$ cm^{-2} for a metal substrate [104], in an agreement with experiment [13].

For a charged micro-channel geometry, the small surface area of liquid helium in each channel leads to a minimum value of the wave vector $q_\mathrm{m} \simeq \pi/w$ much larger than $q_\mathrm{c} = 20$ cm^{-1} near which the instability occurs for the bulk helium case. For instance, a channel width $w = 10$ μm in Fig. 2.16 (b) yields $q_\mathrm{m} \simeq 3.1 \times 10^3$ cm^{-1} $\gg q_\mathrm{c} = 20$ cm^{-1}. This inequality can make $\Omega_{\mathrm{q}}^2 \geq 0$ in equation 2.99 when $q \geq q_{\mathrm{m}}$ and thus the EHD instability is forbidden in this type of geometry. When neglecting the gravity term in equation 2.99 since $q \geq q_{\mathrm{m}} \gg q_{\mathrm{c}}$, the condition for stability reduces to $\sigma q - 4\pi e^2 n_{\mathrm{e}}^2 \geq 0$, which results in a critical density $n_{\mathrm{c}} = \sqrt{\sigma q_{\mathrm{m}}/4\pi e^2}$. For $w = 10$ μm, $n_{\mathrm{c}} \simeq 2 \times 10^{10}$ cm^{-2} is an order of magnitude larger than the above bulk helium case ($n_{\mathrm{c}} \simeq 2.2 \times 10^9$ cm^{-2}). In fact, this maximum density is slightly reduced by the depression of the helium film, which will be discussed in the next subsection.

Film Thickness Depression From Electron Charging

Etz et. al measured the maximum density of surface electrons on a liquid ^{4}He film formed by the Van der Waals interaction and found that their experimental value was significantly larger than theoretical value determined by equation 2.103 [13]. This discrepancy was ultimately resolved by taking into account the film thickness depression due to electron pressure.

For the uncharged Van der Waals helium film with a thickness d_{i} ranging from 200 to 400 Å, the equilibrium thickness after charging is given by [13]

$$d = d_{\mathrm{i}} \left(1 + \frac{2\pi n_{\mathrm{e}}^2 e^2}{\rho g h}\right)^{-1/3}, \tag{2.104}$$

with the assumption that $d_{\mathrm{i}} = (\sigma/\rho g h)^{1/3}$ before charging. Fig. 2.17 shows the experimental confirmation of the change in charged film thickness governed by equation 2.104.

For the micro-channel geometry, the electron pressure affects the curvature of the helium film leading to [103]:

$$R = \frac{\sigma}{\rho g h + 2\pi n_{\mathrm{e}}^2 e^2}. \tag{2.105}$$

Inserting equation 2.105 into equation 2.98, the charged film thickness with electron density

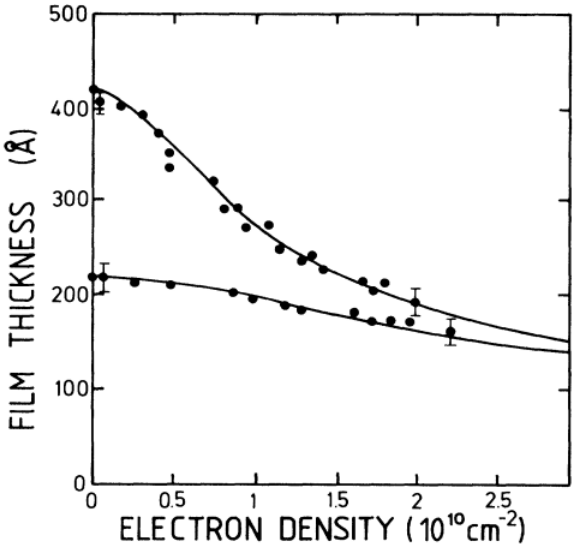

Figure 2.17: Thickness d of charged saturated ^{4}He films wetting a glass substrate (T = 1.6 K) versus the electron density of the films. The thickness of d_0 of the uncharged films was 220 Å and 420 Å, respectively. Figure taken from Ref. [13].

n_e is given by

$$d(n_\mathrm{e}) = d_0 - \frac{w^2}{8\sigma}(\rho g h + 2\pi n_\mathrm{e}^2 e^2) \text{ at the center } (x = 0). \tag{2.106}$$

The maximum electron density n_c can then be obtained from the condition $d(n_\mathrm{c}) = 0$ for the region where $\rho g h \ll 2\pi n_\mathrm{e}^2 e^2$. This is given by

$$n_\mathrm{c} = \sqrt{d_0 \frac{8\sigma}{w^2} \frac{1}{2\pi e^2}}. \tag{2.107}$$

For $w = 10\,\mu$m and $d_0 = 1\,\mu$m, this yields $n_\mathrm{c} \simeq 1.4 \times 10^{10}$ cm^{-2}, which is slightly smaller than the critical density determined by the EHD instability $n_\mathrm{c} \simeq 2 \times 10^{10}$ cm^{-2} discussed above.

Chapter 3

Surface Acoustic Waves (SAWs)

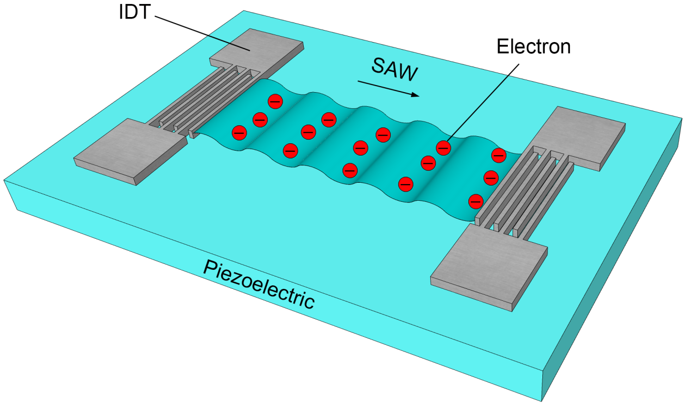

Figure 3.1: Schematic of the SAW-2DES on helium experiment. A SAW is launched from the left interdigitated transducer (IDT) and can, via an evanescent coupling to the electrons, transport electrons in the direction of the travelling wave. A second IDT to the right can act as a SAW detector or acoustic Bragg reflector.

A surface acoustic wave (SAW) is an elastic wave propagating along the surface of a substrate. If the substrate has piezoelectricity, the SAW is accompanied by a co-propagating electric field, which can interact with a 2D electron system (2DES) located within about one wavelength above or below the surface (see Fig. 3.1). Not only is this interaction a versatile tool for study interesting physics in 2D materials [29, 30, 31, 32, 35] but it also can potentially form the basis of single electron devices for metrological current standards [105] or quantum information processing systems [106, 107]. Recently, SAW coupling to quantum systems has also attracted great interest in quantum acoustics with superconducting circuits

[108, 109, 110].

In this chapter we introduce the relevant properties of surface acoustic waves needed to understand our SAW experiments with electrons on helium discussed in chapters 6 and 7. In section 3.1, we start by describing SAW propagation on a piezoelectric substrate. Specifically, we will solve the relevant wave equation and obtain the solution for surface acoustic waves taking into account the appropriate boundary conditions. It should be pointed out that we will only deal with Rayleigh SAW, where the particle motion in the substrate lies in the sagittal plane (partially normal and partially perpendicular to the surface), since this mode is employed in our experiments. In section 3.2, we will describe the coupling of the SAW with a 2DES nearby the surface. Here our interest is restricted to how the 2DES electrically affects the SAW propagation and the mechanical effect on the SAW by an adjoining medium (in our case liquid helium) will be discussed later in chapter 6. Strong coupling leads a fraction of electrons in the 2DES to be trapped by the SAW potential minima and transported at speed of the sound in the substrate, which leads to acoustoelectric charge transport. This latter effect will be described in detail in section 3.3.

3.1 Piezoelectric SAWs

Piezoelectricity is an electric voltage generated in certain solid materials when mechanical stress is applied to them. Reciprocally, the application of the electric voltage can also produces strain in these piezoelectric materials. In these cases, energy is transferred from mechanical to electrical energy or vice versa. The constitutive equations of piezoelectricity are given by

$$T_{ij} = c_{ijkl}S_{kl} - e_{kij}E_k, \tag{3.1}$$

$$D_k = e_{kij}S_{ij} + \varepsilon_{ki}E_i. \tag{3.2}$$

Here c_{ijkl} is the fourth-order stiffness tensor, e_{kij} the piezoelectric tensor, and ε_{ki} the dielectric tensor while T_{ij}, D_k, S_{kl}, and E_k represent the stress tensor, displacement fields, the strain tensor, and electric fields, respectively. For a cubic crystal structure, these constitutive equations have the following matrix form:

$$\begin{bmatrix} T_{11} \\ T_{22} \\ T_{33} \\ T_{23} \\ T_{13} \\ T_{12} \end{bmatrix} = \begin{bmatrix} c_{11} & c_{12} & c_{12} & 0 & 0 & 0 \\ c_{12} & c_{11} & c_{12} & 0 & 0 & 0 \\ c_{12} & c_{12} & c_{11} & 0 & 0 & 0 \\ 0 & 0 & 0 & c_{44} & 0 & 0 \\ 0 & 0 & 0 & 0 & c_{44} & 0 \\ 0 & 0 & 0 & 0 & 0 & c_{44} \end{bmatrix} \begin{bmatrix} S_{11} \\ S_{22} \\ S_{33} \\ 2S_{23} \\ 2S_{13} \\ 2S_{12} \end{bmatrix} - \begin{bmatrix} 0 & 0 & 0 \\ 0 & 0 & 0 \\ 0 & 0 & 0 \\ e_{14} & 0 & 0 \\ 0 & e_{14} & 0 \\ 0 & 0 & e_{14} \end{bmatrix} \begin{bmatrix} E_1 \\ E_2 \\ E_3 \end{bmatrix}, \tag{3.3}$$

$$\begin{bmatrix} D_1 \\ D_2 \\ D_3 \end{bmatrix} = \begin{bmatrix} 0 & 0 & 0 & e_{14} & 0 & 0 \\ 0 & 0 & 0 & 0 & e_{14} & 0 \\ 0 & 0 & 0 & 0 & 0 & e_{14} \end{bmatrix} \begin{bmatrix} S_{11} \\ S_{22} \\ S_{33} \\ 2S_{23} \\ 2S_{13} \\ 2S_{12} \end{bmatrix} + \begin{bmatrix} \varepsilon & 0 & 0 \\ 0 & \varepsilon & 0 \\ 0 & 0 & \varepsilon \end{bmatrix} \begin{bmatrix} E_1 \\ E_2 \\ E_3 \end{bmatrix}. \tag{3.4}$$

In matrix notation the stress tensor and displacement fields can be reduced to the following form for a material possessing cubic symmetry

$$\begin{bmatrix} T_{11} \\ T_{22} \\ T_{33} \\ T_{23} \\ T_{13} \\ T_{12} \end{bmatrix} = \begin{bmatrix} c_{11}S_{11} + c_{12}S_{22} + c_{12}S_{33} \\ c_{12}S_{11} + c_{11}S_{22} + c_{12}S_{33} \\ c_{12}S_{11} + c_{12}S_{22} + c_{11}S_{33} \\ 2c_{44}S_{23} - e_{14}E_1 \\ 2c_{44}S_{13} - e_{14}E_2 \\ 2c_{44}S_{12} - e_{14}E_3 \end{bmatrix}, \quad \begin{bmatrix} D_1 \\ D_2 \\ D_3 \end{bmatrix} = \begin{bmatrix} 2e_{14}S_{23} + \varepsilon E_1 \\ 2e_{14}S_{13} + \varepsilon E_2 \\ 2e_{14}S_{12} + \varepsilon E_3. \end{bmatrix} \tag{3.5}$$

3.1.1 Wave Equations

In the presence of the piezoelectric effect and no external forces, wave equations in the piezoelectric medium can be written as [111]

$$\rho \ddot{u}_i = \partial_j T_{ij} = \partial_j T_{ji}, \quad \partial_k D_k = 0, \tag{3.6}$$

where ρ is the mass density, u_i is the displacement component parallel to the Cartesian axis x_i (i.e. $x_1 = x$, $x_2 = y$, $x_3 = z$), and we have used the notations $\partial_j f = \partial f / \partial x_j$, $\dot{f} = \partial f / \partial t$. Displacement components $u_{i,j}$ have a relationship with the strain tensor component S_{ij} as follows:

$$S_{ij} = S_{ji} = \frac{1}{2}\left(\partial_i u_j + \partial_j u_i\right). \tag{3.7}$$

Inserting equations 3.5 and 3.7 into equation 3.6, one obtains three partial wave equations in the cubic crystal:

$$\begin{aligned}
&\rho\ddot{u}_1 = c_{11}\partial_1^2 u_1 + c_{44}(\partial_2^2 u_1 + \partial_3^2 u_1) + (c_{12}+c_{44})(\partial_1\partial_2 u_2 + \partial_1\partial_3 u_3) + 2e_{14}\partial_2\partial_3\phi, \\
&\rho\ddot{u}_2 = c_{44}\partial_1^2 u_2 + c_{11}\partial_2^2 u_2 + c_{44}\partial_3^2 u_2 + (c_{12}+c_{44})(\partial_1\partial_2 u_1 + \partial_2\partial_3 u_3) + 2e_{14}\partial_1\partial_3\phi, \\
&\rho\ddot{u}_3 = c_{44}\partial_1^2 u_3 + c_{44}\partial_2^2 u_3 + c_{11}\partial_3^2 u_3 + (c_{12}+c_{44})(\partial_1\partial_3 u_1 + \partial_2\partial_3 u_2) + 2e_{14}\partial_1\partial_2\phi, \\
&\varepsilon\nabla^2\phi = 2e_{14}(\partial_2\partial_3 u_1 + \partial_1\partial_3 u_2 + \partial_1\partial_2 u_3),
\end{aligned} \tag{3.8}$$

where ϕ is the electric potential such that $E_i = -\partial_i\phi$. The plane waves solutions u_i and ϕ have the form:

$$\begin{aligned}
u_i &= u_{0i}\, e^{-k_\parallel \alpha z}\, e^{ik_\parallel (lx+my-ct)}, \\
\phi &= \phi_0\, e^{-k_\parallel \alpha z}\, e^{ik_\parallel (lx+my-ct)},
\end{aligned} \tag{3.9}$$

with $l = \cos(\theta)$ and $m = \sin(\theta)$. Here $\vec{k_\parallel} = (k_x, k_y)$ is an in-plane wave vector, α is the decay constant associated with loss of SAW energy, θ is the angle between the x-axis and $\vec{k_\parallel}$, the positive z-axis points into the piezoelectric medium, and c is the phase velocity of the wave (see Fig. 3.2). With solutions of this form, the differential operators in equation 3.8 can be written as

$$\partial_1 \to ik_\parallel l, \quad ,\partial_2 \to ik_\parallel m, \quad \partial_3 \to -k_\parallel \alpha, \quad \partial_t \to -ik_\parallel c. \tag{3.10}$$

Substituting equation 3.9 into the partial wave equations 3.8 and applying the equivalent forms of the operators in equation 3.10, one can get the following matrix form of the wave

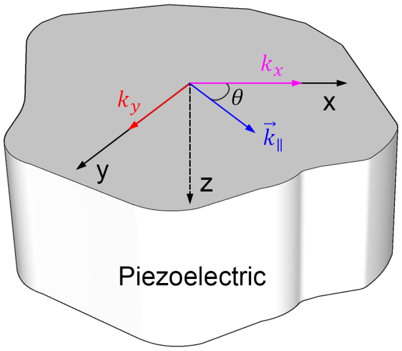

Figure 3.2: Coordinate system for a piezoelectric SAW.

equations:

$$W\begin{bmatrix} u_{01} \\ u_{02} \\ u_{03} \\ \phi_0 \end{bmatrix} = \begin{bmatrix} 0 \\ 0 \\ 0 \\ 0 \end{bmatrix}, \tag{3.11}$$

where

$$W = \begin{bmatrix} c_{11}l^2+c_{44}m^2-\rho c^2-c_{44}\alpha^2 & (c_{12}+c_{44})lm & (c_{12}+c_{44})l\alpha & -2e_{14}im\alpha \\ (c_{12}+c_{44})lm & c_{44}l^2+c_{11}m^2-\rho c^2-c_{44}\alpha^2 & (c_{12}+c_{44})m\alpha & -2e_{14}il\alpha \\ (c_{12}+c_{44})l\alpha & (c_{12}+c_{44})m\alpha & \rho c^2+c_{11}\alpha^2-c_{44} & -2e_{14}lm \\ -2e_{14}im\alpha & -2e_{14}l\alpha & 2e_{14}ml & i\varepsilon(\alpha^2-1) \end{bmatrix}. \tag{3.12}$$

For a non-trivial solution, the determinant of the matrix W should be zero ($|W|= 0$). This is equivalent to an eighth order equation for the decay constant α with real coefficients. Therefore, the eight roots α_j of the secular equation $|W|= 0$ are real or occur in conjugate pairs. Our interest is the surface wave mode which exponentially decays into the bulk of the substrate with increasing z (Fig. 3.2) and thus we choose only four of them α_j ($j = 1, 2, 3, 4$) which have a positive real part. For a given propagation direction θ, α_j depends on the phase velocity c as shown in equation 3.12. This velocity can be determined from the application of appropriate boundary conditions, which will be discussed later. Now the general solution for the displacements u_i and the potential ϕ can be written as a linear combination of equation 3.9 in terms of different α_j's and is given by

$$\begin{aligned} u_i &= \sum_{j=1}^{4} u_{0i}^{(j)}\, e^{-k_\parallel \alpha_j z}\, e^{ik_\parallel (lx+my-ct)}, \\ \phi &= \sum_{j=1}^{4} \phi_0^{(j)}\, e^{-k_\parallel \alpha_j z}\, e^{ik_\parallel (lx+my-ct)}. \end{aligned} \tag{3.13}$$

For each α_j, the ratios of amplitude $u_{01}^{(j)}$, $u_{02}^{(j)}$, $u_{03}^{(j)}$, and $\phi_0^{(j)}$ are related to each other as follows.

$$\frac{u_{01}^{(j)}}{A_j} = \frac{u_{02}^{(j)}}{B_j} = \frac{u_{03}^{(j)}}{C_j} = \frac{\phi_0^{(j)}}{F_j} = K_j, \tag{3.14}$$

where

$$
\begin{aligned}
A_j &= \begin{vmatrix} c_{44}l^2 + c_{11}m^2 - \rho c^2 - c_{44}\alpha_j^2 & (c_{12}+c_{44})m\alpha_j & -2e_{14}il\alpha_j \\ (c_{12}+c_{44})m\alpha_j & \rho c^2 + c_{11}\alpha_j^2 - c_{44} & -2e_{14}lm \\ -2e_{14}l\alpha_j & 2e_{14}ml & i\varepsilon(\alpha_j^2-1) \end{vmatrix} \\
B_j &= \begin{vmatrix} (c_{12}+c_{44})lm & (c_{12}+c_{44})m\alpha_j & -2e_{14}il\alpha_j \\ (c_{12}+c_{44})l\alpha_j & \rho c^2 + c_{11}\alpha_j^2 - c_{44} & -2e_{14}lm \\ -2e_{14}im\alpha_j & 2e_{14}ml & i\varepsilon(\alpha_j^2-1) \end{vmatrix} \\
C_j &= \begin{vmatrix} (c_{12}+c_{44})lm & c_{44}l^2 + c_{11}m^2 - \rho c^2 - c_{44}\alpha_j^2 & -2e_{14}il\alpha_j \\ (c_{12}+c_{44})l\alpha_j & (c_{12}+c_{44})m\alpha_j & -2e_{14}lm \\ -2e_{14}im\alpha_j & -2e_{14}l\alpha_j & i\varepsilon(\alpha_j^2-1) \end{vmatrix} \\
F_j &= \begin{vmatrix} (c_{12}+c_{44})lm & c_{44}l^2 + c_{11}m^2 - \rho c^2 - c_{44}\alpha_j^2 & (c_{12}+c_{44})m\alpha_j \\ (c_{12}+c_{44})l\alpha_j & (c_{12}+c_{44})m\alpha_j & \rho c^2 + c_{11}\alpha_j^2 - c_{44} \\ -2e_{14}im\alpha_j & -2e_{14}l\alpha_j & 2e_{14}ml \end{vmatrix} .
\end{aligned}
\tag{3.15}
$$

Then the general solution for the substrate atomic displacements and potential is given by

$$
(u_1, u_2, u_3, \phi) = \sum_{j=1}^{4} (A_j, B_j, C_j, F_j)\, K_j\, e^{-k_{\parallel}\alpha_j z}\, e^{ik_{\parallel}(lx+my-ct)}, \tag{3.16}
$$

where K_j is only unknown amplitude factors. Their ratios will also be determined by boundary conditions discussed below in section 3.1.2.

3.1.2 Boundary Conditions

In order to proceed with our analysis of the solutions in the previous section, we must apply appropriate boundary conditions. A mechanical boundary condition arises from the fact that the stress on the free surface ($z = 0$) must be zero. Such a stress free condition is equivalent to setting $T_{3j} = 0$ at $z = 0$. From equations 3.5 and 3.7, this boundary condition can be written as:

$$\begin{aligned} T_{31}(z=0) &= c_{44}(\partial_1 u_3 + \partial_3 u_1) + e_{14}\partial_2\phi = 0 \\ T_{32}(z=0) &= c_{44}(\partial_2 u_3 + \partial_3 u_2) + e_{14}\partial_1\phi = 0 \\ T_{33}(z=0) &= c_{12}\partial_1 u_1 + c_{12}\partial_2 u_2 + c_{11}\partial_3 u_3 = 0. \end{aligned} \tag{3.17}$$

Additionally, in the vacuum above the piezoelectric medium, the potential ϕ' must satisfy Laplace's equations and must be continuous across the interface at $z = 0$ if no surface charges exist. Thus, the potential in the vacuum ϕ' can be written as

$$\phi'(x, y, z, t) = \phi(x, y, 0, t)\ \exp(k_\parallel z) = \sum_{j=1}^{4} F_j\, K_j\, e^{k_\parallel z}\, e^{ik_\parallel(lx+my-ct)} \quad (z \leq 0). \tag{3.18}$$

In addition, the normal component of the displacement fields must also be continuous at the interface ($z = 0$):

$$\begin{aligned} D_3|_{z<0} &= -\varepsilon_0\partial_3\phi' \quad \text{(vacuum)}, \\ D_3|_{z>0} &= e_{14}(\partial_1 u_2 + \partial_2 u_1) - \varepsilon\partial_3\phi \quad \text{(piezo-medium)}, \\ -\varepsilon_0\partial_3\phi' &= e_{14}(\partial_1 u_2 + \partial_2 u_1) - \varepsilon\partial_3\phi \quad \text{at } z = 0 \quad \text{(interface)}, \end{aligned} \tag{3.19}$$

where ε_0 and ε denote the dielectric constant of the vacuum and the piezoelectric medium, respectively. Inserting $\partial_3\phi' = k_\parallel\phi'$ and $\phi'|_{z=0} = \phi|_{z=0}$ into equation 3.19, one can rewrite the electrical boundary condition as

$$e_{14}(\partial_1 u_2 + \partial_2 u_1) + \varepsilon_0 k_\parallel \phi - \varepsilon\partial_3\phi = 0 \quad \text{at } z = 0. \tag{3.20}$$

If the assumed solution given in equation 3.16 is substituted into the boundary conditions equations 3.17 and 3.20, we can obtain the matrix form of the combined mechanical and electrical boundary conditions:

$$B = \begin{bmatrix} T_{31}^{(1)} & T_{31}^{(2)} & T_{31}^{(3)} & T_{31}^{(4)} \\ T_{32}^{(1)} & T_{32}^{(2)} & T_{32}^{(3)} & T_{32}^{(4)} \\ T_{33}^{(1)} & T_{33}^{(2)} & T_{33}^{(3)} & T_{33}^{(4)} \\ D_3^{(1)} & D_3^{(2)} & D_3^{(3)} & D_3^{(4)} \end{bmatrix}, \quad B\begin{bmatrix} K_1 \\ K_2 \\ K_3 \\ K_4 \end{bmatrix} = 0, \tag{3.21}$$

where

$$\begin{aligned} T_{31}^{(j)} &= -c_{44}\alpha_j A_j + c_{44} l C_j + e_{14} i m F_j, \quad T_{32}^{(j)} = -c_{44}\alpha_j B_j + c_{44} m C_j + e_{14} i l F_j, \\ T_{33}^{(j)} &= c_{12} l A_j + c_{12} m B_j + c_{11}\alpha_j C_j, \quad D_3^{(j)} = e_{14} i m A_j + e_{14} i l B_j + \varepsilon\alpha_j + \varepsilon_0. \end{aligned} \tag{3.22}$$

For non-trivial solutions of equation 3.21, the determinant of the matrix B must vanish. Since the amplitudes A_j, B_j, C_j, and F_j can be complex numbers, the determinant is in general a complex number. Therefore, the wave velocity can be determined from the condition where the both real and imaginary parts of the determinant vanish independently. Substituting the determined velocity into equations 3.12 and 3.15 for a given propagation angle θ, the decay constant α_j and amplitudes A_j, B_j, C_j, and F_j can be calculated. Only the amplitude cofactor K_j remains to be found to completely specify the plane wave solution given in equation 3.16. However, we can only calculate the relative value of each K_j rather than their absolute value, i.e. only the ratios of K_j can be calculated based on the following relations.

$$\begin{aligned} K_1 \begin{vmatrix} T_{32}^{(2)} & T_{32}^{(3)} & T_{32}^{(4)} \\ T_{33}^{(2)} & T_{33}^{(3)} & T_{33}^{(4)} \\ D_{3}^{(2)} & D_{3}^{(3)} & D_{3}^{(4)} \end{vmatrix}^{-1} &= K_2 \begin{vmatrix} T_{32}^{(1)} & T_{32}^{(3)} & T_{32}^{(4)} \\ T_{33}^{(1)} & T_{33}^{(3)} & T_{33}^{(4)} \\ D_{3}^{(1)} & D_{3}^{(3)} & D_{3}^{(4)} \end{vmatrix}^{-1} \\ = K_3 \begin{vmatrix} T_{32}^{(1)} & T_{32}^{(2)} & T_{32}^{(4)} \\ T_{33}^{(1)} & T_{33}^{(2)} & T_{33}^{(4)} \\ D_{3}^{(1)} & D_{3}^{(2)} & D_{3}^{(4)} \end{vmatrix}^{-1} &= K_4 \begin{vmatrix} T_{32}^{(1)} & T_{32}^{(2)} & T_{32}^{(3)} \\ T_{33}^{(1)} & T_{33}^{(2)} & T_{33}^{(3)} \\ D_{3}^{(1)} & D_{3}^{(2)} & D_{3}^{(3)} \end{vmatrix}^{-1} = K. \end{aligned} \tag{3.23}$$

Note that the determinant of each 3×3 matrix in equation 3.23 can be also calculable if the velocity and the angle are given. Therefore, the wave solution u_i and ϕ have only one unknown amplitude factor K.

3.1.3 SAWs Along [011] Cut of GaAs (100)

When the SAW propagates on the (100) plane of GaAs along the [011] direction ($\theta = 45°$ and $l = m = 1/\sqrt{2}$ in Fig. 3.3), it is convenient to solve the wave equation using a 45 degree rotated coordinate system, where rotated axes x' and y' make angles $\pi/4$ and $3\pi/4$ with the original x axis. This propagation direction is the same as in our SAW experiments on a GaAs substrate, which will be discussed in a chapter 7. For the Rayleigh mode, the atomic displacements are confined to the sagittal plane with one transverse (u_3) and one longitudinal component (u'_1) and thus the matrix form of the wave equations given in equations 3.11 and

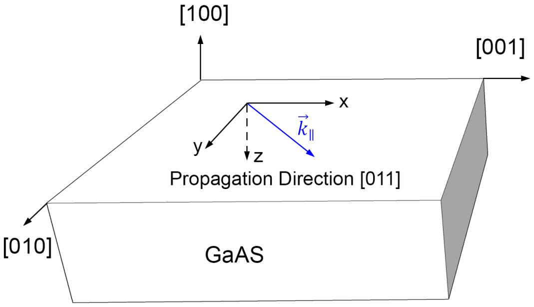

Figure 3.3: Schematic of the SAW propagation along GaAs (100) plane. The direction of the propagation is [011].

3.12 reduce to:

$$W = \begin{bmatrix} \rho c^2 - \frac{c_{11}+c_{12}}{2} - c_{44} + c_{44}\alpha^2 & -(c_{12}+c_{44})i\alpha & -2e_{14}i\alpha \\ -(c_{12}+c_{44})i\alpha & -c_{44}+c_{11}\alpha^2+\rho c^2 & -e_{14} \\ 2e_{14}i\alpha & e_{14} & \varepsilon(\alpha^2-1) \end{bmatrix},$$

$$W \begin{bmatrix} u_{01'} \\ u_{03} \\ \phi_0 \end{bmatrix} = \begin{bmatrix} 0 \\ 0 \\ 0 \end{bmatrix} \tag{3.24}$$

Here $u_{01'}$ represents the amplitude of the displacement along x'-axis, $u_{1'}$. Here we have performed the transformation into the rotated frame using the below relation [112]:

$$y' = 0, \quad u_{2'} = 0, \quad \partial_{2'} = 0, \quad u_1 = u_2 = u_{1'}/\sqrt{2}, \quad \partial_1 = \partial_2 = ik_{\|}/\sqrt{2},$$

with $1' \to x'$ and $2' \to y'$. From the condition that $|W| = 0$, we can obtain the appropriate solution of equation 3.24, $\alpha_j = \alpha_j(c)$, $j = 1, 2, 3$, which have a positive real part as discussed previously. The corresponding general solution is given by

$$(u_{1'}, u_3, \phi) = \sum_{j=1}^{3} (u_{01'}^{(j)}, u_{03}^{(j)}, \phi_0^{(j)})\, e^{-k_\parallel \alpha_j z}\, e^{ik_\parallel (x' - ct)}, \tag{3.25}$$

where

$$u_{01'}^{(j)} = A_j K_j,\ u_{03}^{(j)} = C_j K_j,\ \phi_0^{(j)} = F_j K_j. \tag{3.26}$$

Similarly, the matrix form of the boundary conditions in equation 3.21 is modified and becomes

$$B = \begin{bmatrix} -c_{44}\alpha_1 A_1 + c_{44} i C_1 + i e_{14} F_1 & -c_{44}\alpha_2 A_2 + c_{44} i C_2 + i e_{14} F_2 & -c_{44}\alpha_3 A_3 + c_{44} i C_3 + i e_{14} F_3 \\ i c_{12} A_1 - c_{11}\alpha_1 C_1 & i c_{12} A_2 - c_{11}\alpha_2 C_2 & i c_{12} A_3 - c_{11}\alpha_3 C_3 \\ i e_{14} A_1 + (\varepsilon\alpha_1 + \varepsilon_0) F_1 & i e_{14} A_2 + (\varepsilon\alpha_2 + \varepsilon_0) F_2 & i e_{14} A_3 + (\varepsilon\alpha_3 + \varepsilon_0) F_3 \end{bmatrix},$$

$$B \begin{bmatrix} K_1 \\ K_2 \\ K_3 \end{bmatrix} = 0. \tag{3.27}$$

For GaAs, the mass density is $\rho = 5.307 \times 10^3$ kg/m^3, the elastic constants $c_{11}, c_{12},$ and c_{44} given by 12.26×10^{10}, 5.71×10^{10}, and 6.0×10^{10} N/m^2, the dielectric constant is $\varepsilon \simeq 13$, and the piezoelectric constant is $e_{14} = 0.16$ C/m^2 [14]. As shown in Fig. 3.4, the condition for a non-trivial solution i.e. $\mathrm{Re}(|B|) = \mathrm{Im}(|B|) = 0$, yields a phase velocity of the SAW $c \simeq 2880$ m/s for $\alpha_j(c)$ obtained from equation 3.24 with the above material parameters. This is in a good agreement with the experimental value of $c \simeq 2863$ m/s [113]. With $c \simeq 2880$ m/s, the vanishing determinant of the matrix W in equation 3.24 yields a numerical

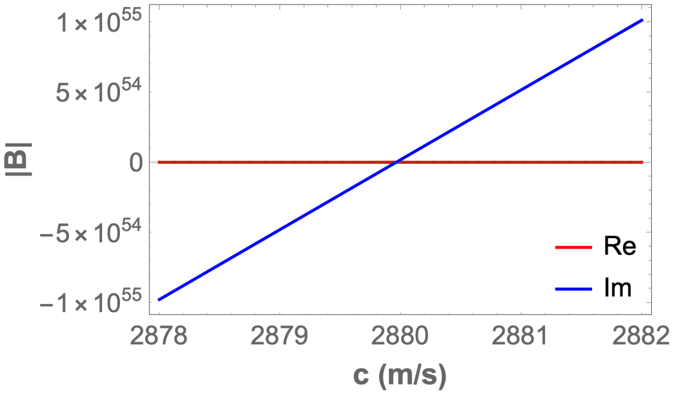

Figure 3.4: The real and imaginary components of the determinant of B as a function of the velocity c for GaAs (100) cut [011] propagation direction. At $c \simeq 2880$ m/s, both components are equal to zero.

value of decay constants:

$$\begin{aligned} \alpha_{1,2} &= 0.497292 \pm 0.481904i, \\ \alpha_3 &= 1. \end{aligned} \tag{3.28}$$

Also, from $|W|= 0$, the amplitude factors A_j, B_j, and F_j are given by

$$A_j = \begin{vmatrix} -c_{44} + c_{11}\alpha_j^2 + \rho c^2 & -e_{14} \\ e_{14} & \varepsilon(\alpha_j^2 - 1) \end{vmatrix}, \; C_j = \begin{vmatrix} -(c_{12} + c_{44})i\alpha_j & -e_{14} \\ 2e_{14}i\alpha_j & \varepsilon(\alpha_j^2 - 1) \end{vmatrix}$$

$$F_j = \begin{vmatrix} -(c_{12} + c_{44})i\alpha & -c_{44} + c_{11}\alpha_j^2 + \rho c^2 \\ 2e_{14}i\alpha_j & e_{14} \end{vmatrix} \tag{3.29}$$

And, from $|B|=0$, another amplitude factor K_j is obtained as

$$
\begin{aligned}
K_1 &= \begin{vmatrix} ic_{12}A_2 - c_{11}\alpha_2 C_2 & ic_{12}A_3 - c_{11}\alpha_3 C_3 \\ ie_{14}A_2 + (\varepsilon\alpha_2 + \varepsilon_0)F_2 & ie_{14}A_3 + (\varepsilon\alpha_3 + \varepsilon_0)F_3 \end{vmatrix} K, \\
K_2 &= \begin{vmatrix} ic_{12}A_1 - c_{11}\alpha_1 C_1 & ic_{12}A_3 - c_{11}\alpha_3 C_3 \\ ie_{14}A_1 + (\varepsilon\alpha_1 + \varepsilon_0)F_1 & ie_{14}A_3 + (\varepsilon\alpha_1 + \varepsilon_0)F_3 \end{vmatrix} K, \qquad (3.30) \\
K_3 &= \begin{vmatrix} ic_{12}A_1 - c_{11}\alpha_1 C_1 & ic_{12}A_2 - c_{11}\alpha_2 C_2 \\ ie_{14}A_1 + (\varepsilon\alpha_1 + \varepsilon_0)F_1 & ie_{14}A_2 + (\varepsilon\alpha_2 + \varepsilon_0)F_2 \end{vmatrix} K.
\end{aligned}
$$

After the amplitude ratios are calculated using equations 3.29, 3.30, and 3.26 with $c \simeq 2880$ m/s and the value of α_j given in equation 3.28, we can numerically estimate the spatial dependence of the plane wave solution of equation 3.25 with one amplitude variable (K). Fig. 3.5 shows the calculation of displacements $u_{1'}$, u_3 and the potential ϕ as a function of $k_{\|}z$. In this figure, both displacements and the potential survive within approximately one wavelength ($k_{\|}z = 2\pi$) below the GaAs surface, indicating that the SAW is localized near the surface.

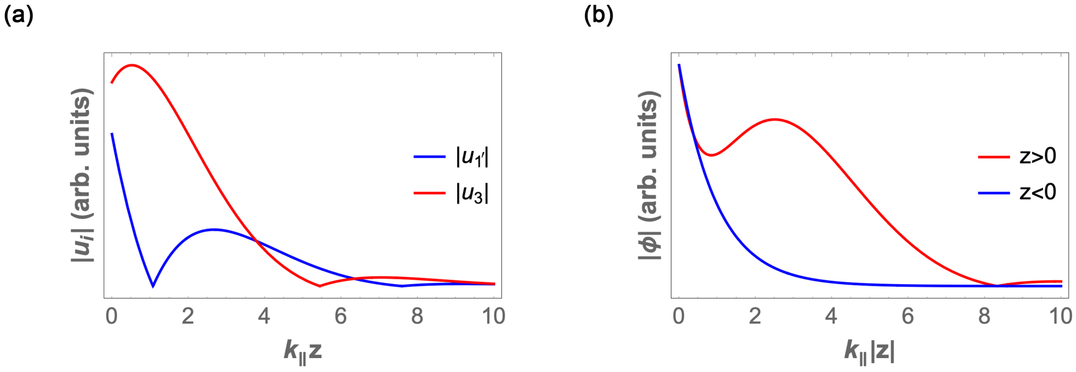

Figure 3.5: Atomic displacements (a) and electric potential (b) of a Rayleigh SAW versus the distance from the surface of GaAs (100) cut [011] propagation direction. $u_{1'}$ and u_3 denote longitudinal and transverse components of the displacements, respectively. A positive value of z indicates a location inside the GaAs substrate while a negative value represents the vacuum above the GaAs surface.

In particular, the SAW potential (red trace in Fig. 3.5 (b)) exhibits sinusoidal oscillation and decay into bulk. This is a direct consequence of the complex decay constants α_j inside the piezoelectric material. Above the GaAs surface with no free charge, the decay constant must be equal to 1 to satisfy Laplace's equations, which causes the SAW potential to exhibit monotonic exponential decay into vacuum (blue trace in Fig. 3.5 (b)).

3.2 SAW Coupling to a 2DES

In the section 3.1, we have discussed SAW propagation along a piezoelectric surface in contact with vacuum. When the adjoining medium is a 2DES or a thin conducting layer, the SAW can be coupled to it through the piezoelectric field. This leads to a velocity shift and an attenuation of the SAW, given by the following relation [14]:

$$\Gamma = k\frac{K^2}{2}\frac{\sigma/\sigma_{\mathrm{m}}}{1+(\sigma/\sigma_{\mathrm{m}})^2}, \tag{3.31}$$

$$\frac{\Delta v}{v} = \frac{K^2}{2}\frac{1}{1+(\sigma/\sigma_{\mathrm{m}})^2}, \tag{3.32}$$

where Γ is the SAW attenuation per unit length, v is the SAW velocity, k is the SAW wave number, K^2 is the piezoelectric coupling constant, σ is the sheet conductivity of the 2D layer, and $\sigma_{\mathrm{m}} = v(\varepsilon_0 + \varepsilon)/4\pi$ is a characteristic conductivity. Here ε is the dielectric constant of the piezoelectric substrate and ε_0 is the dielectric constant of the medium above the surface. The velocity change Δv is defined as $\Delta v \equiv v - v_0$, where v_0 is the velocity when the surface is metallized (i.e. $\sigma \to \infty$). Fig. 3.6 shows the attenuation and the velocity shift versus the sheet conductivity of the 2DES calculated from equations 3.31 and 3.32. For σ far below σ_{m}, both the attenuation and the velocity change are negligibly

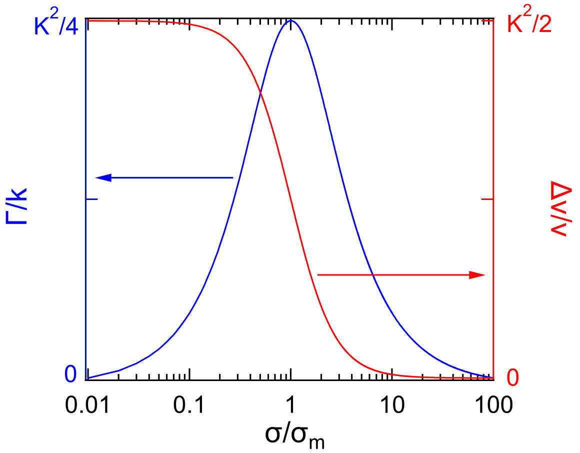

Figure 3.6: SAW attenuation and the velocity shift as a function of the 2DES conductivity.

affected by the 2DES. As σ approaches σ_{m}, both Γ and $\delta v/v$ are strongly modified. The maximum attenuation happens when $\sigma = \sigma_{\mathrm{m}}$ and the velocity changes in a steplike fashion near $\sigma = \sigma_{\mathrm{m}}$. This behavior results from the screening of the piezoelectric potential by mobile charges in the 2DES and the physical meaning of σ_{m} is well described in terms of a transmission line model. In this model, σ_{m} represents the wave impedance of the SAW. When the impedance is matched ($\sigma = \sigma_{\mathrm{m}}$), the energy transfer from the SAW to the 2DES is maximized. For the (100) GaAs surface with a SAW propagating along the [011] direction, $K^2/2 = 3.2 \times 10^{-4}$ and $\sigma_{\mathrm{m}} = 3.3 \times 10^{-7}\ \Omega^{-1}$ [30]. For YZ-cut $\mathrm{LiNbO_3}$ where the SAW travels on the (010) surface along the [001] direction, $K^2/2$ is two orders of magnitude larger than GaAs, $K^2/2 = 4.82 \times 10^{-2}$ [114], and $\sigma_{\mathrm{m}} = 2.1 \times 10^{-6}\ \Omega^{-1}$ [115].

3.2.1 SAW–2DES Interaction Inside a Piezoelectric Substrate

The strength of the SAW-2DES coupling is strongly modified depending on the location of the 2DES below or above a piezoelectric surface and its distance d from that surface. In this section, we describe how $K^2/2$ and σ_{m} change as a function of d when the 2DES is buried below the surface of a piezoelectric substrate such as those formed in GaAs/AlGaAs heterostructures. The SAW coupling to the 2DES located at or above the surface (in our case electrons on helium) will be described in next section 3.2.2.

In case of SAW propagation along the (100) surface of $\mathrm{Al}_{0.37}\,\mathrm{Ga}_{0.63}\,\mathrm{As}$ with [011] direction, experimental values of $K^2/2 = 3.2 \times 10^{-4}$ and $\sigma_\mathrm{m} = 4 \times 10^{-7}\ \Omega^{-1}$ [29] have been measured very similar to pure GaAs case. Generally, a two-dimensional electron system (2DES) at the $\mathrm{GaAs}/\mathrm{Al}_x\,\mathrm{Ga}_{1-x}\,\mathrm{As}$ interface is buried below the surface at a depth d as shown in Fig. 3.7. Both $K^2/2$ and σ_m depend on the location d. Simon [14] theoretically estimated their depth dependence using a simplified model geometry where the actual 2DES in a $\mathrm{GaAs}/\mathrm{Al}_x\,\mathrm{Ga}_{1-x}\,\mathrm{As}$ heterostructure is approximated as existing in a homogeneous AlGaAs slab. This is a reasonable approximation since GaAs and $\mathrm{Al}_x\,\mathrm{Ga}_{1-x}\,\mathrm{As}$ have very similar material properties. He showed that the depth dependence of $K^2/2$ and σ_m are given by

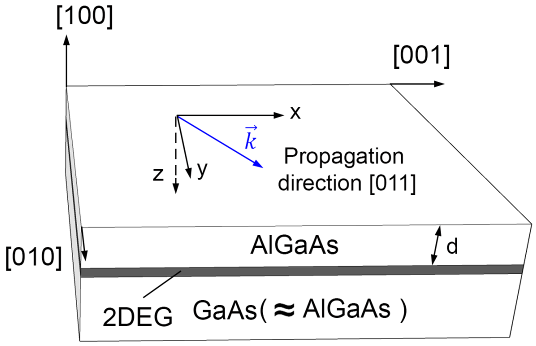

Figure 3.7: Schematic of the SAW propagation along the (100) surface of AlGaAs containing a 2DES. For the calculation of $K^2/2$ and σ_m in Ref. [14] at a depth d, the bottom GaAs layer is approximated by a AlGaAs layer due to their similar material properties.

$$\frac{K^2}{2} = \frac{\varepsilon_\mathrm{eff}(kd)}{4\pi H|C|^2}|\phi(kd)|^2, \tag{3.33}$$

$$\sigma_\mathrm{m} = \frac{v\varepsilon_\mathrm{eff}(kd)}{2\pi}, \tag{3.34}$$

with

$$\frac{1}{\varepsilon_{\text{eff}}} = \frac{1}{\varepsilon}\left(1 + \frac{\varepsilon - \varepsilon_0}{\varepsilon + \varepsilon_0} e^{-2kd}\right), \tag{3.35}$$

where C is the amplitude of the SAW and H is a material dependent constant which is equivalent to $H = U/kC^2$ [14] where U represents the energy of the SAW per unit surface area. For $\mathrm{Al_{0.3}\,Ga_{0.7}\,As}$, the elastic constants c_{11}, c_{12}, and c_{44} are given by 11.922×10^{10}, 5.476×10^{10}, and 5.925×10^{10} N/m^2, the mass density $\rho = 4.852 \times 10^3$ kg/m^3, the piezoelectric constant $e_{14} = 0.1795$ C/m^2, and the dielectric constant $\varepsilon = 12.048$ [116]. Following the same procedure we applied to GaAs (100) cut [011] propagation in the previous section with slightly different material parameters listed above, one can obtain $v = 2989$ m/s and the electric potential as

$$\phi(kd) = \left(\phi_0^{(1)} e^{-\alpha_1 kd} + \phi_0^{(2)} e^{-\alpha_2 kd} + \phi_0^{(3)} e^{-\alpha_3 kd}\right) e^{ik(x-vt)}, \tag{3.36}$$

with

$$\phi_0^{(1)} \simeq (-4.75 - 4.07i)A, \quad \phi_0^{(2)} \simeq (-4.75 + 4.07i)A, \quad \phi_0^{(3)} \simeq 12.47A$$
$$\alpha_1 \simeq 0.50 - 0.48i, \quad \alpha_2 \simeq 0.50 + 0.48i, \quad \alpha_3 = 1,$$

For the case of the vacuum above the surface (i.e. $\varepsilon_0 = 1$), inserting $v = 2989$ m/s in equation 3.35, we can calculate the characteristic conductivity σ_{m} as a function of kd as shown in Fig. 3.8 (a). Using $\phi(kd)$ in equation 3.36 along with $C \simeq (-2.37 \times 10^2 + 1.36 \times 10^2 i)A$ and $H \simeq 2.4 \times 10^{11}$ N/m^2, the piezoelectric coupling constant $K^2/2$ at any depth d can be obtained as shown in Fig. 3.8 (b). The coupling constant $K^2/2$ has a nonmonotonic dependence on kd, which is attributable to complex decay constant α_j of the potential. In the limit of $kd \simeq 0$, the calculated values of σ_m and $K^2/2$ are $3.5 \times 10^{-7}\ \Omega^{-1}$ and 3.6×10^{-4} respectively, in good agreement with experiment [29, 32]. With the depth-dependent $K^2/2$ and σ_m as shown in Fig. 3.8, one can estimate the attenuation and the velocity shift of the SAW for a 2DES at any depth in the GaAs/AlGaAs heterostructure using equations 3.31 and 3.32.

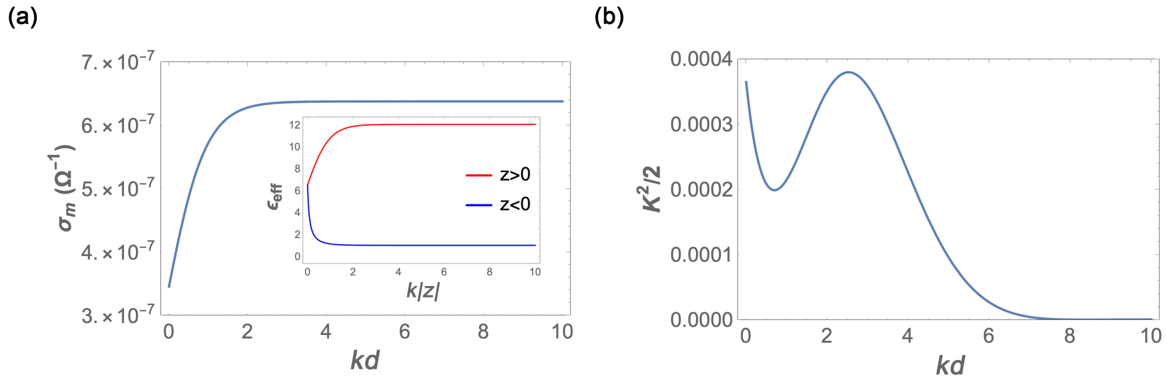

Figure 3.8: Characteristic conductivity σ_m (a) and coupling constant $K^2/2$ (b) as a function of kd are calculated using the approximated model geometry of Fig. 3.7. Here k and d represent the in-plane wave vector and the depth of the 2DES from the piezoelectric surface, respectively. The inset of (a) shows a change in effective dielectric constant with increasing 2DES distance from the surface. The blue trace represents the position of 2DES in vacuum above the surface while the red trace stands for the 2DES position inside the piezoelectric medium.

3.2.2 SAW–2DES Interaction Above a Piezoelectric Surface

For electrons floating on a thin helium film supported by a piezoelectric substrate, the 2DES is located above the piezoelectric surface. For this case, the SAW attenuation Γ and the velocity shift $\Delta v/v$ due to the nearby 2DES can be estimated using an electrical surface perturbation method. We will limit our discussion to the weak coupling approximation where the stress field is unchanged by the perturbation produced by the 2DES since this technique shows the best agreement with exact numerical calculations [117]. In this method, it is assumed that the surface of the piezoelectric substrate is mechanically free, reflecting the fact that the SAW is not mechanically affected by the adjoining medium and is only affected through the electric field. According to B.A. Auld [117], the perturbed potential ϕ' and perturbed displacement D'_y due to the electrical surface perturbation are related to the unperturbed fields ϕ and D_y:

$$\begin{aligned} \phi'|_{y=0} &= \phi|_{y=0} + A, \\ D'_y|_{y=0} &= D_y|_{y=0} + k\varepsilon_{\mathrm{p}}^{\mathrm{T}} A, \end{aligned} \tag{3.37}$$

where $\varepsilon_{\mathrm{p}}^{\mathrm{T}}$ is the dielectric constant of the piezoelectric medium under constant stress and is given by

$$\varepsilon_{\mathrm{p}}^{\mathrm{T}} = \sqrt{\varepsilon_{yy}^{\mathrm{T}}\varepsilon_{zz}^{\mathrm{T}} - (\varepsilon_{yz}^{\mathrm{T}})^2}.$$

The parameter $\varepsilon_{ij}^{\mathrm{T}}$ is the dielectric tensor component, k is the unperturbed wave number, and A is the amplitude. Here the positive $y-$axis points into the piezoelectric medium with the surface located at $y = 0$ and the SAW propagates along $z-$axis. Also, the approximation $k' = k$ has been made. The electrical boundary conditions can be conveniently expressed in terms of the electrical surface impedance, which is given by

$$Z_{\mathrm{E}}(0) = \left(\frac{\phi}{i\omega D_y}\right)_{y=0}, \tag{3.38}$$

where ω is the angular frequency of the SAW. For the unperturbed case, the region above the substrate ($y < 0$) is a semi-infinite vacuum and thus the Laplace equation $\nabla\phi = 0$ yields the unperturbed fields as

$$\begin{aligned} \phi &= e^{ky}e^{ikz}, \\ D_y &= -k\varepsilon_0 e^{ky}e^{ikz}. \end{aligned} \tag{3.39}$$

Therefore, the unperturbed surface impedance $Z_{\mathrm{E}}(0)$ is given by

$$Z_{\mathrm{E}}(0) = -\frac{1}{ik\omega\varepsilon_0}, \tag{3.40}$$

where ε_0 is the dielectric constant of the vacuum. If we introduce the normalized perturbed surface impedance defined by

$$z'_{\mathrm{E}}(0) = \frac{Z'_{\mathrm{E}}(0)}{|Z_{\mathrm{E}}(0)|} = -ik\varepsilon_0 \left(\frac{\phi'}{D'_y}\right)_{y=0}, \tag{3.41}$$

equations 3.40 and 3.41 allow us to express the displacement fields $D_y(0)$ and $D'_y(0)$ in terms of potentials as follows:

$$\begin{aligned} D'_y(0) &= -ik\varepsilon_0\phi'(0)/z'_{\mathrm{E}}(0), \\ D_y(0) &= -k\varepsilon_0\phi(0). \end{aligned} \tag{3.42}$$

Substitution of equation 3.42 into equation 3.37 and elimination of A give

$$\phi'(0) = -iz'_{\mathrm{E}}(0)\frac{\varepsilon_0 + \varepsilon_{\mathrm{p}}^{\mathrm{T}}}{\varepsilon_0 - iz'_{\mathrm{E}}(0)\varepsilon_{\mathrm{p}}^{\mathrm{T}}}\phi(0). \tag{3.43}$$

Inserting equation 3.43 into equation 3.41 yields

$$D'_y(0) = -k\varepsilon_0 \frac{\varepsilon_0 + \varepsilon_{\mathrm{p}}^{\mathrm{T}}}{\varepsilon_0 - iz'_{\mathrm{E}}(0)\varepsilon_{\mathrm{p}}^{\mathrm{T}}} \phi(0). \tag{3.44}$$

The variation of the wave-vector due to electrical perturbation cant be written as [117]

$$\Delta k \equiv k' - k \simeq \omega \left(\frac{\phi' D_y^* - \phi^* D'_y}{4P} \right)_{y=0}, \tag{3.45}$$

where P is the average power flow in the z direction and the asterisk denotes complex conjugation. By the substitution of equations 3.43 and 3.44 into equation 3.45 and use of equation 3.40 we obtain

$$\frac{\Delta k}{k} = -\left(\frac{\Delta v}{v} \right)_{\mathrm{SC}} \frac{1 + iz'_{\mathrm{E}}(0)}{1 - iz'_{\mathrm{E}}\varepsilon_{\mathrm{p}}^{\mathrm{T}}/\varepsilon_0}, \tag{3.46}$$

where

$$\left(\frac{\Delta v}{v} \right)_{\mathrm{SC}} = -\frac{\omega(\varepsilon_0 + \varepsilon_{\mathrm{p}}^{\mathrm{T}})}{4P} |\phi|^2.$$

The quantity $\left(\frac{\Delta v}{v} \right)_{\mathrm{SC}}$ is the relative change in the SAW phase velocity due to a short circuit at the surface (e.g. metalized surface) compared to the metal free surface case. This has a negative value since $v' < v$ and thus $\Delta v \equiv v' - v < 0$. In this context, one can relate the velocity change $(\Delta v/v)_{\mathrm{SC}}$ to the piezoelectric coupling constant [114]:

$$\left(\frac{\Delta v}{v} \right)_{\mathrm{SC}} = -\frac{K^2}{2}$$

Accordingly, the perturbation can be written as

$$\frac{\Delta k}{k} = \frac{K^2}{2} \frac{1 + iz'_{\mathrm{E}}(0)}{1 - iz'_{\mathrm{E}}\varepsilon_{\mathrm{p}}^{\mathrm{T}}/\varepsilon_0}. \tag{3.47}$$

This is the Ingebrigtsen formula for electrical surface perturbations of the piezoelectric SAW. In some limiting cases, the above perturbation is easily estimated. For instance, for a free electrical boundary condition the unperturbed fields $\phi(0)$ and $D_y(0)$ yield $z'_{\mathrm{E}}(0) = i$, leading to $\Delta k/k = 0$. In the limit of a highly conducting surface, insertion of $z'_{\mathrm{E}}(0) = 0$ into equation 3.47 yields

$$\frac{\Delta v}{v}(= -\frac{\Delta k}{k}) = -\frac{K^2}{2}.$$

In general, a perturbed surface impedance $z'_{\mathrm{E}}(0)$ is a complex number and accordingly $\Delta k/k$ is also complex. If we let $k' = k + \beta + i\alpha$, the perturbed phase velocity is

$$v' = \frac{\omega}{k+\beta} = \frac{\omega}{k}\left(1 + \frac{\beta}{k}\right)^{-1} \simeq v\left(1 - \frac{\beta}{k}\right) \text{ since } \beta/k \ll 1. \tag{3.48}$$

Here β and α are an additional phase shift and the attenuation constant for the perturbed wave. These lead to the relation:

$$\frac{\beta}{k} = 1 - \frac{v'}{v} = \frac{v - v'}{v} = -\frac{\Delta v}{v},$$

where v is the unperturbed phase velocity. Now one can express $\Delta k/k$ as

$$\frac{\Delta k}{k} = \frac{k' - k}{k} = \frac{\beta + i\alpha}{k} = -\frac{\Delta v}{v} + i\frac{\alpha}{k} \tag{3.49}$$

Therefore, the velocity shift and the attenuation of the SAW have the following relation:

$$\begin{aligned} \frac{\Delta v}{v} &= -\mathrm{Re}\left(\frac{\Delta k}{k}\right), \\ \frac{\alpha}{k} &= \mathrm{Im}\left(\frac{\Delta k}{k}\right). \end{aligned} \tag{3.50}$$

Note that a purely imaginary $z'_{\mathrm{E}}(0)$ causes $\Delta k/k$ to be a real number in equation 3.47, indicating no attenuation and only velocity shift. This is the case when the adjoining material is lossless, i.e. an electrical insulator. However, when a thin insulating helium film covers the piezoelectric surface, we observed a strong SAW attenuation. This suggests that a mechanical effect from the liquid helium film on the SAW must be taken into account. A possible mechanism for this mechanical effect will be discussed in chapter 6. In the presence of surface electrons above the helium film, the SAW attenuation measurement is in good agreement with this perturbation theory, which will be discussed in detail in chapter 7.

3.3 Acoustoelectric Charge Transport

The ability of a SAW potential to trap and transport charges at the speed of sound can generate a local DC current density via acoustoelectric charge transport. In this section, we will briefly describe the origin of this effect and how to experimentally measure it. When a SAW propagates on the piezoelectric surface along the $x-$axis, the piezoelectric field can be written as [118]

$$E_{\mathrm{p}}(x) = -\frac{\partial}{\partial x}\phi(x,t) = E_{\mathrm{m}} e^{i(kx-wt)}. \tag{3.51}$$

Mobile carriers in a 2DES having a diagonal conductivity σ_{xx} can screen this field and consequently the effective field is given by [30]

$$E_{\mathrm{eff}}(x,t) = \frac{E_{\mathrm{p}}(x,t)}{1 + i\,\sigma_{xx}/\sigma_{\mathrm{m}}}, \tag{3.52}$$

where σ_{m} is the characteristic conductivity. This can be used to drive a local acoustoelectric current density:

$$j_\alpha(x,t) = \sigma_{\alpha x} E_{\mathrm{eff}}(x,t), \quad \alpha = (x,y). \tag{3.53}$$

Since a small amount of charge carriers can be dragged by the traveling SAW potential, the modulated carrier density can be expressed as

$$N_{\mathrm{s}}(x,t) = N_{\mathrm{s}}^0 + \Delta N_{\mathrm{s}} e^{i(kx-wt)}, \tag{3.54}$$

where an amplitude ΔN_{s} is significantly smaller than the equilibrium density N_{s}^0. This leads to a modulated conductivity tensor, which is given by

$$\sigma(x,t) = \sigma_0 + \frac{\partial \sigma}{\partial N_{\mathrm{s}}} \Delta N_{\mathrm{s}}(x,t), \tag{3.55}$$

where σ_0 is the conductivity tensor in the equilibrium. From the continuity equation $\nabla \cdot \vec{j} + \partial/\partial_{\mathrm{t}}(-eN_{\mathrm{s}}) = 0$, one can relate the oscillating charge density $\Delta N_{\mathrm{s}}(x,t)$ to the effective field $E_{\mathrm{eff}}(x,t)$:

$$\Delta N_{\mathrm{s}}(x,t) = \Delta N_{\mathrm{s}} e^{i(kx-wt)} = -\frac{\sigma_{xx} E_{\mathrm{eff}}(x,t)}{ec}, \tag{3.56}$$

where c is the SAW velocity. From equations 3.53, 3.55, and 3.56 the time average of the acoustoelectric current density can be written as

$$\begin{aligned}\langle j_\alpha(x)\rangle_\mathrm{t} &= \langle\left(\sigma^0_{\alpha x} + \frac{\partial\sigma_{\alpha x}}{\partial N_\mathrm{s}}\,\Delta N_\mathrm{s}(x,t)\right) E_\mathrm{eff}(x,t)\rangle_\mathrm{t} \\ &= \langle\sigma^0_{\alpha x}E_\mathrm{eff}(x,t)\rangle_\mathrm{t} - \frac{\partial\sigma_{\alpha x}}{\partial N_\mathrm{s}}\frac{1}{ec}\langle\sigma_{xx}E^2_\mathrm{eff}\rangle_\mathrm{t} \\ &= -\frac{\partial\sigma_{\alpha x}}{\partial N_\mathrm{s}}\frac{1}{ec}\langle\sigma_{xx}E^2_\mathrm{eff}\rangle_\mathrm{t}\end{aligned} \tag{3.57}$$

since $\langle\sigma^0_{\alpha x}E_\mathrm{eff}(x,t)\rangle_\mathrm{t} = 0$. This indicates that the acoustoelectric current is a DC current proportional to E^2_eff arising from SAW-2DES interaction through the piezoelectric field. Additionally, the time averaged SAW attenuation is given by

$$\langle\Gamma\rangle_\mathrm{t} = -\frac{1}{I}\frac{\partial x}{\partial I} = \frac{1}{I}\langle\sigma_{xx}E^2_\mathrm{eff}\rangle_\mathrm{t}, \tag{3.58}$$

where $I = I_0e^{-\Gamma x}$ denotes the intensity of the SAW along the propagation direction. Substituting equation 3.58 into equation 3.57, the time averaged acoustoelectric current density can be expressed in terms of the attenuation:

$$\langle j_\alpha(x)\rangle_\mathrm{t} = -\frac{\partial\sigma_{xx}}{\partial N_\mathrm{s}}\frac{1}{ce}\,\langle I\cdot\Gamma\rangle_\mathrm{t} = -\frac{\mu}{c}\,\langle I\cdot\Gamma\rangle_\mathrm{t}, \tag{3.59}$$

where μ is the mobility of the 2DES.

In an experiment, this type of acoustoelectric effect can be measured using an external circuit. For example, when the 2D electron layer has a length L and a width b that is larger than the SAW beam width W, the terminal current between measurement electrodes at

$x = 0$ and $x = L$ is given by

$$I_{\text{tot}} = W\left[-\sigma_{xx}\frac{\partial V}{\partial x} - \frac{1}{L}\int_0^L \frac{\mu I \Gamma}{c}\,dx\right] = W\left[-\sigma_{xx}\frac{\partial V}{\partial x} + \frac{\mu}{cL}I_0(1-e^{-\Gamma L})\right], \tag{3.60}$$

where V is the voltage difference between the electrodes. Here the time average notation $\langle\,\rangle_{\text{t}}$ is dropped. For a short-circuit geometry ($V = 0$), we find the total current [119]:

$$I_{\text{tot}} = \frac{W\mu}{cL}I_0(1-e^{-\Gamma L}) = \frac{\mu}{cL}P_{\text{d}}, \tag{3.61}$$

where $P_{\text{d}} = WI_0(1-e^{-\Gamma L})$ is the total dissipated power of the SAW. In the case of an open-circuit ($I_{\text{tot}} = 0$ in equation 3.60), the acoustoelectric voltage difference between the electrodes is given by [115]

$$V_{\text{ae}} = \frac{\mu}{\sigma_{xx}cL}\int_0^L I_0(1-e^{-\Gamma L})\,dx = \frac{\mu}{\sigma_{xx}c}I_0(1-e^{-\Gamma L}). \tag{3.62}$$

As we will show in chapter 7, these type of measurements can be used to demonstrate acoustoelectric charge transport in the system of electrons on helium.

Chapter 4

Experimental Setup and Devices

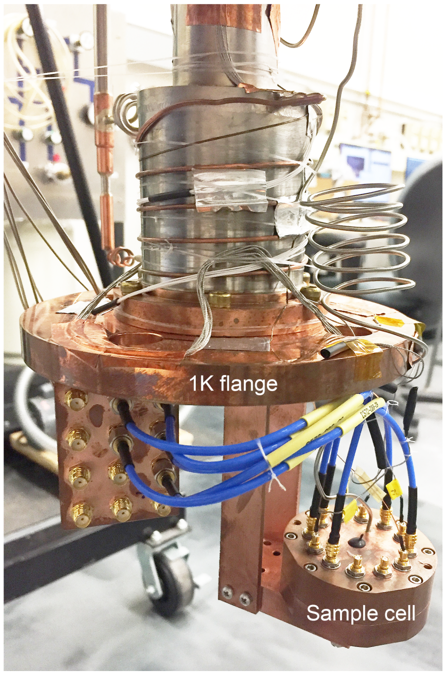

Figure 4.1: A superfluid leak-tight sample cell connected to the 1K flange of a closed cycle cryostat.

Employing surface acoustic waves to electrons on helium requires various experimental techniques and methods such as radio frequency (RF) and DC electrical measurements, nano- and micro- fabrication, and low temperature physics technique as well as cryogenic. A SAW device is composed of a piezoelectric substrate onto which pairs of inter-digitated transducer (IDT) are patterned using optical or e-beam lithography. In our setup, this device is then mounted to a patterned printed circuit board (PCB) inside a superfulid leak-tight copper cell (Fig. 4.1) and covered with a liquid ^{4}He film at cryogenic temperature. Then electrons are produced via thermionic emission from a tungsten filament mounted at a top of the cell and they then float on the top of the liquid ^{4}He film. A set of three rectangular electrodes are patterned on the PCB via conventional photolithography before mounting the SAW chip. These electrodes are used to trap electrons on the helium and simultaneously to detect low-frequency electron transport phenomena. A SAW launched from the input IDT interacts with electrons on helium and its amplitude and velocity change are measured at the receiver IDT. All of the data acquisition and the control of measuring-instruments are done by a python data acquisition software, LabGUI [120].

This chapter describes the details of the experimental techniques used to perform experiments presented in this thesis. In section 4.1, we start with an overview of the cryogenic experimental setup and then discuss cryostat, experimental cell, helium fill line system, electron generation, and measurement principle with circuits. Section 4.2 provides the detail of device fabrication for the experiments.

4.1 Experimental Setup

4.1.1 Setup Overview

All the measurements in this thesis were performed in a continuously operating ^{4}He evaporation cryostat manufactured by Cryomech Inc. This cryostat reaches the base temperature $T \simeq 1.5$ K with a cooling power of ∼200 mW. To form liquid helium inside the experimental cell at this temperature, we fabricated a hermetically sealed copper sample cell, which was then attached to 1K flange of the cryostat as shown in Fig. 4.1. A custom helium gas supply system was built at room temperature to precisely control the amount of helium gas admitted into the cell through a stainless still capillary fill line. A tungsten filament was attached inside the cell to generate electrons thermionically and thus charge the surface of helium with a 2DES. In order to trap and laterally confine electrons floating on the helium, trapping and guard electrodes were patterned on a submerged PCB and they were biased with positive or negative voltages. To access the stability of the surface electrons immediately after charging the helium surface, low-frequency capacitively coupled transport must be continuously monitored. Therefore, we built a low-frequency transport measurement circuit that operates via a standard lock-in technique. Also, both the SAW attenuation and velocity shift readout circuits were set up to characterize the interaction between electrons on helium and an evanescently coupled surface acoustic wave.

4.1.2 Cryostat

The operation of the *Cryomech* closed-cycle 1K cyrostat is based on two separate operating cycles, pulse tube precooling and liquid ^{4}He evaporative cooling. The precooling process is achieved by a continuously operating pulse tube cold head as shown in Fig 4.2. This process implements oscillatory compression and expansion of ^{4}He gas within a closed volume and cools the cold head of the pulse tube and attached cryostat from room temperature to $\sim$4 K. At this temperature, ultra pure ^{4}He gas is provided for approximately $2 \sim 3$ hours to fill the liquid helium container (1K pot) inside the fridge. After filling the cryostat with helium, continuous operation is achieved by ^{4}He evaporation from the 1K pot with a base temperature of $\sim$1.5 K (Please see Fig. 4.2 for additional details). In order to control the temperature of the cooling stages, heaters are mounted on the 4K and 1K flanges respectively. Also, a SI-410 silicon diode, a SI-RO600 RuO_2 resistor, and a CX-1050-CU-HT-1.4L zirconium oxynitride thin-film temperature sensor are mounted on on the 4K stage, 1K stage, and sample cell to monitor temperature real-time. Both heating control and temperature reading are performed using a commercial temperature controller (model number SRS CTC100). For measurement and control of surface acoustic wave experiments with electrons on helium, 10 DC and 12 superconducting copper-nickel coaxial lines were installed in the fridge connecting the room-temperature electronics to the sample cell at 1K fridge. All lines were thermally anchored at each stage of the fridge to minimize heat flow as shown in Fig. 4.3. To turn on the tungsten filament inside the cell with a low bias voltage, two of the DC lines are made of formvar insulated single filament copper clad superconducting wire (superconducting wire core OD = $0.01''$, copper cladding OD = 0.012”) to connect to the filament. The remaining 8 DC lines are made of stainless-steel shielded copper wire in twisted pairs.

4.1.3 Experimental Cell

Superfluid liquid helium can flow through very narrow constrictions, even those having nanometer size due to its vanishing viscosity. This makes it experimentally challenging to construct a leak-tight cell to contain superfluid helium. A convenient and reliable technique for creating a superfluid leak-tight seal is to use wire of indium metal to make a O-ring. Because of its softness, indium can completely fill the gap between two solid surfaces to be sealed together when they are squeezed along with indium in the gap. This leads to reliable cryogenic seal even at mK temperatures. Applying this sealing method, we built a 2.5 inch outer diameter (OD) hermetic copper sample cell with 2 inch inner diameter (ID) and an internal height of 6.5 as shown in Fig. 4.4, following a similar cell design as that used by David Schuster's group at University of Chicago [26, 121]. At the surface of the top of the cell, there are twelve hermetic GPO microwave feedthroughs (GPO Male to GPO Male Thread-in connector, Gilbert 0119-783-1), each having their own 0.02 inch diameter indium seal. It should be pointed out that these hermetic GPO connectors are so robust to tem-

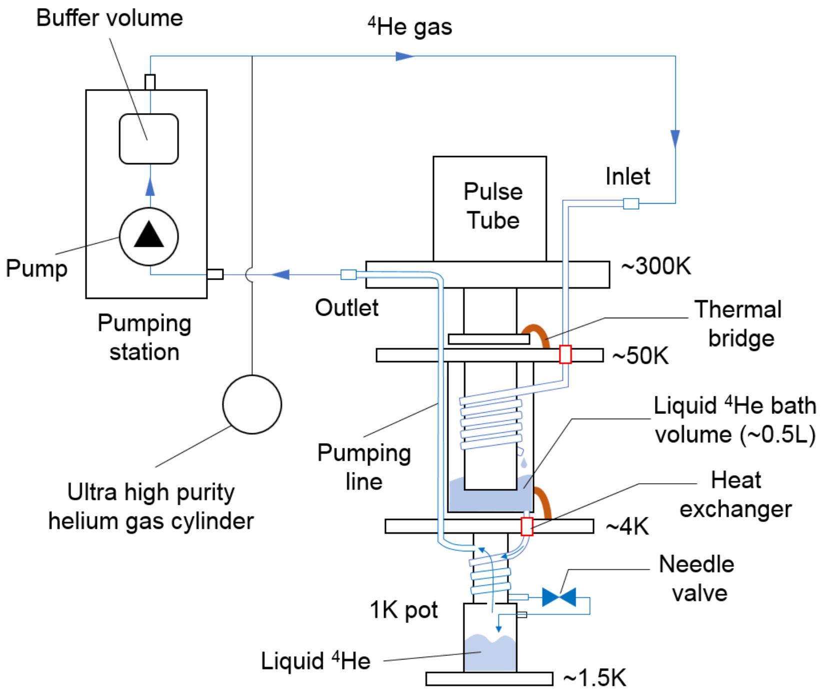

Figure 4.2: Schematic showing operation of the closed-cycle 1K cryostat. The 1K cryostat is precooled by a 4K pulse tube cryocooler (Cryomech PT410-RM) providing 1.0 W cooling power at T = 4.2 K. In the 1K circulation loop (blue color), the inlet ^{4}He gas at the pressure of ∼1 atm is precooled by a heat exchanger on the 50K stage and then condenses at the 4K stage. The condensed helium flows through a counter-flow heat exchanger wrapped around the tube below the 4K stage to be cooled ∼2 K. It then passes through a needle-valve into the 1K pot. To produce evaporation, the 1K pot is pumped by a dry vacuum pump through a pumping line. A buffer volume installed at the pump discharge stabilizes the pressure. If additional helium gas needs to be added, a standard helium gas cylinder is connected to the discharge side of the pump. The base temperature of the 1K system strongly depends on a flow through the needle valve and the pumping rate as well as any additional heat load from measurement wires and the helium fill line inside the fridge.

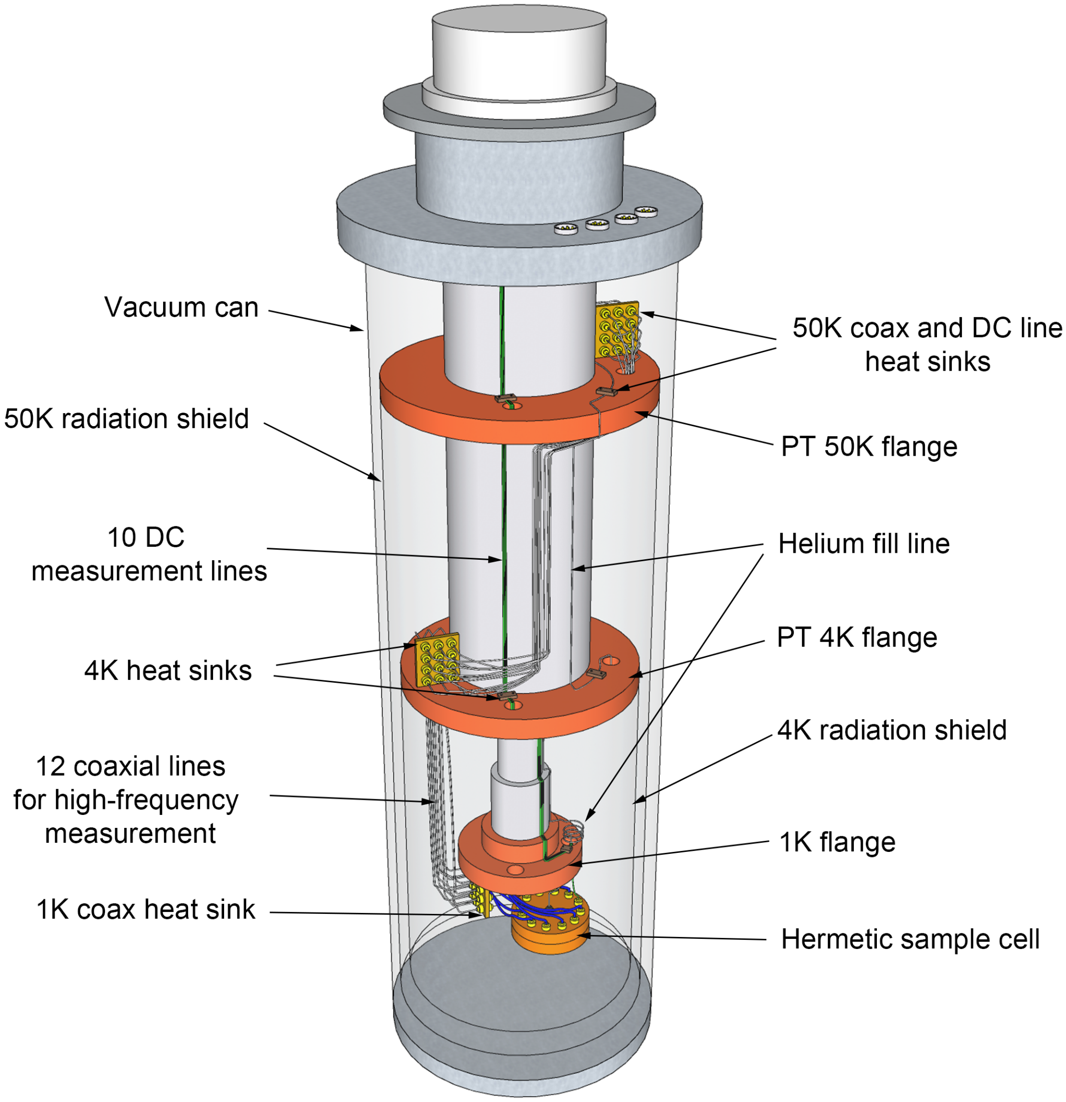

Figure 4.3: A simplified illustration of a closed cycle 1K refrigerator in which a helium fill line, wires, and a sample cell are shown in detail.

perature cycling that we have not found any superleak since they were first mounted years earlier. Also, to introduce helium into the cell, a stainless steel capillary fill line (1/16 inch OD and 0.04 inch ID) is connected to the top of the cell using hard silver solder. Lastly, the superfluid seal between top and bottom part of the cell is made by inserting a 0.03 inch diameter indium wire ring between them and subsequently pressing them against each other evenly with #4−40 screws.

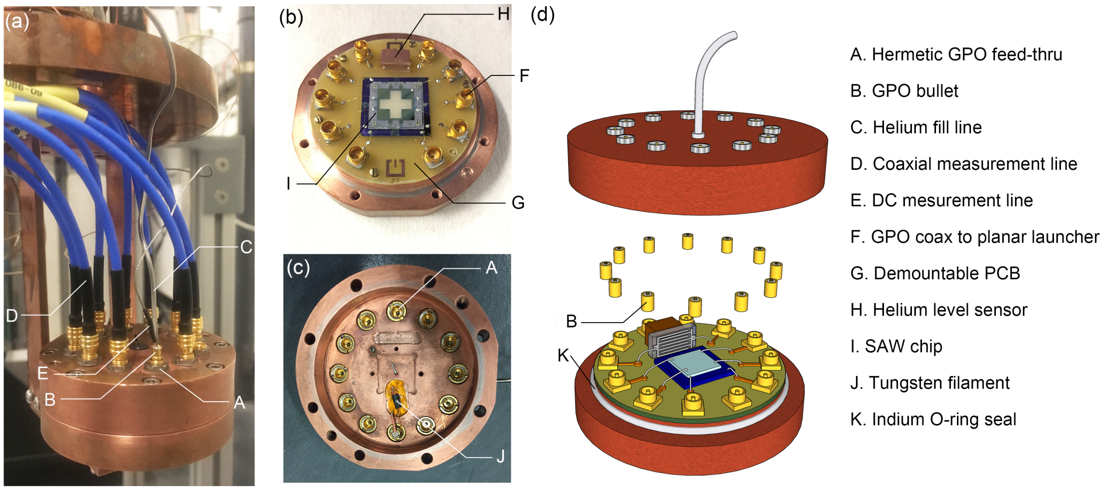

Figure 4.4: (a) Hermetically sealed Cu sample cell. (b) bottom and (c) top part of the cell. (d) 3D drawing of the cell assembly process. A SAW chip and a helium interdigitated capacitor (IDC) level sensor mounted to the PCB are connected to GPO launchers via gold wire bondings. GPO bullets are then inserted on the GPO launcher to link them to the hermetic GPO feedthroughs. An indium wire oring is placed onto the cell bottom and the top part of the cell is evenly pressed against the bottom via tightening screws.

4.1.4 Helium Fill Line and Gas Supply System

Precise regulation of the amount of ^{4}He gas supplied into the sample cell is essential for forming a partial volume of liquid helium with the desired thickness in the cell. To realized this, we built a ^{4}He gas supply system at room temperature, consisting of a gas handling unit (GHU) and a calibrated standard volume of 260 cc as shown in Fig. 4.5 (b). Room tem-

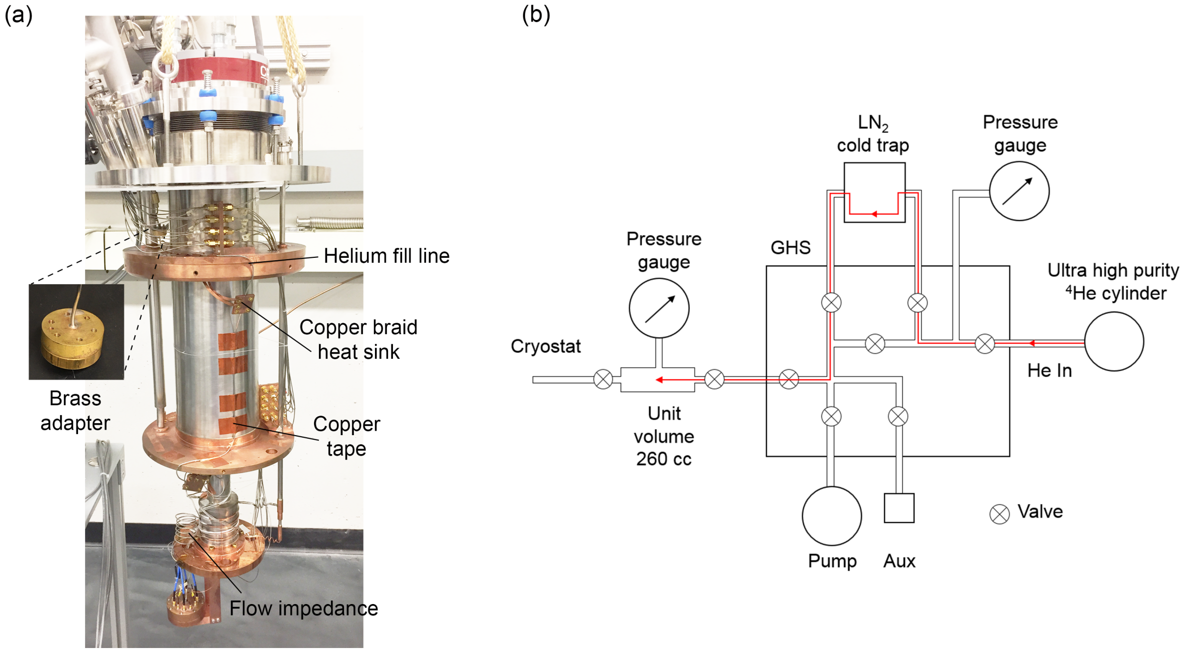

Figure 4.5: (a) Helium fill line in the 1K cyrostat. (b) Schematic of the ^{4}He gas handling system (GHS). Once the unit volume is filled with ^{4}He gas, the valve behind it is closed and then helium gas is provided into the cell from only this volume.

perature ^{4}He gas first passes through liquid a nitrogen cold trap in the GHU for purification and then fills up the standard volume of 260 cc until a desired pressure is achieved. Then the ^{4}He gas is provided into the sample cell at $T \approx 1.5$ K through a 1/16 inch OD and 0.04 inch ID stainless capillary fill line installed inside the fridge. The helium fill line is thermally anchored to the 50K and 4K stage by copper braid and a flow impedance (coil structure) is employed near 1K stage to reduce the heat flow into the sample cell at $T \approx 1.5$ K. Different sections of the capillary tube are connected using custom brass adapter (inset of Fig. 4.5 (a)). In order to minimize low-frequency mechanical vibration mainly due to the pulse tube, the fill line is tightly anchored to the cryostat body using copper tape and dental floss. By varying the pressure in the standard volume, we can determine the liquid helium volume admitted into the cell at $T \approx 1.5$ K and its thickness is measured in real-time using a interdigitated capacitor (IDC) level sensor (Fig. 4.4 (b),(d)). A more detailed description of the IDC level sensor will be presented in section 4.2.

4.1.5 Surface Electron Generation

Electron Source

There are many ways to generate large numbers of electrons including photoemission [122], field emission [123], corona discharge [124], and thermionic emission from a heated tungsten filament [125]. However, charging the surface of liquid helium requires a source of low-energy electrons as the helium surface has ∼1 eV potential energy barrier to penetration of electrons into the liquid from the vacuum. A the well-known method to generate low-energy electrons at liquid helium temperature is to use a tungsten filament covered by superfluid helium, which has been used as a durable and reliable electron source in electrons on helium experiments for many years [126]. Employing this thermionic emission from a tungsten filament allows us to spray electrons onto the liquid helium surface inside the cell. Fig 4.4 (c) shows the tungsten filament (model number, T-3/4 wire terminal by CML) used in our experiments, which is attached to the ceiling of the top portion of the cell with epoxy. Low resistance wires are connected to two of the hermetic GPO feedthroughs via GPO bullets (GPO Female to GPO Female connector, Fariview Microwave SM2608). The other side of these feedthroughs is linked to a room temperature pulse generator through superconducting wires in the cryostat described in subsection 4.1.2. At room temperature, the typical resistance of the filament is ∼25 Ω while the total resistance including the distributed wiring is ∼27 Ω. This ensures that the external applied voltage is mostly dropped across the filament in the cell. At T ≈ 1.5 K, the total resistance of the filament plus wires has substantially reduced value of $R_{\mathrm{T}} < 10\ \Omega$. In order to minimize excessive heating during the electron emission process, the filament is operated in pulsed voltage mode using a waveform generator (HP 8116A) to reduce the duty cycle. Table 4.1 shows the typical pulse parameters for thermionic electron emission. Filament operation with these parameters allows for reliable low-energy electron generation without any significant degradation of the filament. In fact, we never observed the filament to burn out under these settings. Although this operation temporarily increases the base temperature of the 1K stage T $\approx$ 1.5 K by 100 $\sim$ 300 mK, the system generally cools back to its initial value within a few minutes.

Parameter	Value
Peak-to-peak applied voltage	$2 \sim 2.5$ V
Pulse frequency	$0.5 \sim 1$ Hz
Pulse duration	$50 \sim 90$ %
DC offset	$-2 \sim -2.5$ V

Table 4.1: Typical tungsten filament biasing parameters for electron emission using the HP8116A waveform generator.

Surface Electron Confinement

To trap surface electrons on the liquid helium, a set of three rectangular electrodes (trapping electrodes) submerged beneath the liquid helium are used as illustrated in Fig. 4.6, which are patterned onto a 1.5 mm thick PCB mounted in the cell. In addition to these trapping electrodes, a rectangular guard electrode made of 1.63 mm thick square cross section copper wire is located outside of the three coplanar electrodes to laterally confine electrons. The trapping electrodes are biased with a positive voltage typically ranging from 20 to 60 V while the guard electrode is biased with a negative voltage ranging from -1 to -3 V. When the surface of the liquid helium is fully charged with electrons generated from the tungsten

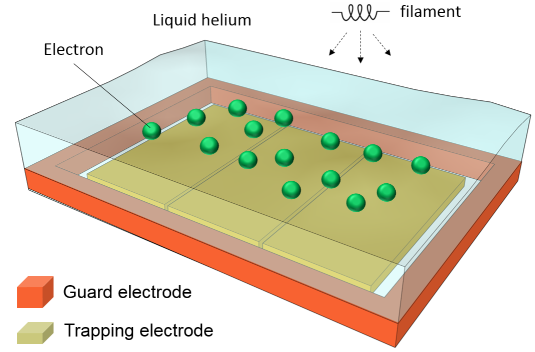

Figure 4.6: Simplified illustration of the process of charging a liquid helium surface with electrons.

filament, the saturation condition of the surface charging requires a vanishing electric field between the top plate and 2DES shown in Fig. 4.7 (a),(b). In this case, the saturated surface density can be calculated from a simple capacitance model (Fig. 4.7 (b)). If we ignore the guard electrode geometry, the electric fields above and below the 2D electron layer are given by $\vec{E}_{+} = \frac{V_{\mathrm{e}} - V_{\mathrm{tp}}}{h}\hat{z}$ and $\vec{E}_{-} = \frac{V_{\mathrm{bt}} - V_{\mathrm{e}}}{\varepsilon_{\mathrm{He}} d}\hat{z}$, respectively. Here V_{e}, V_{tp}, and V_{bt} are the electric potential at electron layer, the top plate and the bottom plate (a set

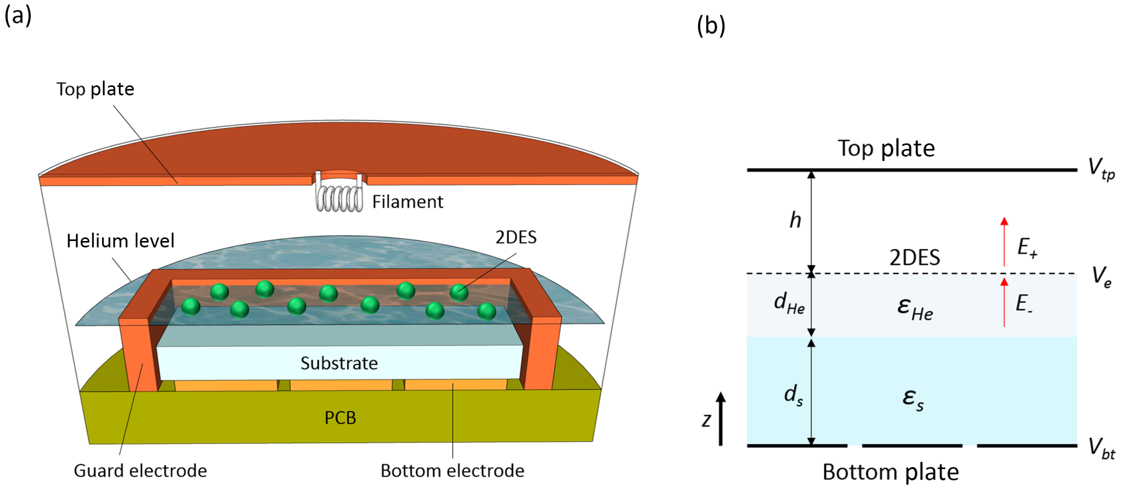

Figure 4.7: (a) Sketch of electrons floating on the surface of liquid helium inside the sample cell and (b) the simple capacitance model for this geometry.

of three trapping electrodes in our device) as shown in Fig 4.7 (b). The distance between the top plate and the 2DES is denoted h and d is the effective distance between the bottom plate and the 2DES, defined as $d = d_{\mathrm{He}}/\varepsilon_{\mathrm{He}} + d_{\mathrm{s}}/\varepsilon_{\mathrm{s}}$, where $\varepsilon_{\mathrm{He}}$ and ε_{s} represent dielectric constant of liquid helium and the underlying substrate while d_{He} and d_{s} are the thickness of the liquid helium and the substrate. The boundary condition for the normal component of the displacement field requires the following relation:

$$\frac{-ne}{\varepsilon_0} = \vec{E}_+ \cdot \hat{z} - \varepsilon_{\mathrm{He}} \vec{E}_- \cdot \hat{z}, \tag{4.1}$$

where n, e, and ε_0 denote the surface electron density, the elementary charge, and the vacuum permittivity. When $\vec{E}_+ = 0$ and $V_{\mathrm{e}} = V_{\mathrm{tp}}$, the electron density is saturated and has a maximum value. With this condition, we can calculate the saturated electron density n_{s} from equation 4.1:

$$n_{\mathrm{s}} e = \varepsilon_0 \frac{V_{\mathrm{bt}} - V_{\mathrm{tp}}}{d_{\mathrm{He}}/\varepsilon_{\mathrm{He}} + d_{\mathrm{s}}/\varepsilon_{\mathrm{s}}}. \tag{4.2}$$

Thus, the maximum saturated density n_{s} can be determined by geometrical capacitance between the 2DES and bottom plate, and voltage difference between the top and bottom plate. Equation 4.2 is not applicable when the electron density is not saturated. For this general case, the surface electron density is estimated from the low-frequency transport measurement, which will be described in chapter 5.

Surface Electron Detection

One of the first ways to check for the presence of electrons in the system is to try and measure their transport properties. However, the measurement of the transport of surface electrons on the liquid helium substrate presents an experimental challenging due to the impossibility of attaching electrical leads directly to the electron layer. Pioneering experiments in this field were performed by Sommer and Tanner [88] using capacitive coupling between underlying electrodes and the surface electron layer. Based on the technique developed by them, surface electron detection in our experiments is realized by measuring a current through the electron layer at T $\approx$ 1.5 K. Fig. 4.8 shows the Sommer-Tanner configuration we used in our experiments, which consists of an array of three planar electrodes (drive, gate, and sense) patterned on the PCB inside the cell. They are submerged under the liquid helium and

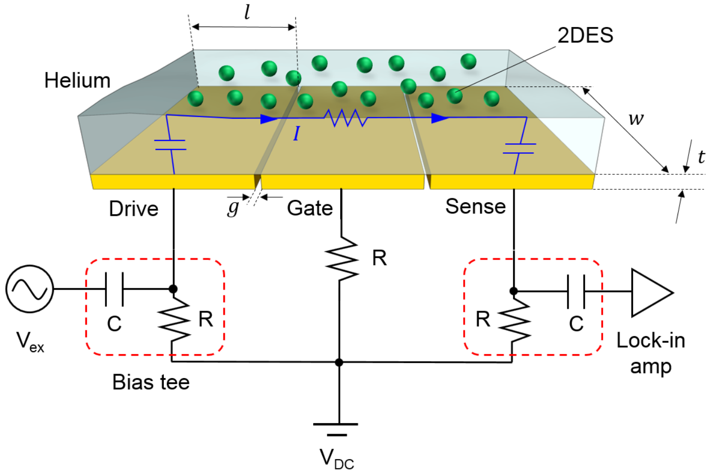

Figure 4.8: Schematic of Sommer-Tanner electrode configuration. A set of three planar electrodes with typical width $w = 8 - 10$ mm and length $l = 3 - 5$ mm are submerged underneath the charged liquid helium surface. The 2DES is excited by applying an AC voltage of V_{ex} $\sim$100 mV to the drive electrode, which induces a current through the electron layer on the sense electrode. This current is measured using standard lock-in techniques. In addition to V_{ex}, a DC voltage of $V_{\text{DC}} = 30 - 60$ V is simultaneously applied to the underlying electrodes to vertically hold surface electrons on helium. A bias tee composed of a resistance of R = 10 MΩ and a capacitance of C = 1 μF, marked by the red-dashed square, is used to apply both a DC an AC voltage.

separated by a very narrow gap. The typical width of the gap g is approximately 0.2 mm while the electrode width w and length l are usually $8 - 10$ mm and $3 - 5$ mm respectively. An AC excitation voltage V_{ex} at the frequency of $60 - 100$ kHz with an amplitude of a few hundred mV is applied to the drive electrode. The sense electrode is connected to the input of a lock-in amplifier (model SR830). Simultaneously, a constant positive DC voltage $V_{\mathrm{DC}} = 30 - 60$ V is applied to all electrodes to vertically hold surface electrons. To prevent the DC signal from being disturbed by the RF content or vice versa, a custom bias tee composed of a 10 MΩ resistor and a 1 μF capacitor is added to both the drive and sense electrode (red dashed box in Fig. 4.8). The underlying gate electrode at the center is only connected to the DC bias V_{DC} (i.e. this electrode is at AC ground), which substantially reduces the direct geometrical capacitance between the drive and sense electrode. A simple description of the measurement principle is as follows: When surface electrons are confined on the liquid helium area above the three electrodes, applying an AC excitation voltage V_{ex} to the drive electrode gives a rise to a local charge density modulation above the electrode due to the capacitive coupling to electrons floating on the helium surface. This induced modulation in charge density propagates to the 2D electron region above the sensing electrode and produces a current into the sense electrode. In particular, the phase difference between the output and input signals depends on the change in resistance of the surface electrons and hence contains information of the electrical conductivity of the 2DES, as will be described in subsection 4.1.7.

4.1.6 Helium Level Sensor

As depicted in Fig. 4.9 (a), the helium level sensor we used in our experiments is an interdigitated capacitor (IDC) vertically mounted on a copper block attached to the PCB. The IDC is fabricated on on a 3.5×8 mm^2 quartz substrate and consists of 125 interlaced aluminum fingers that are 10 μm wide, 10 mm long, and $\sim$100 nm thick. These fingers are separated from each other by 10 μm. Once the sample cell is cooled down to T $\cong$ 1.5 K, it is slowly filled with liquid helium from the unit volume at room temperature. During this condensation process, the change in capacitance C_{IDC} is measured and is proportional to the level of bulk liquid helium in the cell. From the change of C_{IDC} between the empty and fully filled cell, one can relate C_{IDC} to the bulk helium level by linear interpolation [127]. To figure out the maximum of C_{IDC} when the cell is full of the liquid, we continuously provided helium into the cell and simultaneously measure the capacitance change as a function of time using a capacitance bridge (model number, AH2550A) as shown in Fig. 4.9 (b). The maximum

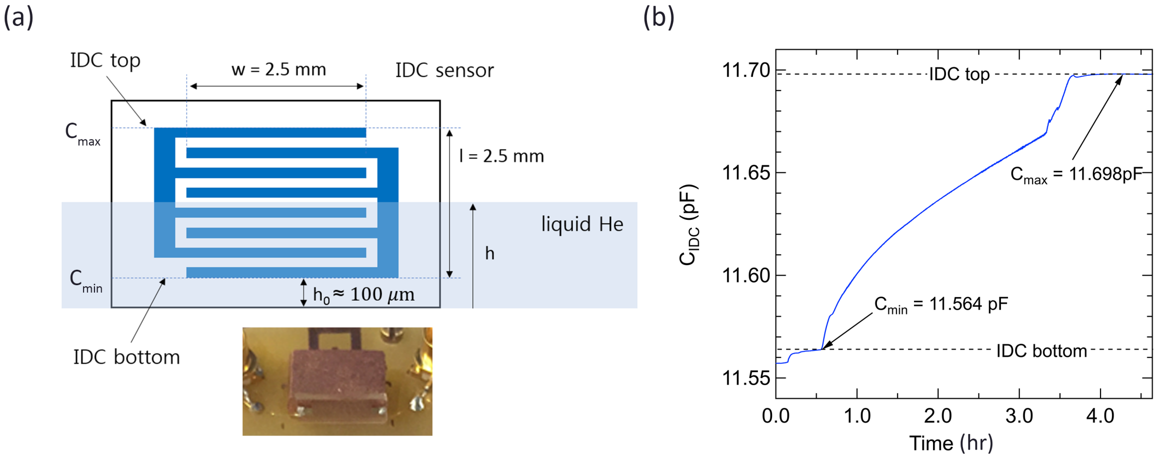

Figure 4.9: (a) Schematic of the IDC helium level sensor inside the cell partially filled with liquid helium. Inset shows an actual image of the IDC sensor vertically mounted on a copper block attached to the PCB. (b) IDC capacitance measurement as a function of time while helium is continuously provided into the cell from a helium gas cylinder at room temperature.

capacitance $C_{\max}$ for completely filled case can be then obtained from the capacitance value measured when helium level touches the top of the IDC (Fig. 4.9 (a)). Also, the minimum capacitance $C_{\min}$ for the empty case coincides with the measured capacitance value when the helium level reaches the bottom of the IDC. A tiny increase in C_{IDC} before the helium touches the bottom of the IDC is attributable to capillary filling of liquid helium in the space between the fingers of the IDC. The expected capacitance change between $C_{\min}$ and $C_{\max}$

is given by [128]

$$\frac{\Delta C}{C} = \frac{C_{\mathrm{max}} - C_{\mathrm{min}}}{C_{\mathrm{min}}} \cong \frac{\varepsilon_{\mathrm{He}} - \varepsilon_0}{\varepsilon_{\mathrm{s}} + \varepsilon_0} \cong 1.18\,\%, \tag{4.3}$$

where $\varepsilon_{\mathrm{He}} \cong 1.057$, $\varepsilon_{\mathrm{s}} \cong 3.82$, and $\varepsilon_0 = 1$ are the dielectric constant of liquid ^{4}He, the quartz substrate, and the vacuum, respectively. The measured capacitance change we find is ∼1.16 %, in a good agreement with the calculated value from equation 4.3. With the measured values of C_{min} at helium level $h = h_0$ and C_{max} at $h = h_0 + l$, a helium level at an intermediate value of C_{IDC} between C_{min} and C_{max} can be estimated from the linear relationship given below:

$$\begin{aligned} h &= \frac{l}{C_{\mathrm{max}} - C_{\mathrm{min}}} \left(C_{\mathrm{IDC}} - C_{\mathrm{min}}\right) + h_0 \\ &\cong 18.66\,\mathrm{mm/pF} \times (C_{\mathrm{IDC}} - 11.564\mathrm{pF}) + 0.1\,\mathrm{mm}, \end{aligned} \tag{4.4}$$

where $C_{\mathrm{min}} = 11.564$ pF, $C_{\mathrm{min}} = 11.698$ pF, $h_0 = 100\,\mu$m is the distance between the IDC bottom and the bottom edge of the substrate (Fig. 4.9 (a)), and $l = 2.5$ mm is the height of the IDC.

4.1.7 Measurement Principle and Circuit for Transport of Electrons on Helium and SAW Experiments

Lock-in Detection for Low-Frequency Measurements of Electrons on Helium

The Sommer-Tanner technique for transport measurements described in subsection 4.1.5 requires phase-sensitive detection of a very small AC current signal for the electron layer ranging from a few tens of pA to several nA in the presence of noise. Lock-in amplifiers are designed for this type of detection and the extremely small bandwith used in this type of measurement enables us to measure only the signal of interest. Thus, all transport measurements presented in this thesis are performed using a lock-in amplifier (Stanford Research SR830). In a standard lock-in measurement, a reference frequency is needed. A device or system (in our case the electrodes in the Sommer-Tanner experiment) is excited at a fixed frequency from a function generator and the lock-in amplifier detects the response of the system at the reference frequency. If a sinusoidal output from the function generator at the reference frequency ω_{R} is used to excite the system, the signal from the system will be $V_{\mathrm{S}}\sin(\omega_{\mathrm{R}}t+\theta_{\mathrm{S}})$. The lock-in amplifier generates its own internal reference signal $V_{\mathrm{L}}\sin(\omega_{\mathrm{R}}t+\theta_{\mathrm{R}})$ by a phase-locked-loop locked to the external reference. These two sine waves are multiplied using a phase-sensitive detector (PSD) and their product is given by

$$\begin{aligned} V_{\mathrm{PSD}} &= V_{\mathrm{S}}V_{\mathrm{L}}\sin(\omega_{\mathrm{R}}t+\theta_{\mathrm{S}})\sin(\omega_{\mathrm{R}}t+\theta_{\mathrm{R}}) \\ &= \frac{1}{2}V_{\mathrm{S}}V_{\mathrm{L}}\{\cos(\theta_{\mathrm{S}}-\theta_{\mathrm{R}})-\cos(2\omega_{\mathrm{R}}t+\theta_{\mathrm{S}}+\theta_{\mathrm{R}})\}. \end{aligned} \tag{4.5}$$

Once the AC component is removed with a low pass filter, the filtered PSD output has only a DC component:

$$V_{\mathrm{PSD}} = \frac{1}{2}\,V_{\mathrm{S}}V_{\mathrm{L}}\cos(\theta_{\mathrm{S}}-\theta_{\mathrm{R}}) \propto V_{\mathrm{S}}\cos\theta, \tag{4.6}$$

where θ is defined as the phase difference between the output signal and the lock-in reference oscillator. In the case of noise at frequencies different from reference frequency ($\omega_{\mathrm{noise}} \neq \omega_{\mathrm{R}}$), the corresponding PSD output has only AC component:

$$V_{\mathrm{PSD}} \propto \cos\left([\omega_{\mathrm{noise}}-\omega_{\mathrm{R}}]t+\theta_{\mathrm{noise}}-\theta_{\mathrm{R}}\right)-\cos\left([\omega_{\mathrm{noise}}+\omega_{\mathrm{R}}]t+\theta_{\mathrm{noise}}+\theta_{\mathrm{R}}\right). \tag{4.7}$$

Such a PSD output from the noise source will be removed by the low pass filter and thus the signal at the reference frequency ω_{R} resulting in a DC output in equation 4.6 is only detected. If a second PSD multiplies the signal with the lock-in internal reference shifted by 90 degrees, the low pass filtered PSD output will be given by

$$V_{\mathrm{PSD2}} = \frac{1}{2} V_{\mathrm{S}} V_{\mathrm{L}} \sin\theta \propto V_{\mathrm{S}} \sin\theta \tag{4.8}$$

Therefore, we get two output signals as shown in equations 4.6 and 4.8: one proportional to cos θ and the other proportional to sin θ. If we call the first output X and the second Y:

$$X = V_{\mathrm{S}} \cos\theta \quad , \quad Y = V_{\mathrm{S}} \sin\theta, \tag{4.9}$$

where X and Y are referred to as the in-phase and quadrature components, respectively. The amplitude and phase of the signal are related to X and Y by

$$R = \sqrt{X^2 + Y^2} \quad , \quad \theta = \tan^{-1}(Y/X). \tag{4.10}$$

In the Sommer-Tanner configuration described in subsection 4.1.5, the resistance of surface electrons on liquid helium is generally much smaller than capacitive reactance (i.e. $R_{\mathrm{e}} \ll X_{\mathrm{c}} = 1/j\omega C$), indicating an almost purely capacitive response from the electrodes. Here C is the capacitance between an underlying electrode and 2D electrons. Thus, most of the measured output current lives in the quadrature component with $\theta \approx \pi/2$.

Circuit Modeling of the Low-Frequency Transport of Electrons on Helium

With the Sommer-Tanner geometry illustrated in Fig. 4.8, low-frequency transport properties at T $\cong$ 1.5 K are analyzed using either a lumped element circuit or transmission line (distributed element) model. We first start with simple lumped element circuit model and extract the electric conductivity σ of the surface electrons form the phase information of the measured signal. Then, we will describes the transmission line analysis to estimate σ via fitting this model to our experimental data. This latter is primarily used in our experiments.

Fig. 4.10 shows the equivalent lumped element circuit model for the Sommer-Tanner configuration with or without electrons on the liquid helium surface. In the absence of electrons (Fig. 4.10 (a)), typical value of the capacitance between two neighbor electrodes with thickness $\simeq$ 35 μm is $C_{12} = C_{23} \simeq 0.5$ pF while the capacitance between the drive and sense electrode is $C_{13} \simeq 5 \times 10^{-3}$ pF because of the shielding provided by the AC-grounded center electrode. No resistive component in this case indicates a purely capacitive circuit. Once surface electrons are formed on the liquid helium, the equivalent circuit model is modified to include a resistor in series with two capacitors as shown in Fig 4.10 (b), where the resistive component R_e comes from the surface electrons and the capacitances C_e are formed be-

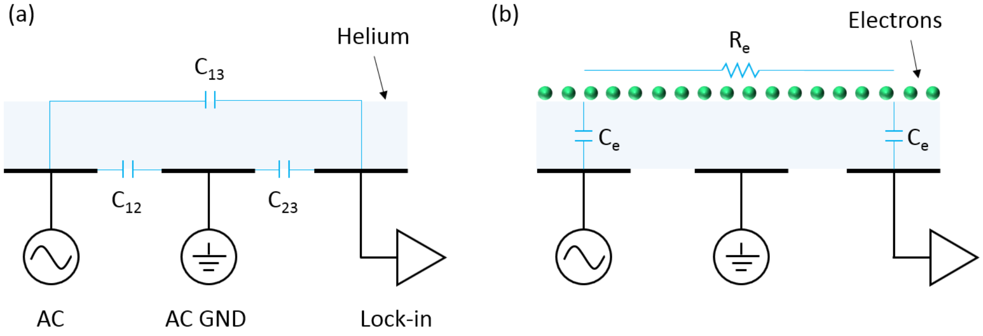

Figure 4.10: Lumped element equivalent circuit model of the Sommer-Tanner measurement configuration for (a) a neutral and (b) charged surface of liquid helium.

tween the electron layer and the drive/sense electrodes. Here, the direct capacitive current flowing between the drive and sense electrode is neglected due to the very small capacitance $C_{13} \cong 5 \times 10^{-3}$ pF between these electrodes as well as the low-frequency excitation $(60 - 100$ kHz).

From a 2D Drude model for the system of electrons and electrodes in our experiment, each of the components in the RC series circuit can be written as

$$R_{\mathrm{e}} = R_{\mathrm{L}} \cdot L \quad , \quad C_{\mathrm{e}} = C_{\mathrm{L}} \cdot L \tag{4.11}$$

with a resistance and a capacitance per unit length: $R_{\mathrm{L}} = \dfrac{1}{\sigma w}$ and $C_{\mathrm{L}} = \dfrac{\varepsilon_0\, \varepsilon_{\mathrm{He}}\, w}{d}$, where σ, w, L, and d denote the electric conductivity of the 2DES, the width of the electrode, the length of three electrodes, and the effective distance of the electron layer from the electrodes defined as $d = d_{\mathrm{He}} + (\varepsilon_{\mathrm{He}}/\varepsilon_{\mathrm{s}})\, d_{\mathrm{s}}$. Here d_{He} and d_{s} are the thickness of the liquid helium and the submerged substrate while $\varepsilon_{\mathrm{He}}$ and ε_{s} represent their dielectric constants. Even if there are no inductive elements in this circuit, the inertia of surface electrons in an AC driving field can lead to a kinetic inductance L_{k}, which is given by

$$\frac{1}{2} L_{\mathrm{k}} I^2 = \frac{1}{2} (nevw)^2 = \frac{n m^* v^2}{2} \quad \rightarrow \quad L_{\mathrm{k}} = \frac{m^*}{n e^2 w^2}, \tag{4.12}$$

where I, n, v, and m^* are the current in the 2DES, the surface electron density, the drift velocity of the electron, and the effective mass of electron. One can see the contribution of L_{k} to electron transport from the following complex Drude conductivity:

$$\sigma(\omega) = \frac{\sigma_0}{1 - j\omega\tau} = \frac{\sigma_0}{1 + \omega^2\tau^2} + j\omega\tau \frac{\sigma_0}{1 + \omega^2\tau^2}, \tag{4.13}$$

where $\sigma_0 = \dfrac{ne^2\tau}{m^*}$ is the DC conductivity. In equation 4.13, ω is the AC excitation frequency and τ is the relaxation time. The imaginary part of equation 4.13 represents the kinetic inductance term while the real part describes the resistive contribution. Electrons on helium have a relaxation time $\tau \leq \tau_\mathrm{R} = \mu_\mathrm{R}\, m^*/e \cong 10^{-10}$ s depending on the temperature, where τ_R and μ_R represent the scattering time and the mobility in the ripplon scattering regime. In the frequency range of our transport experiments ($\omega = 0.04 - 0.06$ MHz), $\omega\tau \ll 1$ yields a vanishing imaginary component in equation 4.13, indicating a negligible effect of the kinetic inductance in our experiments. Thus, the total admittance of the circuit can be written in terms of only R_e and C_e:

$$Y = \frac{I}{V_\mathrm{in}} = \left(R_\mathrm{e} + \frac{2}{j\omega C_\mathrm{e}}\right)^{-1} = \frac{R_\mathrm{e} - 1/j\omega C}{R_\mathrm{e} + 1/\omega^2 C^2} \quad \text{with} \quad C = \frac{C_\mathrm{e}}{2}, \tag{4.14}$$

where V_in is the input voltage used to excite the 2DES. The input impedance $1/j\omega C_\mathrm{s}$ of the lock-in detector is usually very small compared to the impedance Y^{-1} of the electron layer. Thus, the ratio of the output to the input voltage is $V_\mathrm{o}/V_\mathrm{i} = Y/j\omega C_\mathrm{s}$ and their phase difference is equivalent to

$$\Delta\phi = \tan^{-1}\mathrm{Re}(Y)/\mathrm{Im}(Y). \tag{4.15}$$

As discussed earlier, the capacitive circuit ($X_\mathrm{c} = 1/j\omega C_\mathrm{e} \gg R_\mathrm{e}$) in the Sommer-Tanner configuration leads to a small phase difference $\Delta\phi \ll 1$ between the input and output voltages and thus equation 4.15 can be simplified as

$$\Delta\phi \cong \mathrm{Re}(Y)/\mathrm{Im}(Y) = R_\mathrm{e}\, \omega\, C. \tag{4.16}$$

The values of $\Delta\phi$ and ω are experimentally determined while $C = C_\mathrm{e}/2$ is easily calculated by considering the parallel plate capacitor composed of the electron layer and the underlying electrode. Therefore, the electrical conductivity of the 2DES can be extracted using equation 4.16:

$$R_{\mathrm{e}} = \sigma^{-1}\frac{L}{w} \approx \frac{\Delta\phi}{\omega C} \quad \rightarrow \quad \sigma \simeq \frac{L}{w}\frac{\omega C}{\Delta\phi}. \tag{4.17}$$

Furthermore, if the saturated surface charge density is given by

$$ne = \frac{C_{\mathrm{e}}V_{\mathrm{dc}}}{w(L/3)} = \frac{6CV_{\mathrm{dc}}}{wL}, \tag{4.18}$$

substituting equation 4.18 into equation 4.17 yields the electron mobility

$$\mu \simeq \frac{L^2\omega}{6V_{\mathrm{dc}}\Delta\phi}. \tag{4.19}$$

Here V_{dc} is the trapping voltage applied to each of the underlying electrodes. This is very close to the mobility expression $\mu \cong \frac{7}{54}\frac{L^2\omega}{V_{\mathrm{dc}}\Delta\phi}$ derived by Sommer and Tanner using a distributed circuit model [88]. The lumped element approximation is only valid when the phase of the current or voltage wave does not significantly vary over the length of the circuit (i.e. the wavelength of the excitation must be larger compared to the length of the electrodes, $\lambda \gg L$). The wavelength of the voltage wave propagating in the surface electrons on liquid helium can be obtained by solving the two-dimensional wave equation with appropriate boundary conditions, which produces [129]

$$\lambda \simeq \sqrt{\frac{2\sigma}{\omega C_{\mathrm{e}}}}. \tag{4.20}$$

Therefore, the lumped element circuit model will show a discrepancy from the measurements at high frequency and low electron conductivity. This case will be described in detail in chapter 5.

Electrical transport of electrons on helium at arbitrary frequencies and wavelengths can be analyzed using a transmission line (distributed element) model shown in Fig. 4.11. One can relate the output voltage and current to the input voltage and current over a length x of the transmission line formed by the coupled electron-electrode system by a scattering matrix [130]

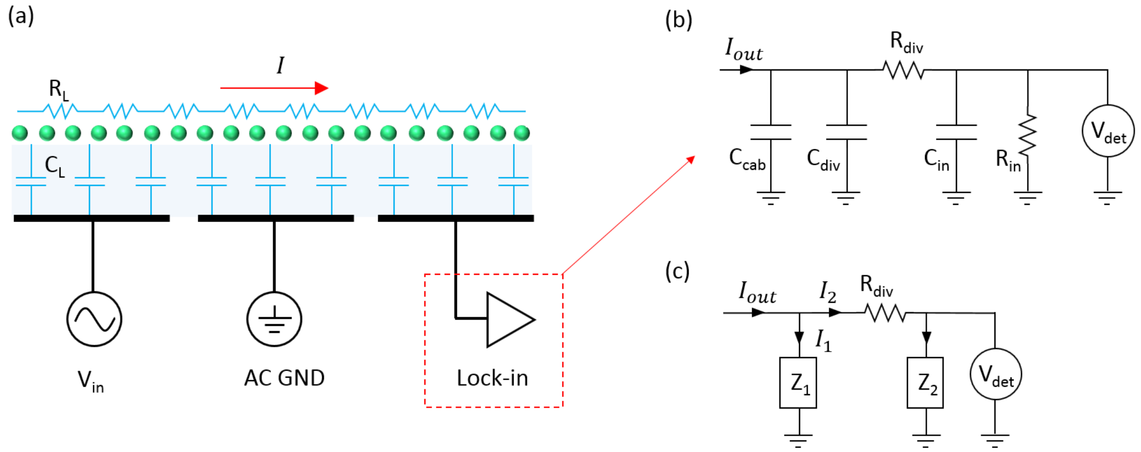

Figure 4.11: (a) Transmission line model of the Sommer-Tanner geometry. (b) Empirical circuit model [15] of the lock-in input impedance Z_{LI}, which consists of cable capacitance $C_{\mathrm{cab}} \simeq 600$ pF, a low-pass current divider stage with a capacitance $C_{\mathrm{div}} = 31$ pF and resistance $R_{\mathrm{div}} = 6.5$ kΩ, and the nominal lock-in input impedance of $R_{\mathrm{in}} = 10$ MΩ in parallel with the capacitance $C_{\mathrm{in}} = 25$ pF. (c) A simplified equivalent circuit of (b). Both Z_1 and Z_2 are composed of two elements in parallel, given by $Z_1 = [j\omega(C_{\mathrm{cab}} + C_{\mathrm{div}})]^{-1}$ and $Z_2 = [j\omega C_{\mathrm{in}} + 1/R_{\mathrm{in}}]^{-1}$.

$$\begin{pmatrix} V_{\mathrm{in}} \\ I_{\mathrm{in}} \end{pmatrix} = \begin{pmatrix} \cosh\gamma x & Z_{\mathrm{c}}\sinh\gamma x \\ Z_{\mathrm{c}}^{-1}\sinh\gamma x & \cosh\gamma x \end{pmatrix} \begin{pmatrix} V_{\mathrm{out}} \\ I_{\mathrm{out}} \end{pmatrix}, \tag{4.21}$$

where Z_{c} is the characteristic impedance of the transmission line

$$Z_{\mathrm{c}} = \sqrt{\frac{R_{\mathrm{L}} + j\omega L_{\mathrm{L}}}{j\omega C_{\mathrm{L}}}} \tag{4.22}$$

and γ is given by

$$\gamma = \sqrt{j\omega R_{\mathrm{L}} C_{\mathrm{L}} - \omega^2 L_{\mathrm{L}} C_{\mathrm{L}}}. \tag{4.23}$$

The quantities R_{L}, C_{L}, and L_{L} denote the resistance, capacitance, and inductance per unit length of the line, respectively. Neglecting the small inductive component L_{L}, one can find the output current I_{out} at the sense electrode from equation 4.21 [129]:

$$I_{\mathrm{out}} = I_0 \left(1 + j\right) \frac{9\sigma}{2L} \frac{\sinh^2(jkL/3)}{\sinh(jkL)} \tag{4.24}$$

with a current amplitude

$$I_0 = \omega C_{\mathrm{A}} \frac{wL}{9} V_{\mathrm{in}}, \tag{4.25}$$

where k is the complex wave vector of the current

$$k = \frac{1 - j}{\sigma}, \tag{4.26}$$

and δ is a two-dimensional skin depth representing the length scale over which charge density fluctuation propagates in the electron layer,

$$\delta = \sqrt{\frac{2\sigma}{\omega C_{\mathrm{A}}}}, \tag{4.27}$$

and C_{A} is the capacitance per unit area between the electron layer and the top and bottom electrodes, and $\sigma = ne\mu$ is the DC conductivity of the 2DES. The voltage V_{det} detected by the lock-in amplifier is determined by the output current I_{out} and its input impedance Z_{LI}

$$V_{\text{det}} = Z_{\text{LI}}\, I_{\text{out}}. \tag{4.28}$$

The nominal input impedance specified by the manufacture for the Standard Research 830 (SR830) lock-in is $R_{\text{in}} = 10$ MΩ in parallel with an input capacitance of $C_{\text{in}} = 25$ pF. This is not adequate for accurate circuit modeling over the frequency range $0.01 - 100$ kHz [15]. Therefore, V_{det} is estimated based on an empirical lock-in input impedance model developed by Kim *et al*. [15], which is illustrated in Fig. 4.11 (b). In its simplified equivalent circuit form (Fig. 4.11 (c)), the current I_2 flowing through impedance Z_2 is determined by Kirchhoff's law,

$$I_2 = \frac{Z_1}{Z_1 + R_{\text{div}} + Z_2} I_{\text{out}}, \quad R_{\text{div}} = 6.5 \text{ k}\Omega, \tag{4.29}$$

where

$$Z_1 = \frac{1}{j\omega(C_{\text{cab}} + C_{\text{div}})} \tag{4.30}$$

and

$$Z_2 = \frac{1}{j\omega C_{\text{in}} + R_{\text{in}}^{-1}}. \tag{4.31}$$

Here the impedance Z_1 consists of the coaxial cable capacitance $C_{\text{cab}} \cong 600$ pF to ground in parallel with the capacitance of $C_{\text{div}} = 31$ pF while the impedance Z_2 is the nominal input impedance described above. Finally, V_{det} is equivalent to the voltage applied to Z_2,

$$V_{\text{det}} = V_{\text{det}}(\sigma, C_{\text{A}}) = Z_2 I_2. \tag{4.32}$$

Since the capacitance per unit area C_{A} can be obtained from the parallel-plate capacitor geometry, the only unknown parameter in equation 4.32 is the conductivity σ of the 2DES, which can be determined by fitting the in-phase and quadrature components of the voltage measured by the lock-in. Once the areal density n of the 2DES is known, the mobility μ of the 2DES can then be estimated from the relation $\sigma = ne\mu$.

SAW Velocity Readout

To measure SAW velocity shifts, we built a custom phase-locked loop (PLL) instrument. Fig. 4.12 shows its simplified circuit diagram. A signal generator is used as a voltage-controlled oscillator (VCO), which drives both the SAW device and the LO (local oscillator) port of a mixer at a frequency $f = f_{\text{base}} + df/dV \cdot V_{\text{out}}$. The RF port of the mixer is driven by the signal coming from the SAW device, which has the phase difference ϕ but the same frequency f as the LO signal. Thus, the IF (intermediate frequency) output signal of the

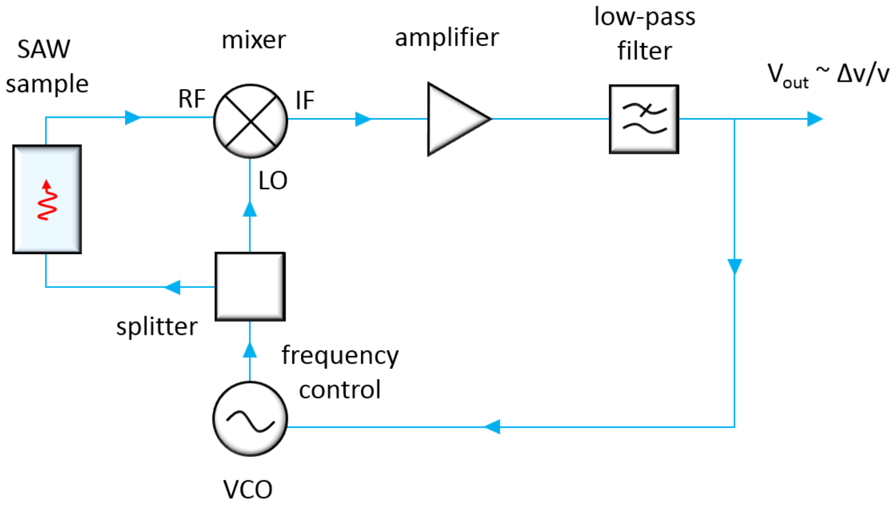

Figure 4.12: Simplified PLL circuit for SAW velocity shift measurements.

mixer can be determined by multiplying the two input signals:

$$V_{\mathrm{IF}} = V_{\mathrm{LO}} V_{\mathrm{RF}} = A_1 \sin(\omega t)\, A_2 \sin(\omega t + \phi) = \frac{A_1 A_2}{2}\{\cos(2\omega t + \phi) - \cos(\phi)\}, \tag{4.33}$$

where $\omega = 2\pi f$, $V_{\mathrm{LO}} = A_1 \sin(\omega t)$, and $V_{\mathrm{RF}} = A_2 \sin(\omega t + \phi)$. The IF output has an oscillating component $\propto \cos(2\omega t + \phi)$ and a DC component $\propto \cos(\phi)$. A low-pass filter isolates the DC component and thus V_{out} is determined by only the $\cos(\phi)$ term. A simple description of how the PLL circuit works is as follows: If we suppose that the phase difference ϕ between the LO and RF signals is $\phi = (n+1/2)\,\pi$, we have $V_{\mathrm{out}} = 0$ and thus the frequency of the VCO is fixed at $f = f_{\mathrm{base}}$. For the more general case where $\phi \neq (n + 1/2)\,\pi$ and $V_{\mathrm{out}} \neq 0$, the PLL loop will attempt to minimize the frequency control voltage ($= V_{\mathrm{out}}$), which eventually brings ϕ to an equilibrium value of ϕ_0 near $(n + 1/2)\,\pi$. For small change in the phase, the loop will adjust the VCO frequency to maintain a constant phase ϕ_0. For example, a change in the areal density of surface electrons or liquid helium thickness leads to a SAW velocity change $v_0 + \Delta v$ and hence a change in ϕ. This leads to a time delay between the RF and LO input of the mixer and their corresponding phase difference can be defined as $\phi = \frac{2\pi}{\lambda} x = 2\pi\,(f/v)\,x$. Here λ, v, and x are the wavelength, velocity, and propagation distance of the SAW while f is the SAW driving frequency, which is equivalent to the VCO output frequency. Again, the PLL tries to maintain a constant phase difference ϕ by adjusting the frequency f so that $(f/v)\,x$ is held constant. A negligible change of x yields $f/v =$ constant or $\Delta f/f_0 = \Delta v/v_0$, where $\Delta f = f - f_0$ and $\Delta v = v - v_0$ are the small changes of the SAW frequency and SAW velocity (i.e. f_0 is the frequency when $\Delta v = 0$). Recall that the SAW frequency f in this PLL circuit is affected by V_{out}, i.e.

$f = f_{\text{base}} + df/dV \cdot V_{\text{out}}$, and the velocity shift of the SAW at constant phase is given by

$$\frac{\Delta v}{v_0} = \frac{\Delta f}{f_0} = \frac{f - f_0}{f_0} = \frac{f_{\text{base}} - f_0}{f_0} + \frac{df}{dV}\frac{V_{\text{out}}}{f_0}. \tag{4.34}$$

If initially $v = v_0$ and $\Delta v = 0$, one can write the frequency f_0 in terms of the initial output voltage $V_{\text{out}}^{(0)}$:

$$f_0 = f_{\text{base}} + \frac{df}{dV} V_{\text{out}}^{(0)}. \tag{4.35}$$

Substituting equation 4.35 into equation 4.34, a subsequent velocity shift $\Delta v/v$ can be determined from $\Delta V_{\text{out}} = V_{\text{out}} - V_{\text{out}}^{(0)}$:

$$\frac{\Delta v}{v} = \frac{1}{f_0}\frac{df}{dV}\Delta V_{\text{out}} \cong \frac{1}{f_{\text{base}}}\frac{df}{dV}\Delta V_{\text{out}}. \tag{4.36}$$

Note that the frequency variation $df/dV \cdot V_{\text{out}}$ of the VCO is generally much smaller than the set frequency f_{base} of the signal generator and thus f_0 can be approximately replaced by f_{base}.

Fig. 4.13 shows a more detailed description of the operation principle of the PLL circuit. The red line is the frequency of the VCO and the blue curve indicates the amplified and filtered IF output of the mixer. At the beginning when the frequency control input is not yet connected, $f = f_{\text{base}}$ and $V_{\text{out}} = \beta \cos(2\pi x f_{\text{base}}/v_0)$, as marked by the open circles, where $\beta = \alpha A_1 A_2\, g\,(df/dV)$. Here α is a constant related to the mixer specifications, A_1 and A_2 are the amplitude of the voltage applied to the LO and RF port and g is the gain of the amplifier. Once the PLL loop is closed with connection to the frequency controller, the VCO moves to a new frequency due to the feed-back signal V_{out}. This process is indicated by the dashed-line phase space trajectory in Fig. 4.13. The PLL adjusts the frequency until reaching the equilibrium values of f and V_{out} in constant phase mode.

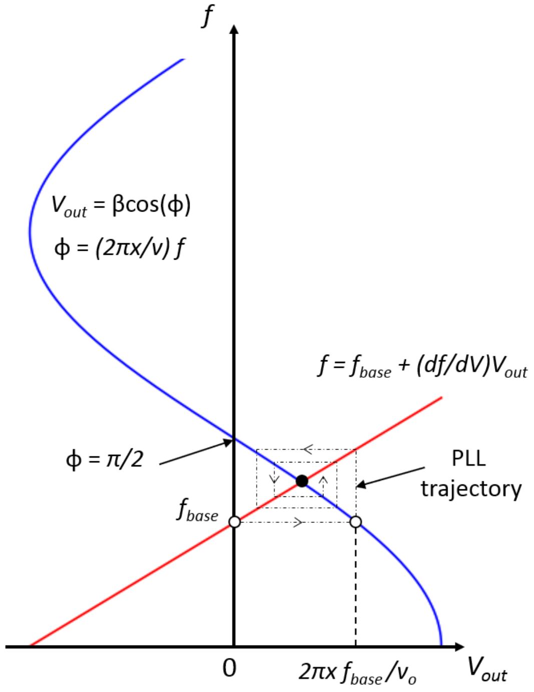

Figure 4.13: Convergence of the SAW PLL. The blue trace is the amplified and filtered output signal from the mixer $V_{\text{out}} = \beta\cos(\phi)$ where $\phi = 2\pi x f/v$, shown in Fig. 4.12. The red line represents the dynamic VCO frequency $f = f_{\text{base}} + (df/dV)V_{\text{out}}$. Initially before the PLL loop is closed (V_{out} is connected to the VCO control frequency input), V_{out} has a value of $V_{\text{out}} = 2\pi x f_{\text{base}}/v_0$ at the frequency of $f = f_{\text{base}}$. In the closed PLL loop, V_{out} moves along the dashed dot trajectory and V_{out} eventually converges at the equilibrium point marked by the solid circle.

As shown in Fig. 4.14, the actual SAW velocity shift measurement circuit is slightly more complicated compared to the version shown in Fig. 4.12 due to several additional components. To avoid the signal arising from the direct capacitive coupling between the input and output SAW transducers, we employ pulsed SAWs rather than a continuous wave (CW) excitation. The switch "C" pulses the RF input signal ($100 - 300$ MHz) close to the SAW resonance frequency ($f = v/\lambda$) at a repetition rate of 1 kHz. The typical pulse length ranges from 1 to 3 μs and to maximize signal one can use the longest pulse without overlapping between the instantaneous capacitive cross-talk and the SAW signal. Mixer "F" in Fig. 4.14 is a level 7

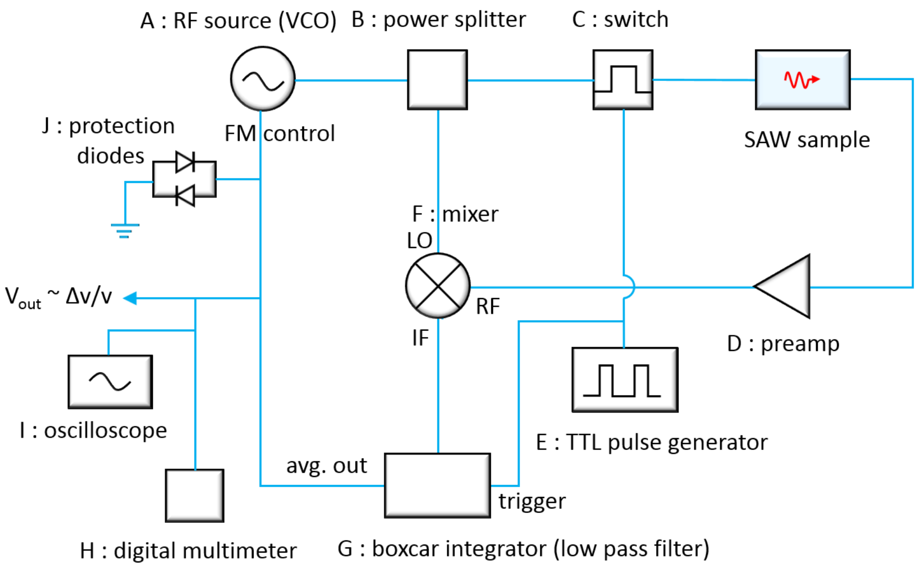

Figure 4.14: SAW $\Delta v/v$ measurement circuit diagram.

mixer, meaning that +7 dBm is supposed to be applied to the LO port. Also, a power level between $0 - 7$ dBm is recommended for driving the RF port of the mixer to avoid DC offsets as well as added noise. It should be noted that the low-pass filter in Fig. 4.12 is replaced by a boxcar integrator in the actual measurement circuit shown in Fig. 4.14. This is a gated integrator enabling the collection of the signal of interest during a specific time period set by the user and to reject any signals from other times. The accepted signal is integrated and then time-averaged over the length of the gate with a repetition rate of 1 kHz. Typically, 1000 samples (cycles) are averaged in our experiments, which leads to a measurement time constant of 1 sec. The protective diodes “J” prevent excessive voltage from being applied to the FM input of the signal generator (model number, HP8648B). In particular, 1 V at the FM input can damage the generator.

Part	Manufacturer / Model number
A	Agilent 8648B with frequency modulation (FM) control
B	Mini-Circuits ZFSC - 2 - 2500 - S power splitter
C	Mini-Circuits ZASWA - 2 -50DR PIN diode switch
D	Mini-Circuits ZKL-2-1 30 dB RF preamp
E	Keysight 33500B waveform generator
F	Mini-Circuits ZEM-4300 mixer
G	SRS 250 gated integrators and boxcar averagers
H	Agilent 34401A digit multimeter
I	Tektronix DPO7054 digital oscilloscope
J	Overvoltage protection diodes (1N4148)

Table 4.2: Parts list corresponding to the measurement circuit in Fig. 4.14

SAW Attenuation Readout

As described previously, a typical SAW delay line device is composed of a pair of interdigitated transducers (IDTs), which is susceptible to noise arising from the almost instantaneous capacitive crosstalk between the IDTs. Thus, accurate SAW measurements require the separation of this crosstalk from the SAW signal of interest. This is achieved by gating on the time delayed SAW signal as described at the end of this section. The attenuation of the SAW signal can be determined from the scattering parameters of the SAW device using a 2-port network analyzer. The scattering matrix is defined only in terms of voltage waves as shown in Fig. 4.15:

$$\begin{pmatrix} V_1^- \\ V_2^- \end{pmatrix} = \begin{pmatrix} S_{11} & S_{12} \\ S_{21} & S_{22} \end{pmatrix} \begin{pmatrix} V_1^+ \\ V_2^+ \end{pmatrix}, \tag{4.37}$$

where V_1^+ and V_1^- are the voltage waves travelling toward and away from IDT1 with wavevector k and the propagation length z. These waves are given by

$$V_1^+ = V_{01}e^{-kz}, \quad V_1^- = V_{01}e^{kz},$$

Similarly, V_2^+ and V_2^- are the voltage waves toward and away from the IDT2 (see Fig. 4.15)

$$V_2^+ = V_{02}e^{-kz}, \quad V_2^- = V_{02}e^{kz}.$$

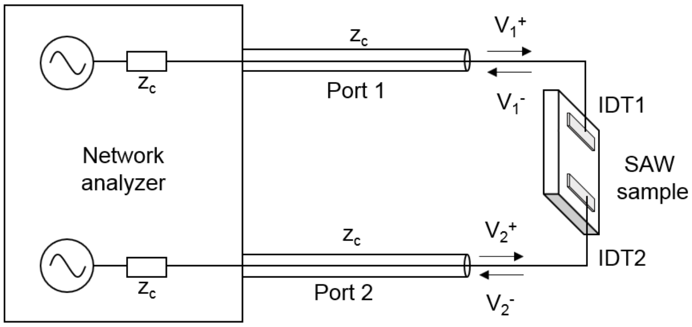

Figure 4.15: A sketch of the S-matrix elements measurement of a SAW delay line using a 2-port network analyzer.

If the voltage wave V_1^+ is applied to IDT1 and no voltage ($V_2^+ = 0$) to IDT2, the elements of the scattering matrix are

$$S_{11} = \frac{V_1^-}{V_1^+}, \quad S_{21} = \frac{V_2^-}{V_1^+}. \tag{4.38}$$

Here S_{11} and S_{21} indicate the voltages reflected from IDT1 and transmitted from port 1 to port 2, respectively. To quantify the SAW power P_{SAW} leaving IDT1 toward IDT2, we need to know the acousto-electric conversion efficiency α_1 of the RF-power P_{in} applied to IDT1.

This can be estimated from the following expression [131]:

$$\alpha_1 = \frac{P_{\mathrm{SAW}}}{P_{\mathrm{in}}} = \frac{1}{2}\left(10^{S_{11}^{(\mathrm{nr})}/10} - 10^{S_{11}^{(\mathrm{r})}/10}\right), \tag{4.39}$$

where $S_{11}^{(\mathrm{nr})}$ and $S_{11}^{(\mathrm{r})}$ are the S_{11} elements measured at the SAW resonance frequency and far from it, respectively. The factor 1/2 arises from the bidirectional nature of the IDT launching two SAW beams in opposite direction. In vacuum, the SAW power arriving at IDT2 is transformed back into a RF signal with power $P_{\mathrm{out}} = \alpha_2 P_{\mathrm{SAW}}$. Since an IDT delay line is a passive and symmetric device, the conversion efficiency α_2 of IDT2 transforming SAW to RF is the same as α_1 from RF to the SAW. Therefore, the SAW device in vacuum will have a transmission coefficient given by

$$S_{21,\mathrm{vac}} = 10\log(P_{\mathrm{out}}/P_{\mathrm{in}}) = 10\log(\alpha_1\alpha_2) = 10\log(\alpha^2) \tag{4.40}$$

In the presence of liquid helium, the piezoelectric surface is covered with liquid helium and leads to SAW attenuation. The corresponding transmission coefficient can be written as

$$S_{21,\mathrm{He}} = 10\log(\alpha^2 e^{-\Gamma_{\mathrm{He}} L}), \tag{4.41}$$

where Γ_{He} is the attenuation coefficient of the SAW due to liquid helium and L is the length of the SAW delay line usually defined as the center-to-center distance between IDTs. For the case of charged helium film, both the surface electrons and the liquid helium film result in SAW attenuation, leading to the transmission coefficient:

$$S_{21,\mathrm{EoH}} = 10\log(\alpha^2 e^{-\Gamma_{\mathrm{EoH}} L}), \tag{4.42}$$

where Γ_{EoH} denotes the attenuation coefficient owing to the charged film of liquid helium. From equations 4.40 and 4.41, Γ_{He} is given by

$$S_{21,\text{He}} - S_{21,\text{vac}} = 10\log(e^{-\Gamma_{\text{He}} L}) \quad \rightarrow \quad \Gamma_{\text{He}} = \frac{|S_{21,\text{He}} - S_{21,\text{vac}}|}{10\log(e)}\frac{1}{L} \quad \text{cm}^{-1}. \tag{4.43}$$

If expressed in dB/cm, Γ_{He} in equation 4.43 is multiplied by a factor of $10\log(e) \cong 4.34$. Similarly, the attenuation coefficient Γ_{EoH} of the SAW interacting with electrons on helium can be written as

$$\Gamma_{\text{EoH}} = \frac{|S_{21,\text{EoH}} - S_{21,\text{vac}}|}{10\log(e)}\frac{1}{L} \quad \text{cm}^{-1}. \tag{4.44}$$

If Γ_{He} is a constant independent of surface electron density, Γ_{EoH} can be expressed in terms of $\Gamma_{\text{EoH}} = \Gamma_{\text{el}} + \Gamma_{\text{He}}$, where Γ_{el} denotes the attenuation caused by 2D electron layer alone. Substituting equation 4.43 into equation 4.44, Γ_{el} can be determined from

$$\Gamma_{\text{el}} = \Gamma_{\text{EoH}} - \Gamma_{\text{He}} = \frac{|S_{21,\text{EoH}} - S_{21,\text{He}}|}{10\log(e)}\frac{1}{L} \quad \text{cm}^{-1}. \tag{4.45}$$

In fact, charging the helium film with electrons exerts an electronic pressure in addition to gravity leading to a reduced thickness of the charged helium film [132]. Thus, a change in the film thickness due to this effect can affect the SAW attenuation by the liquid helium Γ_{He}, which will be discussed in detail in chapter 6. Therefore, Γ_{He} has a different value when electrons float above the helium surface and equation 4.45 is no longer valid.

Although measuring the scattering elements with the network analyzer (NWA) is a simple and straightforward method to estimate the SAW attenuation, the direct electrical crosstalk between IDTs adds a parasitic signal to the SAW signal of interest. In particular, this makes it challenging to measure the S-parameters for SAW devices on weak piezoelectric materials such as GaAs. Fortunately, due to significant difference between the velocities of light ($c = 3 \times 10^8$ m/s) and sound ($v_{\text{saw}} \approx 10^3$ m/s), the crosstalk signal is usually received by the second IDT within nanoseconds while the SAW signal arrives after a few microseconds depending on the length of the SAW delay line. Thus, employing a timing gate, it is possible to exclude this crosstalk as well as some other noise coming from the environment. Another possible way to do this is to use a vector network analyzer (VNA) offering a time domain option. With this approach, the S-parameters are measured in the frequency domain as usual and then analyzed in time domain via an inverse Fourier transform. By setting a band-pass time filter, only the signal arising from the SAW remains and is transformed back into the frequency domain with a Fourier transformation, which enables one to measure the attenuation of the SAW signal [133].

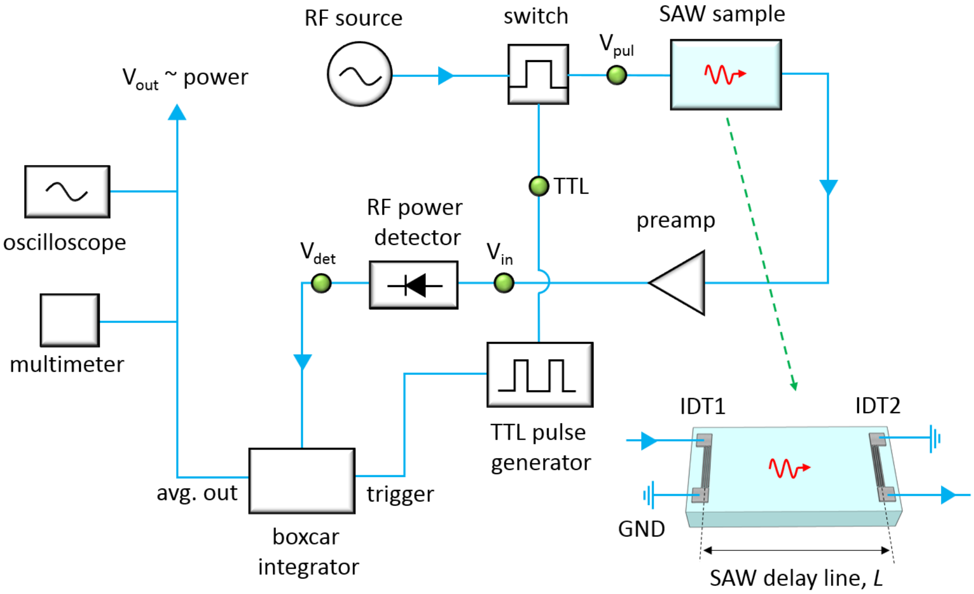

Figure 4.16: SAW attenuation measurement circuit diagram.

Another way to solve this issue is to use a pulsed-SAW excitation with a gated boxcar integrator, which will be discussed in detail below. Basically, the SAW attenuation measurement circuit using pulsed-SAWs is similar to the PLL circuit (Fig. 4.14) described earlier.

A Schottky diode-based RF power detector (Krytar Model 203AK S/N 00277) is added as shown in Fig. 4.16. Thus, all instruments and parts other than the RF power detector are the same as the ones previously described for the SAW read-out circuit. The principle of the SAW attenuation measurement using the RF power detector is as follows: A RF switch gates a high-frequency (∼100 MHz) sinusoidal signal for SAW excitation with a periodic pulse train (TTL) and resultantly produces a pulsed RF signal V_{pul} at its output as shown in Fig. 4.16. This signal excites a pulsed SAW at IDT1 in the device with the waveform shown in Fig. 4.17 (b). The SAW pulse transits the chip and arrives at a IDT2 where it is converted back to an electrical signal and then is amplified with a preamp. Fig. 4.17 (b) shows the amplified SAW signal V_{in} coming from IDT2 along with the instantaneous crosstalk and they are well separated in time by setting the TTL pulse width properly. When this amplified signal is applied to the input of the power detector, the positive half cycles of V_{in} forward bias the diode, which in turn charges the capacitor C as shown in Fig. 4.17 (a).

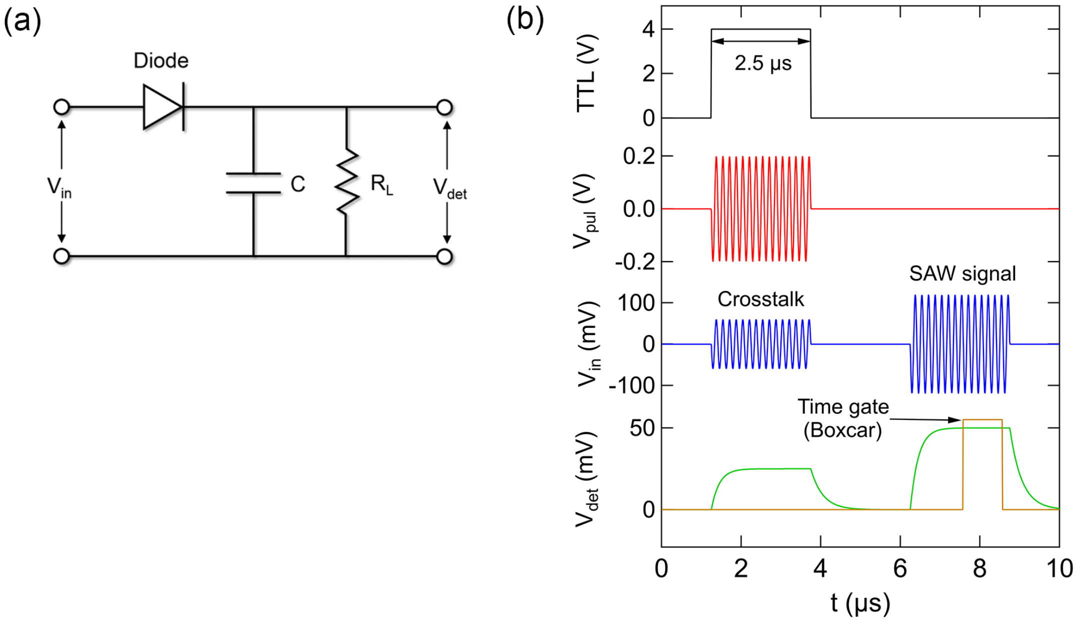

Figure 4.17: (a) Simplified circuit diagram of the RF power detector (b) Sketch of voltage waveforms at different positions on the circuit marked by the green solid circles in Fig. 4.16.

On the negative half cycles, the diode bias reverses and the voltage on the capacitor C yields a DC output proportional to V_{in}. This results in V_{det} (green trace in Fig. 4.17 (b)) with time constant on the rising (falling) edge arising from diode resistance ($\mathrm{R_L}$) and capacitance(C) at the output of the detector. Since V_{det} includes IDT crosstalk, the signal associated with the pulsed SAW is accepted using the time gate (dark yellow in Fig. 4.17 (b)) of the boxcar integrator. Just like the PLL circuit described above, this gated signal is then time-averaged over the length of the timing gate with 1 ms pulse period, producing a DC voltage V_{out} in Fig. 4.16 after taking average over 1,000 samples. From the measured V_{out} containing the SAW amplitude information, the corresponding power level of V_{in} (P_{in}) is determined using the power-voltage calibration curve shown in Fig. 4.18. The attenuation Γ_{saw} of the SAW is then determined with respect to the power level $P_{\text{in}}^{(0)}$ for the empty case. $\Gamma_{\text{saw}}\,(\text{dB}) = P_{\text{in}}\,(\text{dBm}) - P_{\text{in}}^{(0)}\,(\text{dBm})$.

4.2 Device Fabrication

4.2.1 Overview

Fig. 4.19 illustrates the experimental cell and associated devices described in this thesis. A set of three coplanar electrodes for trapping surface electrons on liquid helium are first patterned on a PCB and a rectangular guard electrode made of thick copper wire is then attached around the trapping electrodes for lateral electron confinement. A compact interdigitated capactior (IDC) level sensor is vertically mounted to the PCB to measure the level of the helium reservoir outside of the guard electrode. Lastly, a patterned SAW chip, where SAWs are generated and detected, is separately prepared and mounted to a top of trapping electrodes (for low-frequency transport measurements, a SAW chip is not needed). All device

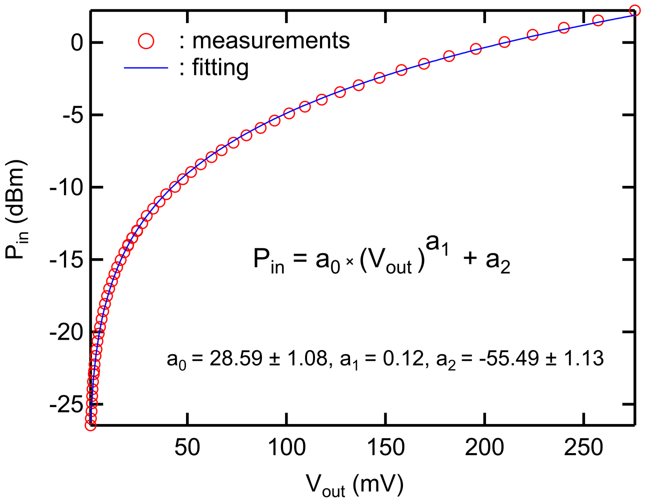

Figure 4.18: Calibration measurement of the output voltage V_{out} of the boxcar integrator at variable input power level P_{in} to the RF power detector. RF pulses with a width of 20 μs are directly applied to the input of the power detector and the input power level is quantified by measuring the RMS voltage within the pulse duration, based on the formula $P_{\text{in}}\,(\text{dBm}) = 20\log\left(V_{\text{rms}}/V_{\text{rms},0}\right)$ where $V_{\text{rms},0} = 224$ mV. Experimental data shows P_{in} is proportional to V_{out}, which well fits a function of $P_{\text{in}} = a_0\left(V_{\text{out}}\right)^{a1} + a_2$. Here $a_0 = 28.59 \pm 1.02$, $a_1 = 0.12$, and $a_2 = -55.49 \pm 1.13$. P_{in} is estimated from this function and the measured value of V_{out}. The shape of the curve is strongly affected by a different DC offset of the boxcar integrator and thus must be kept the same between different measurements by adjusting the offset level properly.

patterning process discussed here are carried out with conventional optical photolithography. A detailed description of these various fabrication processes will be presented in the next section.

4.2.2 PCB Etching

To form the trapping electrodes and GPO launcher pads on the PCB board, we used a pre-sensitized single-sided copper clad circuit board from Jameco. Since the minimum pattern size is a few hundred micrometers, a custom printed transparent sheet is used as a mask (Fig. 4.20). To perform the exposure step, in a dark room the light-block film covering the sensitized PCB is peeled off and the mask is then placed on the photoresist face of the board. An incandescent desk lamp is placed $6-8$ inch away and the light is exposed to the board for twenty minutes. The exposed PCB is then placed into a positive developer solution, where one part 418 positive developer from MG chemical is diluted with 10 parts room-temperature water and the solution is agitated around one minute. This removes the photoresist that was exposed to light during the exposure setup. Thus, the only the photoresist covered by the black area of the mask during exposure remains (Fig. 4.20). If no issues arise during or after development, we move forward to the etching process. Using a ferric chloride solution, the developed PCB is etched for about 20 minutes which removes the exposed copper. Trapping electrodes are formed on the board along with additional electrical leads and pads for connecting the guard electrode and GPO launchers (Fig 4.20 (b)). After etching the remaining photoresist is removed using acetone and followed by a DI water rinse to remove acetone.

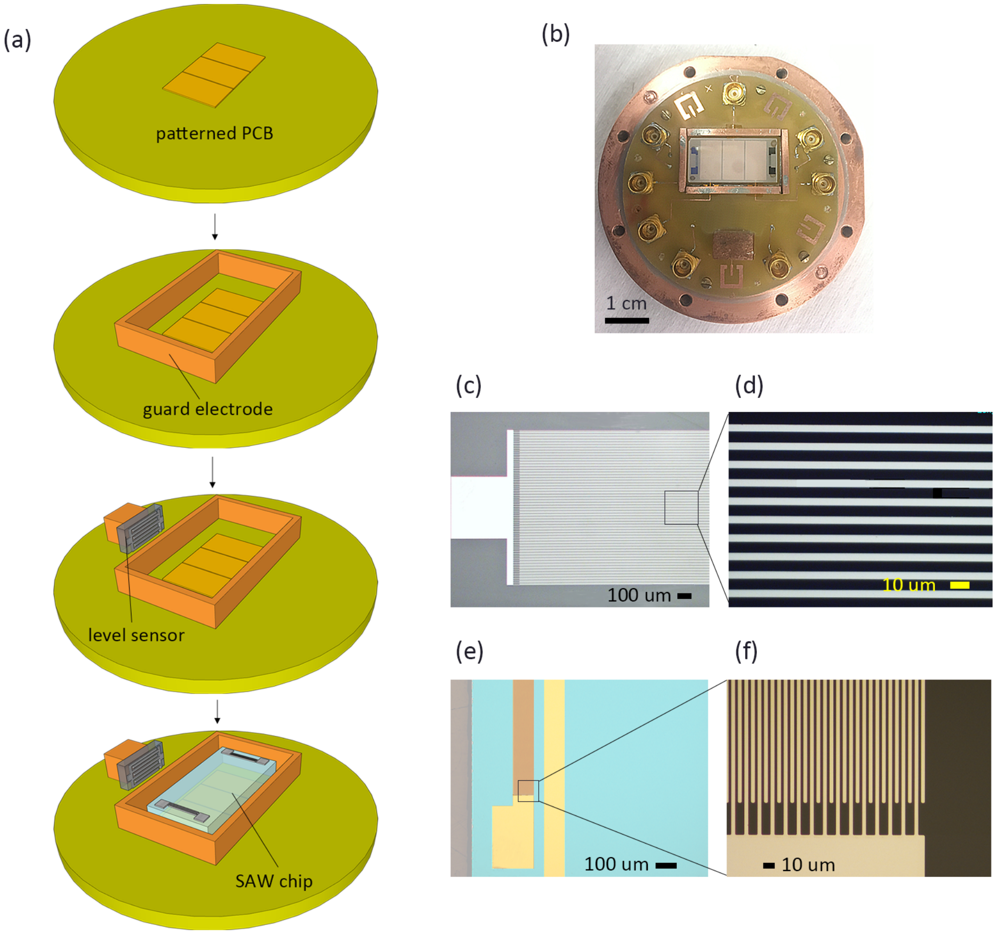

Figure 4.19: Electrons on helium SAW experiment fabrication. (a) Assembly process of main part of the cell PCB. A set of three rectangular electrodes (trapping electrodes) with a width of $8 - 10$ mm, a total length of $9 - 15$ mm, and a thickness of ~ 35 μm are patterned on a 2 inch diameter and 1.5 mm thick PCB. A rectangular guard electrode made of a few mm thick Cu wire is attached around the three planar electrodes for lateral electron confinement. An interdigitated capacitor (IDC) is fabricated from ~ 5 μm wide and ~ 100 nm thick aluminum patterned on a 3.5 mm wide × 8 mm long × 0.5 mm thick quartz substrate and then vertically mounted to the PCB to measure the bulk liquid helium level. A SAW chip containing two identical interdigitated transducers (IDTs) for generation and detection of the SAW is lastly mounted on the trapping electrodes. (b) Picture of the electrons on helium $LiNbO_3$ device after assembly. (c),(d) Optical microscope image of the IDC helium level sensor made of ~ 100 nm thick aluminium on the quartz substrate. The metal line width and spacing are equal (~ 5 μm each) as shown in the magnified image ((d)). (e),(f) Optical microscope image of the SAW chip. The zoom-in image shows an interdigitated transducer (IDT) with $3/3$ μm metal line/spacing, which creates a SAW having a wavelength of $\lambda_{\text{saw}} = 24$ μm when the RF excitation is applied on resonance.

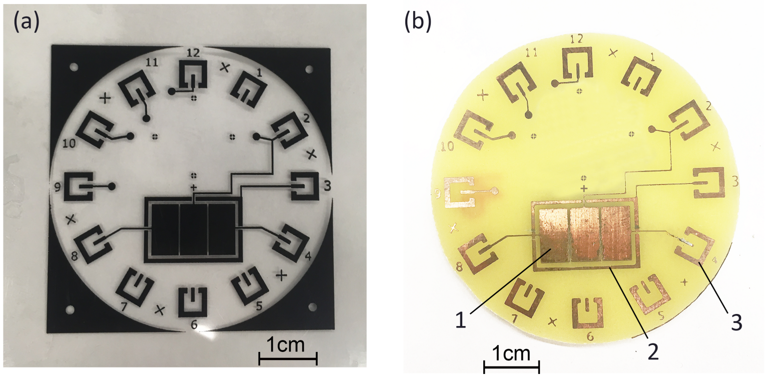

Figure 4.20: (a) Picture of the custom printed transparent sheet used as the mask for the PCB patterning process. Two copies are placed on top of each other with good alignment so that the dark area effectively blocks light during the exposure process. (b) Actual image of a patterned PCB board after completing photolithography (1. trapping electrodes, 2. guard electrode pad, and 3. GPO launcher pad).

4.2.3 Cleanroom Fabrication Processes

A conventional semiconductor lift-off process as shown in Fig. 4.21 is used to fabricate the IDC level sensor and SAW devices. A detailed description of each step is as follows.

Photolithography Mask

All masks were custom made by Photo Science Inc.. These masks are made of chrome on sodalime glass with a 3 μm limit for the minimum pattern size. They are located in the LHQS drawers in the KMF clean room.

Wafers

The insulating substrate for the IDC helium level sensor was a 100 mm diameter and 0.5 mm thick fused quartz (non-crystalline silica, dielectric constant $\varepsilon \cong 3.82$) wafer. After patterning with this wafer, it is diced into various sizes of IDC chips. To fabricate SAW samples, two different kinds of piezoelectric wafers are used. One is a 4 inch YZ-Cut $LiNbO_3$ wafer with a

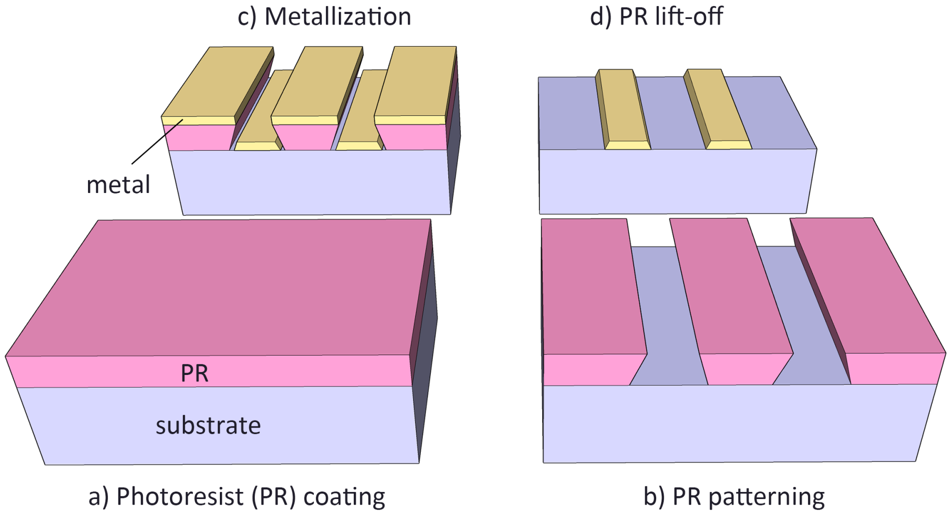

Figure 4.21: Semiconductor lift-off process for sample fabrication. (a) Photoresist (PR) is coated on the substrate using a spin-coater. (b) The PR is patterned with UV exposure followed by a developing process. (c) A thin metal film is deposited onto the patterned PR via thermal evaporation. (d) The PR/metal bi-layer is washed away in acetone or PR stripper, leading to a patterned metal film on the substrate.

thickness of 0.5 mm. Its large piezoelectric coupling constant $K^2/2 = 4.82 \times 10^{-2}$ allows for strong coupling of the SAW to electrons on helium for acoustoelectric measurements. SAW chips diced from this wafer have a (010) normal crystal plane and [001] SAW propagation direction. Additionally, SAW devices were also fabricated on 2 inch diameter and 0.35 mm thick undoped single crystal GaAs wafers with (100) normal crystal plane. SAW samples made of this wafer have a [011] SAW propagation direction and relatively weak piezoelectric coupling constant ($K^2/2 = 3.2 \times 10^{-4}$). These devices were used to study SAW attenuation arising from the screening affects the 2DES on the surface of liquid helium.

Wafer Dicing

The initial step for sample fabrication starts with the cutting of a 2 $\sim$ 4 inch wafer into individual chips. We used a wafer dicing saw to do this. Once the desired dimension and material information are entered into the machine, the wafer dicing with a diamond blade (Part No. 2.187-8A-64RU7-3 from Thermocarbon) automatically proceeds with position precision within to 40 μm. Typical dimensions of the SAW chip are 10 × 20 mm for the $LiNbO_3$ substrate and 17 × 17 mm for the GaAs substrate. For the IDC level sensor, chips have various dimensions with height ranges between 3 and 4 mm at a fixed width of $\sim$13 mm. If the fabrication process is performed on a complete wafer, this dicing step is employed after the patterning process is completed. In this case, a photoresist coating is required before wafer dicing to protect the pattern on the chip from contamination from wafer debris produced during dicing.

Wafer/Chip Cleaning

To remove contaminants from the surface of a wafer or a chip before photoresist coating, a cleaning process is performed. The wafer or chip is sonciated for 5 min in three different solvents in the following order: acetone → IPA → DI water. After this, sample is pre-baked at 100 ^{O}C for 10 min to remove any moisture. Additionally, plasma cleaning with 58 sccm of oxygen at 100 W is employed for 30 seconds to remove photoresist scum left on the developed area right before depositing metal film.

Photolithography

The patterning of samples is performed using standard photolithography techniques at the Michigan State University W.M. Keck microfabriction facility (KMF). The sample surface is spin-coated with photosensitive organic material (photoresist) and the area exposed to UV is then selectively removed through a developing process. The following is a recipe for photolithography using the ABM mask aligner in the KMF.

1. Spincoat 3 $\sim$ 4 drops of hexamethyldisilazane (HMDS) to a diced sample with a micro-pipette at 5000 rpm for 50 sec. This improves photoresist adhesion by turning hydrophilic surfaces into hydrophobic surfaces. If the substrate is a 2 $\sim$ 4 inch wafer, 5 $\sim$ 10 ml of HMDS is dispensed onto the wafer and it is spun under the same condition.

2. Put 3 $\sim$ 4 drops of S1813 photoresist onto the HMDS-coated sample and then spin it at 5000 rpm for 50 sec. Photoresist edge beads usually form during this process with a square substrate. In particular, this problem becomes more pronounced when using a rectangular substrate and results in poor patternability. To solve this issue, we typically run all processes including spin-coating on a full wafer and then cut it into rectangular chips at the end using the dicing saw. For the wafer photoresist coating, after 5 $\sim$ 10 ml of the resist is dispensed onto the wafer, it is rotated with the same speed and time listed above. This gives a $\sim$1.2 μm thick photoresist layer on the substrate.

3. Soft bake the chip or wafer on a hot plate at 110 $^{\mathrm{o}}$C for 60 sec to remove the residual solvent in photoresist film.

4. Place the photoresist coated chip or wafer onto the sample stage vacuum chuck of the mask aligner and align the mask and sample. Raise the sample until the edge beads barely touch the mask, which can be seen by observing the formation of an interference pattern (Newton's rings) through the transparent region of the masks. Then, expose the chip/wafer to UV light for 6 sec at an intensity of 15.5 mW/cm^2.

5. Put the exposed sample in chlorobenzene for 5 min to harden the top of the photoresist. This produces a larger undercut in the photoresist during development, which

is required for a clean lift-off processing.

6. For photoresist developing, dip the sample into 352 developer for 25 sec and then rinse it with DI water to completely remove any residual developer. This allows the UV-unexposed area of photoresist to remain while the UV-exposed areas are washed away in the developer.

Metallization

A $50 \sim 100$ nm thick aluminium film is formed over the entire area of the developed wafer/chip using a thermal evaporator (EDWARDS AUTO 306) in the KMF. The sample is mounted at the top of the chamber and a small aluminium pellet is put into the evaporation boat, the chamber is closed and pumped out until the pressure reaches $10^{-6} \sim 10^{-7}$ torr. Then, the power supply input current for the source boat is slowly increased up to $\sim$2 A until the aluminium pellet starts to melt. At this period, the evaporation source shutter is closed so that aluminium vapor cannot reach the sample. After waiting for a stable deposition rate of $2 \sim 3\,\text{Å}$, the shutter is opened and metal film deposition starts. Once a target thickness is achieved, the shutter is closed and the power is decreased into zero. The thickness is measured using a quartz crystal monitor that provides real-time information on the metal thickness during deposition.

Lift-off

To leave behind only the metal film in the patterned area (i.e. the non-photoresist), the sample is dipped into acetone or PG remover (N-methyl pyrrolidinone) at $\sim$60 $^{\mathrm{o}}$C for $30 - 60$ min and then cleaned with IPA (isopropanol).

4.2.4 Assembly

Once an IDC level sensor and a surface acoustic wave device have been fabricated, they are attached to the PCB as illustrated in Fig. 4.19 (a). First, a copper block ($10 \times 5 \times 3$ mm) is firmly attached to the PCB with rubber cement glue. The IDC chip is then vertically mounted to the side of the block by applying high vacuum grease (DOW CORNING) thinly and evenly to the back of the quartz substrate. Similarly, the SAW chip is mounted to the PCB and held fixed by putting one tiny drop of rubber cement glue to each corner of its back after good alignment with the trapping electrodes. As shown in Fig. 4.19 (b), the SAW beam area has a rectangular shape where the short side coincides with the height of the interalced electrodes of each IDT, which should maximally overlap with three underlying trapping electrodes to achieve a wide-area of interaction between the SAW and the 2DES.

Chapter 5

Low-Frequency Transport of Electrons on Helium

As discussed in subsection 4.1.5, a typical and direct way to demonstrate the formation of surface electrons floating on liquid helium is to measure their low-frequency electrical transport with a homogeneous areal electron density using the Sommer-Tanner measurement technique. When electrons thermionically emitted from the filament are trapped and remain stable above the liquid helium surface, the amplitude of the electrical current typically increases by a factor of $30 \sim 50$ compared to the case before charging the surface with electrons. Such a big difference is a good indicator of a stable 2DES in our experiments. More interestingly, the Sommer-Tanner geometry, where a set of three coplanar electrodes are separated by tiny gaps, allows for precise control of an inhomogeneous spatial distribution of electrons by applying different DC biases to each electrode. In fact, these non-uniform charge devices with electrons on helium have revealed a rich variety of physical phenomena such as the existence of long-lived inter-edge magnetoplasmons [134], dynamic reorganization of the electron density under microwave excitation [135, 136, 137], and electron crystallization [138, 139] and quasi-1D transport [140] under strong spatial confinement. In this chapter, we present the results of electrical transport measurements in this highly non-uniform electron density regime by sweeping the voltage V_{g} at the center electrode at fixed voltages $V_{\mathrm{s}} = V_{\mathrm{d}}$

for the other electrodes. In this mode of operation, the device functions as a macroscopic field effective transistor (FET) of electrons on helium and reveals novel transport phenomena in the system of electrons on helium at elevated temperature and low electron density [16].

5.1 Experiment and Finite Element Method (FEM) Modeling

Fig. 5.1 (a) shows an array of three co-linear rectangular electrodes patterned on a PCB mounted in the cell, which constitutes the source, gate and drain of a FET device (Fig. 5.1 (b)). The device is covered by layer of liquid helium of thickness d $\approx$ 0.5 mm. In contrast to typical transport experiments with this type of electrode configuration, where electrons are evenly distributed over the entire area of the device, we can use differing DC voltages on each electrode to create a spatially inhomogeneous electron density. It is in this way that we can operate the device as a FET where the source and drain biases are equal while the gate electrode voltage is varied. In this mode of operation we apply an AC excitation voltage, $V_{\mathrm{ex}} = 0.1$ V, to the source electrode and detect the gate tunable AC current on the drain electrode using standard phase-sensitive lock-in techniques described previously. We have carried out these measurements in the frequency range $f = 1 \sim 100$ kHz and in the temperature range T $= 1.35 \sim 2.0$ K, which corresponds to the regime where the electron transport mobility is limited by helium vapor atom scattering [9, 10].

We are able to gain physical insight into our experimental results through the use of finite element method (FEM) of the electrostatic potential experienced by the 2DES and the resulting electron density profile n_{s} on the device. Specifically, we solve Poisson's equation using FEM to find the density distribution of the 2DES, $n_{\mathrm{s}}(x)$, along the length L of the FET

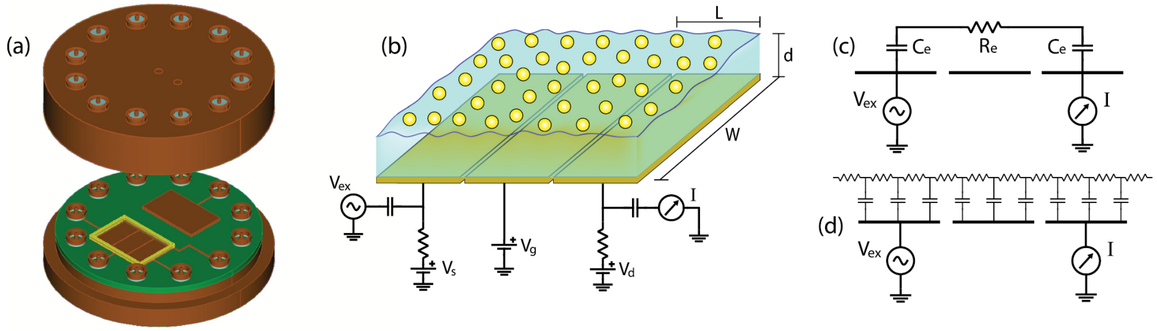

Figure 5.1: Schematic of the experimental setup and circuit modeling of electrons on helium. (a) 3D CAD rendering of the experimental cell with the array of FET electrodes and a liquid helium level sensor. (b) Sketch of the macroscopic FET device composed of electrons on liquid helium. The dimensions of each electrode are L × W = 5 × 10 mm and the gap between them is 0.2 mm. (c) The equivalent lumped RC circuit of the FET device. R_{e} is the resistance of the electron layer above gate electrode and C_{e} is the capacitance of electron system to the source and drain electrodes. (d) Transmission line equivalent circuit model of the electron system on liquid helium. In this transmission line mapping, the resistance of the electron layer and its capacitance to the FET electrodes is spatially distributed.

electrodes. The electron system is modelled as a charge continuum on the helium surface with effective length L_{e}, which is determined by imposing the condition of electrostatic equilibrium. We determine the total number of electrons in the simulation by allowing the electrochemical potential of the charge sheet to change in response to the gate voltage. The areal density distribution is then given by $n_{\mathrm{s}}(x) = -(\varepsilon_0/e)(E_+(x) - \varepsilon E_+(x))$, where $E_{+,-}(x)$ are electrical field distribution above and below the charge sheet, ε_0 is the vacuum permittivity and $\varepsilon = 1.057$ is the dielectric constant of helium.

5.2 Results and Discussion

5.2.1 Electrons on Helium Field Effective Transistor (FET)-IV Characteristics

A typical source-drain current–voltage (I–V) characteristic is shown in Fig. 5.2 for FET operation of the device. For small values of the gate voltage, V_{g}, no current flows through electron layer because all of the electrons are localized above the source and drain electrodes and the area over the gate is depleted. This is illustrated in left inset of Fig. 5.2 where we show the electron density profile simulated using FEM. Upon increasing V_{g} electrons are attracted to the region above the gate leading to the onset of source-to-drain current flow at a threshold value of the gate voltage, V_{th}. This behavior mimics that of a conventional semiconductor FET. However, further increasing V_{g} reveals the first of several phenomena unique to a FET of electrons floating on helium. Unlike a conventional FET, the source-drain current reaches a maximum in the vicinity of uniform areal electron density ($V_{\mathrm{s}} = V_{\mathrm{d}} = V_{\mathrm{g}}$),

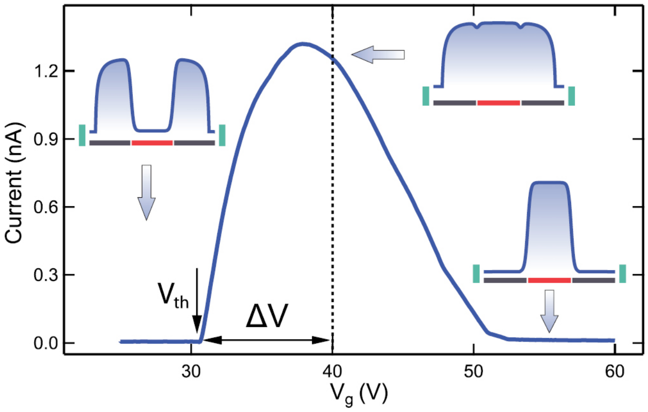

Figure 5.2: Amplitude of the source-to-drain current, $|I|$, as a function of gate voltage at T = 1.35 K for the electrons on helium FET device. For these measurements $V_{\mathrm{s}} = V_{\mathrm{d}} = 40$ V and the guard electrode was biased with -50 V. The insets illustrate the electron charge profile over the FET electrodes obtained by finite element simulation of the device. A uniform electron density is achieved when the source, drain and gate electrodes have equal value (dashed vertical line).

as illustrated by the central inset. After reaching a maximum value, the source-drain current begins to decrease and eventually vanishes with increasing V_g. For sufficiently large V_g all of the electrons will be located above the gate, leading to $|I| = 0$, since the charge sheet is not connected to a ground reservoir of electrons, but rather operates with a fixed number of particles. This effect is highlighted in the right inset of Fig. 5.2 where we show the FEM simulated density profile for large gate voltage.

5.2.2 Electron Density Estimation

In the subsection 4.1.5, we showed that the maximum attainable areal electron density n_m can be determined by voltage difference between the top and bottom electrodes using equation 4.2. For the general case where $n_\mathrm{s} \leq n_\mathrm{m}$, an uniform areal density n_s when $V_\mathrm{s} = V_\mathrm{d} = V_\mathrm{g}$ can be easily estimated from the above FET I-V measurement where V_g is swept at constant $V_\mathrm{s} = V_\mathrm{d}$. At $V_\mathrm{g} = V_\mathrm{th}$, one can assume that electrochemical potential V_e is in equilibrium state with constant value of V_th over all electron regions [141] and thus the number of electrons N above each electrodes can be calculated using the following capacitance model:

$$\begin{aligned} N_\mathrm{g} &= C\,(V_\mathrm{th} - V_\mathrm{e})\,WL/e = 0 \quad \text{(above the gate)} \\ N_\mathrm{s} &= N_\mathrm{d} = C\,(V_\mathrm{s,d} - V_\mathrm{th})\,WL/e \quad \text{(above the source/drain)}, \end{aligned} \tag{5.1}$$

where $C = \varepsilon\varepsilon_0/d$ is geometrical capacitance per unit-area of the electron layer to each electrode, e is the elementary charge, $W = 10$ mm and $L = 5$ mm denote the width and length of the electrode as shown in Fig. 5.1 (b). Supposing that the total number of electrons is conserved ($N_\mathrm{t} = 2\,N_\mathrm{s} = 2\,N_\mathrm{d}$), the uniform areal electron density at $V_\mathrm{s} = V_\mathrm{d} = V_\mathrm{g}$ is given by

$$n_{\mathrm{s}} = \frac{N_{\mathrm{t}}}{3WL} = \frac{2}{3e}C\Delta V, \quad \text{where } \Delta V = V_{\mathrm{s,d}} - V_{\mathrm{th}}. \tag{5.2}$$

For the measurement shown in Fig. 5.2, where $V_{\mathrm{s}} = V_{\mathrm{d}} = 40$ V, the areal density for our electrode dimensions is $n_{\mathrm{s}} \cong 7 \times 10^7$ cm^{-2}, which is consistent with that obtained by FEM simulations.

5.2.3 Observation of Negative Phase of the Electron Layer Current

As described in the subsection 4.1.7, Lock-in measurements allow us to simultaneously measure the in-phase (real) and quadrature (imaginary) components Re(I) and Im(I) of the complex source-drain current. Knowledge of both components is necessary to accurately model the impedance of the system as a function of frequency since it contains both resistive and reactive elements. In Fig. 5.3 we show the gate voltage dependence of the real (a) and imaginary (b) components of the source-drain current measured at T = 1.35 K (blue trace), T = 1.6 K (green trace), and T = 1.95 K (red trace). While at low temperature both Re(I) and Im(I) are positive as expected from the lumped circuit model, in contrast we find that at high temperature the data exhibit an anomalous gate voltage dependence where the imaginary component of the current Im(I) is negative at sufficiently high temperature (shaded red region). This negative current implies that the relative phase angle ϕ between the source-drain current and the AC excitation voltage is also negative at high temperature. Furthermore, negative values of Im(I) are not restricted only to high temperature, but rather also manifest in the vicinity of FET depletion when $V_{\mathrm{g}} \geq V_{\mathrm{th}}$ shown as the shaded green and blue regions in Fig. 5.3 (b).

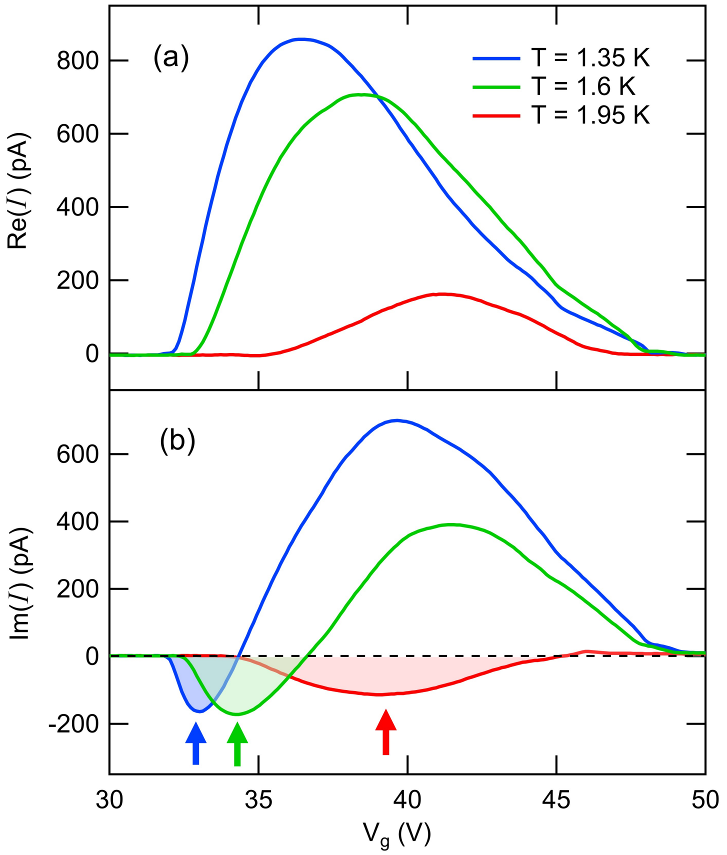

Figure 5.3: Real (a) and imaginary (b) components of the FET source-drain current as a function of gate voltage measured at T = 1.35 K (blue curve), T = 1.6 K (green curve), and T = 1.95 K (red curve) at f = 60 kHz. For these measurements $V_{\rm s} = V_{\rm d} = 40$ V and the guard electrode was biased with -50 V. The negative values of $\mathrm{Im}(I)$, indicated by the vertical arrows and shaded regions, represent a unique departure from the lumped RC circuit model for an FET made of electrons on helium.

5.2.4 Transmission Line Mapping

Both the geometric and the kinetic inductance in electrons on helium are negligible in the range of temperature studied here and thus the lumped RC model for AC transport cannot explain this negative value of the quadrature source-drain current (i.e. both $\mathrm{Re}(I)$ and $\mathrm{Im}(I)$ are expected to be strictly positive for all values of R_{e} and C_{e}). To understand values of $\mathrm{Im}(I) < 0$ the wave nature of the propagating electrical signal must be taken into account and the 2DES on helium should be considered as a transmission line with spatially distributed resistance and capacitance (Fig. 5.1 (d)). Assuming that no variation in the voltage and current along the width W of the electrodes, modeling of the system reduces to a one-dimensional RC transmission line, where a damped voltage wave propagates from the source to the drain with the boundary condition that the current density is zero at both of these electrodes. The complex current $I = \mathrm{Re}(I) + j\,\mathrm{Im}(I)$ produced by this voltage wave can have the same form as the equation 4.24 in the chapter 4 with $L \to 3L$. This is because L in equation 4.24 denotes the total length of the three electrodes.

The wave nature of the current itself already provides a qualitative understanding of the data depicted in Fig. 5.3. As expressed in equation 4.26, the complex wavevector of the current wave is given by

$$k = \frac{1-j}{\delta} \quad \text{with } \delta = \sqrt{\frac{2\sigma}{\omega C}}. \tag{5.3}$$

Here $\sigma = n_{\mathrm{s}} e \mu$ is the Drude conductivity of the 2DES with the electron mobility μ, $\omega = 2\pi f$ is the angular excitation frequency, and δ is a two-dimensional AC skin depth [142]. When δ is comparable or smaller than the total length of the FET electrodes, $\delta \leq 3L$, the imaginary component of the source-drain current reverses sign since the phase angle between the current and driving voltage $\phi = \pi/2 - 3kL$ becomes negative. At low temperature the electron mobility, and corresponding conductivity, are relatively high. As a result δ is larger than the overall length of the FET electrodes and $\mathrm{Re}(I)$ and $\mathrm{Im}(I)$ remain positive. Increasing the temperature leads to an exponential increase of the density of helium vapor atoms and hence to a marked decrease of the electron mobility. In the range of temperatures $\mathrm{T} = 1.35 \sim 1.95$ K the reduction of mobility is approximately an order of magnitude, which reduces δ to a value much smaller than the total length of the electrodes leading to the negative values of $\mathrm{Im}(I)$ we observe in our measurement. Furthermore, our finding that $\mathrm{Im}(I) < 0$ at low temperature ($\mathrm{T} = 1.35$ K) but only in the vicinity of FET turn-on can be understood in a similar fashion. When $V_{\mathrm{g}} \cong V_{\mathrm{th}}$ the number of electrons present in the gate region is small and their resistivity is relatively high leading to a decrease in δ and $\mathrm{Im}(I) < 0$. As V_{g} is further increased more electrons are attracted to the region above the gate electrode, which increases the 2DES conductivity and tunes the sign of $\mathrm{Im}(I)$ to positive values.

We have also performed a quantitative analysis based on the transmission line model for the case where the electron density is homogeneously distributed over the device. This model is defined by the following expression, which relate the mobility $\mu = \sigma n_{\mathrm{s}}^{-1} e^{-1}$ to the frequency dependent complex source-drain current:

$$I = I_0\,(1+j)\,\frac{3\sigma}{2L}\frac{\sinh^2(jkL)}{\sinh(3jkL)} \quad \text{with } I_0 = \omega C \frac{WL}{3} V_{\mathrm{ex}}. \tag{5.4}$$

The comparison between a fit based on this model (dashed curves), with the transport mobility μ as a fitting parameter, and the experimental data (solid curves) is shown in Fig. 5.4, where the frequency dependence of both components of the measured current is plotted at low ($\mathrm{T} = 1.35$ K) and high ($\mathrm{T} = 1.95$ K) temperatures. For the data in Fig. 5.4

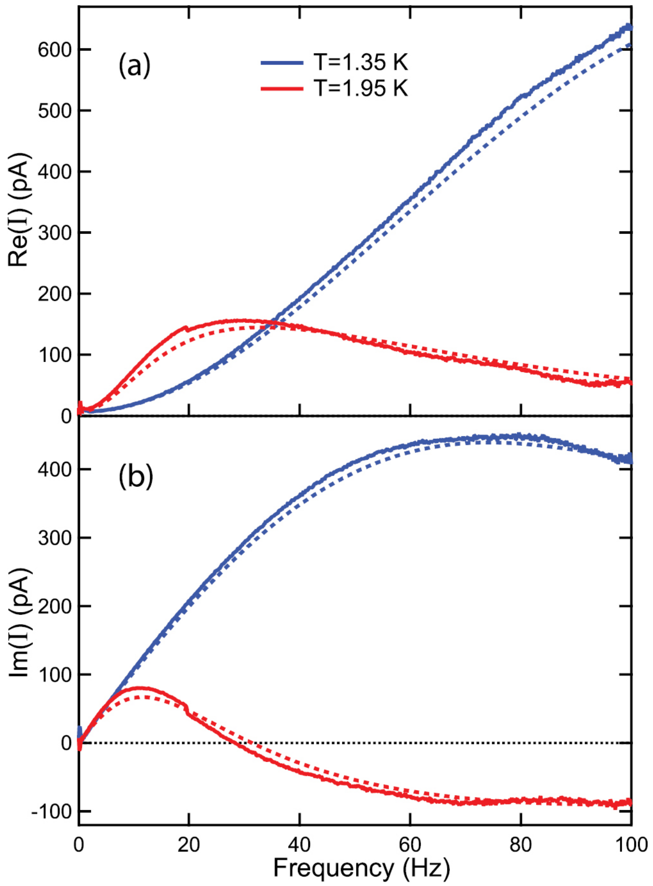

Figure 5.4: Frequency dependence of the real Re(I) (a) and imaginary Im(I) (b) components of the source-drain current with a uniform electron density above all three FET electrodes corresponding to $V_{\mathrm{s}} = V_{\mathrm{d}} = V_{\mathrm{g}} = 40$ V. For these measurements the guard electrode was biased with -5 V. The solid traces show the experimental data obtained at T = 1.35 K (blue) and T = 1.95 K (red). The correspondingly colored dashed lines are calculated using the transmission line model described in the text.

the DC bias potential is the same for all FET electrodes $V_{\mathrm{s}} = V_{\mathrm{d}} = V_{\mathrm{g}} = 40$ V and the electron density is $n_{\mathrm{s}} = 7 \times 10^{7}$ cm^{-2}. The value of the mobility obtained from this fitting is 2.8×10^{4} cm^{2} V^{-1} s^{-1} at T = 1.35 K and 0.45×10^{4} cm^{2} V^{-1} s^{-1} at T = 1.95 K. These values are in reasonable agreement with previous measurements [9] and the theoretical values given by Saitoh [10].

5.3 Conclusion

We have investigated the operation of a macroscopic field effect transistor composed of electrons on liquid helium in a regime where electron scattering from helium vapor atoms is the dominant form of disorder. In this FET mode of operation the electron density can be made highly non-uniform and we find that the imaginary component of the source-drain current changes sign from positive to negative when the systems is subjected to sufficiently high temperatures or when the electron density is made maximally inhomogeneous. These transport regimes can be understood by considering the system of electrons as a voltage wave propagating in a transmission line composed of the electrons floating above the metallic electrodes under the helium surface. We anticipate that an FET mode of operation could find application in studying other nonequilibrium phenomena such as ultrahot electron on helium [143, 144, 145, 146], electrons strongly confined in helium microchannel devices or for future high frequency surface acoustic wave experiments.

Chapter 6

SAW Coupling to Liquid Helium

The physics of the underlying liquid helium substrate is pivotal to better understanding the unique properties of 2D electrons on helium. In particular, when piezoelectric SAWs propagate along the surface of a piezoelectric crystal underneath surface electrons on helium, they can interact with not only the 2D electrons but also the liquid helium film, leading to SAW attenuation and velocity shift. Thus, understanding SAW coupling to the helium film is a prerequisite for the SAW measurements of the 2DES created on the surface of the liquid. In this chapter, we present pulsed measurements of the absolute attenuation of high-frequency SAWs on the surface of lithium niobate caused by bulk layers and thin films of liquid helium [147].

6.1 Experiment

The SAW attenuation experiments reported here were performed using a YZ-cut lithium niobate ($LiNbO_3$) single crystalline wafer as a substrate for SAW propagation. The lithium niobate substrate was diced into a rectangle with a length of 20 mm and a width of 10 mm. To excite and detect SAWs, two identical interdigitated transducers (IDT) having 40 pairs of 3 μm wide fingers were patterned on the surface of the $LiNbO_3$ chip in the form of a delay line, having a length of 16.5 mm, along the crystallographic x-axis using conventional photo-lithography (see Fig. 6.1 (a)). The transducers were fabricated from aluminum and

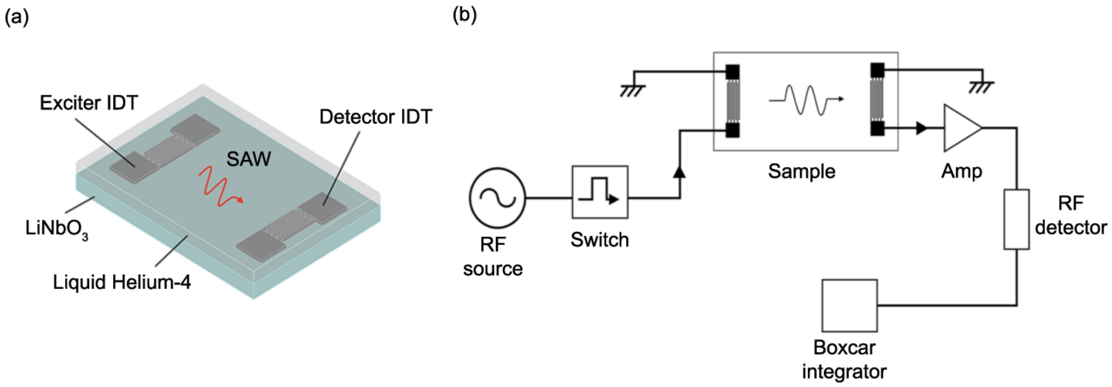

Figure 6.1: Pulsed surface acoustic wave experimental setup. (a) Schematic of the lithium niobate chip used for exciting and detecting SAW via aluminum interdigitated transducers (IDT), which were directly fabricated onto the surface of the substrate. (b) Block diagram of the circuit used for measuring the attenuation of pulsed SAWs. As described in the text, by measuring the time-of-flight signal we are able to disentangle direct capacitive crosstalk between the two interdigitated transducers as well as multiply reflected SAW pulses.

had a thickness of approximately 70 nm and a width of 4 mm defining the width of the SAW beam within the delay line. We note that in this geometry the IDTs are positioned 1.75 mm from the diced edge of the chip. Resonant SAWs are launched by applying a high-frequency signal between the transducer fingers of the exciter to create an elastic distortion of the piezoelectric substrate beneath the IDT. In this configuration, Rayleigh mode surface acoustic waves with components parallel (longitudinal) and perpendicular (transverse) to the wave propagation are launched along the $LiNbO_3$ surface toward the detector IDT. The fundamental resonant frequency of our Rayleigh wave SAW device is $\nu = v_S/\lambda = 291$ MHz, dictated by the IDT finger periodicity, $\lambda = 12$ μm, and the speed of sound in YZ cut $LiNbO_3$, $v_S = 3488$ m/s. The frequency response of the SAW delay used in our attenuation measurements was characterized using an Agilent N5230A vector network analyzer. Fig. 6.2 shows the measured transmission coefficient, S_{12}, of the delay line as a function of frequency at T = 1.55 K in vacuum. The resonance in the transmitted power at $\nu \cong 296$ MHz is associated with the generation of SAW in the substrate. The measured resonance is a few percent larger than the expected value, likely due to an increase in the elastic moduli of $LiNbO_3$ at cryogenic temperature. Fig. 6.1 (b) shows a diagram of the circuit used to measure the attenuation of the piezoelectric waves. Pulsed SAWs are created by gating a continuous wave signal using a fast solid-state switch. For the measurements reported here, the pulses had a width of 3 μs and were repeated at a frequency of 1 kHz. The received SAW signal at the detector IDT was amplified by 30 dB and measured using a calibrated crystal diode detector (Krytar Model 203AK S/N 00277). A boxcar integrator was used for time-of-flight measurements. This mode of operation allows us to disentangle the piezoacoustic signal from direct capacitive crosstalk between the two IDTs as well as multiply reflected surface acoustic wave pulses within the delay line. The SAW device was mounted inside of a hermetically sealed copper cell attached to a closed cycle 1K cryostat. Helium gas was supplied into the cell at T ≅ 1.55 K through a capillary fill line. A resistive thermometer located outside of

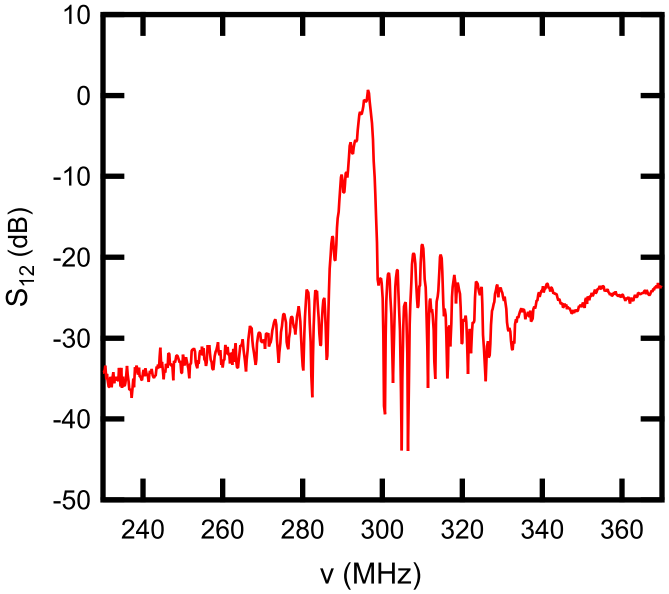

Figure 6.2: Frequency dependence of the transmission coefficient (S_{12}) of the SAW delay line at T = 1.55 K in vacuum. The resonant peak at ν = 296 MHz is associated with the generation of surface acoustic waves in the IDT delay line.

the cell and calibrated relative to the known superfluid transition temperature of ^{4}He was used to measure the temperature of the liquid helium. The liquid helium volume admitted into the cell was determined by varying the pressure in a calibrated standard volume of 260 cc at room temperature. As expressed in equation 2.96 of the chapter 2, the thickness of the helium film can be estimated as follows.

$$d = \left(\frac{\gamma}{\rho g H} \right)^{1/4}, \tag{6.1}$$

where γ is the van der Waals constant, ρ is the mass density of ^{4}He, g is the acceleration due to gravity, and H is the distance from the $LiNbO_3$ surface down to the liquid helium level in the reservoir volume in the cell. Three-dimensional modelling of the experimental cell open volume was used to calculate H from the volume of helium admitted into the cell from the calibrated volume at room temperature.

6.2 Results and Discussion

6.2.1 SAW Attenuation by Bulk Liquid Helium

Before presenting our results on thin liquid helium films, we first demonstrate that we are able to use our measurement setup to reproduce the known temperature dependence of Rayleigh wave attenuation by bulk liquid helium. Rayleigh mode surface acoustic waves are attenuated by contact with a bulk liquid due to the surface-normal component of the particle motion and that of the co-propagating piezoelectric field. These components generate longitudinal compressional waves upward into the liquid, dissipating most of the acoustic energy [148, 149]. This method of energy loss is closely related to the problem of the Kaptiza resistance based on the acoustic mismatch between liquid helium and a solid substrate [11, 150], whereby longitudinal waves having a velocity v are emitted into the liquid from the substrate surface at an angle $\phi = \arcsin(v/v_{\mathrm{s}})$. In addition to this mechanism, the in-plane shear component of the SAW can also radiate energy into a fluid over the viscous penetration depth,

$$L = \sqrt{\frac{\eta}{\pi\nu\rho}} \tag{6.2}$$

where η and ρ are the viscosity and mass density of the fluid. However, SAW energy lost to shear is two to three orders of magnitude smaller than longitudinal absorption in our temperature range and is negligible even for our measurements in thin helium films. Our results for the temperature dependence of the SAW attenuation produced by bulk liquid helium are shown in Fig. 6.3 as the solid red curve. For comparison, we also show the

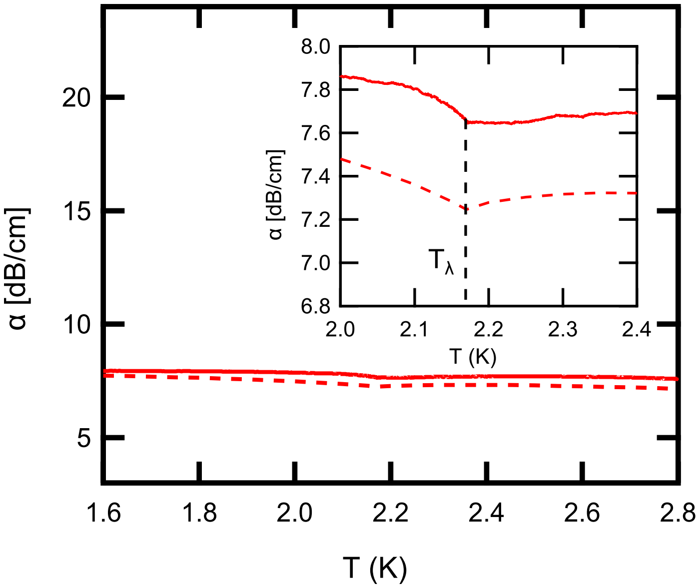

Figure 6.3: Attenuation, α, of Rayleigh waves on $LiNbO_3$ in contact with bulk liquid helium. Our measurements (solid red curves) at $\nu = 296$ MHz are in good agreement with the theory (dashed red curve) of Dransfeld and Salzmann [22] for energy loss due to radiation of longitudinal compressional waves into the liquid (Inset). The local minimum of the SAW attenuation at $T_\lambda = 2.17$ K is associated with the transition from normal to superfluid ^{4}He.

prediction for the attenuation (dashed red curve) based on the loss of SAW energy in the form of longitudinal compressional waves [149]. As expected, our measurements are in good correspondence with theoretical prediction. Moreover, our results for bulk helium are also in good agreement with previous measurements of the attenuation of piezoelectric Rayleigh waves by liquid helium [148, 151, 152, 153].

6.2.2 Anomalous Attenuation of SAWs by Thin Liquid Helium Films

Unexpectedly, we find that when the thickness of the liquid helium layer is sufficiently reduced an anomalously large attenuation can be induced. In Fig. 6.4, we show measurements of the SAW attenuation (solid blue data) at $T = 1.55$ K while increasing the volume of helium in the cell by small increments. With an increasing amount of helium, we observe a rapid increase in the SAW attenuation once the thickness of the superfluid film reaches $\approx 60 \sim 70$ nm ($H \cong 0.28$ mm) and continues to increase and quickly exceeds the attenuation produced by bulk helium. For reference, we plot the SAW attenuation measured in bulk helium at the same temperature as the red horizontal line in Fig. 6.4. We emphasize that this anomalously large attenuation is reproducible on multiple fillings of the experimental cell and additionally is insensitive to the tilt of the cryostat with respect to vertical. With further increasing film thickness, the SAW attenuation will eventually recover the value measured for bulk helium. However in this crossover regime ($d \sim 1 - 10$ μm) the film thickness on the substrate is exceedingly sensitive to fluctuations in H and also to the tilt of the cryostat leading to non-reproducibility. Future experiments, using microchannel geometries could allow for controlled measurement in this regime of film thickness. Moreover, we find that this phenomenon is not restricted to superfluid helium but rather persists into the normal state.

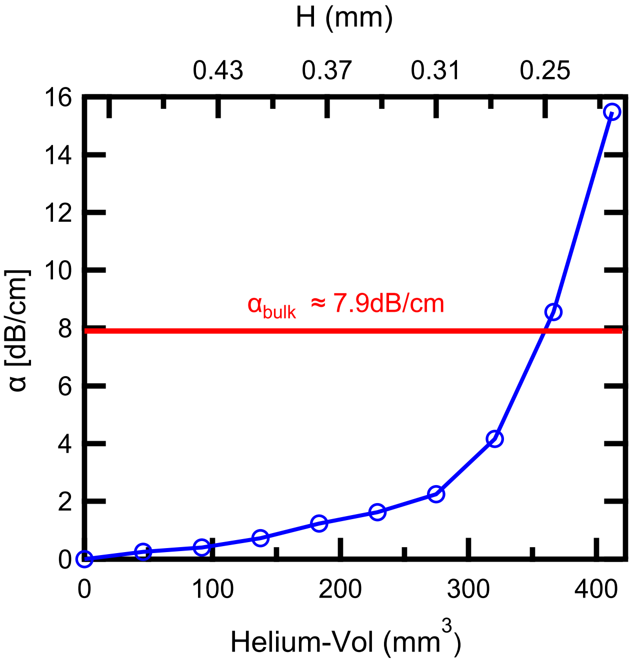

Figure 6.4: Attenuation, α, of Rayleigh waves on $LiNbO_3$ in contact with thin films of liquid helium at T= 1.55 K and ν = 296 MHz. The measurements are made by incrementally admitting small amounts of helium gas into the cell from a standard volume at room temperature (lower horizontal axis). The vertical dashed line indicates the estimated thickness of the helium film on the $LiNbO_3$ surface based on equation 6.1 and the height H from the substrate to the bulk helium reservoir level in the cell (top horizontal axis). For comparison, the horizontal solid red line indicates the SAW attenuation due to bulk liquid helium at the same temperature. The calculated thicknesses of the helium film for the final two data points above the bulk value are 73 nm and 76 nm. Finally, we note that the IDT fingers are expected to fill completely with helium via capillary action for very small amounts of helium introduced into the cell, i.e. already at $H = 0.46$ mm.

To our knowledge, no prior measurements of the attenuation of high-frequency SAW have been made in this regime of helium thickness nor is there a theory describing the coupling of SAWs to such films. We speculate that the occurrence of the attenuation anomaly reported here for thin helium films can qualitatively be understood in terms of a coupling between the piezoelectric surface wave on the $LiNbO_3$ substrate and excitations in the helium surface.

While the physical displacement of atoms associated with the SAW is at the angstrom scale, the SAW piezoelectric field has a spatial extent on the order of the SAW wavelength, which in our case is $\sim$12 μm. In fact, it is well-known that an electric field gradient can exert a force to move liquid helium via electrostriction, an effect which has even been utilized in developing a number of recent superfluid optomechanical systems [154, 155, 156, 157]. It is possible that an electrostrictive coupling between the $LiNbO_3$ surface wave and the liquid helium surface conspire to produce a new mode of energy loss not present in bulk helium. Finally, we note that our observation of enhanced attenuation in thin normal helium films is able to rule out the coupling of SAWs to third sound as the sole mechanism for increased SAW energy loss.

6.3 Conclusion

In conclusion, we have performed high-frequency SAW attenuation measurements in thin films of superfluid and normal ^{4}He where we find an anomalously large loss of energy from the piezoelectric surface wave into the liquid. We suspect that this increased attenuation is associated with electromechanical excitation of the helium film surface via a coupling of the SAW electric field to the dielectric constant of liquid helium.

Chapter 7

SAW Coupling to Electrons on Helium

We have investigated the coupling of SAWs to the 2DES on liquid helium surface. We show that this coupling is mediated through the piezoelectric field of the SAW. In the weak piezoelectric field regime, the screening of the piezoelectric potential by the mobile 2DES results in energy and momentum transfer from the SAW to the 2DES. This leads to a change in the attenuation and the velocity of SAWs as described in section 3.2. Measurements of these quantities provide information about electrons on helium films. In particular, the SAW detects the conductivity of the 2DES with high sensitivity as described in section 3.2. This ability allows for the measurement of the conductivity of electrons on helium at much higher frequencies and shorter wavelength than in conventional transport experiments. The coupling of SAWs to electrons on helium were originally theoretically studied by Lawrence A. Wilen [122]. Based on an electrical surface perturbation method described in subsection 3.2.2, he showed that an evanescent piezoelectric coupling of the SAW to the 2DES yields the SAW velocity shift $\Delta v/v \cong 2$ ppm (parts per million) and the SAW attenuation $\Gamma \cong 1.5$ dB/cm for a SAW frequency of $f = 180$ MHz and an areal electron density $n_{\mathrm{e}} = 10^{10}$ cm^{-2}. To measure the SAW attenuation in the presence of electrons on helium, we used a [011] cut of GaAs (100) as the piezoelectric substrate due to its relatively weak piezoelectric coupling constant $K^2/2 \cong 3.2 \times 10^{-4}$. With this piezoelectric substrate covered by a thin film of liquid helium, we observe that the SAW attenuation is strongly affected by surface charge density and is in a reasonable agreement with Wilen's calculation. With an increasing distance d from the 2D electrons to the surface of the piezo-substrate (GaAs) along which the SAW propagates, the SAW attenuation decreases and eventually disappears when $d \gg$ SAW wavelength λ, reflecting the evanescent coupling of electrons on helium and the SAW potential. These results and discussion are presented in section 7.1.

In the strong piezoelectric field regime, the SAW potential is able to trap and transport surface electrons and leads to a local DC current so-called acoustoelectric charge transport as introduced in the section 3.3. This effect has been observed in many low-dimensional electron systems ranging from [33, 34, 115, 158, 159, 160]. In particular, it has recently attracted particular attention as a means of controlling and transporting single electron for metrology [38], quantum optics [161], and quantum information processing [106, 107]. To date, considerable progress in these fields has been made with GaAs 2DESs. However, crystalline imperfections and foreign impurities (chemical donors or acceptors) in this system make it challenging to reach long electron coherence times [162], which is required for a practical quantum computing hardware. Also, these defects have limited the performance of a single electron transport devices [163, 164, 165]. A SAW-electrons on helium coupling device has the potential to naturally solve these problems due to the lack of such defects in electrons on helium. To demonstrate the acoustoelectric effect in electrons on helium, we have fabricated a SAW device on a YZ cut lithium niobate ($LiNbO_3$, crystal plane (010) with SAW propagation direction [001]), which has a nearly two orders of magnitude higher piezoelectric coupling constant $K^2 \cong 4.82 \times 10^{-2}$, compared to GaAs. In section 7.2 we report the first observation of this effect in electrons on the surface of thin liquid helium film

[166].

7.1 SAW Attenuation by Electrons on Helium

7.1.1 Experiment

The SAW device for studying electrons on liquid helium is locted inside a superfluid leak-tight copper cell. Fig. 7.1 (a) and (b) illustrate the schematic diagram of the device. A 17 mm square GaAs (100) chip with a thickness of 350 μm is used as the piezo-substrate on which surface acoustic waves propagates. A layer of 1.2 μm thick hard-baked photoresist (S1813G2) is patterned on the GaAs substrate to produce monolayer microchannel arrays consisting of approximately two hundred identical channels having a width and spacing of 15 μm. ^{4}He gas is supplied into the cell at T $\cong$ 1.55 K from a standard volume of 260 cc at room temperature to condense liquid helium in the cell. The liquid helium film is formed in the microchannel region by capillary action. Its thickness is estimated to be $d_{\text{ch}} = 1.16 \sim 1.18$ μm from equation 7.9 depending on an areal electron density n_{e}. At the same time, the top of the photoresist is also covered with a very thin liquid film $d_{\text{van}} = 60 \sim 80$ nm due to the Van der Waals interaction. Electrons generated from a filament are trapped on the surface of the helium film by applying a DC bias to a set of three electrodes (the source, the gate, and the drain electrode) underneath the GaAs as shown in Fig. 7.1 (b). Each electrode has a dimension of 5.5 mm length, 3 mm width, and 0.18 mm gap. Two pairs of interdigitated transducers (IDTs) made of 100 nm thick aluminum are deposited around the microchannel geometry to create and detect Rayleigh mode SAWs. In this study, only the set of opposite IDTs near the gate electrode (exciter IDT1 - detector IDT1) are operated. This simplifies the analysis of the SAW attenuation measurement since only electrons above the gate electrode contribute to the attenuation as shown in Fig. 7.1 (c). Note that if we use the other set of IDTs (exciter IDT2 - detector IDT2), SAWs interact with electrons over each electrode. This complicates the analysis of the attenuation of SAWs due to an inhomogeneous distributions of electrons over the electrodes. Each of the IDTs we used, consists of 22 pairs of 6 μm wide fingers. The width of the IDT is 2.96 mm defining the width of the SAW beam to be slightly smaller than 3 mm wide gate electrode so that the SAW can interact with electrons above the gate electrode with a propagation direction perpendicular to the channel (Fig. 7.1 (c)). Fig. 7.1 (c) shows the circuit diagram used to measure the attenuation of pulsed Rayleigh SAWs. An RF power of 5 dBm at 119.2 MHz was applied to the exciter IDT1 via a fast solid-state switch to generate pulsed SAWs having a wavelength $\lambda = 24$ μm, typical pulse width of 2.5 μs, and a period of the pulse $T = 1$ ms. The received SAW signal at the detector

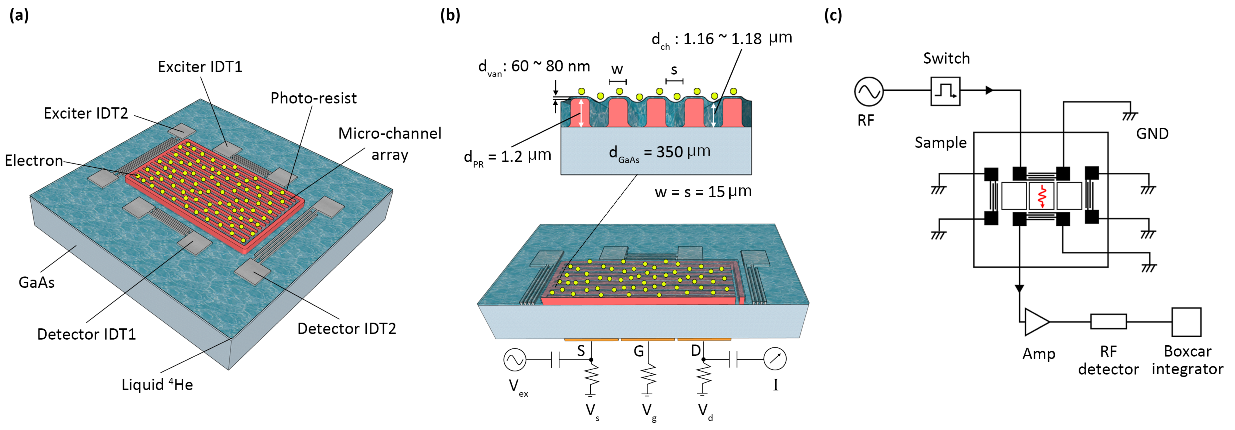

Figure 7.1: Experimental setup for measuring the attenuation of SAWs by electrons on helium. (a),(b) Top and cross-section view of the SAW device for studying electrons on helium. Electrons on the helium films formed in microchannel arrays are held in place by applying a positive DC bias to three undelying electrodes beneath the GaAs substrate at T ≅ 1.55 K. Two pairs of interdigitated transducers (IDTs) are located around the microchannel structure to excite and receive SAW signal. (c) Block diagram of the circuit used for measuring SAW attenuation. The exciter IDT1 and the detector IDT1 are operated so that pulsed SAWs can interact with 2D electron sheet above the gate electrode. In this region of the sample, the electron density can be varied from zero to its maximum value.

IDT1 is amplified by 30 dB and converted to a measurement of power using a calibrated crystal diode detector (Krytar Model 203AK S/N 00277). A boxcar integrator is used to improve the signal to noise ratio by excluding the instantaneous capacitive cross-talk signal between the IDTs. The boxcar integrator also averages the SAW pulses over typically 1,000 samples. Simultaneous low-frequency transport measurements of the electrons on helium is performed with the underlying electrodes. An AC excitation voltage $V_{\mathrm{ex}} = 0.1$ V is applied to the source electrode and the current is detected with a lock-in amplifier connected to the drain electrode (Fig. 7.1 (b)). We find that this current does not interfere with the Rayleigh SAW attenuation by the 2D electrons above the gate and thus they can be simultaneously measured with the electron density varied during a gate voltage V_{g} sweep.

7.1.2 Theory

Geometric Effect on SAW attenuation

Piezoelectric SAWs propagating beneath the surface of electrons on helium interact with not only the 2D electrons but also the underlying liquid helium substrate and thus both can result in attenuation of the SAW amplitude. In addition to that, a periodic array of inhomogenities like photoresist trenches in our device, on the surface of the piezoelectric substrate (Fig. 7.7) can cause attenuation too. In particular, when the SAW wavelength λ is comparable to the period of irregularties l, the SAW amplitude is reduced by Bragg reflection when $\lambda = 2l$, or the SAW loses energy by emitting phonons into the bulk due to its scattering with the periodic array structure when $\lambda \approx l$ [167]. Since $\lambda = 24$ μm is approximately similar to $l = 30$ μm in our device, the geometric effect on the SAW attenuation is mainly associated with the latter. More specifically, the periodic array structure on the piezoelectric surface scatters the SAW into a bulk wave having the same wavelength as the SAW. This bulk wave propagates into both the piezo-substrate and the adjoining medium (liquid helium in our case). However, for a thin helium film in our device, where the film thickness is much smaller than the wavelength of the SAW, bulk waves generated by SAW-periodic structure scattering mostly propagate into the piezoelectric medium. This leads to approximately constant attenuation over the film thickness change, which is not our interest in this work. Therefore, we remove it by measuring relative attenuation in electrons on helium in the presence of the periodic structure.

SAW Interaction with Surface Electrons on Helium

The interaction between SAWs and 2D electrons on liquid helium through the SAW piezoelectric field was theoretically investigated by Wilen [168] and we derive an expression for the SAWs attenuation applicable for our device geometry following his method. For weak piezomaterials such as GaAs and quartz, the attenuation by a perturbing 2DES can be calculated using the Ingebrigtsen formula (electrical surface perturbation) [169]. This perturbation approach allows to estimate a ratio of the perturbed electric potential to the perturbed electric field in the presence of 2D electrons above the piezoelectric surface. One can relate this ratio to the attenuation and the velocity shift of SAWs as described in subsection 3.2.2. In this formulation, the attenuation is given by

$$\frac{\alpha}{k} = \left(\frac{K^2}{2}\right) \mathrm{Im}\left(\frac{1 + iz^{'}(0)}{1 - i\epsilon_{\mathrm{p}} z^{'}(0)}\right), \tag{7.1}$$

where

$$z^{'}(0) = -ik\left(\frac{\phi^{'}}{D_{\mathrm{z}}^{'}}\right)_{z=0}, \quad \epsilon_{\mathrm{p}} = \sqrt{\epsilon_{zz}\epsilon_{xx} - \epsilon_{zx}^2}. \tag{7.2}$$

Here, Rayleigh SAWs propagates in the direction of the x axis and the positive z axis points out of piezoelectric plane located at $z = 0$. The normalized surface impedance $z^{'}(0)$ is defined by a ratio of perturbed potential $\phi^{'}(0)$ and the normal component of the perturbed displacement $D_{\mathrm{z}}^{'}(0)$ at the piezoelectric surface. The effective dielectric constant for the piezo-substrate ϵ_{p} is determined by dielectric tensor element ϵ_{ij}. The parameters α, k, and $\frac{K^2}{2}$ denote the SAW attenuation constant, the SAW wave number, and piezo-electric coupling constant of the substrate material. Note that equation 7.1 does not include mechanical losses of SAW energy and only describes losses from coupling to a mobile 2DES through the electric field. This is a good approximation for the present device where both the thickness of the charged helium film and the photoresist ($\mathrm{d_{ch}} \leq 1.18$ μm, $\mathrm{d_{van}} \leq 80$ nm, and $\mathrm{d_{PR}} \cong 1.2$ μm, see Fig. 7.7) is significantly smaller than the SAW wavelength of 24 μm [119]. Since the only unknown parameter in equation 7.1 is $z^{'}(0)$, estimation of the attenuation is a matter of solving for the electric potentials using appropriate electrical boundary conditions. From Poisson's equation, the potential inside the different regions in Fig. 7.2 can be expressed as

$$\begin{aligned} \phi_1 &= e^{ikx-i\omega t}\left(Ae^{-kz}+Be^{kz}\right), \\ \phi_2 &= e^{ikx-i\omega t}\left(Ce^{-kz}+De^{kz}\right), \\ \phi_3 &= e^{ikx-i\omega t}\left(Ee^{-kz}\right)-4\pi\sigma_0 z, \end{aligned} \tag{7.3}$$

where σ_0 and $\omega = 2\pi f$ are the equilibrium charge density of the 2DES and the angular frequency of the SAW. There are five unknown amplitude constants (A - E) and they can be expressed in terms of only one unknown from the electrical boundary conditions, a continuity equation, and relaxation time approximation (see appendix A.1 for detail). This yields a formula for the normalized surface impedance $z^{'}(0)$ and the SAW attenuation divided by the

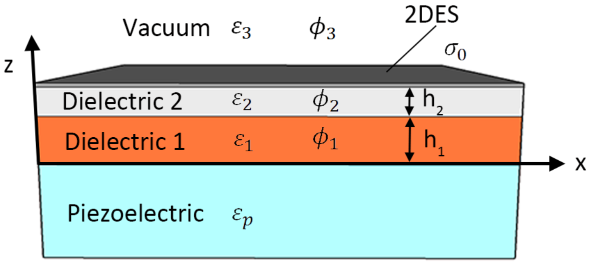

Figure 7.2: Approximate model geometry for SAWs experiments. SAWs propagate along the positive x-axis and the positive z-axis points out of the piezoelectric plane.

wavenumber α/k as follows:

$$z^{'}(0) = -ik\left(\frac{\phi^{'}}{D^{'}_{\mathrm{z}}}\right)_{z=0} = i\epsilon_1^{-1}\frac{r_{\mathrm{A}}+r_{\mathrm{B}}}{r_{\mathrm{A}}-r_{\mathrm{B}}}, \tag{7.4}$$

$$\frac{\alpha}{k} = \left(\frac{K^2}{2}\right)\mathrm{Im}\left(\frac{r_{\mathrm{A}}-r_{\mathrm{B}}-\epsilon_1^{-1}(r_{\mathrm{A}}+r_{\mathrm{B}})}{r_{\mathrm{A}}-r_{\mathrm{B}}+\epsilon_{\mathrm{p}}/\epsilon_1(r_{\mathrm{A}}+r_{\mathrm{B}})}\right), \tag{7.5}$$

where

$$r_{\mathrm{A}} = \left(\frac{\epsilon_1+\epsilon_2}{2\epsilon_1}r_{\mathrm{C}} + \frac{\epsilon_1-\epsilon_2}{2\epsilon_1}e^{2kh_1}\right), \quad r_{\mathrm{B}} = \left(\frac{\epsilon_1-\epsilon_2}{2\epsilon_1}e^{-2kh_1}r_{\mathrm{C}} + \frac{\epsilon_1+\epsilon_2}{2\epsilon_1}\right), \tag{7.6}$$

and

$$r_{\mathrm{C}} = \frac{\left[(\epsilon_2+1)\omega^2-\omega_{\mathrm{p}}^2\right]\tau+(\epsilon_2+1)i\omega}{\left[(\epsilon_2-1)\omega^2+\omega_{\mathrm{p}}^2\right]\tau+(\epsilon_2-1)i\omega}e^{2k(h_1+h_2)}. \tag{7.7}$$

Here $h_{1,2}$ and $\varepsilon_{1,2}$ denote the thickness and dielectric constant of dielectric 1 and 2 (see Fig. 7.2) while ω and ω_{p} are the angular frequency of the SAW and the plasma frequency in the 2D case (i.e. $\omega_{\mathrm{p}}^2 = 4\pi|\sigma_0|ek/m_{\mathrm{e}}$), and σ_0, e, and m_{e} are the equilibrium charge density of the 2DES, the elementary charge, and the electron mass, respectively. A derivation of equations 7.4 and 7.5 is presented in appendix A. Note that a minus-sign is dropped on the right-hand side of equation 7.4 due to the fact that in Ingebrigtsen formula (equations 7.1 and 7.2) the positive z-axis points into the piezoelectric medium while the negative z-axis does so in our derivation. For the simple case of one dielectric film (ϵ_1) between the piezo-substrate and the 2DES, the expression for the SAW attenuation reduces to

$$\frac{\alpha}{k} = \left(\frac{K^2}{2}\right) \mathrm{Im} \left(\frac{r_\mathrm{C} - 1 - \epsilon_1^{-1}(r_\mathrm{C} + 1)}{r_\mathrm{C} - 1 + \epsilon_\mathrm{p}/\epsilon_1(r_\mathrm{C} + 1)}\right), \tag{7.8}$$

with $\epsilon_2 = \epsilon_1$ and $h_2 = 0$.

In the region of the microchannel, the SAW attenuation can be calculated using equations 7.7 and 7.8 with $\epsilon_1 = \epsilon_\mathrm{He}$ and $h_1 \cong d_\mathrm{ch}$. ϵ_He denotes the dielectric constant of liquid ^{4}He and d_ch is the thickness of ^{4}He film at the center of the channel, which can be calculated from [170]

$$d_\mathrm{ch} = d_\mathrm{PR} - \frac{\mathrm{w}^2}{8\sigma_\mathrm{s}} \left(\rho g H + 2\pi \frac{n_\mathrm{e}^2 e^2}{\epsilon_\mathrm{He}}\right), \tag{7.9}$$

where d_PR, w, and σ_s are the thickness of the photoresist, the channel width, and the surface tension of liquid ^{4}He while ρ, g, H, and n_e denote the mass density of liquid ^{4}He, the gravitational acceleration, the distance from the piezoelectric surface down to the liquid helium level in a lower-lying reservoir, and the areal electron density.

For the photoresist region of our device as shown in Fig. 7.2 (b), equations 7.5, 7.6, and 7.7 can be used to estimate the attenuation with $\epsilon_1 = \epsilon_\mathrm{PR}$, $\epsilon_2 = \epsilon_\mathrm{He}$, $h_1 = d_\mathrm{PR}$, and $h_2 = d_\mathrm{van}$. The parameter ϵ_PR is dielectric constant of the photoresist and Van-der-Waals helium film above the photoresist can be obtained from [50]

$$d_\mathrm{van} = d_0 \left(1 + 2\pi n_\mathrm{e}^2/\rho g H\right)^{-1/3}, \quad d_0 = (a/\rho g H)^{1/3}, \tag{7.10}$$

where a is van-der-Waals constant and d_0 is the film thickness before charging electrons onto the surface of the liquid helium. For both regions (i.e. within the microchannel and on top of the photoresist), ω_p and τ in equation 7.7 are determined by the electron mobility μ_e and electron density n_e using $\omega_\mathrm{p} = \sqrt{4\pi \frac{n_\mathrm{e} e^2}{m_\mathrm{e}} k}$ and $\tau = \frac{\mu_\mathrm{e} m_\mathrm{e}}{e}$.

7.1.3 Results and Discussion

SAW attenuation by liquid helium

Before studying the attenuation of Rayleigh SAWs caused by the electrons floating above the helium surface, we first investigated the effect of liquid helium by measuring the attenuation as a function of the liquid helium volume inside the sample cell as shown in Fig. 7.3. In the helium film regime where the helium level is below the surface of 350 μm thick GaAs substrate ($H \geq 0.2$ mm), a strong attenuation is observed with a maximum value $\alpha_\mathrm{max} \cong 9$ dB/cm at $H \cong 0.24$ mm as described in chapter 6 for a thin liquid helium film on the $\mathrm{LiNbO_3}$ substrate. For the helium level far exceeding the substrate surface, the attenuation shows nearly constant value (∼10 dB/cm) indicating a bulk helium coverage. Note in these measurements we have chosen the distance from the GaAs surface down to the liquid helium level ($H \leq 0.2$ mm) to avoid the massive attenuation in the thin film region (see chapter 6). This is required in order to observe the relatively small SAW attenuation produced by the 2D electrons (∼1 dB/cm).

SAW Attenuation by 2D Electrons on a Helium Thin Film

To characterize the SAW attenuation produced by the system of electrons on helium, we measured the SAW attenuation as the electron density n_e was increased from zero during a positive sweep of the gate bias V_g. Note the SAWs only interact with electrons in the region

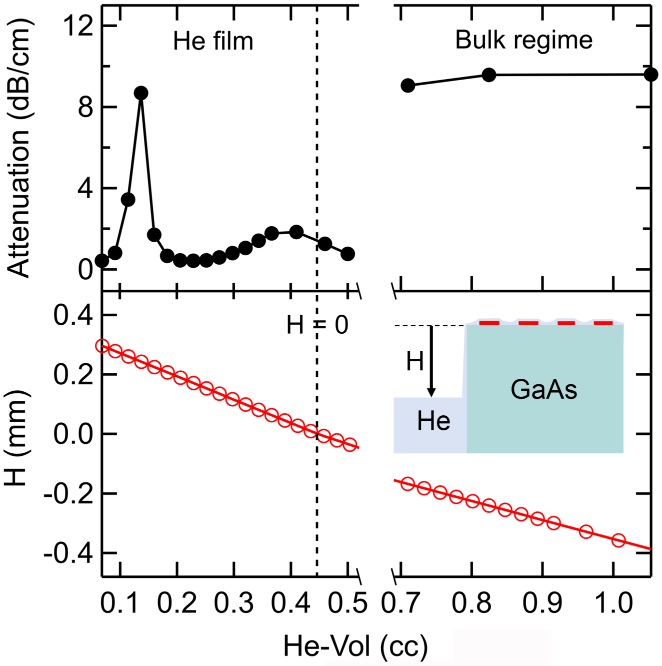

Figure 7.3: Attenuation of Rayleigh SAWs in contact with liquid helium. These measurements are done at T ≅ 1.55 K by incrementally providing small amounts of helium gas into the sample cell. The volume of the liquid helium in the cell was determined from the pressure in a standard volume of 260 cc at room temperature. The corresponding bulk helium level is estimated from 3D CAD modeling of the liquid helium filling the cell, which determines the distance between the GaAs substrate and the level of the helium reservoir, H. The SAW attenuation shown is the relative value with respect to empty cell. The vertical dashed line indicates when the reservoir helium level meets the substrate surface. Negative values of H represent a helium level that exceeds the piezoelectric surface (GaAs).

over the gate electrode (Fig 7.1 (c)). Thus, n_{e} here indicates the electron density in this region unless otherwise stated. Simultaneous measurement of the low-frequency transport as well as finite element method (FEM) simulation allows for the estimation of n_{e} at different value of V_{g} (see appendix A.3 for details). The contribution of the microchannel structure to the capacitance between the electron layer and the underlying electrodes is negligible and we assume that electrons are evenly distributed inside of and outside of the channels above the gate. Once n_{e} is estimated, we can calculate the helium film thicknesses d_{ch} and d_{van} above the gate electrode as a function of V_{g} using equations 7.9 and 7.10. This calculation produces $d_{\mathrm{ch}} \cong 1.18$ μm and $d_{\mathrm{van}} \cong 80$ nm for the neutral film, and a significant change in the charged film thickness at higher V_{g} due to the electron pressure (Fig. 7.4 (b) and (c)). The electron density n_{e} versus V_{g} in seen Fig. 7.4 (a) shows that for values of $V_{\mathrm{g}} < 35$ V no electrons exist above the gate since all of them are attracted to the regions above the source and drain electrode ($V_{\mathrm{s}} = V_{\mathrm{d}} = 60$ V) and n_{e} is a linearly increasing function of V_{g} when $V_{\mathrm{g}} \geq 35$ V.

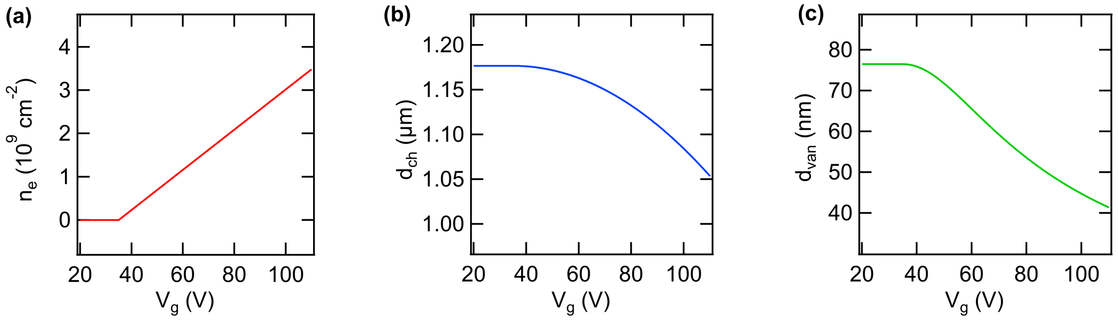

Figure 7.4: (a) Electron density n_{e} estimation in the 2D electron region above the gate electrode during a sweep of V_{g} at $V_{\mathrm{s}} = V_{\mathrm{d}} = 60$ V. Based on this n_{e} estimation, we have determined the thickness of the charged helium film in the channel (b) and the photoresist area (c) with $H \cong 207$ μm. Here d_{ch} and d_{van} denote the liquid helium thickness within the channels and on top of the photoresist while H is the distance between the GaAs surface and the level of helium in a reservoir adjacent to the substrate.

In the following discussion the SAW attenuation is measured relative to the case with no electrons. Experimental data of the attenuation (the blue closed circles in Fig. 7.5) reveals that the onset of SAW attenuation matches the value of V_g when electrons start moving to the region above the gate electrode. We can confirm that this signal arises from the electrons by repeating the experiment without electrons on the helium film as shown in the blue open circles of Fig. 7.5. In this case, the attenuation is zero for all values of V_g. In addition, we note that the calculation of d_{ch} and d_{van} in Fig. 7.4 (b) and (c) show that at $V_g \cong 40$ V there is a negligible change of both film thicknesses of less than ∼1 %, which suggests that the peak of the attenuation curve is not strongly affected by a film thickness change.

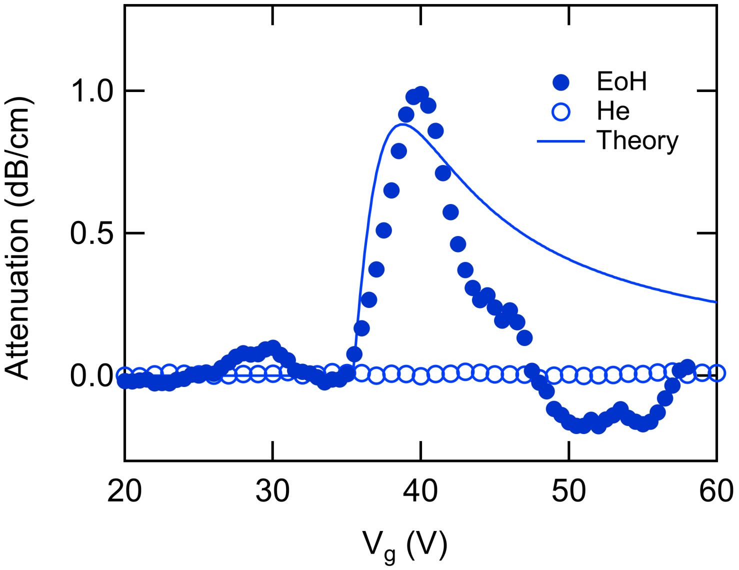

Figure 7.5: SAW attenuation during a gate voltage sweep. Blue closed circles show relative measurements of the attenuation during a V_g sweep at $V_s = V_d = 60$ V in which the electron density n_e is linearly proportional to V_g as seen in Fig. 7.4(a). The blue line shows the theoretically calculated average of the attenuation in the channel and photoresist regions. This theory only includes the piezoelectric coupling to electrons floating on helium film. After removing electrons, no noticeable change in SAW signal was observed (blue open circles). With $H \cong 207$ μm, the initial helium film thickness with no electrons in the microchannel array is estimated to be $d_{ch} \cong 1.18$ μm and $d_{van} \cong 80$ nm. In the presence of electrons, the V_g dependence of the film thickness is given in Fig. 7.4 (b) and (c).

We have also performed a quantitative analysis based on the well-developed theory discussed previously, which only considers the piezoelectric coupling between the SAW and

2DES and neglects the mechanical loading of the microchannel array and the helium film. The SAW attenuation versus V_g in the microchannel was calculated using equations 7.7 and 7.8 with $\epsilon_1 = \epsilon_\mathrm{He} = 1.057$, $\epsilon_\mathrm{p} = \epsilon_\mathrm{GaAs} = 13$, and $h_1 \cong d_\mathrm{ch}$. For the photoresist region, equations 7.7, 7.6, and 7.5 were used to calculate the attenuation with $\epsilon_1 = \epsilon_\mathrm{PR} = 4$, $\epsilon_2 = \epsilon_\mathrm{He} = 1.057$, $h_1 = d_\mathrm{PR} = 1.2$ μm, and $h_2 = d_\mathrm{van}$. Here d_ch and d_van are calculated values shown in Fig. 7.4 (b) and (c). For both cases, we have used the coupling constant $K^2/2 = 3.2 \times 10^{-4}$ for GaAs [115]. The calculation of n_e in Fig. 7.4 (a) was used to determine the plasma frequency ω_p at different V_g which is needed in equation 7.7. The relaxation time τ in equation 7.7 can be obtained from the electron mobility transverse to the channel μ_t. However, with the present sample, we were only able able to estimate the mobility μ_l in the direction along the channel under a homogeneous distribution of electrons over all these electrodes at $V_\mathrm{s} = V_\mathrm{g} = V_\mathrm{d}$ (see appendix A.3). Neglecting the small vertical holding field effect on μ_l with changing V_g in the helium vapor scattering at T $\cong$ 1.55K [10] (i.e. $\mu_l =$ constant) with the assumption of $\mu_\mathrm{t} < \mu_l$, we have obtained τ using $\tau = f\frac{\mu_l m_\mathrm{e}}{e}$ where $\mu_l = 1.4 \times 10^4$ cm^2/Vs and $f < 1$ is a scale factor. This value of τ was inserted into equation 7.7 to determine α in equation 7.5. With these parameters, we have calculated the SAW attenuation resulting from the electrons in both the channel and photoresist regions. The blue line in Fig. 7.5 shows their average with $f = 0.44$, which is in good correspondence with the experimental data for $V_\mathrm{g} < 40$ V where d_ch and d_van negligibly change with gate voltage. A deviation appears when the film thickness is strongly reduced for $V_\mathrm{g} > 40$ V (Fig. 7.4 (b) and (c)). This discrepancy could be associated with enhanced attenuation produced by a decrease of the film thickness. Despite this discrepancy when taken on balance the SAW attenuation peak we observe with increasing n_e is strong evidence for SAW energy loss to the 2DES via the piezoelectric coupling to the sheet of the 2D electrons above the helium film.

In order to systematically investigate the piezoelectric coupling strength with increasing distance d from the 2DES to the piezoelectric surface, we have measured the SAW attenuation versus $V_{\rm g}$ with increasing charged helium film thickness by incrementally adding liquid helium (left inset of Fig. 7.6). The maximum attenuation measured along with the theoretical prediction is shown in Fig. 7.6. The theoretical curve agrees fairly well with the experiments

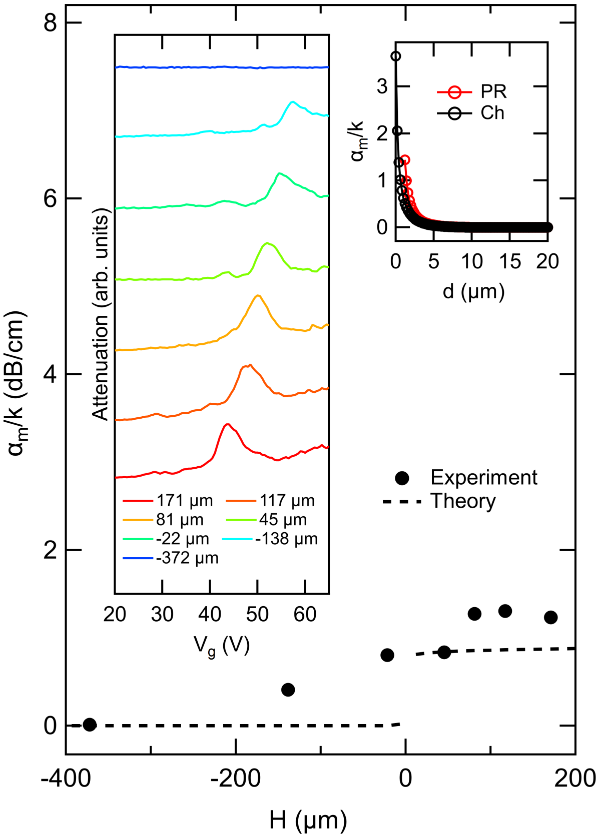

Figure 7.6: SAW attenuation versus helium level in the cell. Liquid helium was slowly and incrementally added to the charged helium film by supplying helium gas into the cell at T ≅ 1.55 K. This film thickening raised the 2D electron layer away from the piezoelectric surface (GaAs) and reduced the piezoelectric coupling. The black closed circles and dashed line show the measured values and the calculation of the maximum attenuation $\alpha_{\rm m}$ at different H. Here $H < 0$ means the helium level is higher than the GaAs surface. The left inset shows the measurements of the attenuation versus $V_{\rm g}$ at various H while the right inset shows the calculation of maximum attenuation $\alpha_{\rm m}$ as a function of the distance d from the 2DES to the piezoelectric surface. Note that d is equivalent to $|H|$ for bulk region ($H < 0$).

but shows some notable deviations. First, the experimental data of the maximum attenuation α_{m} is approximately 30 % larger than theoretical prediction in the thin film region where $H > 0$. This could be associated with a modification of piezoelecric coupling constant from the combined effects of mechanical contact of the photoresist as well as liquid helium with the GaAs substrate [119] and a rising background signal due to a helium film thickness decrease with increasing electron pressure. Second, when the film is transitioning to a bulk layer ($H \leq 0$), the measured values of α_{m} are larger than zero in contrast to the exponential decay predicted in the theory (upper right inset of Fig. 7.6), which arises from the evanescent waves-like nature of the SAW potential [111] in which α_{m} exponentially decays as a function of kd. A probable reason for this discrepancy can be slight inaccuracy in determining helium level from the 3D CAD simulation or a small tilt angle of the device relative to gravity, which could lead to a portion of the device is still in contact with the helium film.

To understand the positive shift of the attenuation peak position with increasing d, we have also theoretically estimated the characteristic electron density n_{m} at which the attenuation has a maximum value ($\alpha = \alpha_{\mathrm{m}}$) as a function of the electron mobility at different liquid helium levels in the cell (see appendix A.4). Fig. A.3 in appendix A reveals that the liquid level does not strongly affect n_{m} in either the thin film or bulk liquid helium regimes and only influences n_{m} in the transition region when $H \cong 0$ if the mobility is constant versus d. Thus, a liquid helium level change at constant mobility alone cannot explain the continuous shift of the peak we observe. However, if μ_{t} decreases with increasing helium level, our calculations predict that n_{m} increase with the rising level and thus a more positive V_{g} is required to reach n_{m} and could lead to the positive shift of V_{g} at $n_{\mathrm{e}} = n_{\mathrm{m}}$. This scenario seems unlikely since the mobility for electrons on bulk helium is much larger compared to electrons on a helium film due to the surface roughness of the underlying substrate [171]. A more reasonable explanation for our observation might be a small amount of heating of the sample or weaker holding field from the underlying trapping electrodes each time helium was added to the cell, resulting in a loss of some electrons from the microchannel arrays. In this case, a more positive V_g would be required to compensate the electron loss as the liquid level rises, which can give a rise to the positive shift of the attenuation peak position we observe.

7.1.4 Conclusion

Using a GaAs microchannel arrays device, we have measured the attenuation of Rayleigh SAWs as a function of the surface charge density in the system of electrons on helium for the first time. The electron density is controlled by varying a bias voltage on an underlying gate electrode and estimated from simultaneous low-frequency transport measurement. An increase of the attenuation is observed when electrons exist on the surface of the helium film and our experiments suggest only a minor effect of the film thickness on the attenuation peak. We have also performed numerical comparison of the measured attenuation induced by the 2DES using Wilen's method, which is in reasonable agreement with our experiments. Thus, the appearance of the SAW attenuation peak during the gate voltage weep is attributable to the piezoelectric coupling to electrons floating on helium film.

The attenuation measurements with increasing charged film thickness show the gradual decrease and then disappearance of the SAW attenuation as the distance d from 2DES to piezoelectric surface increases. This behavior, which is qualitatively correct, does not match the fast exponential decay expected from our calculation. This disagreement could be due to either slight inaccuracy in the helium level estimation or a small tilt of the device, or a combination of both. Regardless, the measurements described in this section represent the first successful measurements of the attenuation of a SAW by electrons on helium and open the door to using the wavevector and frequency dependent attenuation $\alpha(k, \omega)$ as a probe of the physics of this non-degenerate 2DES.

7.2 Acoustoelectric Transport in Electrons on Helium

7.2.1 Experiment

We have also developed a device for measuring acoustoelectric transport of electrons on helium, which was measured inside a superfluid leak-tight copper cell, where a sheet of electrons produced from a tungsten filament were floating on top of a ∼70 nm thick liquid helium film (see appendix B.1 for the description of the helium film thickness determination). The same YZ cut lithium niobate ($LiNbO_3$) single crystalline chip used for the SAW measurements of liquid helium described in chapter 6 was utilized as the substrate for the experiments described in this chapter as illustrated in Fig. 7.7 (a) and (b). The SAWs in this device were designed with a fundamental frequency $\nu = \lambda/v = 291$ MHz, a wavelength $\lambda = 12\,\mu$m, and a speed of the sound $v = 3488$ m/s. The measured value of the SAW resonance frequency was $\nu = 296$ MHz (see Fig. 7.7 (c)). The slight difference compared to the expected value ($\nu = 291$ MHz) is attributable to contraction of the substrate at cryogenic temperatures. With this experimental setup, the acoustoelectric (ae) transport of electrons on helium was measured via capacitive coupling between electrons floating on the helium surface and a detection electrode beneath the lithium niobate at T ≅ 1.55 K (see Fig. 7.7 (b)). For frequency domain analysis of ae transport, an amplitude modulated continuous wave signal was applied to the exciter IDT using an Agilent 8648B RF signal generator and the generated ae-current was measured using standard lock-in technique. In order to study the time response of the ae-current, time-resolved measurements employing SAW pulses at 296 MHz were carried out using the same RF signal generator. The real-time ae current data was collected via a SR570 low noise current preamplifier using a Tektronix DPO7054 digital oscilloscope with waveform averaging over 10,000 samples to improve signal to noise ratio. Also, an Agilent N5230A vector network analyzer was used to measure the SAW resonance frequency and to estimate SAW intensity.

7.2.2 Results and Discussion

7.2.2.1 Frequency Response of the Acoustoelectric Current

The CW acoustoelectric response is shown in Fig. 7.7 (d) and coincides with the independently measured SAW resonance at 296 MHz. This acoustoelectric current I_{ae} is equivalent to the flux per unit time of electrons passing through the region above the underlying detection electrodes. No acoustoelectric current is observed without electrons present on the superfluid film (dashed blue trace in Fig. 7.7 (d)) confirming that the signal arises from the electron layer floating on the helium surface. Moreover, we find that I_{ae} vanishes when the electrons are moved far away from the surface of the piezo-substrate by increasing the thickness of the superfluid layer (solid red trace in Fig. 7.7 (d)) as would be expected given the evanescent character of the SAW potential above the piezoelectric surface. The acoustoelectric current signal shown in Fig. 7.7 (d) exhibits a periodic superimposed oscillation on top of the the main resonance. This corrugation in the acoustoelectric current is attributable to reflections of the SAW from the edge of the substrate, as is evident from the Fourier transform of the signal into the time domain (inset Fig. 7.7 (d)). Together these experiments confirm that the acoustoelectric current is generated by the transport of electrons on the superfluid surface via the SAW electric field extending up from the underlying substrate.

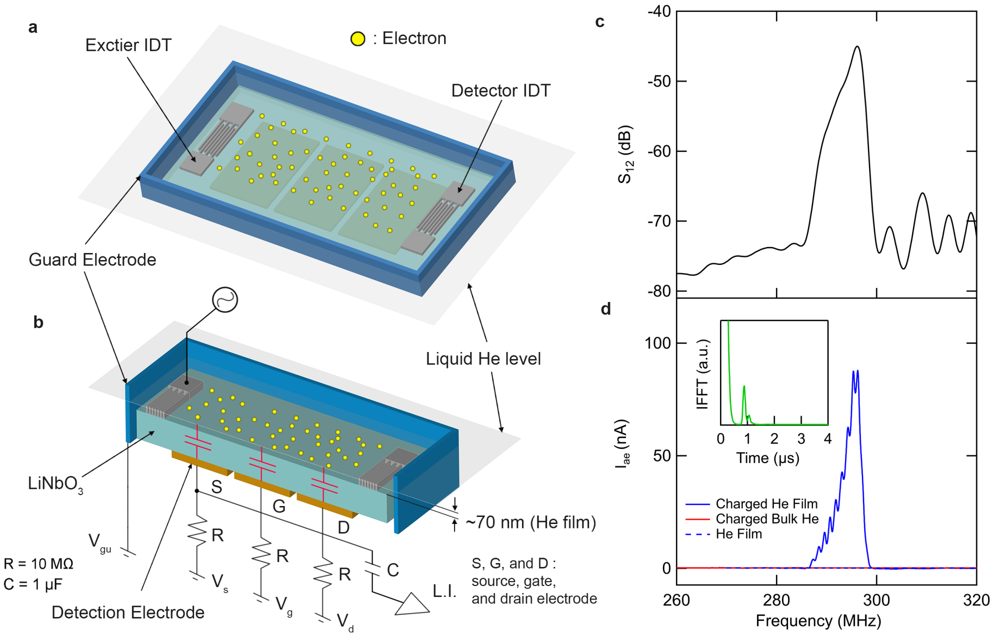

Figure 7.7: Schematic of the experimental setup and demonstration of acoustoelectric transport of electrons on helium. (a) Top and (b) cross-section views of the device for measuring SAW-driven transport of electrons on helium. Two opposing interdigitated transducers (IDTs) are used to excite and receive SAWs. A saturated superfluid ^{4}He film is formed on the surface of the LiNbO$_3$ piezo-substrate at T = 1.55 K. Thermionically emitted electrons are trapped above the surface of the superfluid film by applying a positive bias voltages to three underlying electrodes arranged in a field-effect transistor (FET) configuration with a source (s), gate (g) and drain (d) [16]. Lateral confinement of the electron layer is achieved with a negative bias to guard electrode positioned on the outside of the LiNbO$_3$ substrate. (c) Frequency dependence of the transmission coefficient (S_{12}) of the SAW device demonstrating an expected resonance at 296 MHz. (d) Measured acoustoelectric current $I_{\rm ae}$ of electrons on helium driven by a piezo-SAW as a function of frequency. For these measurements the FET electrode voltages were $V_{\rm s} = V_{\rm g} = V_{\rm d} = 40$ V, corresponding to an electron density of $n \cong 0.8 \times 10^9$ cm^{-2}, and the guard was biased with -3.2 V. Inset: Inverse Fourier transform of the acoustoelectric current signal which reveals a peak at $t \approx 0.9$ μs. This time scale corresponds to a SAW propagation distance of 3.2 mm, roughly the same as twice the distance between the launching IDT center and the near-edge of the LiNbO$_3$ substrate, which implicates SAW reflections as responsible for the superimposed oscillations present on the acoustoelectric current peak.

7.2.2.2 SAW Power and Gate Bias Dependence

A characteristic feature of acoustoelectric transport in 2DESs is a linear dependence of the measured signal, in this case I_{ae}, on the SAW intensity and hence excitation power (see equation 3.59 in chapter 3). Fig. 7.8 (a) and (b) show the SAW power dependence of I_{ae} for electrons on helium supported by a $\mathrm{LiNbO_3}$ and a GaAs piezoelectric substrate, respectively. At the SAW resonance I_{ae} increases linearly with the RF input power consistent with this expected linear response (i.e. see inset Fig. 7.8 (a) and (b)), which serves to further confirm the acoustoelectric origin of the measured signal from the system of electrons on helium. The measured value of I_{ae} with the GaAs substrate is two orders of magnitude smaller than that with the $\mathrm{LiNbO_3}$ substrate. This significant difference of I_{ae} is mainly due to the much smaller piezoelectric coupling constant of GaAs, $K^2/2 = 3.2 \times 10^{-4}$, compared to $\mathrm{LiNbO_3}$, $K^2/2 = 4.82 \times 10^{-2}$, (i.e. see equations 3.31 and 3.59 in chapter 3).

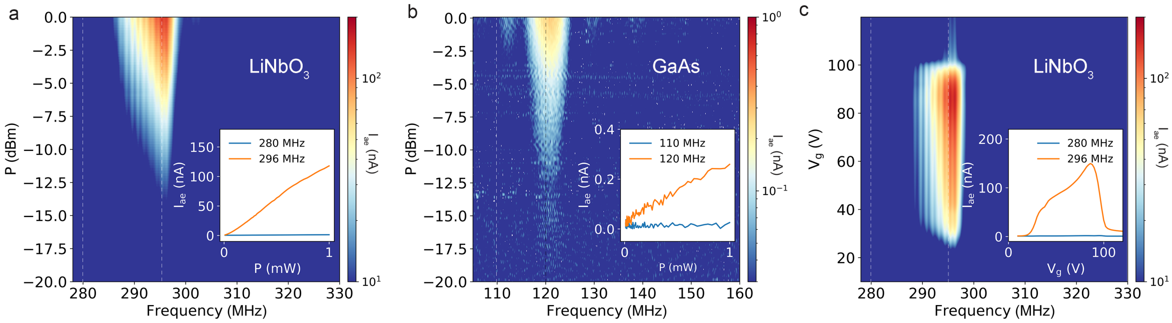

Figure 7.8: Power dependence and gate-tunability of the acoustoelectric effect with electrons on helium. Acoustoelectric current I_{ae} measured as a function of the SAW driving frequency and power for electrons floating on a helium thin film on a (a) $\mathrm{LiNbO_3}$ and a (b) GaAs piezo-substrate. Each inset shows that I_{ae} is linear in the driving power when the frequency corresponds to the SAW resonance. (c) Demonstration of an acoustoelectric field effect transducer (aFET) with electrons on helium on the $\mathrm{LiNbO_3}$ substrate. The inset shows line-cuts of I_{ae} both on- and off-resonance with the SAW. The gate voltage (V_{g}) sweep is performed at fixed source and drain voltages ($V_{\mathrm{s}} = V_{\mathrm{d}} = 40$ V).

Field effect control is crucial for the development of acoustoelectric device for precise electron control using SAWs. In Fig. 7.8 (b) we show a novel form of gate controlled SAW-driven electron transport. By tuning the gate bias voltage V_{g} we can turn I_{ae} ON and OFF, in effect creating an *acoustoelectric field effect transistor* (aFET). When V_{g} is different from the source voltage V_{s}, electrons dragged by the travelling SAW encounter an effective potential energy barrier $U_{\mathrm{eff}} = -e(V_{\mathrm{g}} - V_{\mathrm{s}})$ in the region above the gate. As shown in the orange trace of the Fig. 7.8 (b) inset, for sufficiently small values of V_{g}, acoustoelectric charge transport is blocked by a large positive U_{eff}, which results in zero current. Upon increasing V_{g}, electrons transported by the SAW are allowed to enter the region above the gate due to a decrease in U_{eff}, which leads to an increase in I_{ae} at a threshold value of V_{g} determined by the overall areal electron density. Further increasing V_{g} eventually leads to a suppression of I_{ae} once the region above the source has been depleted of electrons (see Fig. 7.8 (b) inset).

7.2.2.3 Pulsed measurements of Acoustoelectric Current from Electrons on Helium

An important step for future SAW-based metrological or quantum information experiments with electrons on helium is the ability to precisely control the number of SAW-transported electrons. This can be accomplished by gating the SAW in time, i.e. by performing pulsed acoustoelectric measurements, which we show in Fig. 7.9. In these pulsed measurements the SAW IDT is excited on resonance for a fixed period of time, t_{p}, which launches a surface acoustic wave packet having a duration in time equal to t_{p}. The envelope of the SAW-packet contains the high-frequency acoustoelectric field, which picks up electrons and carries them in the propagation direction of the SAW-pulse (see subsection 7.2.1). For an areal electron

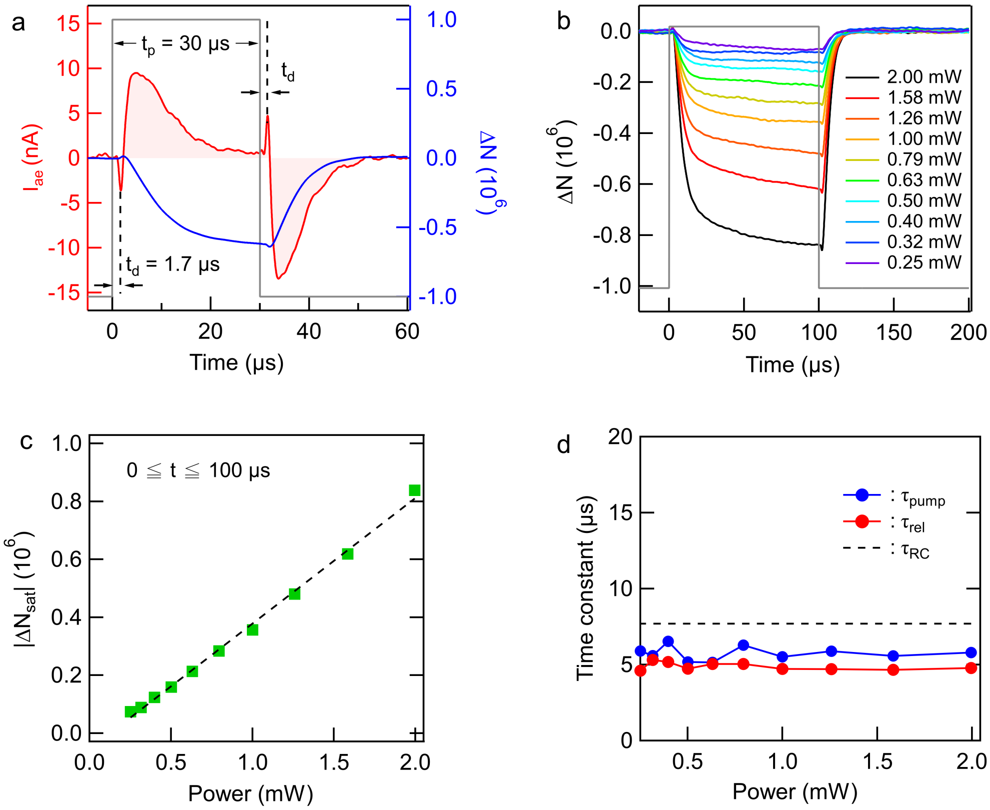

Figure 7.9: Pulsed acoustoelectric measurements of electrons on helium. (a) Time of flight measurement of I_{ae} (red curve) using a gated pulse (gray line) of SAWs at a fixed RF power (0 dBm) and at the SAW resonance frequency (296 MHz). In these measurements the number of electrons above the detection electrode is $N \cong 0.4 \times 10^9$. The blue trace is the calculated change in the equilibrium number of electrons ΔN, which is obtained from the time integral of I_{ae} (red trace). (b) ΔN and (c) $|\Delta N_{\text{sat}}|$ for a steady state SAW pulse at various values of the driving RF power. In these measurements the equilibrium number of electrons is $N \cong 0.8 \times 10^9$. (d) Dynamical response of two-dimensional electrons on helium to SAWs pulses at different RF power with $N \cong 0.8 \times 10^9$. The time constants τ_{pump} (τ_{rel}) are those associated with the rising (falling) edge of the SAWs pulse and are determined from fitting $I_{\text{ae}}(t)$. The time constant τ_{RC} (dashed line) is that determined from from low frequency transport of electrons on helium.

density n the continuity equation for the acoustoelectric current density j_{ae},

$$\partial n/\partial t + \nabla \cdot j_{\mathrm{ae}} = 0 \tag{7.11}$$

predicts that an acoustoelectric current should appear once SAW-driven electrons flow past the boundary between the detecting electrodes. This behavior is shown in Fig. 7.9 (a) for the case where $t_{\mathrm{p}} = 30$ μs, where I_{ae} starts sharply increasing at a time $t_{\mathrm{d}} \cong 1.7$ μs after the SAW is launched. This delay in the onset of I_{ae} corresponds to the arrival time of the leading-edge of the SAW pulse at the boundary above the detection electrode. The pulse continues to drive electrons across the boundary, progressively building up an increasing charge imbalance in the electron layer. This charge imbalance produces an electric field that opposes the SAW-induced electron flow and leads to a decrease in Iae as shown in Fig. 7.9 (a) (red trace). Once the trailing edge of the SAW pulse transits past the edge of the detection electrode (i.e. once $t = t_{\mathrm{p}} + t_{\mathrm{d}}$) a current reappears but having the opposite polarity. In contrast to other 2DESs, these features are unique to electrons on helium and arise from the fact that this 2DES has a fixed total number of electrons. The SAW pulse dynamical redistributes the electrons above the surface of the superfluid creating a non-equilibrium density, which then relaxes back to equilibrium after the passage of the SAW pulse.

We can quantitatively analyze this SAW-induced charge imbalance by calculating the time integral of I_{ae} to extract the change in the number of electrons $|\Delta N|$ above the detection electrode (blue trace Fig. 7.9 (a)), which reaches a saturated steady state value, $|\Delta N_{\mathrm{sat}}|$, in the limit of long SAW pulses. Increasing the SAW power can be used to tune the magnitude of $|\Delta N_{\mathrm{sat}}|$ as shown in Fig. 7.9 (b), and in the regime of linear response this power dependence allows us to estimate the minimum number of transported electrons that can be detected per SAW pulse (see Fig. 7.9 (c)). For these measurements where $t_{\mathrm{p}} = 100$ μs we find that for the lowest power as little as $|\Delta N/N| \leq 0.01$ % of the number of electrons $N \cong 0.8 \times 10^{9}$ can be transported by each SAW pulse (i.e. see appendix B.2). These initial acoustoelectric transport proof-of-concept experiments are promising and we anticipate that optimization of device geometry to include a combination of microchannel lateral confinement [138] and single electron transistor charge detection [172] is a fruitful path forward for future single electron acoustoelectric measurements.

Finally, pulsed SAW measurements allow us to extract information about the dynamical response of the many-electron system on helium by analyzing the build-up and relaxation of the SAW-induced charge pumping. Specifically, we fit the rising and falling edges of the pulsed acoustoelectric signal to an exponential and extract time constants τ_{pump} and τ_{rel}, which are shown in Fig. 7.9 (d). In both cases, the time constants do not depend on the SAW power and we find $\tau_{\mathrm{pump}} = 5.7 \pm 0.1$ μs and $\tau_{\mathrm{rel}} = 4.9 \pm 0.1$ μs (i.e. see appendix B.3). These time constants are ultimately determined by the underlying mechanisms that lead to electron scattering in the system. In the case of the present experiments, which were performed at T $\cong$ 1.55 K, a strong scattering mechanism is the collision of electrons with helium vapor atoms above the superfluid surface. These scattering events occur at a frequency (∼300 GHz, i.e. see appendix B.2) much larger than that of the SAW electric field (296 MHz). Therefore the time constants extracted from the SAW measurements should be similar in magnitude to the RC time constant determined from conventional transport measurements, which we shown in Fig. 7.9 (d). We find that $\tau_{\mathrm{RC}} = 7.7$ μs (i.e. see appendix B.2), which is in reasonable agreement with our SAW measurements. In addition to demonstrating controlled charge pumping, these measurements show that SAWs are a versatile new tool for interrogating the dynamical processes in electrons on helium including, when extended to lower temperature, investigations of plasmon modes and ripplo-polaronic excitations of the Wigner solid [173].

7.2.3 Conclusion

Here we have reported on the coupling of electrons on helium to an evanescent piezoelectric SAW. The electrons surf with the piezoelectric wave and we demonstrate high-frequency charge pumping in this system for the first time. With this piezoacoustic method we can precisely transport as little as ~0.01 % of the total number of electrons, opening the door to quantized charge pumping, the possibility of electrical metrology, and ultimately single electron state transfer with electrons on helium. We also show that SAWs are a route to directly investigating the high-frequency dynamical response, and relaxational processes, of collective excitations of the electronic liquid and solid phases of electrons on helium.

Chapter 8

Conclusions and Future Directions

By employing the surface acoustic waves technique used to study semiconduct-based 2D electron systems, we have explored electrons floating on the surface of liquid helium. For the first time ever, we have measured SAW attenuation and acoustoelectric charge transport in this system. These results represent a first demonstration of the coupling of SAWs to surface electrons on liquid helium and pave the way for a number of exciting new experimental possibilities. In this chapter, we briefly discuss a few particularly exciting future directions.

2D Phase Transition

One interesting feature of the electron crystal (Wigner solid, WS) in the electron on helium system is the strongly nonlinear conductivity. Each electron emits helium surface capillary waves (ripplons) when their velocity exceeds the ripplon phase velocity, a process analogous to the emission of Cherenkov radiation. Moreover, the ripplons radiated from each electron can interfere constructively if the ripplon wave number is equal to the reciprocal lattice vector of the WS. This resonant Bragg-Cherenkov emission of ripplons leads to a limitation on the maximum electron velocity [174]. As a result, a sharp decrease of the nonlinear conductivity takes place during the phase transition from the electron liquid to the WS [175]. The high level of sensitivity of SAWs in detecting conductivity changes of a 2DES could possibly provide a novel method to examine this phase transition in electrons on helium. Furthermore, the SAW technique is also sensitive to the presence of inhomogenity of the 2D electron system when the average conductivity is very low [35]. This aspect might possibly allow for exploring inhomogeneous spatial characteristics in the vicinity of the 2D melting point, such as the existence of a hexatic phase [75].

Commensurate Incommensurate Transitions

The mobility of 2D electrons on helium in the presence of a 1D periodic potential submerged below the helium surface has very recently been studied using molecular dynamics simulations [176]. Interestingly, for the maximum commensurability case in the electron liquid phase, where the periodicity of the 1D potential is equal to the interelectron distance of the WS, even a very weak potential strongly affects the mobility, leading to a Wigner solid transition at lower temperature. In particular, the typical electron-electron distance a_e for electrons on helium is $\sim 1\,\mu$m and thus a 1D potential with a period $\sim 1\,\mu$m can be easily implemented with conventional lithographic patterning technology for future experiments of commensurability effects. Also, the ability to precisely control the electron density allows for the ability to change a_e to experimentally study a incommensurate state as well. Furthermore, a standing wave field [177] established from the interference of two counter-propagating SAWs could be utilized to investigate not only the effect of spatial but also temporal periodic potentials on the transport properties of electrons on helium.

SAW-driven Quantized Charge Pumping

A SAW can transport a well-defined small number of electrons along its propagation direction. In semiconductors, this has been extended down to a single electron transport through a gate-defined quasi-1D channel [105]. These types of experiments attracted interest for the exploration of SAW-driven flying qubits [106] as well as quantum acoustodynamics experiments with single electrons [109]. In particular, when 2D electrons are transported through the quasi-1D channel by SAWs, the plateau in this SAW-driven current ($I = Nef$) as a function of the voltage applied to the side gates on each side of the channel reveals an integer number N of electrons trapped in each SAW minima. Here e and f represent the elementary charge and the frequency of the SAW. This feature has been proposed to be utilized to develop metrological standards of electrical current [38]. Although considerable progress in these quantum metrology applications has been made using semiconductor 2D electron systems such as those in AlGaAs/GaAs heterostructures, issues arising from impurities and disorder in these systems still remain and have limited performance [163, 164, 165]. A SAW-driven single electron device with electrons on helium could be a possible alternative path due to the ultra-clean environment provided by the superfluid. In addition to that, tunable electron confinement in a microchannel device filled with liquid helium [178] allows for the realization of well-controlled quasi-1D channels.

APPENDICES

Appendix A

Studies of Electrons on Helium Using a GaAs SAW Device

A.1 Perturbation Formula for SAW Attenuation

Since the GaAs substrate used in the experiments described in chapter 7 has a weak piezoelectricity, the attenuation produced by a 2DES can be estimated using the Ingebrigtsen formula [169] as follows,

$$\frac{\alpha}{k} = \left(\frac{K^2}{2}\right) \mathrm{Im}\left(\frac{1 + iz^{'}(0)}{1 - i\epsilon_{\mathrm{p}} z^{'}(0)}\right), \tag{A.1}$$

where

$$z^{'}(0) = -ik\left(\frac{\phi^{'}}{D^{'}_{\mathrm{z}}}\right)\bigg|_{z=0}, \quad \epsilon_{\mathrm{p}} = \sqrt{\epsilon_{zz}\epsilon_{xx} - \epsilon^2_{zx}}. \tag{A.2}$$

Here, Rayleigh SAWs propagate along the x-axis and the positive z-axis points out of piezoelectric plane located at $z = 0$. The effective dielectric constant ϵ_{p} for the piezo-substrate is determined from the dielectric tensor element ϵ_{ij}. In equation A.1 α, k, and $\frac{K^2}{2}$ denote the attenuation constant, the wave number, and the piezoelectric coupling constant. In our GaAs microchannel array device, the 2DES is located above a helium contained microchannel or on the photoresist regions covered with a thin helium film between microchannels. These two different regions are represented by one model geometry as seen in Fig. 7.2. For the former region both dielectric 1 and 2 are liquid helium while dielectric 1 and 2 are a photoresist and a helium thin film for the latter region. We derive the SAW attenuation formula applicable for both regions using this model geometry. Poisson's equation gives the electric potential inside dielectric 1 and 2 and in vacuum as seen in Fig. 7.2, which is given by

$$\begin{aligned}\phi_1 &= e^{ikx-i\omega t}\left(Ae^{-kz}+Be^{kz}\right),\\ \phi_2 &= e^{ikx-i\omega t}\left(Ce^{-kz}+De^{kz}\right),\\ \phi_3 &= e^{ikx-i\omega t}\left(Ee^{-kz}\right)-4\pi\sigma_0 z,\end{aligned} \tag{A.3}$$

where σ_0 and $\omega = 2\pi f$ are the equilibrium charge density of the 2DES and the angular frequency of the SAW. The electric potential and normal component of the displacement field must be continuous at $z = h_1$. Thus, $\phi_1(h_1) = \phi_2(h_1)$ and $\epsilon_1 \frac{\partial\phi_1}{\partial z}\Big|_{z=h_1} = \epsilon_2 \frac{\partial\phi_2}{\partial z}\Big|_{z=h1}$ yield

$$\begin{aligned}A &= \frac{\epsilon_1+\epsilon_2}{2\epsilon_1}C + \frac{\epsilon_1-\epsilon_2}{2\epsilon_1}e^{2kh_1}D,\\ B &= \frac{\epsilon_1-\epsilon_2}{2\epsilon_1}e^{-2kh_1}C + \frac{\epsilon_1+\epsilon_2}{2\epsilon_1}D.\end{aligned} \tag{A.4}$$

Here the interface between two dielectric films (ε_1, ε_2) above the piezoelectric substrate is located at $z = h_1$. The ability of the SAW potential to trap and drag charges at the speed of sound (i.e. acoustoelectric transport) leads to a small fluctuation of the charge density $\delta\sigma$ at $z = h_1 + h_2$, which satisfies the relation

$$-\frac{\partial\phi_3}{\partial z}\Big|_{z=h_1+h_2} + \epsilon_2\frac{\partial\phi_2}{\partial z}\Big|_{z=h_1+h_2} = 4\pi\left(\sigma_0+\delta\sigma\right). \tag{A.5}$$

$$\delta\sigma = \frac{k}{4\pi} e^{ikx-i\omega t} [\, e^{-k(h_1+h_2)} E - \epsilon_2 e^{-k(h_1+h_2)} C + \epsilon_2 e^{k(h_1+h_2)} D] \tag{A.6}$$

Momentum transfer between the SAW and the charges in the 2DES causes a small momentum fluctuation $\delta P = m_{\mathrm{e}} \delta v$ of the electron in the 2D sheet. The corresponding velocity fluctuation δv can be obtained from the acoustoelectric equation of motion using the relaxation time approximation

$$\frac{d}{dt}(\delta P) = \left(e\frac{\partial \phi}{\partial x} - \frac{\delta P}{\tau} \right) \Big|_{z=h_1+h_2}. \tag{A.7}$$

Taking $\frac{d}{dt} \to -i\omega$ and $\phi \to \phi_3$ gives,

$$\delta v = ike^{ikx-i\omega t} \left(Ee^{-kz} \right) \frac{e\tau}{m_{\mathrm{e}}} \frac{1}{1-i\omega\tau} \Big|_{z=h_1+h_2}, \tag{A.8}$$

where τ and m_{e} represent the momentum relaxation time and the electron mass. The following continuity equation must hold at $z = h_1 + h_2$

$$\frac{\partial \delta\sigma}{\partial t} + \frac{\partial}{\partial x}(\sigma_0 \delta v) = -i\omega\delta\sigma + ik\delta v\sigma_0 = 0. \tag{A.9}$$

Substituting for $\delta\sigma$ and δv from equations A.4 and A.8 leads to

$$i\omega[\, Ee^{-k(h_1+h_2)} - \epsilon_2 Ce^{-k(h_1+h_2)} + \epsilon_2 De^{k(h_1+h_2)}] = \frac{\omega_{\mathrm{p}}^2 \tau}{1-i\omega\tau} Ee^{-k(h_1+h_2)}, \tag{A.10}$$

where $\omega_{\mathrm{p}}^2 = 4\pi \frac{|\sigma_0| ek}{m_{\mathrm{e}}}$ is the 2D plasma frequency. The electric potential must be continuous at $z = h_1 + h_2$ as well

$$Ce^{-k(h_1+h_2)} + De^{k(h_1+h_2)} = Ee^{-k(h_1+h_2)}. \tag{A.11}$$

Solving equations A.10 and A.11 determines the amplitude ratio of ϕ_2 as follows

$$\frac{C}{D} = r_{\mathrm{C}}, \tag{A.12}$$

with

$$r_{\mathrm{C}} = \frac{[\,(\epsilon_2+1)\omega^2 - \omega_{\mathrm{p}}^2]\,\tau + (\epsilon_2+1)i\omega}{[\,(\epsilon_2-1)\omega^2 + \omega_{\mathrm{p}}^2]\,\tau + (\epsilon_2-1)i\omega} e^{2k(h_1+h_2)}. \tag{A.13}$$

Similarly, from equations A.4 and A.12, the amplitude of ϕ_1 can be expressed in terms of the amplitude ratio r_{c} in region 2:

$$A = r_{\mathrm{A}}D, \quad B = r_{\mathrm{B}}D, \tag{A.14}$$

where

$$r_{\mathrm{A}} = \left(\frac{\epsilon_1+\epsilon_2}{2\epsilon_1} r_{\mathrm{C}} + \frac{\epsilon_1-\epsilon_2}{2\epsilon_1} e^{2kh_1}\right), \quad r_{\mathrm{B}} = \left(\frac{\epsilon_1-\epsilon_2}{2\epsilon_1} e^{-2kh_1} r_{\mathrm{C}} + \frac{\epsilon_1+\epsilon_2}{2\epsilon_1}\right). \tag{A.15}$$

Inserting $\phi^{'}(0) = \phi_1(0) = De^{ikx-i\omega t}\,(r_{\mathrm{A}}+r_{\mathrm{B}})$ and $D_{\mathrm{z}}^{'}(0) = -\left.\frac{\partial\phi_1}{\partial z}\right|_{z=0} = D\epsilon_1 e^{ikx-i\omega t}\,(kr_{\mathrm{A}} - kr_{\mathrm{B}})$ into equation A.2 gives the normalized surface impedance

$$z^{'}(0) = -ik\left.\left(\frac{\phi^{'}}{D_{\mathrm{z}}^{'}}\right)\right|_{z=0} = i\epsilon_1^{-1}\frac{r_{\mathrm{A}}+r_{\mathrm{B}}}{r_{\mathrm{A}}-r_{\mathrm{B}}}. \tag{A.16}$$

This yields the formula for finding the SAW attenuation arising from the 2DES above two dielectric films:

$$\frac{\alpha}{k} = \left(\frac{K^2}{2}\right)\mathrm{Im}\left(\frac{r_{\mathrm{A}}-r_{\mathrm{B}}-\epsilon_1^{-1}(r_{\mathrm{A}}+r_{\mathrm{B}})}{r_{\mathrm{A}}-r_{\mathrm{B}}+\epsilon_{\mathrm{p}}/\epsilon_1(r_{\mathrm{A}}+r_{\mathrm{B}})}\right). \tag{A.17}$$

Note that the minus-sign is dropped on the right-hand side of equation A.16 due to using a different coordinate system in which the z-axis points out of the piezoelectric surface whereas it points in the opposite direction in the Ingebrigtsen formula (equations A.1 and A.2).

A.2 Helium Level Estimation

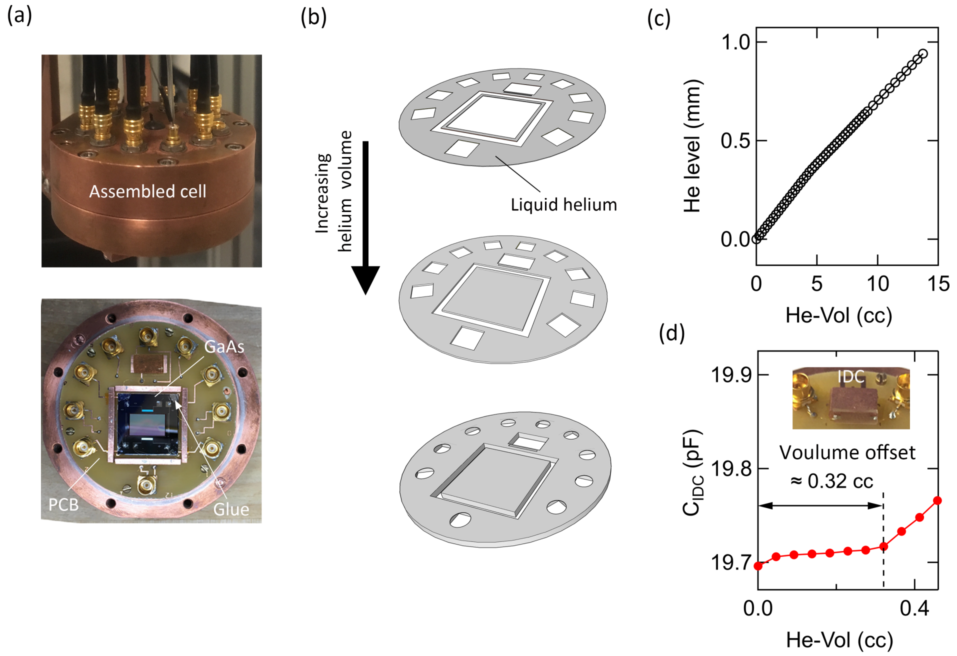

Figure A.1: The experimental sample cell and helium level estimation. (a) Pictures of the copper cell used in our experiments. The cell contains a GaAs device (shiny black) located inside the guard electrode on the printed circuit board (PCB). Beneath this substrate, three rectangular electrodes are patterned on the PCB, which are not shown in the picture. (b),(c) He level estimation as a function of the liquid helium volume using 3D CAD simulation. The gray volume represents the liquid helium in the cell. (d) Level sensor capacitance change while condensing liquid helium into the sample cell. This was measured using the interdigitated capacitor (IDC) sensor as shown in the inset of the plot. A linear increase of the capacitance starts happening when the liquid volume ≅ 0.32 cc, which indicates that the liquid helium reaches the bottom of the IDC..

To form liquid helium inside the cell at $T \cong 1.55$ K (Fig. A.1 (a)), helium gas was provided from a standard volume of 260 cc at room temperature. The volume of liquid helium admitted into the cell was determined by the pressure in the standard volume and corresponding helium level was estimated using the 3D CAD simulation as seen in Fig. A.1 (b)(c). We have consistently observed that liquid helium starts collecting in the cell after injecting a considerable amount of helium gas into the cryostat through the fill line. This amount of helium corresponds to approximately 0.32 cc of liquid (Fig. A.1 (d)). This dead volume is likely associated with liquid in the fill line. In fact, the volume of the fill line below the 4k-stage is approximately 0.4 cc. Therefore, the helium volume determination from the pressure was calibrated with this dead volume taken into account.

A.3 Electron Density and Mobility Estimation

For the low-frequency transport measurements described in this thesis, the capacitive redistribution of electrons during a V_{g} sweep at fixed $V_{\mathrm{s}} = V_{\mathrm{d}}$ can be used to estimate the electron density n_{e} versus V_{g} using the relation

$$n_{\mathrm{e}} = \frac{2}{3} c (V_{\mathrm{g}} - V_{\mathrm{th}}) e^{-1}, \tag{A.18}$$

where c is the capacitance per unit area between the electron layer and the underlying electrodes and V_{th} is the threshold voltage in the low-frequency IV curve (Fig. A.2 (b)). This capacitance c in the channel and in the photoresist regions can be determined from geometry:

$$c_{\mathrm{ch}} = c_{\mathrm{PR}} \cong \frac{\epsilon_0}{d_{\mathrm{g}}/\epsilon_{\mathrm{He}} + d_{\mathrm{GaAs}}/\epsilon_{\mathrm{p}}}. \tag{A.19}$$

Here $d_{\mathrm{g}} \cong 50$ μm denotes the gap between the transport electrodes and the GaAs substrate resulting from the rubber cement glue used to mount the GaAs chip to the PCB

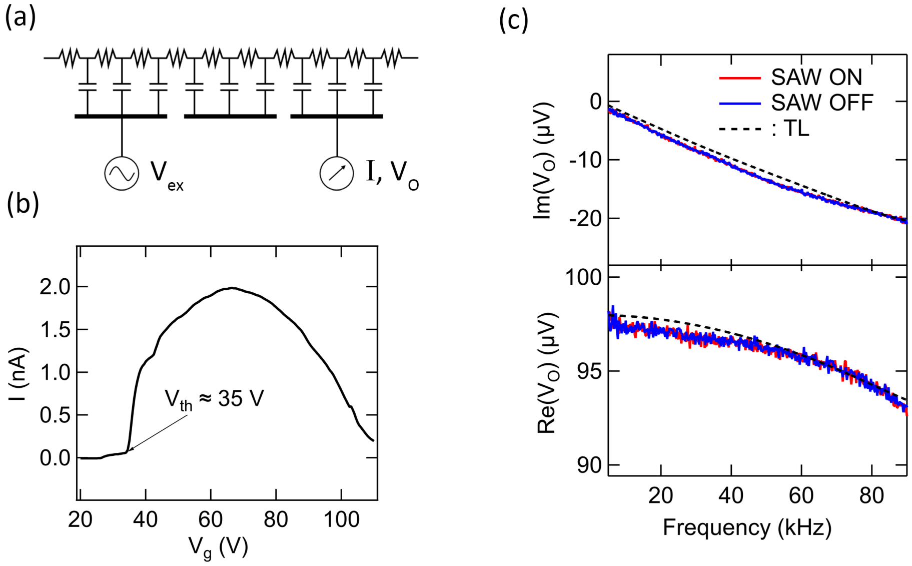

Figure A.2: (a) Transmission line (TL) circuit modeling of electrons on helium (b) Current of electrons on a helium film as a function of V_g inthe low-frequency regime. The current was induced by applying a 0.1 mV, 60 kHz excitation V_{ex} and detected using standard lock-in techniques. The source and drain voltage were fixed at 60V. (c) Output voltage V_o as a function of the frequency of V_{ex}. The output voltage V_o corresponds to the voltage drop at the internal impedance of the signal detector (Lock-in amplifier) due to current flow in 2D electrons floating helium film. The blue and red solid traces represent experimental values with and without SAW excitation while the dashed trace is the theoretical curve. The frequency response is independent of SAW excitation, which implies that the low frequency transport is not affected by the SAW. For these measurement, all three electrodes were biased with 60 V.

board (Fig. A.2 (a)) and $d_{\mathrm{GaAs}} = 350\ \mu$m represents the thickness of the GaAs substrate. It should be noted that the helium film and the photoresist on the GaAs negligibly affect c since $d_{\mathrm{ch}}/\epsilon_{\mathrm{He}}$, $d_{\mathrm{van}}/\epsilon_{\mathrm{He}}$, $d_{\mathrm{PR}}/\epsilon_{\mathrm{PR}} << d_{\mathrm{g}}/\epsilon_{\mathrm{He}}$, $d_{\mathrm{GaAs}}/\epsilon_{\mathrm{p}}$. Thus, it is assumed that the channel and photoresist regions have the same electron density. With $V_{\mathrm{th}} \cong 35$ V and $c_{\mathrm{ch}} = c_{\mathrm{PR}} \cong 1.14 \times 10^{-7}$ F/m^2, n_{e} versus V_{g} in Fig. 7.4 (a) in section 7.1 was calculated using equation A.18, which is in good agreement with finite element method (FEM) simulations.

Using the transmission line circuit analysis [129, 130], we have estimated the mobility μ_l in the direction along the channel for a homogeneous electron density distribution (i.e. $V_{\mathrm{s}} = V_{\mathrm{g}} = V_{\mathrm{d}} = 60$ V). The conductivity of electrons on helium $\sigma = 2.6 \times 10^{-6}\ \Omega^{-1}$ was obtained by matching the frequency response measurement to a fit based on the transmission line model (Fig. A.2 (c)). Using the Drude model ($\sigma = n_{\mathrm{e}} e \mu_l$) with $n_{\mathrm{e}} = 1.16 \times 10^9/\mathrm{cm}^2$ yields $\mu_l = 1.4 \times 10^4$ cm^2/Vs.

A.4 Characteristic Electron Density Estimation

The characteristic electron density n_{m}, corresponding to the maximum attenuation shown in Fig. 7.5 and 7.6, is calculated from the condition

$$\left(\frac{\partial \alpha}{\partial \omega_{\mathrm{p}}}\right)_{\omega_{\mathrm{p}}=\omega_{\mathrm{m}}} = 0, \text{ where } \omega_{\mathrm{m}}^2 = \frac{4\pi e^2 k}{m_{\mathrm{e}}} n_{\mathrm{m}}. \tag{A.20}$$

Fig. A.3 shows the mobility dependence of n_{m} at different helium levels in the cell. For both the helium thin film and bulk layers, the characteristic electron density n_{m} is dominated by the electron mobility transverse to the channel μ_{t} and shows negligible variation with increasing liquid helium level. A significant change of n_m due to the helium level is only expected in the transition region between the thin film and a bulk liquid layer.

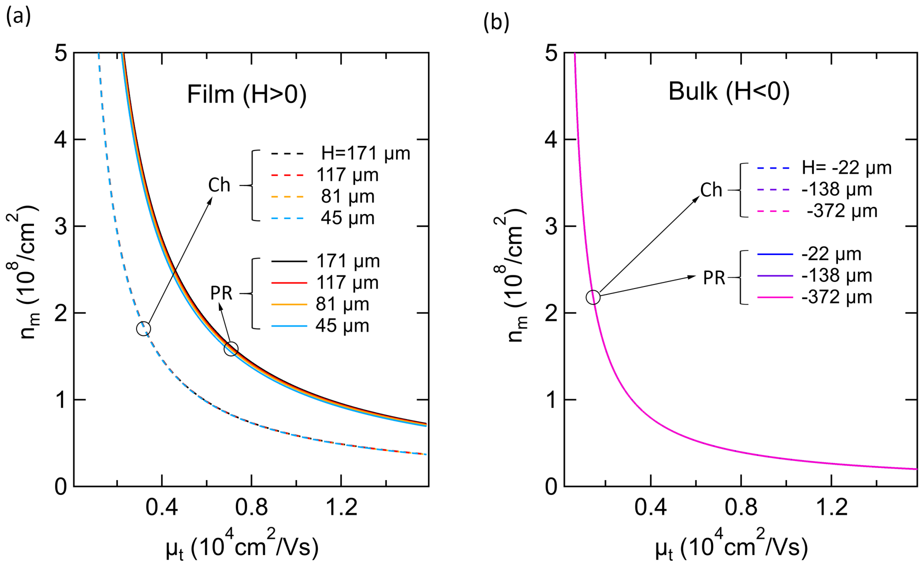

Figure A.3: Characteristic electron density n_m as a function of the mobility transverse to the channel μ_t at different H in the helium film (a) and bulk (b) regimes. The parameter H denotes the distance between the GaAs substrate and the level of the helium reservoir right next to the substrate. When $H > 0$, the level of the helium reservoir is below the surface of the GaAs while the helium level exceeds the GaAs surface when $H < 0$.

Appendix B

Studies of Electrons on Helium Using a $LiNbO_3$ SAW Device

B.1 Superfluid Film Thickness

Fig. B.1 (a) shows the hermetically sealed copper cell used for the measurements of electrons on helium supported on top of a $LiNbO_3$ substrate. To fill the cell with superfluid ^{4}He, helium gas was supplied into the cell at $T \cong 1.55$ K through a capillary line at room temperature. The liquid helium volume admitted into the cell was determined by varying the pressure in a calibrated standard volume ($V = 260$ cc) located at room temperature. The thickness of a saturated helium film, d_0, can be estimated from [11],

$$\frac{\alpha}{{d_0}^4} = \rho g H, \tag{B.1}$$

where α is the van der Waals constant, g is the gravitational acceleration, ρ is the mass density of helium, and H is the distance from the $LiNbO_3$ substrate top surface down to the liquid helium surface in the reservoir volume inside the cell. We calculated H as a function of the volume of helium admitted into the cell using 3D modeling of the cell open volume (see Fig. B.1 (b),(c)). For the thin film measurements in section 7.2, $H = 0.2$ mm, which

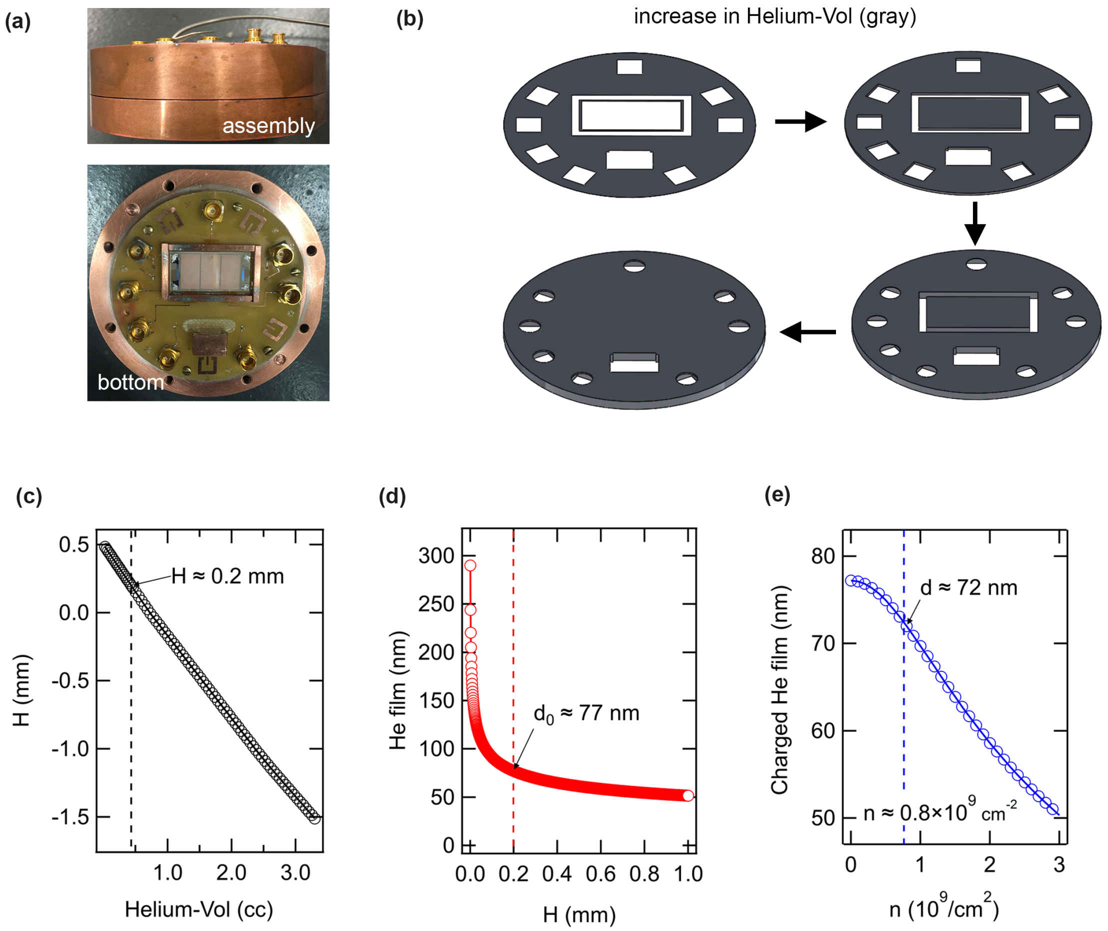

Figure B.1: The experimental sample cell and helium film thickness determination. (a) Photograph of the copper cell used for the SAW-based measurements of electrons on helium. The bottom portion of the cell contains a $LiNbO_3$ device (semi-transparent white) mounted on a printed circuit board (b) 3D CAD modeling of the liquid helium volume inside the experimental cell during filling with helium. (c) Calculation of H, the distance between the piezo-substrate top and the liquid helium level in the cell reservoir volume from the 3D CAD modeling of the open cell volume. The calculated value of H in the experiments is 0.2 mm for a helium vol. = 0.44 cc (vertical dashed black line). (d) Helium film thickness versus H before charging the film (see equation B.1). For an uncharged helium film $d_0 \approx 77$ nm (vertical dashed red line). (e) Charged helium film thickness versus electron density from equation B.2. The charged helium film thickness is calculated to be $d \cong 72$ nm for an electron density of $n \cong 0.8 \times 10^9$ cm^{-2} (vertical dashed blue line).

corresponds to a thickness of the superfluid film, $d_0 \cong 77$ nm, from equation B.1. Charging the helium film with electrons exerts an electronic pressure film [132] in addition to gravity and thus reduces the thickness of the charged helium film, d, which can be calculated from,

$$\frac{\alpha}{d^4} = \rho g H + p_{\text{el}} = \frac{\alpha}{{d_0}^4} + 2\pi n^2 e^2, \tag{B.2}$$

where p_{el} is the electronic pressure, n is the electron density and e is the electron charge. We note that due to quantum electrodynamic effects, for thick films (>60 nm) the van der Waals potential energy is proportional to $1/d^4$ rather than $1/d^3$ [179, 180]. In most of the acoustoelectric measurements reported in section 7.2, the areal electron density is estimated to be $n \simeq 0.8 \times 10^9$ cm^{-2} from field effect transistor (FET) measurement, which are described in appendix B.2. This yield a charged helium film thickness of $d \cong 72$ nm from equation B.2.

B.2 Low-Freqeuncy Characterization of The Electron System on Helium

Field Effect Transistor Transport Measurements

Fig. B.2 (a) and (b) illustrate the measurement set-up and the equivalent transmission line circuit model for the low-frequency transport properties of electrons on helium on a LiNbO$_3$ substrate. After charging a helium film with electrons, we characterize the electron distribution with low-frequency field effect transistor (FET) operation of the device [16]. These measurements are done with a gate voltage V_{g} sweep at fixed source and drain voltage at a frequency of 60 kHz as shown in Fig. B.2 (c). For sufficiently small values of the gate voltage, $V_{\mathrm{g}} < V_{\mathrm{th}}$, all of the electrons are localized over the source and drain electrodes creating a depletion region above the gate, which leads to zero current through electron layer. At a threshold value of the gate $V_{\mathrm{g}} = V_{\mathrm{th}}$ an AC current onsets from electrons being attracted to the region above the gate. As V_{g} increases beyond V_{th}, source-drain current quickly rises and reaches a maximum in a vicinity of uniform electron density ($V_{\mathrm{s}} = V_{\mathrm{d}} = V_{\mathrm{g}}$). After reaching its maximum value, the current begins decreasing and eventually vanishes as electron depletion over the source and drain electrode occurs. This ability to change the electron density above the individual electrodes with the application of a bias voltage enables the electrically switching ON and OFF of the acoustoelectric current in electrons on helium system (see Fig. 7.8 (b) in section 7.2).

Electron Density

A homogeneous areal electron density n above all electrodes is achieved when $V_{\mathrm{s}} = V_{\mathrm{g}} = V_{\mathrm{d}}$ and the electron density can be calculated from the FET transport data by measuring the difference ΔV between the case where the electron density is uniform and V_{th} (see Fig. B.2 (c)) [16],

$$n = \frac{2}{3}\frac{c_l}{e}\Delta V. \tag{B.3}$$

Here, c_l is the capacitance per unit area between electron layer and underlying electrodes from geometrical configuration, which is given by

$$c_l = \epsilon_0 \left(\frac{1}{\frac{d_{\mathrm{g}}}{\epsilon} + \frac{d_{\mathrm{s}}}{\epsilon_{\mathrm{s}}} + \frac{d}{\epsilon}} \right) \cong \epsilon_0 \left(\frac{1}{\frac{d_{\mathrm{g}}}{\epsilon} + \frac{d_{\mathrm{s}}}{\epsilon_{\mathrm{s}}}} \right) \quad (\text{for } d \ll d_{\mathrm{g}}), \tag{B.4}$$

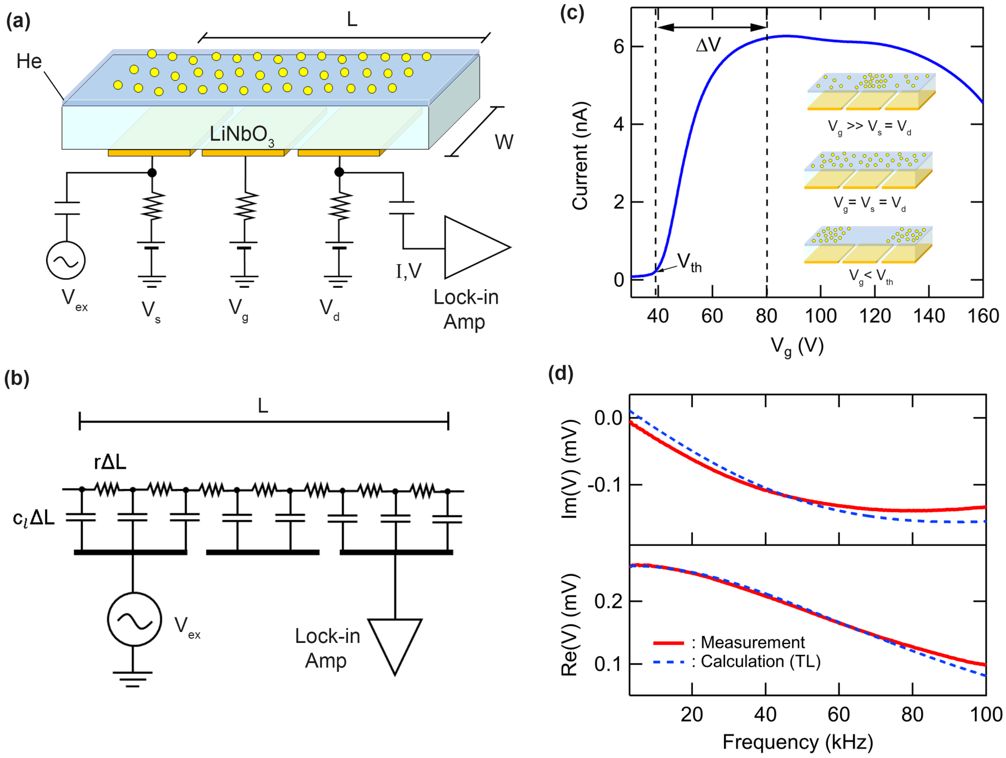

Figure B.2: Experimental setup, circuit model, and measurement data for low frequency transport of electrons on helium. (a) Sketch of the electrons on helium device. A DC bias voltage is applied to the three underlying electrodes to trap electrons above helium surface. An AC excitation voltage ($V_{\mathrm{ex}} = 0.1$ V) applied to the source electrode induces a current through electrons on helium, which is capacitively detected using the drain electrode. (b) The equivalent transmission line circuit model for this device. The resistance of the electron sheet and the capacitance between this sheet and the three electrodes are spatially distributed per unit length, $r\Delta L$ and $c_l\Delta L$, where r and c_l represent the resistance per unit length and the capacitance per unit length. (c) Current-voltage characteristics for FET operation of the electrons on helium device. For this representative data, the source-drain current amplitude was measured during a gate voltage sweep with $V_{\mathrm{s}} = V_{\mathrm{d}} = 80$ V. The insets show the corresponding electron density profiles over the electrodes for different values of V_{g}. A uniform areal density distribution is achieved at $V_{\mathrm{g}} = V_{\mathrm{s}} = V_{\mathrm{d}}$. (d) Frequency dependence of the transport characteristics of the system of electrons on helium. The red and blue traces represent the experimental data and the calculation based on the transmission line model respectively. For these measurement, all three electrodes were biased with 80 V ($V_{\mathrm{g}} = V_{\mathrm{s}} = V_{\mathrm{d}} = 80$ V).

where ϵ_0 is the vacuum permittivity, $\epsilon = 1.057$ is the dielectric constant of helium, $\epsilon_{\mathrm{s}} \cong 35$ is the effective dielectric constant of the $\mathrm{LiNbO_3}$, $d_{\mathrm{g}} \cong 70\mu\mathrm{m}$ is the gap between the $\mathrm{LiNbO_3}$ substrate and the bottom electrodes, $d_{\mathrm{s}} = 0.5$ mm is the thickness of the $\mathrm{LiNbO_3}$ substrate, and d is the charged helium film thickness. The effective dielectric constant ϵ_{s} for $\mathrm{LiNbO_3}$ is given by $\epsilon_{\mathrm{s}} = \sqrt{\epsilon_{11}\epsilon_{33} - \epsilon_{13}^2}$ where ϵ_{11}, ϵ_{33}, and ϵ_{13} are the dielectric tensor elements of $\mathrm{LiNbO_3}$ at constant stress [133]. These dielectric elements are given in Ref. [181] as $\epsilon_{11} = 44.3$, $\epsilon_{33} = 27.6$, and $\epsilon_{13} = 0$. With $c_l \cong 1.08 \times 10^{-7}$ F/m^2 obtained from equation B.4, the uniform areal electron density is found to be $n \simeq 0.8 \times 10^9$ cm^{-2} for most of acoustoelectric measurements reported on $\mathrm{LiNbO_3}$. For the power dependent pulsed SAW measurements (Fig. 7.9 (b)-(d)), the value of n is about 1.9 $\times 10^9$ cm^{-2}. We note that in the gate-tunable acoustoelectric measurements shown in Fig. 7.8 (b), n is no longer a uniform density but rather varies as a function of V_{g}, however the total number of electrons over the device is fixed.

Electron Mobility

The conductivity σ of electrons on helium in the low-frequency transport measurements can be determined by fitting the frequency response measurement to a RC transmission line model [129, 130] with σ as fitting parameter [16]. Fig. B.2 (d) shows this frequency response for the representative case where $V_{\mathrm{s}} = V_{\mathrm{g}} = V_{\mathrm{d}} = 80$ V, which shows good agreement with this model fit. The value of the conductivity from this fit is $\sigma \cong 1.58 \times 10^{-6}\ \Omega^{-1}$. The mobility μ of electrons is then calculated based on a Drude model analysis ($\sigma = ne\mu$). For an electron density of $n = 1.9 \times 10^9$ cm^{-2} the mobility is $\mu \cong 5.3 \times 10^3$ cm^2/Vs with $d \cong 60$ nm. This mobility is roughly two orders of magnitude less than the mobility of electrons on bulk ^{4}He at the same temperature [9]. Such a low mobility for electrons on a thin superfluid film is consistent with previous measurements and can be explained by the close proximity of the electron layer to the underlying substrate [171].

RC Delay Time Constant

The RC delay time constant, τ_{RC}, introduced in section 7.2 is calculated based on the transmission line modeling described above (see Fig. B.2 (b)) and the Elmore delay model [182], which is encapsulated by the following equation

$$\tau_{\mathrm{RC}} = r c_l L^2 \frac{1+N}{2N} \cong \frac{R_{\mathrm{tot}} C_{\mathrm{tot}}}{2} \quad \text{(for large N)}, \tag{B.5}$$

where r and c_l are the resistance per unit length and the capacitance per unit length of the electron system and L, R_{tot}, C_{tot}, and N represent the total length, the total resistance, the total capacitance, and the number of nodes in the entire transmission line. $R_{\mathrm{tot}} = \sigma^{-1} W^{-1} L$ and $C_{\mathrm{tot}} = cWL$ are approximately 1.06 MΩ and 14.6 pF for $W = 9$ mm (the width of the electrodes in the SAW device) and $L = 15$ mm, which yields $\tau_{\mathrm{RC}} \approx 7.7\ \mu$s in the low-frequency transport regime.

Electron Collision Rate with Helium Vapor Atoms

At a temperature T = 1.55 K, ^{4}He vapor atoms are a strong source of electron scattering. The collision rate $1/\tau_{\mathrm{He}}$ is determined by

$$\frac{1}{\tau_{\mathrm{He}}} = \frac{e}{\mu m^*} \tag{B.6}$$

with the effective electron mass $m^* = m_\mathrm{e}$ (bare electron mass) and the electron mobility $\mu \cong 5.3 \times 10^3$ cm^2/Vs. This yields $1/\tau_\mathrm{He} \sim 300$ GHz.

B.3 Determination of SAW Charge Pumping Time Constants

The time constants for SAW-driven charge pumping (τ_pump) and subsequent relaxation (τ_rel) for different RF power levels was determined from an exponential curve fitting of the acoustoelectric current (I_ae) data as shown in Fig. B.3 and the resulting values are tabulated in the table below.

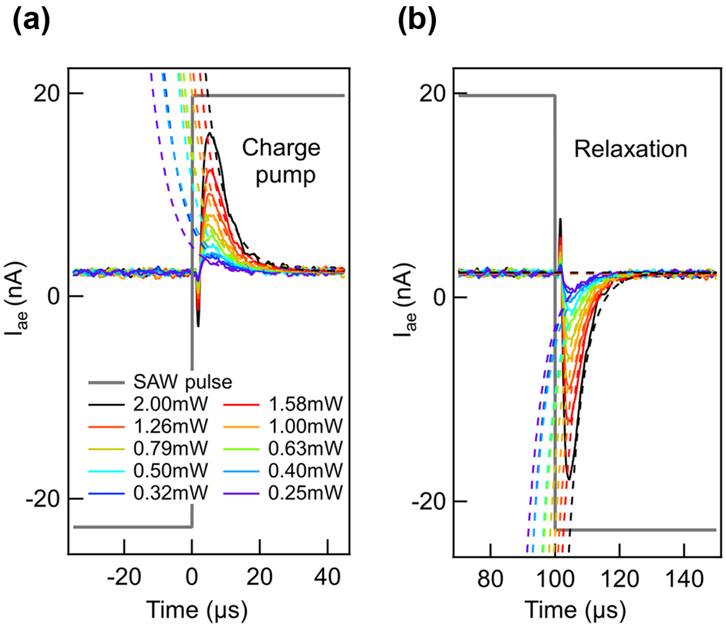

Figure B.3: Determination of acoustoelectric time constants. These time constants were determined from exponential fits to the acoustoelectric current data during (a) SAW excitation (charge pumping) and (b) relaxation after the SAW drive was removed.

Table B.1: Values of the time constants obtained from the exponential curve fits in Fig. B.3.

RF (mW)	τ_{pump} (μs)	τ_{rel} (μs)
0.25	5.9	4.6
0.32	5.6	5.3
0.40	6.5	5.2
0.50	5.2	4.7
0.63	5.2	5.0
0.79	6.3	5.0
1.00	5.5	4.7
1.26	5.9	4.7
1.58	5.6	4.7
2.00	5.8	4.8

BIBLIOGRAPHY

BIBLIOGRAPHY

[1] Grimes, C. C., Brown, T. R., Burns, M. L. & Zipfel, C. L. Spectroscopy of electrons in image-potential-induced surface states outside liquid helium. *Phys. Rev. B* **13**, 140–147 (1976). xi, 7, 9, 10

[2] Platzman, P. M. & Fukuyama, H. Phase diagram of the two-dimensional electron liquid. *Phys. Rev. B* **10**, 3150–3158 (1974). xi, 16, 17, 18

[3] Marcus, A. H. & Rice, S. A. Observations of first-order liquid-to-hexatic and hexatic-to-solid phase transitions in a confined colloid suspension. *Phys. Rev. Lett.* **77**, 2577–2580 (1996). xi, 24

[4] Bonsall, L. & Maradudin, A. A. Some static and dynamical properties of a two-dimensional wigner crystal. *Phys. Rev. B* **15**, 1959–1973 (1977). xii, 22, 25, 26

[5] Grimes, C. C. & Adams, G. Evidence for a liquid-to-crystal phase transition in a classical, two-dimensional sheet of electrons. *Phys. Rev. Lett.* **42**, 795–798 (1979). xii, 1, 3, 13, 16, 17, 22, 28, 30, 34

[6] Fisher, D. S., Halperin, B. I. & Platzman, P. M. Phonon-ripplon coupling and the two-dimensional electron solid on a liquid-helium surface. *Phys. Rev. Lett.* **42**, 798–801 (1979). xii, 1, 28, 29, 31, 34

[7] Grimes, C. C. & Adams, G. Observation of two-dimensional plasmons and electron-ripplon scattering in a sheet of electrons on liquid helium. *Phys. Rev. Lett.* **36**, 145–148 (1976). xii, 3, 25, 33, 36, 40

[8] Rybalko, A. & Kovdrya, Y. Z. Mobility of electrons along the liquid helium surface in strong retarding electric fields. *J. Low Temp. Phys.* **18**, 219–227 (1975). xii, 33, 36

[9] Iye, Y. Mobility of electrons in the surface state of liquid helium. *J. Low Temp. Phys.* **40**, 441–451 (1980). xii, 33, 36, 128, 137, 190

[10] Saitoh, M. Warm electrons on the liquid 4he surface. *J. Phys. Soc. Jpn* **42**, 201–209 (1977). xii, 9, 33, 36, 37, 39, 41, 128, 137, 159

[11] Pobell, F. *Matter and methods at low temperatures*, vol. 2 (Springer, 2007). xii, 42, 43, 47, 142, 185

[12] Donnelly, R. J. & Barenghi, C. F. The observed properties of liquid helium at the saturated vapor pressure. *J. Phys. Chem. Ref. Data* **27**, 1217–1274 (1998). xii, 44, 46

[13] Etz, H., Gombert, W., Idstein, W. & Leiderer, P. Stability of charged ^{4}He films. *Phys. Rev. Lett.* **53**, 2567–2570 (1984). xiii, 50, 51, 52

[14] Simon, S. H. Coupling of surface acoustic waves to a two-dimensional electron gas. *Phys. Rev. B* **54**, 13878–13884 (1996). xiii, 65, 68, 70, 71

[15] Kim, B. S. *et al.* Generalized four-point characterization method using capacitive and ohmic contacts. *Rev. Sci. Instrum* **83**, 024703 (2012). xv, 103, 105

[16] Nasyedkin, K. *et al.* Unconventional field effect transistor composed of electrons floating on liquid helium. *J. Phys. Condens. Matter* **30**, 465501 (2018). xxi, 128, 165, 187, 188, 190

[17] Wigner, E. On the interaction of electrons in metals. *Phys. Rev.* **46**, 1002–1011 (1934). 1, 12

[18] Dykman, M. I., Lea, M. J., Fozooni, P. & Frost, J. Magnetoresistance in 2d electrons on liquid helium: Many-electron versus single-electron kinetics. *Phys. Rev. Lett.* **70**, 3975–3978 (1993). 1, 3

[19] Dykman, M., Fang-Yen, C. & Lea, M. Many-electron transport in strongly correlated nondegenerate two-dimensional electron systems. *Phys. Rev. B* **55**, 16249 (1997). 1

[20] Lea, M. J., Fozooni, P., Richardson, P. J. & Blackburn, A. Direct observation of many-electron magnetoconductivity in a nondegenerate 2d electron liquid. *Phys. Rev. Lett.* **73**, 1142–1145 (1994). 1

[21] Monarkha, Y. P., Ito, S.-i., Shirahama, K. & Kono, K. Inelastic quantum magnetotransport in a highly correlated two-dimensional electron liquid. *Phys. Rev. Lett.* **78**, 2445–2448 (1997). 1

[22] Shirahama, K., Ito, S., Suto, H. & Kono, K. Surface study of liquid3he using surface state electrons. *J. Low Temp. Phys.* **101**, 439–444 (1995). 1

[23] Platzman, P. & Dykman, M. Quantum computing with electrons floating on liquid helium. *Science* **284**, 1967 (1999). 1

[24] Lyon, S. Spin-based quantum computing using electrons on liquid helium. *Phys. Rev. A* **74**, 052338 (2006). 1

[25] Schuster, D. I., Fragner, A., Dykman, M. I., Lyon, S. A. & Schoelkopf, R. J. Proposal for manipulating and detecting spin and orbital states of trapped electrons on helium using cavity quantum electrodynamics. *Phys. Rev. Lett.* **105**, 040503 (2010). 1

[26] Yang, G. *et al.* Coupling an ensemble of electrons on superfluid helium to a superconducting circuit. *Phys. Rev. X* **6**, 011031 (2016). 1, 84

[27] Kawakami, E., Elarabi, A. & Konstantinov, D. Image-charge detection of the rydberg states of surface electrons on liquid helium. *Phys. Rev. Lett.* **123**, 086801 (2019). 1

[28] Koolstra, G., Yang, G. & Schuster, D. I. Coupling a single electron on superfluid helium to a superconducting resonator. *Nat. Commun.* **10**, 5239 (2019). 1

[29] Wixforth, A., Kotthaus, J. P. & Weimann, G. Quantum oscillations in the surface-acoustic-wave attenuation caused by a two-dimensional electron system. *Phys. Rev. Lett.* **56**, 2104–2106 (1986). 2, 53, 70, 72

[30] Wixforth, A. *et al.* Surface acoustic waves on GaAs / $\mathrm{Al}_x\mathrm{Ga}_{1-x}\mathrm{As}$ heterostructures. *Phys. Rev. B* **40**, 7874–7887 (1989). 2, 53, 69, 77

[31] Pollanen, J., Eisenstein, J., Pfeiffer, L. & West, K. Charge metastability and hysteresis in the quantum hall regime. *Phys. Rev. B* **94**, 245440 (2016). 2, 53

[32] Willett, R. L. *et al.* Anomalous sound propagation at ν=1/2 in a 2d electron gas: Observation of a spontaneously broken translational symmetry? *Phys. Rev. Lett.* **65**, 112–115 (1990). 2, 53, 72

[33] Shilton, J. M. *et al.* Experimental study of the acoustoelectric effects in GaAs-AlGaAs heterostructures. *J. Phys. Condens. Matter* **7**, 7675–7685 (1995). 2, 147

[34] Lane, J. R. *et al.* Flip-chip gate-tunable acoustoelectric effect in graphene. *J. Appl. Phys.* **124**, 194302 (2018). `https://doi.org/10.1063/1.5047211`. 2, 147

[35] Tracy, L., Eisenstein, J., Lilly, M., Pfeiffer, L. & West, K. Surface acoustic wave propagation and inhomogeneities in low-density two-dimensional electron systems near the metal–insulator transition. *Solid State Commun.* **137**, 150–153 (2006). 2, 53, 173

[36] Kukushkin, I. V., Umansky, V., von Klitzing, K. & Smet, J. H. Collective modes and the periodicity of quantum hall stripes. *Phys. Rev. Lett.* **106**, 206804 (2011). 2

[37] Willett, R. L., Ruel, R. R., West, K. W. & Pfeiffer, L. N. Experimental demonstration of a fermi surface at one-half filling of the lowest landau level. *Phys. Rev. Lett.* **71**, 3846–3849 (1993). 2

[38] Blumenthal, M. D. *et al.* Gigahertz quantized charge pumping. *Nat. Phys.* **3**, 343–347 (2007). 2, 147, 174

[39] Cole, M. W. & Cohen, M. H. Image-potential-induced surface bands in insulators. *Phys. Rev. Lett.* **23**, 1238–1241 (1969). 3

[40] Shikin, V. Motion of helium ions near a vapor-liquid surface. *Sov. Phys. JETP* **31**, 936 (1970). 3, 5

[41] Williams, R., Crandall, R. S. & Willis, A. H. Surface states of electrons on liquid helium. *Phys. Rev. Lett.* **26**, 7–9 (1971). 3

[42] Andrei, E. Y. Observation of the polaronic transition in a two-dimensional electron system. *Phys. Rev. Lett.* **52**, 1449–1452 (1984). 3

[43] Dykman, M. & Khazan, L. Effect of the interaction between nondegenerate electrons localized in a thin surface layer on the cyclotron resonance and on the magnetoconductance. *Zh. Eksp. Teor. Fiz* **77**, 1488–1502 (1979). 3

[44] Monarkha, Y. & Kono, K. *Two-dimensional Coulomb liquids and solids*, vol. 142 (Springer Science & Business Media, 2013). 4, 14, 29, 32, 38

[45] Woolf, M. A. & Rayfield, G. W. Energy of negative ions in liquid helium by photoelectric injection. *Phys. Rev. Lett.* **15**, 235–237 (1965). 4

[46] Sommer, W. T. Liquid helium as a barrier to electrons. *Phys. Rev. Lett.* **12**, 271–273 (1964). 4

[47] Sanders, T. M. & Weinreich, G. Energies of external electron surface states on liquid helium. *Phys. Rev. B* **13**, 4810–4814 (1976). 7

[48] Grimes, C. C. & Brown, T. R. Direct spectroscopic observation of electrons in image-potential states outside liquid helium. *Phys. Rev. Lett.* **32**, 280–283 (1974). 9

[49] Shikin, V. & Monarkha, Y. P. On the interaction of surface electrons in liquid helium with oscillations of the vapor-liquid interface. *J. Low Temp. Phys.* **16**, 193–208 (1974). 10, 33, 39

[50] Andrei, E. Y. *Two-Dimensional Electron Systems: On Helium and Other Cryogenic Substrates*, vol. 19 (Springer Science & Business Media, 2012). 10, 15, 38, 154

[51] Huang, W., Rudnick, J. & Dahm, A. Sound modes of a two-dimensional electron gas bound to a helium film. *J. Low Temp. Phys.* **28**, 21–27 (1977). 12

[52] Dahl, D. A. & Sham, L. J. Electrodynamics of quasi-two-dimensional electrons. *Phys. Rev. B* **16**, 651–661 (1977). 12, 25

[53] Peeters, F. M. & Platzman, P. M. Electrons on films of helium: A quantum mechanical two-dimensional fermion system. *Phys. Rev. Lett.* **50**, 2021–2023 (1983). 12, 15

[54] Crandall, R. & Williams, R. Crystallization of electrons on the surface of liquid helium. *Phys. Lett. A* **34**, 404–405 (1971). 12

[55] Andrei, E. Y. *et al.* Observation of a magnetically induced wigner solid. *Phys. Rev. Lett.* **60**, 2765–2768 (1988). 13

[56] Świerkowski, L., Neilson, D. & Szymański, J. Enhancement of wigner crystallization in multiple-quantum-well structures. *Phys. Rev. Lett.* **67**, 240–243 (1991). 13

[57] Yankowitz, M. *et al.* Tuning superconductivity in twisted bilayer graphene. *Science* **363**, 1059–1064 (2019). 13

[58] Padhi, B., Setty, C. & Phillips, P. W. Doped twisted bilayer graphene near magic angles: Proximity to wigner crystallization, not mott insulation. *Nano Lett.* **18**, 6175–6180 (2018). 13

[59] Drummond, N. D. & Needs, R. J. Phase diagram of the low-density two-dimensional homogeneous electron gas. *Phys. Rev. Lett.* **102**, 126402 (2009). 14

[60] Marty, D., Poitrenaud, J. & Williams, F. Observation of liquid-to-crystal transition in a two dimensional electronic system. *J. Phys. (Paris), Lett.* **41**, 311–314 (1980). 16

[61] Gallet, F., Deville, G., Valdes, A. & Williams, F. Fluctuations and shear modulus of a classical two-dimensional electron solid: experiment. *Phys. Rev. Lett.* **49**, 212 (1982). 16

[62] Mehrotra, R., Guenin, B. & Dahm, A. Ripplon-limited mobility of a two-dimensional crystal of electrons: Experiment. *Phys. Rev. Lett.* **48**, 641 (1982). 16

[63] Kajita, K. Wigner crystallization of two dimensional electrons formed on the surface of solid neon. *J. Phys. Soc. Jpn* **54**, 4092–4095 (1985). 16

[64] Mellor, C. & Vinen, W. Experimental observation of crystallization and ripplon generation in a two-dimensional pool of helium ions. *Surf. Sci.* **229**, 368–370 (1990). 16

[65] Shirahama, K. & Kono, K. Dynamical transition in the wigner solid on a liquid helium surface. *Phys. Rev. Lett.* **74**, 781 (1995). 16

[66] Peeters, F. M. Electrons on liquid helium film. In *The Physics of the Two-Dimensional Electron Gas*, 393–420 (Springer, 1987). 15

[67] Gor'kov, L. & Chernikova, D. Concerning the structure of a charged surface of liquid helium. *Sov. JETP Lett.* **18**, 68 (1973). 15

[68] Ikezi, H. & Platzman, P. M. Stability of helium films charged with electrons. *Phys. Rev. B* **23**, 1145–1148 (1981). 15, 49, 50

[69] Peierls, R. Quelques propriétés typiques des corps solides. In *Annales de l'institut Henri Poincaré*, vol. 5, 177–222 (1935). 19

[70] Landau, L. Zur theorie der phasenumwandlungen ii. *Phys. Z. Sowjetunion* **11**, 26–35 (1937). 19

[71] Mermin, N. D. & Wagner, H. Absence of ferromagnetism or antiferromagnetism in one-or two-dimensional isotropic heisenberg models. *Phy. Rev. Lett.* **17**, 1133 (1966). 19

[72] Mermin, N. D. Crystalline order in two dimensions. *Phys. Rev.* **176**, 250 (1968). 19

[73] Kosterlitz, J. M. & Thouless, D. J. Ordering, metastability and phase transitions in two-dimensional systems. *J. Phys. C Solid State Phys.* **6**, 1181 (1973). 19

[74] Halperin, B. & Nelson, D. R. Theory of two-dimensional melting. *Phys. Rev. Lett.* **41**, 121 (1978). 19

[75] Nelson, D. R. & Halperin, B. Dislocation-mediated melting in two dimensions. *Phys. Rev. B* **19**, 2457 (1979). 19, 20, 23, 173

[76] Young, A. Melting and the vector coulomb gas in two dimensions. *Phys. Rev. B* **19**, 1855 (1979). 19

[77] Jancovici, B. Infinite susceptibility without long-range order: The two-dimensional harmonic "solid". *Phys. Rev. Lett.* **19**, 20–22 (1967). 20

[78] Thouless, D. Melting of the two-dimensional wigner lattice. *J. Phys. C Solid State Phys.* **11**, L189 (1978). 22

[79] Morf, R. H. Temperature dependence of the shear modulus and melting of the two-dimensional electron solid. *Phys. Rev. Lett.* **43**, 931–935 (1979). 22, 27

[80] Strandburg, K. J. Two-dimensional melting. *Rev. Mod. Phys.* **60**, 161 (1988). 23

[81] Bohm, D. & Gross, E. P. Theory of plasma oscillations. a. origin of medium-like behavior. *Phys. Rev.* **75**, 1851–1864 (1949). 24

[82] Shikin, V. 2d coulomb crystals on a liquid substrate. In *Two-Dimensional Electron Systems*, 33–52 (Springer, 1997). 26, 28

[83] Deville, G., Valdes, A., Andrei, E. Y. & Williams, F. I. B. Propagation of shear in a two-dimensional electron solid. *Phys. Rev. Lett.* **53**, 588–591 (1984). 26

[84] Shikin, V. Excitation of capillary waves in helium by a wigner lattice of surface electrons. *Sov. JETP Lett.* **19**, 335 (1974). 28

[85] Monarkha, Y. P. & Shikin, V. Theory of a two-dimensional wigner crystal of surface electrons in helium. *Zh. Eksp. Teor. Fiz* **68**, 1423–1433 (1975). 31

[86] Cole, M. W. Properties of image-potential-induced surface states of insulators. *Phys. Rev. B* **2**, 4239–4252 (1970). 33

[87] Crandall, R. S. Hot electrons on liquid helium. *Phys. Rev. B* **12**, 119–124 (1975). 33

[88] Sommer, W. T. & Tanner, D. J. Mobility of electrons on the surface of liquid ^{4}He. *Phys. Rev. Lett.* **27**, 1345–1349 (1971). 33, 93, 102

[89] Brown, T. R. & Grimes, C. C. Observation of cyclotron resonance in surface-bound electrons on liquid helium. *Phys. Rev. Lett.* **29**, 1233–1236 (1972). 33

[90] Bridges, F. & McGill, J. F. Mobility of electrons on the surface of liquid helium. *Phys. Rev. B* **15**, 1324–1339 (1977). 33

[91] Mehrotra, R., Guo, C. J., Ruan, Y. Z., Mast, D. B. & Dahm, A. J. Density-dependent mobility of a two-dimensional electron fluid. *Phys. Rev. B* **29**, 5239–5242 (1984). 33

[92] O'Malley, T. F. Extrapolation of electron-rare gas atom cross sections to zero energy. *Phys. Rev.* **130**, 1020–1029 (1963). 35

[93] Landau, L. Em lifshitz, fluid mechanics. *Course of theoretical physics* **6** (1959). 37

[94] Donnelly, R. J. The two-fluid theory and second sound in liquid helium. *Phys. Today* **62**, 34–39 (2009). 43, 45

[95] Landau, L. Theory of the superfluidity of helium ii. *Phys. Rev.* **60**, 356 (1941). 43

[96] Bar-Cohen, Y. *High temperature materials and mechanisms* (CRC Press, 2014). 44

[97] Vinen, W. The physics of superfluid helium (2004). 44

[98] Atkins, K. R. Third and fourth sound in liquid helium ii. *Phys. Rev.* **113**, 962–965 (1959). 46

[99] Everitt, C. W. F., Atkins, K. R. & Denenstein, A. Detection of third sound in liquid helium films. *Phys. Rev. Lett.* **8**, 161–163 (1962). 46

[100] Rudnick, I. & Shapiro, K. A. Fourth sound in he ii. *Phys. Rev. Lett.* **9**, 191–193 (1962). 46

[101] Dzyaloshinskii, I. E., Lifshitz, E. M. & Pitaevskii, L. P. The general theory of van der waals forces. *Adv. Phys.* **10**, 165–209 (1961). 47

[102] Glasson, P. *et al.* Microelectronics on liquid helium. *Physica B Condens. Matter* **284-288**, 1916–1917 (2000). 48

[103] Marty, D. Stability of two-dimensional electrons on a fractionated helium surface. *J. Phys. C Solid State Phys.* **19**, 6097–6104 (1986). 48, 51

[104] Hu, X. L. & Dahm, A. J. Stability of charged thin helium films. *Phys. Rev. B* **42**, 2010–2013 (1990). 50

[105] Shilton, J. M. *et al.* High-frequency single-electron transport in a quasi-one-dimensional GaAs channel induced by surface acoustic waves. *J. Phys. Condens. Matter* **8**, L531–L539 (1996). 53, 174

[106] Barnes, C. H. W., Shilton, J. M. & Robinson, A. M. Quantum computation using electrons trapped by surface acoustic waves. *Phys. Rev. B* **62**, 8410–8419 (2000). 53, 147, 174

[107] McNeil, R. *et al.* On-demand single-electron transfer between distant quantum dots. *Nature* **477**, 439–442 (2011). 53, 147

[108] Gustafsson, M. V. *et al.* Propagating phonons coupled to an artificial atom. *Science* **346**, 207–211 (2014). 54

[109] Manenti, R. *et al.* Circuit quantum acoustodynamics with surface acoustic waves. *Nat. Commun.* **8**, 975 (2017). 54, 174

[110] Moores, B. A., Sletten, L. R., Viennot, J. J. & Lehnert, K. W. Cavity quantum acoustic device in the multimode strong coupling regime. *Phys. Rev. Lett.* **120**, 227701 (2018). 54

[111] FARNELL, G. 3 - properties of elastic surface waves. vol. 6 of *Physical Acoustics*, 109–166 (Academic Press, 1970). 56, 161

[112] Stoneley, R. The propagation of surface elastic waves in a cubic crystal. *Proceedings of the Royal Society of London. Series A. Mathematical and Physical Sciences* **232**, 447–458 (1955). 64

[113] Flannery, C. M., Chilla, E., Semenov, S. & Frohlich, H. . Elastic properties of gaas obtained by inversion of laser-generated surface acoustic wave measurements. In *1999 IEEE Ultrasonics Symposium. Proceedings. International Symposium (Cat. No.99CH37027)*, vol. 1, 501–504 vol.1 (1999). 65

[114] Ciplys, D. & Rimeika, R. Measurements of electromechanical coupling coefficient for surface acoustic waves in proton-exchanged lithium niobate. *Ultragarsas" Ultrasound"* **33**, 14–20 (1999). 69, 75

[115] Rotter, M., Wixforth, A., Ruile, W., Bernklau, D. & Riechert, H. Giant acoustoelectric effect in gaas/linbo3 hybrids. *Appl. Phys. Lett.* **73**, 2128–2130 (1998). 69, 80, 147, 159

[116] Material parameters of semiconductor compounds. `http://www.ioffe.ru/SVA/NSM/Semicond/index.html`. Accessed: 2020-07-24. 71

[117] Auld, B. A. *Acoustic fields and waves in solids* (Wiley, New York, 1973). 72, 73, 75

[118] Esslinger, A. *et al.* Ultrasonic approach to the integer and fractional quantum hall effect. *Surf. Sci.* **305**, 83– 86 (1994). 77

[119] Ingebrigtsen, K. Linear and nonlinear attenuation of acoustic surface waves in a piezoelectric coated with a semiconducting film. *J. Appl. Phys.* **41**, 454–459 (1970). 80, 152, 161

[120] Labgui description. `https://libraries.io/github/LabGUI/LabGUI`. Accessed: 2020-11-13. 82

[121] Koolstra, G. *Trapping a Single Electron on Superfluid Helium Using a Superconducting Resonator*. Ph.D. thesis (2019). 84

[122] Wilen, L. A. & Giannetta, R. W. Cryogenic photoemissive electron source. *Rev. Sci. Instrum.* **56**, 2175–2176 (1985). 89, 146

[123] Fowler, R. H. & Nordheim, L. Electron emission in intense electric fields. *Proceedings of the Royal Society of London. Series A, Containing Papers of a Mathematical and Physical Character* **119**, 173–181 (1928). 89

[124] Chang, J. ., Lawless, P. A. & Yamamoto, T. Corona discharge processes. *IEEE T. Plasma Sci.* **19**, 1152–1166 (1991). 89

[125] Spangler, G. E. & Hereford, F. L. Injection of electrons into he ii from an immersed tungsten filament. *Phys. Rev. Lett.* **20**, 1229 (1968). 89

[126] Silvera, I. F. & Tempere, J. Electron emission in superfluid and low temperature vapor phase helium. *Phys. Rev. Lett.* **100**, 117602 (2008). 89

[127] Saitoh, M., Ikegami, H. & Kono, K. Electrostatic manipulation of level of bulk liquid for studies of saturated superfluid 3 he films. *J. Low Temp. Phys.* **158**, 716 (2010). 95

[128] Abu-Abed, A. S. & Lindquist, R. G. Capacitive interdigital sensor with inhomogeneous nematic liquid crystal film. *Prog. Electromagn. Res.* **7**, 75–87 (2008). 96

[129] Lea, M., Stone, A., Fozooni, P. & Frost, J. The ac response of a 2-d electron gas on liquid helium in a magnetic field. *J. Low Temp. Phys.* **85**, 67–89 (1991). 102, 104, 183, 190

[130] Mehrotra, R. & Dahm, A. Analysis of the sommer technique for measurement of the mobility for charges in two dimensions. *J. Low Temp. Phys.* **67**, 115–121 (1987). 103, 183, 190

[131] Liou, Y.-T. *et al.* Acousto-electric transport in mgo/zno-covered graphene on sic. *J. Phys. D Appl. Phys.* **50**, 464008 (2017). 113

[132] Leiderer, P. Electrons at the surface of quantum systems. *J. Low Temp. Phys.* **87**, 247–278 (1992). 114, 187

[133] Müller, C. *et al.* Surface acoustic wave investigations of the metal-to-insulator transition of v 2 o 3 thin films on lithium niobate. *J. Appl. Phys.* **98**, 084111 (2005). 115, 190

[134] Sommerfeld, P., Steijaert, P., Peters, P. & Van der Heijden, R. Magnetoplasmons at boundaries between two-dimensional electron systems. *Phys. Rev. Lett.* **74**, 2559 (1995). 127

[135] Konstantinov, D., Chepelianskii, A. & Kono, K. Resonant photovoltaic effect in surface state electrons on liquid helium. *J. Phys. Soc. Jpn* **81**, 093601 (2012). 127

[136] Badrutdinov, A., Abdurakhimov, L. & Konstantinov, D. Cyclotron resonant photoresponse of a multisubband two-dimensional electron system on liquid helium. *Phys. Rev. B* **90**, 075305 (2014). 127

[137] Chepelianskii, A. D., Watanabe, M., Nasyedkin, K., Kono, K. & Konstantinov, D. An incompressible state of a photo-excited electron gas. *Nat. Commun.* **6**, 1–7 (2015). 127

[138] Rees, D. G., Beysengulov, N. R., Lin, J.-J. & Kono, K. Stick-slip motion of the wigner solid on liquid helium. *Phys. Rev. Lett.* **116**, 206801 (2016). 127, 170

[139] Badrutdinov, A., Smorodin, A., Rees, D., Lin, J. & Konstantinov, D. Nonlinear transport of the inhomogeneous wigner solid in a channel geometry. *Phys. Rev. B* **94**, 195311 (2016). 127

[140] Klier, J., Doicescu, I. & Leiderer, P. First dc measurements of electrons on liquid helium: the helium-fet. *J. Low Temp. Phys.* **121**, 603–608 (2000). 127

[141] Rees, D. G. *et al.* Transport measurements of strongly correlated electrons on helium in a classical point-contact device. *J. Low Temp. Phys.* **166**, 107–124 (2012). 131

[142] Lea, M., Frost, J., Stone, A. & Fozooni, P. Ac skin depths in a screened 2-d electron gas in a magnetic field. *Physica B Condens. Matter* **165**, 881–882 (1990). 134

[143] Konstantinov, D. *et al.* Microwave-resonance-induced resistivity: Evidence of ultrahot surface-state electrons on liquid ^{3}He. *Phys. Rev. Lett.* **98**, 235302 (2007). 137

[144] Nasyedkin, K., Sivokon, V., Monarkha, Y. P. & Sokolov, S. Nonlinear surface electron transport over liquid helium. *Low Temp. Phys.* **35**, 757–765 (2009). 137

[145] Chepelianskii, A. D., Watanabe, M. & Kono, K. Can warmer than room temperature electrons levitate above a liquid helium surface? *J. Low Temp. Phys.* **195**, 307–318 (2019). 137

[146] Kleinbaum, E. I. & Lyon, S. A. Thermopower-based hot electron thermometry of helium surface states at 1.6 k. *Phys. Rev. Lett.* **121**, 236801 (2018). 137

[147] Byeon, H. *et al.* Anomalous attenuation of piezoacoustic surface waves by liquid helium thin films. *J. Low Temp. Phys.* **195** (2019). 138

[148] Arzt, R., Salzmann, E. & Dransfeld, K. Elastic surface waves in quartz at 316 MHz. *Appl. Phys. Lett.* **10**, 165–167 (1967). 141, 143

[149] Dransfeld, K. & Salzmann, E. Physical acoustics (1970). 141, 143

[150] Pollanen, J., Choi, H., Davis, J., Rolfs, B. & Halperin, W. Low temperature thermal resistance for a new design of silver sinter heat exchanger. In *Journal of Physics: Conference Series*, vol. 150, 012037 (IOP Publishing, 2009). 142

[151] Tokumura, M. & Akao, F. Measurement of the acoustic impedance of liquid ^{4}He by acoustic surface waves. *Phys. Lett. A* **72**, 131–132 (1979). 143

[152] Cheeke, J. & Morisseau, P. Attenuation of rayleigh waves on a $LiNbO_3$ crystal in contact with a liquid ^{4}He bath. *J. Low Temp. Phys.* **46**, 319–330 (1982). 143

[153] Aoki, Y. *et al.* Application of surface acoustic wave sensors for liquid helium-4 and helium-3. *J. Low Temp. Phys.* **134**, 945–958 (2004). 143

[154] Harris, G. *et al.* Laser cooling and control of excitations in superfluid helium. *Nat. Phys.* **12**, 788–793 (2016). 145

[155] De Lorenzo, L. A. & Schwab, K. C. Ultra-high Q acoustic resonance in superfluid ^{4}He. *J. Low Temp. Phys.* **186**, 233–240 (2017). 145

[156] Souris, F., Christiani, H. & Davis, J. Tuning a 3D microwave cavity via superfluid helium at millikelvin temperatures. *Appl. Phys. Lett.* **111**, 172601 (2017). 145

[157] Childress, L. *et al.* Cavity optomechanics in a levitated helium drop. *Phys. Rev. A* **96**, 063842 (2017). 145

[158] Reulet, B. *et al.* Acoustoelectric effects in carbon nanotubes. *Phys. Rev. Lett.* **85**, 2829–2832 (2000). 147

[159] Miseikis, V., Cunningham, J. E., Saeed, K., O'Rorke, R. & Davies, A. G. Acoustically induced current flow in graphene. *Appl. Phys. Lett.* **100**, 133105 (2012). 147

[160] Meyer, N. & Jørgensen, M. Acoustoelectric effects in piezoelectric semiconductors with main emphasis on cds and zno. In Madelung, O. (ed.) *Advances in Solid State Physics*, 21 – 124 (Pergamon, 1970). 147

[161] Hermelin, S. *et al.* Electrons surfing on a sound wave as a platform for quantum optics with flying electrons. *Nature* **477**, 435–438 (2011). 147

[162] Schlosshauer, M. Quantum decoherence. *Phys. Rep.* **831**, 1–57 (2019). 147

[163] Talyanskii, V. *et al.* Quantized current in one-dimensional channel induced by surface acoustic waves. *Physica B Condens. Matter* **249**, 140–146 (1998). 147, 174

[164] Chen, S. & Song, L. The fractional acoustoelectric current plateau induced by the energy-dependent tunnelling from dynamic quantum dots into an impurity dot. *EPL (Europhysics Letters)* **115**, 37009 (2016). 147, 174

[165] Ebbecke, J. *et al.* Acoustoelectric current transport through a double quantum dot. *Phys. Rev. B* **72**, 121311 (2005). 147, 174

[166] Byeon, H. *et al.* Piezoacoustics for flying electron qubits on helium. *arXiv preprint arXiv:2008.02330* (2020). 148

[167] Gulyaev, Y. V. & Plesskiĭ, V. P. Propagation of acoustic surface waves in periodic structures. *Sov. Phys. Uspekhi* **32**, 51–74 (1989). 150

[168] Wilen, L. A. *Study of electrons on the surface of helium.* Ph.D. thesis, Princeton University (1986). 151

[169] Ingebrigtsen, K. Surface waves in piezoelectrics. *J. Appl. Phys.* **40**, 2681–2686 (1969). 151, 176

[170] Fragner, A. A. *Circuit Quantum Electrodynamics with Electrons on Helium.* Ph.D. thesis (2013). 154

[171] Shikin, V., Klier, J., Doicescu, I., Würl, A. & Leiderer, P. Dip problem of the electron mobility on a thin helium film. *Phys. Rev. B* **64**, 073401 (2001). 161, 191

[172] Schoelkopf, R., Wahlgren, P., Kozhevnikov, A., Delsing, P. & Prober, D. The radio-frequency single-electron transistor (rf-set): A fast and ultrasensitive electrometer. *science* **280**, 1238–1242 (1998). 170

[173] Badrutdinov, A., Rees, D., Lin, J., Smorodin, A. & Konstantinov, D. Unidirectional charge transport via ripplonic polarons in a three-terminal microchannel device. *Phys. Rev. Lett.* **124**, 126803 (2020). 171

[174] Dykman, M. & Rubo, Y. G. Bragg-cherenkov scattering and nonlinear conductivity of a two-dimensional wigner crystal. *Phys. Rev. Lett.* **78**, 4813 (1997). 172

[175] Ikegami, H., Akimoto, H. & Kono, K. Nonlinear transport of the wigner solid on superfluid he 4 in a channel geometry. *Phys. Rev. Lett.* **102**, 046807 (2009). 172

[176] Moskovtsev, K. & Dykman, M. I. Mobility of a spatially modulated electron liquid on the helium surface. *Phys. Rev. B* **101**, 245435 (2020). 173

[177] Yeo, L. Y. & Friend, J. R. Surface acoustic wave microfluidics. *Annu. Rev. Fluid Mech.* **46**, 379–406 (2014). 173

[178] Rees, D. G. *et al.* Structural order and melting of a quasi-one-dimensional electron system. *Phys. Rev. B* **94**, 045139 (2016). 174

[179] Takita, M. *et al.* *Electrons on superfluid helium: towards single electron control.* Ph.D. thesis, Princeton University (2015). 187

[180] Klier, J., Schletterer, F., Leiderer, P. & Shikin, V. Equilibrium helium film in the thick-film limit. *Low Temp. Phys.* **29**, 716–719 (2003). 187

[181] Jazbinšek, M. & Zgonik, M. Material tensor parameters of $LiNbO_3$ relevant for electro- and elasto-optics. *Appl. Phys. B* **74**, 407–414 (2002). 190

[182] Rabaey, J. M., Chandrakasan, A. & Nikolic, B. *Digital Integrated Circuit Design a Design Perspective* (Prentice Hall, 2002), 2nd edn. 191